Shelf-sea gross and net production estimates from triple oxygen isotopes and oxygen-argon ratios in relation with phytoplankton physiology

by

Maria Isabel Seguro Requejo

Thesis submitted in fulfilment of the requirements
for the degree of

Doctor of Philosophy

University of East Anglia
School of Environmental Science

December 2017

© This copy of the thesis has been supplied on condition that anyone who consults it is understood to recognise that its copyright rests with the author and that use of any information derived there from must be in accordance with current UK Copyright Law. In addition, any quotation or extract must include full attribution.

Abstract

Shelf seas represent only 10 % of the ocean area, but support 30 % of oceanic primary production. There are few measurements of biological production at high spatial and temporal resolution in such physically dynamic systems. Here, I use dissolved oxygen-to-argon (O_2/Ar) ratios and triple oxygen isotopes ($\delta(^{17}O)$, $\delta(^{18}O)$) to estimate net and gross biological production seasonally in the Celtic Sea between summer 2014 and summer 2015, as part of the NERC Shelf-Sea Biogeochemistry programme. O_2/Ar was measured continuously using a shipboard membrane inlet mass spectrometer. Discrete water samples from hydrocasts were used to measure O_2/Ar, $\delta(^{17}O)$ and $\delta(^{18}O)$ depth profiles. The data were combined with wind-speed based gas exchange parameterisations to calculate biological air-sea oxygen fluxes. These fluxes were corrected for non-steady state and diapycnal diffusion to give net community production ($N(O_2/Ar)$) and gross O_2 production ($G(^{17}O)$). $N(O_2/Ar)$ was highest in spring at (33±41) mmol m^{-2} d^{-1}, and $G(^{17}O)$ was highest in summer at (494±370) mmol m^{-2} d^{-1}, while autumn was net heterotrophic with $N(O_2/Ar)$ = (–14±28) mmol m^{-2} d^{-1}. During spring, biological production was spatially heterogeneous, highlighting the importance of high-resolution biological production measurements. The ratio of $N(O_2/Ar)$ to $G(^{17}O)$, $f(O_2)$, was highest in spring at 0.18±0.03 corresponding to 0.34±0.06 in carbon equivalents; about 0.05 in summer and < 0 in autumn/winter. Statistical measurement uncertainties increase when terms other than air-sea exchange fluxes are included in the calculations. Additionally, electron transfer rate derived from fast repetition rate fluorometry measurements was compared with $G(^{17}O)$, but no simple relationship was found. This study characterised the seasonal biological patterns in production rates and shows that the Celtic Sea is a net carbon sink in spring and summer. Such measurements can help reconcile the differences between satellite and *in situ* productivity estimates, and improve our understanding of the biological carbon pump.

List of Figures

Figure 1.1. The Celtic Sea in a broader context 23

Figure 1.2. Schematic plot of $\delta^{17}O$ versus $\delta^{18}O$ 39

Figure 2.1. Area of study, the Celtic Sea 48

Figure 2.2. Optode's optical design (*Aanderaa* model 3830, serial no. 241) 51

Figure 2.3. Schematic of MIMS set-up. Figure 2.4. MIMS' isolation test 53

Figure 2.4 MIMS' isolation test. 56

Figure 2.5. Oxygen calibration of CTD sensor by the Winkler method 57

Figure 2.6. Modified schematic diagram of sample extraction unit 59

Figure 2.7. Extraction line set up 60

Figure 2.8. Schematic diagram showing the separation line for dissolved gases as seen with the LabVIEW 2013 software 61

Figure 2.9. Schematic diagram of a tube cracker 62

Figure 2.10. Schematic diagram of the Dual Inlet System from the 252 MAT operating manual 64

Figure 2.11. Results of six imbalance tests 68

Figure 2.12. Results of nine tests done by adding different amounts of nitrogen to aliquots of oxygen and argon mixtures 69

Figure 2.13. Equilibrated water experimental set-up 73

Figure 2.14. Results of seven equilibrated water experiments 75

Figure 2.15. Results of seven equilibrated water experiments 75

Figure 2.16. MIMS calibration with EW 78

Figure 2.17. Test for biofouling effect in $\Delta O_2/Ar$ showed from no significant differences between discrete USW and near surface CTD 79

Figure 2.18. USW $\Delta O_2/Ar$ measurements with MS and MIMS on summer 80

cruise 2014 (DY026) and 2015 (DY033), and spring cruise 2015 (DY029)

Figure 2.19. Biofouling effect in $\Delta O_2/Ar$ showed from the differences between USW samples measured before and after the 50 μm filter 81

Figure 2.20. MIMS data affected by biofouling (blue), MIMS data corrected (dark orange) and discrete samples used for the calibration (black) 82

Figure 3.1. Gas exchange coefficients based on wind speed parameterisations according to Wanninkhof (2014) (W2014) and Nightingale et al. (2000) (N2000) 85

Figure 3.2. Wind speed (m s-1) comparison between ship's winds and CCMP winds during cruise time 86

Figure 3.3. Wind speed comparison between CCMP winds and ODAS buoy at the CCS station during the same period as the cruise 86

Figure 3.4. Diapycnal diffusion based in different definitions of mixed layer depth (density in blue and oxygen in orange) 88

Figure 4.1. Area of study in the Celtic Sea, with sampling stations 97

Figure 4.2. $\Delta(O_2/Ar)$ along the cruise track in the Celtic Sea and English Channel 104

Figure 4.3. O_2/Ar supersaturation ($\Delta(O_2/Ar)$) from the USW during April 2015 105

Figure 4.4. Time variations in F_{bio} accounting for diapycnal diffusion 106

Figure 4.5. $\Delta(O_2/Ar)$ time variation for the 13-17 April 107

Figure 4.6. Net community production, diapycnal diffusion and temporal non-steady state oxygen fluxes 108

Figure 4.7. Zonal variations of net community oxygen production ($N(O_2/Ar)$) along the Celtic Sea 109

Figure 4.8. Zonal variations of gross oxygen production ($G(^{17}O)$) based on oxygen triple isotopic measurements from CTD along the Celtic Sea 110

Figure 4.9. Net oxygen community production ($N(O_2/Ar)$) vs. gross oxygen production ($G(^{17}O)$) from CTD water samples in the Celtic Sea 111

Figure 5.1. Sea surface temperature (ºC) (SST) of the west European shelf 124

Figure 5.2. $\Delta O_2/Ar$ samples from the CTD cast measured by MS and MIMS 126

Figure 5.3. USW $\Delta O_2/Ar$ by MIMS 132

Figure 5.4. Zonal variations of biological fluxes (F_{bio}) 133

Figure 5.5. Zonal variations of gross oxygen production (G_{ss}) 134

Figure 5.6. Time variations of mixed layer and euphotic zone 135

Figure 5.7. Zonal variations of $N_{ml}(O_2/Ar)$ (top) and $N_{eu}(O_2/Ar)$ (bottom) samples taken in autumn 2014 (DY018) 137

Figure 5.8. Zonal variations of $N_{ml}(O_2/Ar)$ (top) and $N_{eu}(O_2/Ar)$ (bottom) samples taken in spring 2015 (DY029) 138

Figure 5.9. Zonal variations of $N_{ml}(O_2/Ar)$ (top) and $N_{eu}(O_2/Ar)$ (bottom) samples taken in summer 2015 (DY033) 140

Fig 5.10. Zonal variations of $G_{ml}(^{17}O)$ (mmol m^{-2} d^{-1}) (top) and $G_{eu}(^{17}O)$ (bottom) samples taken in autumn 2014 (DY018) 142

Figure 5.11. Zonal variations of $G_{ml}(^{17}O)$ (mmol m^{-2} d^{-1}) (top) and $G_{eu}(^{17}O)$ (bottom) samples taken in spring 2015 (DY029) 143

Figure 5.12. Zonal variations of $G_{ml}(^{17}O)$ (mmol m^{-2} d^{-1}) (top) and $G_{eu}(^{17}O)$ (bottom) samples taken in spring 2015 (DY033) 145

Figure 5.13. Water column representation in station CCS (top) and CS2 (bottom) 148

Figure 5.14. $^{17}\Delta$ and $\Delta O_2/Ar$ depth profiles 149

Figure 5.15. F_{bio} vs. G_{ss} from CTD samples 151

Figure 5.16. $N_{ml}(O_2/Ar)$ vs. $G_{ml}(^{17}O)$ from CTD samples 152

Figure 5.17 Vertical profiles of chlorophyll (Chl *a*) 154

Figure 6.1. Vertical profiles of temperature (I), salinity (II), chlorophyll (III), and photosynthetic active radiation (IV) 168

Figure 6.2. Vertical profiles of nitrate + nitrite (I), ammonium (II), silicate (III), and phosphate (IV) 169

Figure 6.3. Relationship of $^{17}\Delta$ (ppm) with Chl *a* (mg m^{-3}) and DO (µmol l^{-1}) 170

Figure 6.4. Relationship of ETR with Chl *a* (mg m^{-3}) and DO (µmol l^{-1}) 171

Figure 6.5. ETR μmol photons m^{-3} s^{-1} against $^{17}\Delta$ ppm 172

Figure 6.6. Mean ETR μmol photons m^{-3} s^{-1} against $^{17}\Delta$ ppm 173

Figure 6.7. ETR μmol photons m^{-3} s^{-1} and $^{17}\Delta$ ppm per time of the day 174

Figure 6.8. ETR_{int} μmol photons m^{-3} s^{-1} against PAR μmol photons m^{-2} s^{-1} at each depth 174

Figure 6.9. Mean values of ETR μmol photons m^{-3} s^{-1} against $^{17}\Delta$ ppm in the mixed layer (ML) 175

Figure 6.10. ETR_{int} μmol photons m^{-2} s^{-1} against G(^{17}O) mmol m^{-2} d^{-1} in the mixed layer (ML) 176

Figure 6.11. ETR_{int} μmol photons m^{-2} s^{-1} and $^{17}\Delta$ ppm per date of the cruise 176

Figure 6.12. SIMPROF dendogram of a Bray–Curtis for the analysis of similarity based in a matrix of physicochemical parameters transformed with Log (X+1) 180

Figure 6.13. nMDS plot of a Bray–Curtis similarity matrix 181

Figure 6.14. Integrated values of ETR μmol photons m^{-2} s^{-1} against $G(^{17}O)$ mmol m^{-2} d^{-1} in the mixed layer (ML) 182

List of Tables

Table 2.1. From left to right, cruise ID for the RRS Discovery, month and year when the cruise began and season, cruise length, number of days the MIMS was measuring continuously O_2/Ar from the underway sea water supply (USW), number of CTD casts from which water samples for O_2/Ar and triple oxygen isotopes samples were taken, and number of CTD casts from which FRRF samples were taken for analysis in this thesis…….……....47

Table 4.1. Net community production at steady-state or biological O_2 fluxes (F_{bio}), gross production at steady-state ($G_{ss}(^{17}O)$), diapycnal diffusion (F_v) and $f(O_2)$ for all stations visited. Temporal non-steady state term (F_{nss}), production below the mixed layer (F_{bml}) and entrainment (F_e) for the stations visited repeatedly (units: mmol m^{-2} d^{-1} of O_2 equivalents). Stations on the first column as per order sampled. Hypens mean there is no sample…….…..…..112

Table 4. 2. Summary of previous results on biological production during the Celtic Sea spring bloom in comparison to the present study (units: mmol m^{-2} d^{-1} of O_2 equivalents). Different methods are shown in brackets. *G* stands for gross production; *P* for primary production, which is expected to be closer to *N* for 24 h. *N* stands for net community production……...…116

Table 5.1. Absolute uncertainty (σ), and relative uncertainty σ % of each term in the calculation of G_{ss}, F_{bio}, $G_{eu}(^{17}O)$, $N_{eu}(O_2/Ar)$……....130

Table 5.2. Seasonal representation (mean±sd) of F_{bio}, $N_{ml}(O_2/Ar)$, $N_{eu}(O_2/Ar)$, G_{ss}, $G_{ml}(^{17}O)$, $G_{eu}(^{17}O)$, R, R_{ml}, R_{eu} (mmol m^{-2} d^{-1}) in the Celtic Sea……...….146

Table 6.1. Definitions of photosynthetic parameters……....….165

Table 6.2. Mean values on the mixed layer of salinity (S), temperature (T), light

extinction coefficient (K_d), chlorophyll a (Chl *a*), nitrate and nitrite (NO^{-3} + NO^{-2}), silicate (SiO_4^{-4}), phosphate (PO_3^{-4}), integrated electron transport rate (ETR_{int}), and gross oxygen production ($G(^{17}O)$). The name of the stations is in order north to south……....178

Table of Contents

ABSTRACT 3

LIST OF FIGURES 4

LIST OF TABLES 8

ACKNOWLEDGMENTS 15

INTRODUCTION 16

CHAPTER 1. OVERVIEW OF METHODS TO ESTIMATE PRIMARY PRODUCTION IN HIGHLY DYNAMIC AREAS 21

1.1 PRIMARY PRODUCTION IN SHELF SEA AREAS 21

1.2 THE CELTIC SEA 23

1.3 INCUBATION AND BOTTLE METHODS TO MEASURE PRODUCTIVITY 25

1.3.1 THE STABLE ISOTOPES OF OXYGEN 28

1.3.2 ADVANTAGES OF MEASURING WITH STABLE ISOTOPES OF OXYGEN AND ARGON 32

1.4 NET PRODUCTION ESTIMATES BASED ON O_2/AR RATIOS. 33

1.4.1 GAS TRANSFER VELOCITY FROM WIND SPEED PARAMETERISATION (K) 35

1.4.2 MEMBRANE INLET MASS SPECTROMETRY (MIMS). 37

1.5 GROSS PRODUCTION ESTIMATES BASED ON $^{17}O/^{16}O$ AND $^{18}O/^{16}O$ RATIOS AND, THE DUAL METHOD. 38

1.5.1 ISOTOPE RATIO MASS SPECTROMETRY (IRMS) 41

1.6 REMOTE SENSING TO ESTIMATE PRIMARY PRODUCTION. 43

1.7 PHYTOPLANKTON PHOTOPHYSIOLOGY FROM FAST REPETITION RATE FLUOREMETRY (FRRF). 44

CHAPTER 2. SAMPLING AND METHODS FOR MEASURING ΔO_2/AR USING MEMBRANE INLET MASS SPECTROMETER (MIMS) AND TRIPLE OXYGEN ISOTOPES USING DUAL INLET ISOTOPE RATIO MASS SPECTROMETER (IRMS) 46

2.1 INTRODUCTION 46

2.2 SAMPLING 46

2.2.1 DISCRETE SAMPLING 48

DISCRETE SEAWATER SAMPLING FOR ANALYSIS USING THE WINKLER METHOD 49

DISCRETE SEAWATER SAMPLING FOR THE MEASUREMENT OF DISSOLVED GASES USING MIMS 49

DISCRETE SEAWATER SAMPLING FOR TRIPLE ISOTOPE MEASUREMENTS USING IRMS 49

2.2.2 CONTINUOUS SAMPLING FROM THE USW 50

OXYGEN OPTODE 50

MEMBRANE INLET MASS SPECTROMETER 51

SETTING UP FOR CONTINUOUS MEASUREMENTS ON BOARD 52
MODIFICATIONS 55

2.3 WINKLER METHOD FOR OXYGEN DETERMINATION AND CTD CALIBRATION 56

2.4 STABLE ISOTOPE ANALYSIS BY DUAL INLET ISOTOPE RATIO MASS SPECTROMETRY (IRMS) 58

2.4.1 DISSOLVED GAS SAMPLE EXTRACTION AND PURIFICATION 58
EXTRACTION OF DISSOLVED GASES 58
SEPARATION LINE 60
2.4.2 DUAL INLET ISOTOPE RATIO MASS SPECTROMETER (IRMS) 63
ZERO ENRICHMENT 66
2.4.3 MASS IMBALANCE CORRECTION 66
2.4.4 NITROGEN CORRECTION 68
2.4.5 DRY AIR CALIBRATION 70
2.4.6 CORRECTION FOR THE GAS PARTITION BETWEEN THE HEADSPACE AND WATER (Q) 71

2.5 EQUILIBRATED WATER WITH THE ATMOSPHERE (EW) 72

2.6 O_2/AR ANALYSIS BY MEMBRANE INLET MASS SPECTROMETER (MIMS) 76

2.6.1 BIOFOULING CORRECTION 78

CHAPTER 3. NET COMMUNITY PRODUCTION AND GROSS PRODUCTION CALCULATION 83

3.1 INTRODUCTION 83

3.2 NET COMMUNITY PRODUCTION 83

3.2.1 BIOLOGICAL AIR-SEA EXCHANGE FLUX (F_{BIO}) 83
3.2.2 WIND SPEED PARAMETERISATION FOR GAS EXCHANGE CALCULATION (K) 84
3.2.3 DIAPYCNAL DIFFUSION 88
3.2.4 ENTRAINMENT 89
3.2.5 TEMPORAL CHANGES 89
3.2.6 $N(O_2/AR)$ BELOW THE MIXED LAYER 90
3.2.7 DIFFERENCES IN O_2 AND AR SOLUBILITIES 90

3.3 GROSS PRODUCTION 90

3.3.1 DIAPYCNAL DIFFUSION 91
3.3.2 ENTRAINMENT 92
3.3.3 TEMPORAL CHANGES 92
3.3.4 GP BELOW THE MIXED LAYER 93

3.4 CALCULATION OF ƒ-RATIO 93

CHAPTER 4. HIGH-RESOLUTION NET AND GROSS BIOLOGICAL PRODUCTION DURING A CELTIC SEA SPRING BLOOM 95

4.1 INTRODUCTION 95

4.2 MATERIAL AND METHODS 96

4.2.1 STUDY AREA 96
4.2.2 METHODS 97

4.2.3 CALCULATION OF NET COMMUNITY PRODUCTION, $N(O_2/Ar)$ 99
4.2.4 CALCULATION OF GROSS PRODUCTION, $G(^{17}O)$ 102
4.2.5 CALCULATION OF *F* RATIO 103

4.3 RESULTS 103

4.3.1 METABOLIC BALANCE 103
4.3.2 BIOLOGICAL OXYGEN SEA-AIR FLUXES FROM CONTINUOUS SAMPLING 105
4.3.3 NET COMMUNITY PRODUCTION, DIAPYCNAL DIFFUSION AND TEMPORAL CHANGES 106
4.3.4 NET COMMUNITY PRODUCTION, GROSS PRODUCTION AND *F* RATIO FROM DISCRETE SAMPLES 109

4.4 DISCUSSION 113

4.4.1 EVOLUTION OF THE SPRING BLOOM 113
4.4.2 BIOLOGICAL PRODUCTION IN THE CELTIC SEA 114
4.4.3 CARBON EXPORT EFFICIENCY OF THE SHELF SEA DURING THE SPRING BLOOM 116

4.5 CONCLUSIONS 119

CHAPTER 5. INTERANNUAL AND SEASONAL VARIABILITY OF GROSS BIOLOGICAL PRODUCTION AND NET COMMUNITY PRODUCTION IN THE CELTIC SEA 121

5.1 INTRODUCTION 121

5.2 MATERIAL AND METHODS 123

5.2.1 AREA OF STUDY 123
5.2.2 METHODS 124
CONTINUOUS MEASUREMENTS 124
DISCRETE MEASUREMENTS 125
NET COMMUNITY AND GROSS BIOLOGICAL PRODUCTION CALCULATION IN THE MIXED LAYER AND THE EUPHOTIC ZONE 126
UNCERTAINTY QUANTIFICATION 127

5.3 RESULTS 131

5.3.1 INTERANNUAL AND SEASONAL CYCLE OF $\Delta O_2/Ar$ AND BIOLOGICAL FLUXES 131
5.3.2 SEASONAL GROSS PRODUCTION AND NET COMMUNITY PRODUCTION 134
EUPHOTIC ZONE VS. MIXED LAYER DEPTH 134
NET COMMUNITY PRODUCTION SEASONALLY 135
GROSS PRODUCTION SEASONALLY 140
5.3.3 CCS AND CS2 SEASONALITY 146
5.3.4 SEASONAL VARIATIONS OF $^{17}\Delta$ AND $\Delta O_2/Ar$ IN THE WATER COLUMN. 149
5.3.5 SEASONAL *F* RATIO 150

5.4 DISCUSSION 152

5.4.1 SEASONALITY OF BIOLOGICAL PRODUCTION PATTERNS 152
5.4.2 PRODUCTION RATES IN SHELF SEAS 154
5.4.3 SEASONAL *F*-RATIO 156

5.5 CONCLUSION 158

CHAPTER 6. COMPARING TWO POWERFUL AQUATIC GROSS PRODUCTION TECHNIQUES IN PHYSICALLY COMPLEX WATERS: OXYGEN ISOTOPE SIGNATURES VERSUS ELECTRON TRANSFER RATES. 160

6.1 INTRODUCTION 160

6.2 MATERIAL AND METHODS 162

6.2.1 STUDY AREA 162
6.2.2 METHODS 162
GROSS OXYGEN PRODUCTION ESTIMATED FROM PHOTOSYNTHETIC ISOTOPIC SIGNATURES 163
6.2.4 GROSS OXYGEN PRODUCTION ESTIMATION BY FAST REPETITION RATE FLUOROMETRY 164
6.2.6 STATISTICAL ANALYSIS 166

6.3 RESULTS 167

6.3.1 PHYSICOCHEMICAL STATE IN THE CELTIC SEA DURING THE STUDY PERIOD 167
6.3.2 RELATIONSHIP OF FRRF AND TRIPLE OXYGEN ISOTOPES WITH ENVIRONMENTAL VARIABLES 170
6.3.3 VARIABILITY OF K_{O2} 171
6.3.4 THE CELTIC SEA ASSEMBLAGES DURING THE SPRING BLOOM 177

6.4 DISCUSSION 182

ANALYSIS OF GROSS PRODUCTION DISCREPANCIES 183

6.5 CONCLUSION 185

CHAPTER 7. CONCLUSIONS AND FUTURE WORK 186

CONCLUSIONS 186
FUTURE WORK 188

APPENDIX A: PROTOCOLS 191

1. WINKLER METHOD FOR DISSOLVED OXYGEN 191
SAMPLING 191
FIXING 193
STANDARDISATION OF SODIUM THIOSULFATE 194
SAMPLE TITRATION 196
2. LIQUID PHASE DISPLACEMENT AND EXTRACTION OF DISSOLVED GASES FROM SEAWATER HEADSPACE 197
SAMPLE EXTRACTION 197
TRANSFERRING SAMPLES TO SEALED TUBES 199
3. SEPARATION OF N_2 FROM O_2 AND AR IN AUTOMATED GC LINE 202
4. PREPARATION OF REFERENCE GAS (4.7 % AR IN O_2) 204
5. ANALYSIS OF STABLE ISOTOPES IN IRMS - MAT 252 206
ZERO ENRICHMENT 206
DRY AIR AND SAMPLES 207
6. PRESSURE IMBALANCE TEST OF MAT 252 O_2 ISOTOPOLOGUE MEASUREMENTS 209
7. N_2 INTERFERENCE TEST OF MAT 252 O_2 ISOTOPOLOGUE MEASUREMENTS 211
8. BELLOWS CALIBRATION IN MAT 252 213
9. DATA DOWNLOAD FROM MAT 252 215
JAVA DESKTOP APPLICATION 216

APPENDIX B: MIXED LAYER AND EUPHOTIC ZONE DEPTHS 219

GLOSSARY 221

REFERENCES 225

Acknowledgments

This thesis was possible thanks to the funding support from UK Natural Environment Research Council (NERC) grant number NE/l000172/1 and a Cefas CASE studentship. This work contains data supplied by NERC, for which James Fox and Malcolm Woodward are data originators.

Thanks. I would like to thank my supervisor, Jan Kaiser, for giving me the opportunity to do this PhD and always trust on me *"I am sure you can do it Chata"*.

Thanks also to my other four supervisors, Alina Marca, Su Painting, Jamie Shutler and David Suggett. They all taught me a lot of science from different disciplines, but especially thanks to Alina for her thorough teaching in the stable isotope lab.

Thanks to my office colleagues: Alida, Chan, Gianfranco, Geoff, Dave, Yanhui, Fazrin, Maria, Seth, Karina and Elise. 4 years of amazing environment in the office, sharing science, advices, and gossip… Guys, you made the 01.37K my second home. Looking forward for the next international dinner! Thanks to Umberto, Richard, Osgur, Michael, Marina, Tahmeena, Elena, and Clare O. for the coffee breaks, ice cream breaks (and pints) that help to survive the sometimes-tough thesis.

Thanks to the PhD students from the Kaiser Lab, every group activity was great fun. My hips will not forget the delicious Thursday's cakes.

Thanks to all the scientists and crew from the SSB and RAPID cruises. Baby-Clare, Charlotte, Sharon, Alex, Mark, Pete, Delphine, Sam, Chris, etc. You know guys you are too many to fit here, but be sure that all of you and the magic moments fit perfectly in my memories.

Thanks to those that although are not part of the PhD, they have been always next to me: Thanks to Jan (again) for introducing me to the Hash House Harriers "running" club, I learnt a lot about the English culture and got rid of some of the Thursday's cakes…thanks to Niki and the kids for bringing always good vibes.

Thanks to the Cai's people, Gina, Nestor, Silvana, Ana, Marta, Marina, Julio, Juanlu, Alfonso, Emilio and Sok. Also to Marta B. and Caroline, it is great to know that those good friends are always up for little "quedadas" around the world.

And most importantly, to my family and best friends, mamá, Eña, Marco, Alvaro, Vero, Anabel, Patri, Caro, gata, and of course Ramon, all of them are the greatest support that I could ever have.

Science is better when we work together; remain.

Introduction

Background on Shelf sea biogeochemistry

Shelf seas are key areas in the biogeochemical cycle of carbon, acting as a source of carbon to the open adjacent oceans or as a sink for inputs of terrestrial waters (Chen, 2010).

Biologically, the shelf sea areas are more productive than open oceans (Muller-Karger, 2005, Simpson and Sharples, 2012). Accurate measurements and improved understanding of carbon exchange between the shelf sea and the atmosphere is of special interest for predicting changes in atmospheric CO_2 and understanding its linkages to climate change. It is uncertain how future climate change would affect the global carbon cycle (Bopp and Le Quéré, 2013). Thus understanding carbon uptake within the shelf seas and its exchange with the atmosphere is crucial understanding the carbon cycle.

The oxygen cycle is closely coupled to the carbon cycle through the processes of photosynthesis and respiration. Due to this link, it is possible to stoichiometrically relate oxygen measurements based estimates of net community production with carbon production estimates (Laws, 1991, Marra, 2002). The amount of organic carbon that stays in the mixed layer is very little compared to the net community production (NCP), therefore NCP approximately represents the carbon export production (Huang et al., 2012).

Shelf seas experience different physical and biogeochemical processes than those that take place in open oceans (Simpson and Sharples, 2012). Physical conditions are mostly driven by weather seasonality, climate and tides. The sources of inputs (e.g. nutrients) from the land waters make the shelf seas more heterogeneous, with a wide range of biochemical processes and in which anthropogenic activities have a direct impact.

The Shelf Sea Biogeochemistry (SSB) research programme

This study is part of the National Environmental Research Council (NERC) Shelf Sea Biogeochemistry (SSB) programme (http://www.uk-ssb.org). The scope of the programme is to better understand the fundamental biogeochemical processes in European shelf seas, such as the role of shelf seas in carbon storage, nutrient cycling, primary and secondary production, and air-sea exchange of greenhouse gases (CO_2 and N_2O). This thesis focuses on primary production and rates of air-sea exchange of oxygen. Data were obtained during 4 research cruises in the Celtic Sea during 2014-2015, and data interpretation and contextualisation was supported by remote sensing data and environmental information collected by other scientists participating in the SSB programme.

Motivation

In the last few centuries greenhouse gas concentrations have increased in the atmosphere (Cubasch, 2013), due to anthropogenic activities, and CO_2 emissions, play an important role in the climate change, with the consequences for the environment. Currently, about 25% of anthropogenic CO_2 emissions are taken up and stored in the oceans (Le Quéré et al., 2010). The oceans can store 50 times more CO_2 than the atmosphere. There is a flux of anthropogenic CO_2 into the oceans because of the partial pressure disequilibrium between atmosphere and the sea surface (Bopp and Le Quéré, 2013). Records of annual exchanges of carbon with the atmosphere suggest that shelf sea areas are sinks of carbon. Shelf seas receive dissolved inorganic carbon and particulate organic carbon mainly from the rivers and estuaries but also from open oceans. Calculating annual exchanges of carbon is difficult because past studies often present a fragmented picture due to the low spatial and temporal resolution of the sampling and because the complexity of air-sea gas exchange parameterizations (Wanninkhof et al., 2013, Le Quéré et al., 2010). This research produced seasonal estimates of oxygen between the atmosphere and the shelf sea, which are proportional to the carbon exchanges in the shelf sea.

Approach

The aim of this study is to quantify primary production in the Celtic Sea using two different techniques; 1) O_2/Ar ratios to estimate net community production (NCP) and 2) the "dual delta method" to estimate gross primary production ($G(^{17}O)$); both combined with gas exchange parameterisations and remote sensing.

Net production can be obtained from continuous high-resolution measurements in the surface and snapshots deeper in the water column. Gross production can be estimated using the triple oxygen isotopes based on discrete dissolved gas samples taken from the surface and deeper in the water column. Other parameters and environmental variables will be used to correlate the primary production with the shelf sea conditions.

Sampling in spring, summer and late autumn will allow the calculation of seasonal production. Satellite images of ocean colour and sea surface temperature were used to place the sampling area in a wider context. Gross production estimated using the dual isotope method will be compared with state-of-the art in fast repetition rate fluorometry (FRRf) protocols to better understand the data from the fluorescence technique. It is worth mentioning that the two techniques together can provide direct estimates of the export efficiency (*f* ratio) of the biological shelf carbon pump, avoiding the need for gas exchange parameterisations.

The specific objectives of this thesis are:

- Infer spatial variations of net and gross oxygen production rates from O_2/Ar and triple oxygen isotopes in the Celtic Sea during the spring season.
- Estimate seasonal production from cruise-to-cruise changes.
- Compare $G(^{17}O)$ with FRRf-based physiological turnover.

This thesis contributes to two of the four main questions of the SSB programme:

- What are the current annual exchanges of carbon in shelf seas?
- What are the physical and biochemical controls of shelf primary production?

Thesis structure

In Chapter 1 I give an overview of previous studies of primary production in the Celtic Sea. Then a review of traditional methods used to measure primary production followed by a literature review of the two methods used in this thesis. I finish this chapter covering briefly two novel high-resolution methods to estimate primary production that will be combined with the two main methods used here.

In Chapter 2 I describe the sampling and measurement methodologies that I followed prior to calculating primary production based on continuous measurements of dissolved sea water gases while onboard of a research ship using a membrane inlet mass spectrometer (MIMS) and based on discrete sea water samples that I measured on a dual inlet isotope ratio mass spectrometer (IRMS) in the UEA lab. I also included the sampling and methodology for the analysis of dissolved oxygen concentrations using the Winkler method.

In Chapter 3 I explain the calculations necessary to estimate net community production and gross production, including non steady state terms like diffusion, entrainment, changes over time and production below the mixed layer. I also explain how to calculate the efficiency of the biological pump.

In Chapter 4 I present the results from the 2015 spring cruise in which the peak of the spring phytoplankton bloom was captured and support that data with satellite images. In this chapter I highlight the importance of measuring primary production at high resolution, especially in the spring season when biological changes occur rapidly.

This chapter has been published as "Isabel Seguro, Alina D. Marca, Suzanne J. Painting, Jamie D. Shutler, David J. Suggett, Jan Kaiser, (2017). "High-resolution net and gross biological production during a Celtic Sea spring bloom". Progress in Oceanography. https://doi.org/10.1016/j.pocean.2017.12.003

In Chapter 5 I calculate seasonal net community production and gross production. I also show the interannual production at steady state in the Celtic Sea, evaluate the importance of non steady state calculations seasonally and estimate the carbon fraction

that is available for carbon export.

In Chapter 6 I combine gross production estimated from fast repetition rate fluorometry with gross production estimated from triple oxygen isotopes. In this chapter I performed a statistical analysis to assess whether or not environmental variables drive the variability between the two techniques.

In Chapter 7 I present the conclusions of each chapter and suggest future work that could improve or move forward the achievements from this research.

Chapter 1. Overview of methods to estimate primary production in highly dynamic areas

1.1 Primary production in shelf sea areas

The oceans cover around 70 % of the Earth's surface and contain much more carbon than the atmosphere (Bopp and Le Quéré, 2013). There are two processes that move CO_2 from the atmosphere into the oceans: the physical and the biological pump. An increase in CO_2 in the atmosphere (e.g. anthropogenic CO_2 emissions) creates a partial pressure difference that induces invasion of CO_2 into the ocean. Once in the ocean, the CO_2 can be taken up biologically by phytoplankton, part of which is fixed (e.g. phytoplankton photosynthesis) (Eq. 1.1). A fraction of this fixed organic carbon sink to the deep ocean or seabed in the form of particulate organic carbon (POC) (e.g. dead cells), known also as export production. This chain of processes reduces the partial pressure of CO_2 in the surface and enables more CO_2 to be taken up by the ocean. The key process in the carbon pump is then the primary production and is defined as the synthesis of organic matter from inorganic compounds. A simplified representation of the phytoplankton photosynthesis reaction is:

$$CO_2 + H_2O \rightleftharpoons CH_2O + O_2 \quad (1.1)$$

The photosynthesis reaction occurs in presence of light, while respiration (reverse reaction equation 1.1) mainly occur in darkness. Photosynthesis by oceanic phytoplankton contributes between 40 – 60 % of the total carbon fixed on Earth (Sakshaug et al., 1997, Wilhelm et al., 2004, Falkowski, 2007). Only 5 % of the primary production at sea is already equivalent to the total amount of anthropogenic CO_2 emissions (Wilhelm et al., 2004).

Although shelf sea areas only cover about 7 – 10 % of the oceans, they contribute 15 – 30 % to oceanic primary production (Hickman et al., 2012, Simpson and Sharples, 2012). Principal limiting factors of primary production in the oceans are light

availability and nutrients. Coastal waters are usually more turbid than open oceans, however, the euphotic zone generally does not reach depths below 200 m. Shelf seas have a depth of about up to 200 m, therefore photosynthesis could in theory occur anywhere within the water column. The shelf seas are the first receptors of continental runoff and riverine input. High light availability and nutrients, arriving mainly from land but also from open ocean, make these regions very productive (Rees et al., 1999). This high phytoplankton productivity affects the whole food chain, enabling the shelf seas to provide more than 90% of the fish caught for consumption (Simpson and Sharples, 2012). As shelf seas have higher biological production than open oceans, then these areas should also act as a greater source of O_2 and C sink.

The climate is changing as a result of increasing greenhouse gases emissions such as CO_2 (Cubasch, 2013). CO_2 is currently the dominant carbon bearing trace gas with the higher concentration, well above methane or carbon monoxide (Ciais, 2013). Fluxes of atmospheric CO_2 to the ocean are known to be sensitive to climate change. Carbon cycle model predictions show that climate change could reduce ocean CO_2 uptake (e.g. by changing ocean stratification), which in turn, would increase global warming (Le Quéré et al., 2010, Poulton et al., 2014, Bopp and Le Quéré, 2013, Ciais, 2013). Therefore it is crucial to understand and quantify shelf sea primary production to be able to accurately model the carbon cycle and predict its response under a changing climate.

Previous studies of primary production show discrepancies, pointing out that the spatial and temporal variation of the primary production in shelf seas is not fully understood (Daniels et al., 2015, Robinson et al., 2009, Hickman et al., 2012, Poulton et al., 2014, Rees et al., 1999, Joint et al., 2001). Existing methods for determining primary production rates often disagree and their low spatio-temporal resolution means that they cannot resolve the heterogeneity of shelf seas (Robinson et al., 2009). This thesis describes and demonstrates how primary production can be quantified by measuring the dissolved oxygen in the water. This novel method is first evaluated, compared and contrasted with previous studies in the Celtic Sea and then used to study and characterise the efficiency of the carbon pump seasonally. The method is able to capture the heterogeneity of the shelf seas even during the quick changing spring

bloom. The following section (1.2) provides an overview of the shelf sea that forms the focus of this study; while from section (1.3) provides and overview of traditional methods used to measure primary production followed by the methods used in this thesis.

1.2 The Celtic Sea

The temperate Celtic Sea comprises an area of the North Atlantic Ocean and is also a part of the larger NW European shelf. It is bordered by the Irish coast and Saint George's Channel at its northern limit, the British coast and the Bristol Channel at the east, the coast of France at its southern limit, and by the end of the continental shelf at its western boundary (200 m isobath) (Fig. 1.1). Its entire boundary coast is used by major industrialised nations (Ireland, France, United Kingdom).

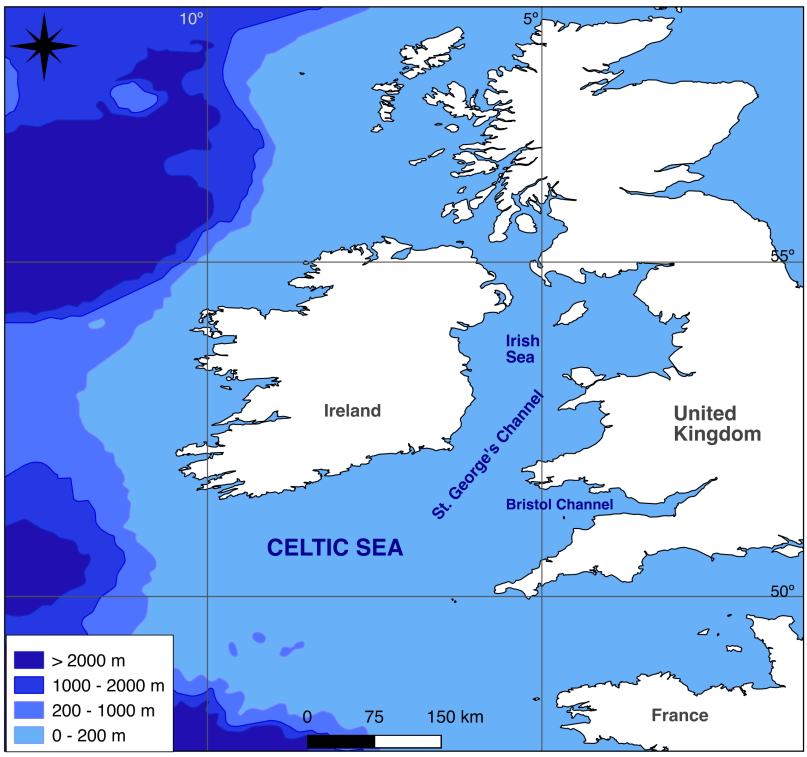

Figure 1.1. The Celtic sea in a broader context. Different tones of blue define bathymetry. The edge of the shelf is delimited by the 200 m isobath. White patches represent land.

The water column in the Celtic shelf is typically well mixed by the effect of wind,

currents and internal tides during autumn and winter. It becomes stratified due to surface heating and weaker winds during spring and summer (Hickman et al., 2012). The barotropic M_2 tide at the edge of the shelf sea of the Celtic Sea cause currents that would gradually vary between 0.1 to 0.3 m s^{-1} from the southwest to the St. George's Channel respectively (Pingree et al., 1976, Pingree et al., 1984, Brown et al., 2003). From the Bristol Channel to the shelf edge the bottom depth increases from 50 m to 200 m. A zone named 'Celtic Deep' extends via the St. George's Channel into the southern Irish Sea. Stronger currents in this channel (up to 0.3 m s^{-1}) have resulted in a deeper bottom depth (~100 m) in this area. In the Celtic Deep, the currents follow a baroclinic cyclonic circulation. At the southward area, the currents follow anticyclonic circulation (Brown et al., 2003). Overall, this currents have been considered weak and spatially variable compared with the adjacent areas of the European Shelf Sea (Holt et al., 2001)

The spring bloom occurs normally in April, when the water column becomes stratified, and can continue for between two weeks to two months (Rees et al., 1999, Sharples et al., 2006). During the spring bloom the production in the Celtic Sea is generally dominated by phytoplankton that are >2 μm in size, whereas during winter the water column is fully mixed and a more balanced size distribution of phytoplankton from pico- to microplankton size classes are evident (Rees et al., 1999). A subsurface chlorophyll (Chl *a*) maximum below the mixed layer typically occurs during summer (Moore et al., 2006).

The Celtic Sea, like many other coastal zones, is an important economic and recreational resource. Early publications concerning the Celtic Sea can be predominantly found in fisheries journals. There was little or no information about spatial and temporal distribution of phytoplankton production in the Celtic Sea before the study by Pingree et al. (1976). Hundred of rivers discharge in this sea; human activities and climate change effect can be detected by changes in patterns of the primary production, that in turn affects the fisheries (Painting et al., 2017). Papers such as that in Sharples et al. (2013) show the clear correlation between fishing areas and high primary production. This demonstrate how important it is to know accurately the magnitude of primary production in shelf seas and its sensitivity to climate change, because among other things, it may affect commercially exploited species of this

highly populated coasts.

1.3 Incubation and bottle methods to measure productivity

Primary production (PP) in aquatic systems is defined as the rate of inorganic carbon transformed into organic matter by phytoplankton photosynthesis. In the literature we can find that different authors speak about primary production in terms of carbon, oxygen, nitrogen, Chl *a* etc., as it is possible to estimate primary production from many methods and "currencies". C and O_2 are obvious ways because the two products from the photosynthesis are carbohydrates (CH_2O) and dissolved O_2. Energy used in the photosynthesis process is not only used to fix carbon, but also to fix nitrogen, meaning that the methods to measure primary production using nitrogen are also plausible (Laws, 1991, Sakshaug et al., 1997, Davies et al., 2003). Many of these quantities can be converted to others, for example, the ratio of O_2/CO_2 is known as the photosynthetic quotient (PQ). PQ values then allow a link between oxygen and carbon units.

The term gross production in terms of O_2 is the rate at which O_2 is produced by the splitting of water during the photosynthesis and not reduced for losses to respiration. In terms of carbon, gross primary production (GPP) is to the total rate of organic carbon production over 24 hours (Sakshaug et al., 1997). It can also be defined as the rate of photosynthetic electron transport flow to terminal electron acceptors in absence of any respiratory losses (Falkowski, 2007).

Net primary production (NPP) is the difference between the carbon taken up by GPP and that lost to respiration (Falkowski, 2007). Direct measurements of net primary production (NPP) in nature are fundamentally impossible because the difference between oxygen production and respiration cannot be isolated from the influence of biological and physical process of the surrounding environment, for example, discerning from algal respiration to total respiration losses (Falkowski, 2007). In reality, not only autotrophs contribute to the PP, as the process also includes the heterotrophs, so the correct term is net community production (NCP). This term encompasses O_2 consumption by all metabolic processes (dark respiration, Mehler

reaction, photorespiration, chlororespiration, alternative pathway, and nitrification) (Reuer et al., 2007). In terms of the implication for the carbon pump, NCP is the net amount of carbon removed from the atmosphere by aquatic phytoplankton through photosynthesis (Stanley et al., 2010). The rate of this removal is dependent on light, that in aquatic systems changes with the dissolved organic materials, absorption and scattering (Falkowski, 2007). Because photosynthesis is only possible in the euphotic zone, PP is generally estimated until the depth when the photosynthetic active radiation (PAR) is 1% of the surface incident light. Unless stated otherwise all production terms are presented with reference to oxygen.

Gross and net community production was first estimated by the light and dark bottles method. This method is based in the estimation of dissolved oxygen evolution inside light (photosynthesis) and the dark (respiration) bottles, and it typically analysed by Winkler titration (Winkler, 1888). Incubation can be performed on the deck of a ship, in the lab, or *in situ* by placing the samples within closed bottles at the same depth at which they were collected (Robinson et al., 2009, Kitidis et al., 2014, Soria-Píriz et al., 2017). These discrete samples need long incubation times, typically 24 hours to estimate NCP and 2-4 hours to estimate GPP, under controlled conditions (light, temperature, turbulence) that likely diverge from natural environmental conditions. Moreover, one can never be sure that the conditions inside the bottles truly represent the natural phytoplankton populations. The technique is reliable if it is known that the autotrophs are dominating the phytoplankton within the sample. If it is not the case then biases can occur. For example, if too many heterotrophs dominate the respiration the NCP could be underestimated. When the production is evaluated in oligotrophic areas, the application of the technique has to be very accurate and precise to achieve realistic measurements (Bender, 1987, Wilhelm et al., 2004). When the production is evaluated in eutrophic areas, high rates of production can alter the gas concentration inside the incubation bottle decreasing the photosynthesis and increasing the respiration (Deb et al., 1999). Nevertheless, is not possible to include the effect in the light variation due to the entrainment of the phytoplankton cell in the euphotic zone during the vertical turbulent movements (Macintyre et al., 2000). Thus, the light and dark oxygen method was the principal method to estimate gross and net community production until the discovery of the ^{14}C method in (Nielsen, 1952).

More advanced bottle incubations methods now exist which use tracers by labelling the samples with isotopes, ^{14}C, ^{15}N and ^{18}O. The ^{14}C method is one of the most commonly used methods for measuring biological production. The methods consist in the spike of radioactive ^{14}C in the form of inorganic carbon, bicarbonate ($H^{14}CO_3$) that after incubation is measured as assimilated carbon. This method is quite straightforward, sensitive and precise. The disadvantage with the approach is that the results are very sensitive to the incubation time and may actually represent the GPP if short incubation periods are used or NPP if longer periods are used (Falkowski, 2007). Furthermore, results of short incubation periods are often difficult to extrapolate to daily cycles and long incubation periods can underestimate NPP. Another disadvantage is its radioactivity.

The ^{14}C technique can be combined with ^{15}N using the dual isotope tracer technique to obtain carbon and nitrogen uptake rates. The methods consist in the spike of radioactive ^{15}N in the form $K^{15}NO_3$ or $^{15}NH_4CI$. With this technique incubations times are between 4 –7 hours, followed by filtration before analysis of the sample in a mass spectrometer (Lee et al., 2007). Similarly to the ^{14}C methods, the stable isotope ^{13}C can be used to estimate primary production by adding bicarbonate ($H^{13}CO_3$) or sodium bicarbonate ($NaH^{13}CO_3$) to the seawater sample. The main advantage of this method is that the isotope is not radioactive, but the approach is less sensitive to changes in production than that of the ^{14}C method (Cullen, 2001).

The ^{18}O method consists in the injection of this minor isotope in form of $H_2{}^{18}O$ in a water sample or in the headspace of the sample bottle. From the three natural stable isotopes of oxygen, ^{18}O accounts for only 0.2%, thus it can be used as a tracer of photosynthesis. It is then necessary to perform the incubation in light and measure the amount of ^{18}O produced during photosynthesis. The disadvantages of this particular method are that it is only possible to measure gross production GPP without taking into account the intracellular recycled oxygen (Bender, 1987, Falkowski, 2007) and the biases due to bottle effect. A recent study has used new incubation method which measures "*in situ"* productivity of sea ice algae using a ^{13}C and ^{15}N isotope tracer technique (Song et al., 2016), and although the measurements are performed *in situ*, incubation bottles are still used. A final way to measure primary production using incubation *in situ* is the closed-chamber CO_2–flux method (Migné et al., 2002). The

method relies on measurements of CO_2 exchanges within closed chambers using an infrared gas analyzer (IRGA). The main limitation of this method is the need of soft sediment and shallow waters. This incubation *in situ* method limits measurements of the PP to very shallow waters or to the bottom part of the water column.

The "dilution-method" improves upon the method proposed by Landry and Hassett (1982) and tries to solve the disadvantages of the traditional incubation bottle methods. By diluting the sample, it is possible to measure growing rates of phytoplankton under different conditions of grazing pressure (Wilhelm et al., 2004). The advantages of this method are the increase in the number of the samples possible from a single water sample, avoidance of long incubations, and the consideration of phytoplankton community structure; but the validity of assuming exponential growth rates have not been demonstrated (Kimmance et al., 2007). Also, a recent study suggests that this technique can overestimate phytoplankton growth (Paterson et al., 2008).

With all of these methods the results are a snapshot of the time and place sampled, and risk missing physical oceanography events such as eddies, which translates to a low-resolution study in the shelf sea. Further complications are possible due to the sample being confined in a bottle e.g. alteration of the natural conditions as grazing by exclusion, community sampling biases, leaching of chemicals from the bottle and/or heavy metal adsorption to the glass walls can lead to photosynthesis inhibition (Wilhelm et al., 2004).

Within this thesis, two different biogeochemical techniques are used to measure PP in shelf seas, which avoid the use of bottle confinement and allow the heterogeneity to be captured. These methods are the "dual delta method" and the O_2/Ar ratio method.

1.3.1 The stable isotopes of oxygen

For the purpose of primary production measurements we focus on oxygen isotopes. Oxygen has three stable isotopes of atomic mass numbers 16, 17, and 18, with abundances of 99.763%, 0.0375% and 0.1995% respectively (Garlick, 1974). Before

the discovery of isotopes, it was assumed that all atoms of an element had the same behavior (Urey 1946). Due to it mass, the nucleus of an atom defines its physical properties while its external electronic structure determines its chemical characteristics (Hoefs, 2004). However, isotopes are atoms of an element that differ only in the number of neutrons (Kendall and Mcdonnell, 1998), or molecules with different isotopes of the same element that present small differences in physicochemical properties. The differences, which result from variations in atomic masses, are called "isotope effects". There are about 300 stable isotopes divided between 59 elements.

The theory of isotope effects and isotope fractionation (explained below) has been studied in detail (Bigeleisen and Mayer, 1947, Urey, 1947, Monse, 1960, Muller, 1994, Mook, 2001). Here follows an overview of the basics to allow understanding of the remaining chapters of this thesis.

Isotope fractionation

Physical (evaporation, condensation, melting, crystallization, etc.), biological (e.g. photosynthesis) and isotopic exchange in chemical equilibrium, leads to separation of isotopic compounds called isotopic fractionation (Luz et al., 2014). During these reactions the isotopes will "redistribute" light and heavy ones according to their physico-chemical properties. Molecules vibrate with different fundamental frequencies, which are dependent on the mass of the isotopes. Translation and rotation motions have no effect on isotope fractionation, except for H, where rotation counts. Heavier molecules have lower zero point energies. According to this, heavier bonds are more difficult to "break" during a reaction, causing isotopic fractionation. For example, the molecule $H_2{}^{16}O$ compared to $H_2{}^{18}O$ has lower density, lower viscosity, and lower melting and boiling points (Hoefs, 2004). Therefore, fractionation processes give us information about the sources or the processes that formed the molecules (Kendall and Mcdonnell, 1998).

The fractionation process can occur during isotope exchange reactions or kinetic processes.

Kinetic processes are unidirectional or incomplete reactions in which the equilibrium constant changes and needs to be calculated from the partition function ratios (Hoefs,

2004, Kendall and Mcdonnell, 1998). Kinetic processes occur during water evaporation, diffusion, condensation, photosynthesis, etc.

Isotope exchange reaction is a special case of chemical equilibrium with no net reaction, in which the reactant and the product stay in contact during the reaction. The variables that most affect these isotope exchange reactions are temperature and pressure. In an isotope exchange reaction there are changes in the distribution of the isotopes:

$$A_1+B_2 \rightleftharpoons A_2+B_1 \tag{1.2}$$

where A and B represent chemical substances containing light or heavy isotopes represented by the subscripts 1 and 2. An example of isotope exchange reaction is the exchange of oxygen isotopes between H_2O and $CaCO_3$.

Isotope fractionation factor

The isotope fractionation factor (a) of any isotope is defined as the ratio (R) of two isotope ratios. This factor expresses the relative isotope composition of heavy and light isotopes. In general, a is close to 1, therefore in 1981, Mariotti et al. included the term $\varepsilon = a - 1$, that is called fractionation constant (Kaiser et al., 2004), where ε can also be expressed as equation 1.3 in ‰:

$$\varepsilon = \frac{R_B}{R_A} - 1 \tag{1.3}$$

Delta values

Isotopic compositions are represented as delta (δ) values. Delta is obtained by the derivation of the isotope ratio differences of a measured sample relative to a standard or reference material (e.g. Ar and O_2 mixture) (Eq. 1.4). For example, the $^{17}\delta$ of a molecule of O_2, is the ratio ($^{17}O/^{16}O$) of the less abundant isotope to most abundant one and is calculated as follow:

$$^{17}\delta \equiv \frac{(^{17}O/^{16}O)_{sam} - (^{17}O/^{16}O)_{ref}}{(^{17}O/^{16}O)_{ref}}$$

(1.4)

Because units of δ are smaller than 10^{-3} and the precision is about 10^{-6}, values will be multiplied by 10^3 and will be represented in ‰ (Kaiser, 2011b, Luz et al., 2014).

Mass dependent and non-mass dependent isotope effect

Fractionation can be mass or non-mass dependent. The terminology used in the literature is often unclear. The same terms referring to the same concept can be found called differently: non-mass dependencies or mass-independent fractionation, mass dependent or mass independent anomaly, isotope anomaly or isotope excess. Furthermore, the coefficients used to calculate isotope anomalies vary between authors making any comparison between laboratories very complicated. An effort is currently being undertaken by the IUPAC Project 2009-046-2-200 to define the terminology and physical quantities used to measure these anomalies. The IUPAC recommendations are taken into account within this thesis.

Isotope fractionation can be mass-dependent when the reaction rate or chemical equilibrium constant differences are directly proportional to the mass of the isotopes. Non-mass dependent fractionation occurs when the separation is due to its nuclear structure rather than on the difference in masses (Kendall and Caldwell, 1998). In other words, deviations from a range of values of mass-dependent fractionation are due to non-mass-dependent fractionation.

In the case of stable isotopes of oxygen, the empirical relationship or expected slope (λ) between $\delta^{17}O$ and $\delta^{18}O$ is about 0.516 ± 0.015 (Kaiser, 2008, Urey, 1947):

$$\delta^{17}O / \delta^{18}O = (1/32 - 1/33)/(1/32 - 1/34)$$

$$\delta^{17}O = 0.516\ (\pm\ 0.015)\ \delta^{18}O$$

(1.5)

Any deviation from this range indicates non-mass dependent fractionation. An example of non-mass dependent fractionation is the atmospheric O_2 isotopic composition. Isotopic fractionation in the stratosphere depletes the atmospheric oxygen equally in $\delta^{17}O$ and $\delta^{18}O$ due to ultraviolet induced interactions of O_2, O_3 and CO_2 (Luz and Barkan, 2000, Lämmerzahl et al., 2002). Mass dependent fractionation occurs for example by photosynthesis and respiration. Therefore, compared to atmospheric O_2, biological production of dissolved oxygen in water is enriched in ^{17}O and called ^{17}O excess.

As explained before, we can find different terminology and symbology in the literature. The ^{17}O excess is also found as isotope anomaly or ^{17}O balance (Kaiser, 2011b). In the following, ^{17}O excess is referred to as $^{17}\Delta$. The $^{17}\Delta$ has been defined in different ways (Kaiser et al., 2004). Finally, in this work we use the equation from Thiemens et al. (1995b) for calculating $^{17}\Delta$ that can be intuitively derived from equation 1.5 and the value of $\lambda = 0.5179 \pm 0.0006$ based on the weighted average ratio between the $^{17}O/^{16}O$ and $^{18}O/^{16}O$ isotope fractionations during respiration from Luz and Barkan (2005), Kaiser (2011b) for the mass-dependent isotope fractionation:

$$^{17}\Delta \equiv \delta^{17}O - 0.5179\ (\pm\ 0.0006)\ \delta^{18}O \qquad (1.6)$$

1.3.2 Advantages of measuring with stable isotopes of oxygen and argon

In aquatic systems there are two types of photosynthetic response, those that occur on short and long timescales. As we have seen in section 1.2 some short timescale responses, such as physical, biogeochemical, and physiological processes, are difficult to measure accurately in shelf seas by traditional methods due to their high variability.

The advantages of measuring with stable isotopes of oxygen are several. Stable isotopes of oxygen can be used to calculate gross and net production without incubation, obtaining data *in situ* and with less laborious preparation than bottle and/or incubation methods. Ratios of O_2/Ar recorded continuously by membrane inlet mass

spectrometer (MIMS) provide unprecedented high spatial and temporal resolution (Kaiser et al., 2005). Only remote sensing satellites can allow synoptic scale observations. However they only estimate primary production within the sea surface layer and the accuracy of the approach is dependent upon the calibration from *in situ* sampling. The MIMS technique requires instrument setup before sampling begins and minimal regular maintenance during sampling. The accuracy can be improved by calibration with discrete samples taken from the same source of water, which are then analysed by isotope ratio mass spectrometry (IRMS). Because primary production occurs along the euphotic zone, potentially within a depth of a few hundreds meters, discrete samples of the water column can be collected to allow a profile of primary production. These samples are measured with the IRMS to determine the $^{16,17,18}O$ stable isotopes and O_2/Ar. From $^{16,17,18}O$ stable isotopes and O_2/Ar is possible to calculate GPP and NCP. Moreover, when these two techniques are combined (NCP/GPP) provide direct estimates of the export ratio (Laws et al., 2000) in terms of oxygen.

The main disadvantage of the approach results from the calculation of the atmosphere-ocean gas fluxes, due to the uncertainty in the gas transfer wind speed parameterisations (Wanninkhof, 2014). However, no one of the two methods ($^{16,17,18}O$ stable isotopes and O_2/Ar) incur in the bottle potential biases mentioned above and combines sampling in the surface and in the water column, obtaining high-resolution measurements. The advantages and limitations of MIMS and IRMS instruments complement each other. Although this approach has its limitations, the high-resolution, accuracy and adaptability to any aquatic system has been a clear advantage (Juranek and Quay, 2013).

1.4 Net production estimates based on O_2/Ar ratios.

The dissolved O_2 in seawater can be used to estimate the NCP. The maximum of dissolved O_2 produced during spring or summer is typically found at the bottom of the mixed layer and within the euphotic zone (Stanley et al., 2009, Nicholson et al., 2014). Intuitively, an increase in oxygen *in situ* could mean an increase of the NCP; inversely a decrease could indicate less production or more respiration. However, it is not an

accurate way to estimate NCP because it does not consider any physical processes. Physical process such as variations in temperature and pressure, transport fluxes, diffusion and bubble injection also change the amount of dissolved O_2 in seawater. Recent studies have demonstrated that considering steady state conditions in the water column and therefore excluding vertical entrainment, lateral advective fluxes and mixing will likely introduce bias or error (Hamme et al., 2012, Nicholson et al., 2012, Nicholson et al., 2014). It is clear that we need a tracer that separates oxygen produced biologically from that added or removed by physical processes. Noble gases have a very low chemical reactivity, however, not all of the noble gases have the same physical properties as oxygen. From the noble gases dissolved in air and water, argon (Ar) is the most abundant and therefore the easiest to measure. Argon does not react during photosynthesis or respiration and has similar solubility and diffusivity to that of O_2. This makes Ar a good tracer to separate O_2 supersaturation (ΔO_2) from that of O_2 due to biological and physical processes. Craig and Hayward (1987) were the first to describe a technique for using O_2 and Ar differences to determinate NCP. The equation that describes the O_2/Ar supersaturation ($\Delta(O_2/Ar)$), and is defined as:

$$\Delta(O_2/Ar) = [c(O_2)/c(Ar)]/[(c_{sat}(O_2)/c_{sat}(Ar)] - 1 \quad (1.7)$$

where c is the dissolved gas concentration (mol m^{-3}) and c_{sat} is the saturation concentration at known temperature, pressure and salinity. In this way, variation in O_2 concentration due to biological production can be separated from physical forces. Physical surface processes such as warming and air injection due to strong winds and waves cause disequilibrium, while diffusion restores the equilibrium (Stanley et al., 2006). In this sense, it is necessary to consider air-sea exchange to allow the method to estimate NCP. Air-sea gas exchange coefficients (k) are used for surface waters as most of the exchange occurs due to molecular transfer in the top few centimeters. The gas exchange coefficient (k) is a measure of velocity as its units refer to a distance per unit of time (m d^{-1}). The O_2 produced is expressed in concentration units per volume (mmol m^{-3}). Then, NCP together with k will be expressed in mmol m^{-2} d^{-1}. NCP can be calculated from O_2 saturation and k using equation 1.8 (Reuer et al., 2007):

$$NCP = k(O_2)c_{sat}(O_2)\Delta(O_2/Ar) \quad (1.8)$$

1.4.1 Gas transfer velocity from wind speed parameterisation (*k*)

To calculate the aquatic O_2 photosynthetic contribution to the atmosphere it is necessary to know the rates of exchange or flux between the two phases.

Transfer of slightly soluble gases such us O_2 or CO_2 occur due to differences in the partial pressure of those gases in atmosphere and ocean surface. A simple starting equation defines the flux (F; mol m^{-2} s^{-1}) of soluble non-reactive gases as the gas concentration difference between two phases (C_2-C_1) per gas transfer velocity k (m d^{-1}):

$$F = k\,(C_2 - C_1) \tag{1.9}$$

Concentrations C_1 and C_2 can be applied to any phases, water-water or water-air, if the later, then we have to take into account the differences in solubilities and apply the dimensionless Ostwald solubility coefficient (α_{sol}) and the equation becomes:

$$F = k\,(C_w - \alpha_{sol}\,C_{atm}) \tag{1.10}$$

where C_w and C_{atm} are the concentration in water and atmosphere respectively. As the reference system to calculate the differences in concentration is arbitrary (from water to air or vice versa), by convention the reference system is from the ocean to the atmosphere, subsequently, positive values means fluxes from the water surface to the atmosphere and negative values when fluxes are into the water.

As mentioned in section 1.1, fluxes occur because differences in the partial pressure pO_2 (Pa), then if we write equation 1.10 based on its thermodynamic notation, a single coefficient of aqueous phase multiplies the partial pressure differences K_0 (mol m^{-3} Pa^{-1}) and the equation becomes $F = k\,K_0\,(pO_{2W} - pO_{2atm})$. For ideal gases K_0 is related to α_{sol} by $K_0 = \alpha_{sol}\,(R\,Tw)^{-1}$ where R (m^3 Pa K^{-1} mol^{-1}) is the ideal gas constant and Tw is the water temperature (Wanninkhof et al., 2009). Equation 1.10 applies for non-reactive gases, but for reactive gases the dimensionless chemical enhancement factor ε_f should be added at low gas transfer velocities (Wanninkhof and Knox, 1996).

$$F = k\,\varepsilon_f\,(C_w - \alpha_{sol}\,C_{atm}) \tag{1.11}$$

At this point, the calculation of the flux seems to be very simple and straightforward, however the calculation of k has been subject of debate since the two layer model was proposed from Liss and Slater (1974).

The first calculations of k were derived from Fick's first law (k = D/z) where D is the coefficient of molecular diffusion and z is the thickness of layer (Liss and Slater, 1974). Since then, the wind speed u has been corrected to 10 meters above the sea level (u_{10}) (Liss and Merlivat, 1986) and normalized by the dimensionless Schmidt number (Sc) that depends of the water temperature and density. The parameterization of k is not an easy task as the transfer is controlled and influenced by many different processes including wind speed, sea state, surface biological slicks and temperature. The units of k (m s^{-1}) revealed that it is mainly a velocity parameter, thus the main forcing parameters are the wind speed (u) and the state of the waves (Wanninkhof, 1992). These two parameters are difficult to measure accurately in a constant natural environment, and then several authors have tried to do relationships of k as a function of u to improve the approximation (Wanninkhof and Mcgillis, 1999, Nightingale et al., 2000, Sweeney et al., 2007, Wanninkhof et al., 1985, Liss and Merlivat, 1986, Wanninkhof, 2014).

The concentration of oxygen measured will be the result of the net oxygen remaining in the water and gas exchange history of the surface water. Reuer et al. (2007) proposed the weighted average of the wind speed parameterisation (k_w) during 60 days before sampling, but other authors suggest shorter periods, e.g. Huang et al. (2012). The numbers of days used to calculate k_w should be conditional of the variability of the winds in the sampling place and the mixed layer depth, as both together will give an approximation of the resident time of the gas in the water. A deeper mixed layer will extend the residence time, and strong winds will reduce it.

For this study I will use the parameterization of Nightingale et al. (2000) because gas exchange rates can vary from global parameterizations to shelf seas and Nightingale et al. (2000) used a dual tracer experiment in an area close to the Celtic Sea to calculate

the *k* dependence on wind speed.

1.4.2 Membrane Inlet Mass Spectrometry (MIMS).

Membrane inlet mass spectrometry provides information about phytoplankton photosynthesis and respiration through the analysis of certain dissolved gases (Beckmann et al., 2009). In order to increase the sampling resolution of dynamic waters such as shelf seas, continuous underway measurement systems have been developed.

Membrane inlet mass spectrometry is a technique invented by Hoch and Kok in 1963. This technique allows the sampling of dissolved gases from a liquid phase. The principle of the MIMS technique is to separate the dissolved gases with a semipermeable membrane and then detect the molecules directly with a mass spectrometer. This technique was considered very sensitive (Hoch and Kok, 1963), but even modern MIMS lack the ultra-high precision of IRMS (Beckmann et al., 2009).

Originally, an equilibrator chamber was used to extract the gases, but the time required for gas equilibration was too long (minutes to hour) (Tortell, 2005). The efficiency to extract dissolved gases depends on the material of the membrane and the flow. As the thickness of the membrane increases, the flow rate has to be reduced. Silicon membrane tubes need low flow rates < 1mL min^{-1} to be efficient (Kana et al., 1994). Such a slow rate reduces the sampling resolution of the approach. The silicon is also more permeable to water vapour than desired, which obligates to use a cryotrap to remove the water vapour before entering to the mass spectrometer. Teflon membrane tube has demonstrated to be less permeable to the water vapor without loosing permeability to dissolved gases (Kaiser et al., 2005) and so here a Teflon AF membrane (*Random Technologies*) was used.

MIMS needs to be calibrated against air-equilibrated water standards. Cassar et al. (2009) proposed an equilibrator in the inlet mass spectrometer (EIMS) that does not require air-equilibrated water standards. However, the time response of the EIMS is significantly longer and less sensitive than a MIMS system. Thus this method could be more appropriate for open ocean waters than in shelf seas. Marine systems with high

heterogeneity and productivity, such as the shelf seas, needs of quick time response measurements, consequently the MIMS is more suitable approach for this study. Recent studies use also the MIMS technology combined with ^{18}O tracer to understand molecular processes of CO_2 and HCO_3 fixation (Tolleter et al., 2017).

There are several advantages of the MIMS approach. MIMS can be mounted onboard, which permits the *in situ*, continuous and simultaneous analysis of several dissolved gases of seawater (CO_2, N, O_2, Ar). This is also a very simple technique to analyze volatile gases, it does not require exhaustive preparation of sampling materials, or the use of chemicals, and measurements are recorded directly without the need of post sample analysis in the laboratory. The parameters, flow, temperature and pressure need to be as constant as possible to avoid fluctuations in the measurements. Major problems are the presence of bubbles in the water sample that will dramatically alter the signal and the presence of particles that can reduce the permeability of the membrane, or reduce the water flow. The instability of the water flow increases the risk of isotopic fractionation (Sarma et al., 2006). These effects of the instability in the water flow can be minimized if ratios of two gases are used for any resulting analysis (i.e. O_2/Ar) (Tortell, 2005, Craig and Hayward, 1987).

NCP is analysed within this study by measuring O_2/Ar ratios with MIMS technique according to Kaiser et al. (2005).

1.5 Gross production estimates based on $^{17}O/^{16}O$ and $^{18}O/^{16}O$ ratios and, the dual method.

The three oxygen isotope exchange method was first introduced by Matsuhisa et al. (1978) when measuring the isotope exchange between water and quartz. Using the triple oxygen ratios Thiemens et al. (1995a) made important improvements in the knowledge of atmospheric chemical process in isotope non-mass dependent fractionation. Luz et al. (1999) later used the triple atmospheric oxygen for the estimation of global biosphere productivity. They state that the tropospheric ^{17}O anomaly works as a tracer of global biosphere production (for extended explanation see previous section 1.3.1, Mass

dependent and non-mass dependent isotope effect). One year later (Luz and Barkan, 2000) described an approach for estimating production of photosynthetic oxygen, based on the isotopic composition of dissolved oxygen of seawater and the rate of air-sea exchange (Fig. 1.2).

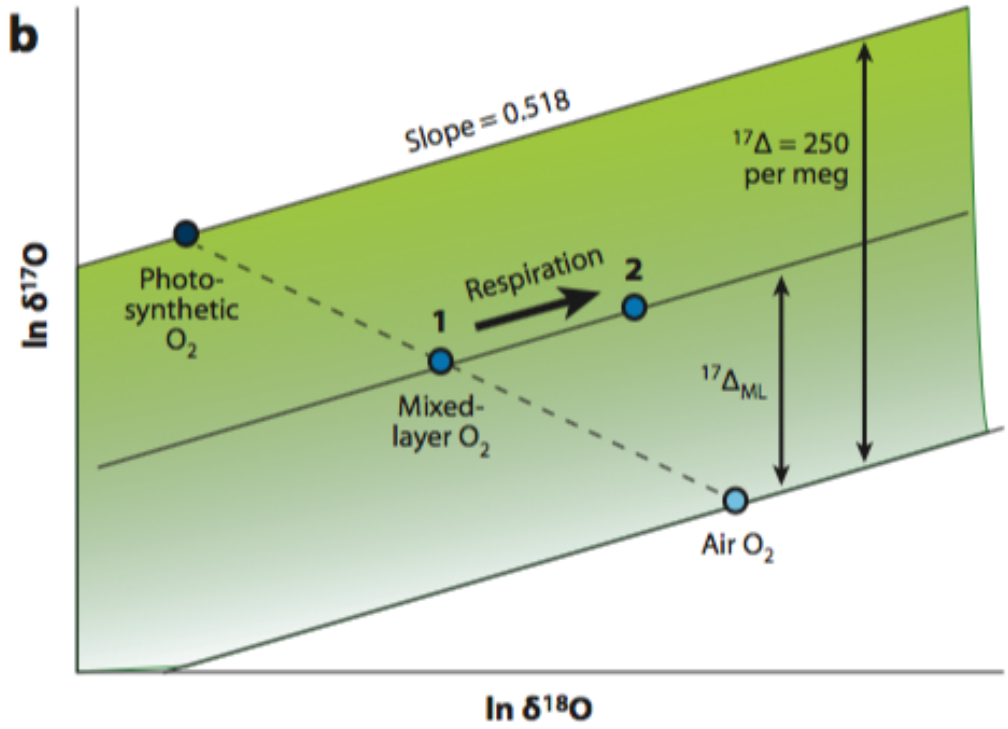

Figure 1.2. Schematic plot of $\delta^{17}O$ versus $\delta^{18}O$ extracted from (Juranek and Quay, 2013). $^{17}\Delta$ = 250 represents the maximum photosynthetic value. $^{17}\Delta_{ML}$ is the value in a two-end-members mixing model (ratio of gross production and air-sea exchange). Note how respiration doesn't have an effect in $^{17}\Delta$ because it has the same slope as photosynthetic fractionation.

Since then, several authors have used this technique to identify the signature of oxygen compounds, such as CO_2, O_2, O_3, NO_2, in terrestrial, atmospheric and aquatic realms, (Lämmerzahl et al., 2002, Helman et al., 2005, Sarma et al., 2006, Thiemens et al., 2014, Manning et al., 2017, Kaiser et al., 2004) but with slightly different equations that have been recently improved (Kaiser, 2011b, Prokopenko et al., 2011). The triple isotope technique has also been exploited within numerical models for assessing global PP (Nicholson et al., 2014).

Previous studies have used the ^{17}O excess to calculate an approximation of GPP according to Luz and Barkan (2000):

$$GPP = kc_{sat}\frac{^{17}\Delta - {}^{17}\Delta_{sat}}{^{17}\Delta_P - {}^{17}\Delta} \quad (1.12)$$

were k is the gas transfer velocity, c_{sat} is the oxygen in the water at saturation, $^{17}\Delta$ is the measured value and $^{17}\Delta_{sat}$ and $^{17}\Delta_P$ are the values at saturation concentration and the maximum photosynthetic value respectively. The ratio (g=GPP/kc_{sat}) of gross oxygen production and gross oxygen influxes from the atmosphere (kc_{sat}) has been widely used in the calculation of gross production (Luz and Barkan, 2000, Juranek and Quay, 2005, Sarma et al., 2006, Stanley et al., 2010).

In 2011, Kaiser's technical note presented a consistent calculation that allows the measurement of GPP without the previous associated assumptions and approximations (e.g. Ar is at saturation (Hendricks et al., 2004)) (Kaiser, 2011b). If we consider production, respiration and gas exchange in the mixed layer to calculate g (at steady state), it can be derived as:

$$g = \frac{(1+s)\varepsilon_E(1+\delta)\varepsilon_I + \delta}{\delta_P - \delta - (1-f)\varepsilon_R(1+\delta)} \quad (1.13)$$

where s is the O_2/Ar supersaturation f = net production/production and ε_E, ε_I and ε_R are the isotopic fractionations during evasion, invasion and respiration respectively. The temporal trend in the isotopic composition (dδ/dt) has been omitted because it tends to zero in steady state. The gas exchange frequency (v_{mix}=k/z) has also been omitted, as this is a product of the temporal trend. From that equation all the parameters can be measured with enough precision to calculate g. Still, ε_R introduce uncertainties because cannot be obtained with enough precision and f is calculated from s/g introducing additional uncertainties (Quay et al., 1993, Hendricks et al., 2004, Kaiser, 2011b).

If we calculate g directly from $^{17}\delta$, $^{18}\delta$ and s, and then eliminate the terms that introduce uncertainty (e.g. removing ε_R by combining the budget of relative $^{17}O/^{16}O$ and $^{18}O/^{16}O$ isotope ratios) in the equation 1.12, we get the following equation called "dual delta method" (Kaiser, 2011; eq. 48):

$$G(^{17}\mathrm{O}) = k(\mathrm{O}_2)c_{\mathrm{sat}}(\mathrm{O}_2)\frac{(1+{}^{17}\varepsilon)\dfrac{{}^{17}\delta - {}^{17}\delta_{\mathrm{sat}}}{1+{}^{17}\delta} - \gamma(1+{}^{18}\varepsilon)\dfrac{{}^{18}\delta - {}^{18}\delta_{\mathrm{sat}}}{1+{}^{18}\delta} + s({}^{17}\varepsilon - \gamma\,{}^{18}\varepsilon)}{\dfrac{{}^{17}\delta_{\mathrm{P}} - {}^{17}\delta}{1+{}^{17}\delta} - \gamma\dfrac{{}^{18}\delta_{\mathrm{P}} - {}^{18}\delta}{1+{}^{18}\delta}} \tag{1.14}$$

were $G(^{17}O)$ is the gross oxygen production at steady state in the mixed layer and ε is the kinetic isotope fractionation during O_2 evasion ($^{18}\varepsilon$ = –2.095 ‰ (Knox et al., 1992) and $^{17}\varepsilon$ = –1.463 ‰ (based on a mass-dependent relationship between $^{18}O/^{16}O$ and $^{17}O/^{16}O$ fractionation with an exponent of 0.522 (Kaiser, 2011b) and δ_{sat} at the measured temperature and salinity, i.e. $^{17}\delta_{sat}$ = (0.373±0.02) ‰ and $^{18}\delta_{sat}$ = (0.695±0.04) ‰ (Luz and Barkan, 2009). $\gamma = {}^{17}\varepsilon_R / {}^{18}\varepsilon_R = 0.5179$ is the triple isotope fractionation coefficient during respiration. $^{17}\delta_P$ = –11.644 ‰ and $^{18}\delta_P$ = –22.832 ‰ are assumed as the photosynthetic end-member delta values (Kaiser, 2011b, Kaiser and Abe, 2012, Kaiser, 2011a). Equation 1.14 is called "dual delta method" because it uses the two deltas, $^{17}\delta$ and $^{18}\delta$ to calculate g. This method avoids the uncertainty due to the non-linearity $^{17}\Delta$ definition that it has been demonstrated to finish in different results when coming from different definitions (Kaiser, 2011b). The dual delta results together with the appropriate wind speed gas exchange parameterization can be used to estimate GPP rates.

1.5.1 Isotope Ratio Mass Spectrometry (IRMS)

Wilhelm Wien in 1898 was the first to develop mass spectrography to study gas ionization (Audi, 2006). In 1907 Thomson built a spectrograph with electric and magnetic fields and was the first to observe two different nuclidic species of one element and the first mass spectrometer (MS) was built by Arthur Jeffrey Dempster in 1918 (Audi, 2006). In 1940s, Alfred Nier and co-workers created the IRMS with the

same basis as we use in actual mass spectrometers (Jochmann and Schmidt, 2012). The mass spectrometry is now the recognised technique for measuring stable isotopes (Hoefs, 2004).

Mass spectrometry is an analytical method that ionises the chemicals of interest and then sorts their ions based on their mass. The IRMS technique selectively separates gases with charged atoms or molecules according to their masses and motions in magnetic and/or electrical fields (Beckmann et al., 2009, Hoefs, 2004). The dispersion of the beam due to its charged ions results in the collection of specific ion shapes, with lighter ions been deflected more than heavier ones in the magnetic field. This means that mass spectrometers need accurately positioned cups to detect the isotopes of an element. From a single water sample, IRMS makes it possible to measure multiple gases and their isotopes with high precision (Kana et al., 1994).

There are two types of IRMS, dual inlet and continuous flow. The continuous flow approach works with a single aliquot per sample analysis. Samples are prepared at atmospheric pressure and it is possible to simultaneously measure multiple isotope ratios (Hoefs, 2004). The dual inlet approach requires several cycles per sample analysis. Samples are prepared under vacuum and with pure gases. The dual inlet accounts with a change over valve that allows rapid and consecutive analysis between sample and reference gas. The use of a reference gas allows any drift in the measurement to be corrected. This ability to correct drift makes the dual inlet approach more accurate than the continuous flow approach. For this reason the work within this thesis uses a dual inlet mass spectrometer. However, the analysis of the water samples with the dual inlet technique requires extensive sample preparation.

For the analysis of triple oxygen isotopes and O_2/Ar ratios, it is necessary to collect the samples in pre-evacuated bottles that have been poisoned with $HgCl_2$ (to stop biological activity). IRMS instruments are expensive and sensitive to motion, and so are not suitable for use on board research vessels. Therefore the samples have to be sealed and stored safely (Luz et al., 2002). Before placing the sample in the dual inlet IRMS, the gases that are not of interest need to be removed from the sample to avoid interferences during the analysis. This time-consuming disadvantage is compensated with its high sensitivity results.

1.6 Remote sensing to estimate primary production.

The variations measured by the MIMS along a cruise track can be large, but they will always be spatially and temporally limited to the cruise track itself. Primary production can be approximated from chlorophyll and temperature measurements if carbon uptake per unit of chlorophyll is known. In this way satellites can estimate primary production at global scales from ocean colour chlorophyll estimates and thermal infrared temperature measurements (Behrenfeld et al., 2005). The main advantage of satellite remote sensing methods in the studies of the shelf seas is that it can capture synoptic scale observations allowing the seasonality to be captured. However, there are some limitations in the use of satellite observations. Cloud cover, sunglint at the sea surface and high levels of aerosols in the atmosphere can prevent observations. Moreover, satellite detection of ocean colour in shelf seas is mostly limited to the surface, and so will miss the typical chlorophyll subsurface maximum during summer (Joint and Groom, 2000). It is also noted that satellite measurements of primary production depend of *in situ* measurements for calibration. Overall, this technique provides great advantage to understand and quantify primary production at synoptic scales (i.e. > 1 km). Moreover, this data is crucial to feed production models. Export production or NCP might also be quantified from ocean color data (Tilstone et al., 2015) using simple temperature-dependent models as proposed by (Laws et al., 2000). The first satellite able to estimate sea production was the Coastal Zone Color Scanner (CZCS), which was launched in 1978 and was operated until 1986 (Mitchell, 1994). Since then, the number of satellite sensors that measure ocean color has continued to increase (e.g. sea-viewing wide-field-of-view sensor (SeaWiFS), ocean color temperature sensor (OCTS), moderate-resolution imaging spectroradiometer (MODIS), medium-resolution imaging spectroradiometer (MERIS), geostationary ocean color imager (GOCI), visible infrared imaging radiometer suite (VIIRS), and Sentinels). The algorithms and calibrations continue to be improved and developed. Therefore, the methods are now a baseline tool in many experiments and research cruises.

The combination of the accurate techniques (MIMS and IRMS) described here and remote sensing will provide a wider view of to the primary production in the heterogenic shelf sea.

1.7 Phytoplankton photophysiology from Fast Repetition Rate fluoremetry (FRRf).

The main process of the photosynthesis, the photosynthetic water splitting (or oxygen evolution) can be measured by active fluorometry. Oxygen evolution can be detected by exposing dark-adapted photosynthetic material to a series of single turnover flashes. Because gross production is the rate at which O_2 is produced by the splitting of water during the photosynthesis, an alternative method to yield gross O_2 production is possible through active fluorometry, and notably Fast Repetition Rate Fluorometry (Kolber et al., 1998). This technique enables physiological data to be collected from in situ measurements of phytoplankton and probe photosynthesis. This bio-optical technique specifically yields an electron flux (electron transport rate (ETR)) through the O_2 evolving complex (photosystem II (PSII) reaction centers) per unit of volume of sea water at frequencies of seconds, providing unprecedented high spatial and temporal resolution measurements (Kolber and Falkowski, 1993). These data can be used to estimate gross production because is generally the main sink of gross ETR. Numerous studies have compared FRRf-based ETRs with corresponding measurements of carbon uptake but surprisingly few have included O_2 evolution (Suggett et al., 2009, Sarma et al., 2005, Suggett et al., 2001, Hancke et al., 2015, Robinson et al., 2009). Gross ETR should be related to gross photosynthesis, whereas carbon measurements approximates more to net carbon fixation (Suggett et al., 2001). Such comparison studies with carbon uptake have shown that ETR derived from FRRf can be converted to carbon fixation rates (C_{uptake}) if the electron requirement for carbon fixation (K_C) is known, K_C = ETR / C_{uptake}. The calculation of K_C had previously led to many different values (Kolber and Falkowski, 1993, Suggett et al., 2001, Suggett et al., 2009). More recent studies show that discrepancies could be due to the dependency of K_C on environmental variables, but the reasons for this variability is not fully understood (Zhu et al., 2016), thus highlighting the need of more studies. A recent study suggests that there is a co-variability between K_C and light availability (R^2 = 0.70 – 0.81) when size of

phytoplankton population are included in the algorithms for the calculation of net primary production (Zhu et al., 2017). However, the study concludes that additional knowledge of physico-chemical conditions are needed to effectively improve the robustness of the analysis.

In spite of the interests in reconciling FRRf with carbon-based measures of productivity, few studies have in fact attempted to reconcile FRRf with gross production measurements, i.e. rates that should more directly scale with the ETRs themselves. Numerous processes act to decouple ETRs from C-uptake (e.g. Suggett et al. 2009) whereas fewer processes, e.g. cyclic flow around Photosystem II, act to decouple ETRs from gross O_2. Sarma et al. (2005) compared gross production from FRRf and triple oxygen isotopes for a limited number of discrete samples and found similar tendencies between both. Lefebvre et al. (2007) found a linear relationship between classical oxygen evolution and ETR in single diatom culture experiment. Fujiki et al. (2008) attempted to estimate *in situ* daily gross oxygen production from an underwater profiling buoy system. However, no relationship with independent production measurements was found. No studies using ETR requirements for studying gross oxygen production in physical complex systems like shelf seas were found in the literature.

Chapter 2. Sampling and methods for measuring $\Delta O_2/Ar$ using membrane inlet mass spectrometer (MIMS) and triple oxygen isotopes using dual inlet isotope ratio mass spectrometer (IRMS)

2.1 Introduction

In this chapter I detail sample collection, measurement methodology used and the calibration of instrumentation. My main goal here is to present the steps taken to obtain biological oxygen production from MIMS-based O_2/Ar and IRMS-based O_2 triple isotopologue ratio measurements, and the problems one can encounter.
Detailed protocols of how to use specific equipment and software can be found in the appendix A.

2.2 Sampling

Sampling for the four cruises on RRS Discovery involved two methods:

1. discrete water sampling for dissolved oxygen triple isotope measurements and O_2/Ar from hydrocasts of Niskin bottles attached to a rosette frame as well as from the ship's underway scientific seawater supply (nominal depth of 6 m) (section 2.2.1),
2. continuous sampling recording of dissolved surface gases (O_2 and Ar) (section 2.2.2) using the underway water supply .

Due to a technical problem with the MIMS it was not possible to record O_2 and Ar continuously during the autumn 2014 cruise. However, we took discrete samples to measure O_2/Ar and triple oxygen isotopes from hydrocasts. Additionally, during the spring cruise, FRRf (fast repetition rate fluorometry) samples were collected in conjunction with other scientist, in order to study phytoplankton photophysiology. I used the physiological parameters provided (e.g. Initial fluorescence yield in dark chamber (F_o)) to calculate electron transport rates (ETR). FRRf measurements are

presented in chapter 6 of this thesis. Table 2.1 presents a summary of the data collected during each cruise.

Table 2.1. From left to right, cruise ID for the RRS Discovery, month and year when the cruise began and season, cruise length, number of days the MIMS was measuring continuously O_2/Ar from the underway sea water supply (USW), number of CTD casts from which water samples for O_2/Ar and triple oxygen isotopes samples were taken, and number of CTD casts from which FRRf samples were taken for analysis in this thesis.

Cruise ID	Date / season	Cruise days	USW days	CTD casts	FRRf casts
DY026	Aug 14 / summer	12	9	22	–
DY018	Nov 14 / autumn	24	–	23	–
DY029	Apr 15 / spring	30	28	34	27
DY033	Jul 15 / summer	23	21	24	–

In all cruises, at least three stations were sampled: Celtic Deep (A), Central Celtic Sea (CCS) and Celtic Shelf edge (CS2) (Fig 2.1). Celtic Deep is the name given to the innermost station situated on the shelf between Ireland and United Kingdom. It is called Celtic Deep because the area is deeper than the surrounding areas. The muddy seabed is at up to 100 meters depth due to strong currents in the middle of St George's Channel (Fig 1.1).

The Celtic Shelf edge is, as its name suggests, the edge of the shelf sea and our outermost station on the shelf. It is the deepest station on the shelf at about 200 meters bottom depth.

The Central Celtic Sea station is almost half way through an imaginary straight line between the two main stations. At least one ship transect, passing by these three main stations was carried out during each cruise. Depending on the cruise, intermediate stations (J2, J4, J6, J8, O2, O4), in between the three main ones, were visited as well (Fig 2.1).

There were three short transects (Fe1, Fe2, Fe3) outside of the shelf, through which we also sampled vertical profiles. As the Celtic Sea has been previously studied, there is already information about currents, which are expected to be tidally-driven and in clockwise direction on the outer shelf and anticlockwise closer to St George's Channel (Stephens, 2007, Sharples et al., 2013). A transect thus covers a wide range of environmental variables' gradients and allowed us to minimise the cruise time, compared to a grid sampling strategy.

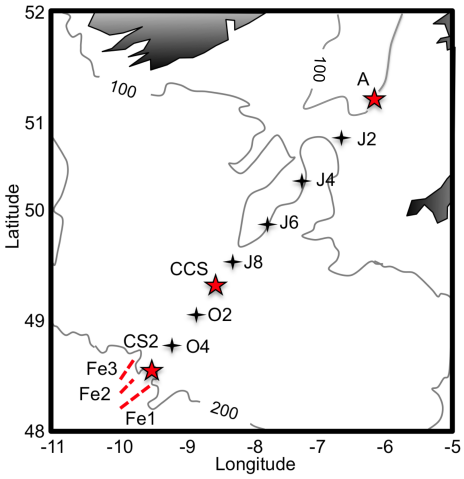

Figure 2.1. Area of study, the Celtic Sea. Grey patches represent Ireland (north) and UK (east). Red stars indicate the approximate location of the three main stations (A, CCS, CS2). Black stars indicate the location of other stations where at least 1 CTD cast was taken (J2, J4, J6, J8, O2, O4). Dashed red lines represent transects of multiple stations off the shelf (Fe1, Fe2, Fe3). Grey lines represent the bathymetry at 100 and 200 metres depth, the latter one also representing the shelf edge. The map was plotted using QGIS software.

2.2.1 Discrete sampling

Generally, at least one midday-cast was carried out at every station. We sampled at six different depths: one near the surface at about 5 m depth and two more samples in the mixed layer and three below the mixed layer. When needed, samples for oxygen Winkler titration were taken, in which case those samples were taken first. Afterwards, 300 ml pre-evacuated bottles with Louwers-Hapert high-vacuum stopcocks and pre-treated with 7 mg of $HgCl_2$ were filled for IRMS analyses, and finally 500 ml borosilicate bottles with ground glass stoppers, for MIMS analyses (without

preservation since these samples were analysed within 2 hours of sampling). The three sampling methods are detailed below.

Discrete seawater sampling for analysis using the Winkler method

Discrete water samples for Winkler analysis were taken from 4 to 6 Niskin bottles to calibrate the oxygen sensor of the stainless steel and titanium CTD following Culberson (1991) with some modifications (presented in Appendix A). The mean standard deviation was (0.7±0.4) μmol L^{-1}. Samples were drawn carefully into borosilicate glass bottles avoiding bubbles and overflowing. Immediately after collection, samples were fixed with the pickling reagent $MnSO_4$ (or $MnCl_2$ depending on the cruise) and a solution of NaOH/NaI. We collected samples from each cast, stored for 2-4 days and analysed them together to the thiosulfate standardisation. This reduced the need for repeated thiosulfate standardisations. Analysis was done by whole-bottle Winkler titration using a photometric (or potentiometric depending on the cruise) endpoint detector (see section 2.3). We also collected USW samples for calibration of our optode (see section 2.2.2).

Discrete seawater sampling for the measurement of dissolved gases using MIMS

The same six depths were sampled using the 500 ml borosilicate bottles for the analysis of O_2/Ar. To take the samples for dissolved gases we used Tygon tubing. The tube has to be free of bubbles at the moment of sampling. The bottles were rinsed, filled and left to overflow three times, avoiding bubbles, then stoppered.

Discrete seawater sampling for triple isotope measurements using IRMS

Discrete seawater samples were collected for O_2 isotopologue analysis following Emerson et al. (1995). Prior to the water sampling, the glass flasks were prepared in the lab. The glass flasks have a volume of about 330 ml and are equipped with one Viton o-rings stopcock (Louwers Hapert). The flask volumes were calibrated in the lab, spiked with 100 μl of $HgCl_2$ saturated solution, which was then evaporated to dryness in an

oven at 50 ºC. $HgCl_2$ preserves the dissolved oxygen by stopping biological activity. The o-rings of the stopcock were lightly greased to facilitate a smooth operation. The flasks were then evacuated using a vacuum line to a pressure of approximately 5 x 10^{-6} mbar, to enable filling with seawater. The evacuated flasks were used for sampling seawater from the CTD Niskin bottles and from the USW inlet. Three of the six depths (surface, mixed layer and below mixed layer) were sampled with the evacuated bottles. To take seawater samples for dissolved gases I used Tygon tubing of smaller diameter than the inner diameter of the side arm of the bottle. The flasks were filled taking extreme care, first by overflowing the side arm with seawater, making sure there were no bubbles in the water, then with the side arm full of bubble-free seawater, the stopcock of the pre-evacuated bottle was slightly opened thus sucking the seawater slowly into the bottle while still overflowing. If any atmospheric air got into the bottle, the sample was discarded and another evacuated bottle was used to take a new sample.

The bottles were filled to approximately two thirds of the total volume, thus creating a headspace in which the dissolved gases would partition until they reach equilibrium. The optimum headspace size for extraction of gases is determined by their solubility. For O_2 and Ar the ideal headspace would have been about 15 % of the total bottle volume (Seguro et al., 2017). Once the bottle was closed, the side arm was filled with seawater and capped. This system ensures that the sample stays free of potentially incoming atmospheric air due to the bottle still being under pressurised even after water filling (Luz et al., 2002). Duplicates were randomly taken in order to assess the reproducibility of the method.

2.2.2 Continuous sampling from the USW

Oxygen optode

O_2 concentrations were measured continuously with an optode (*Aanderaa* model 3830, serial no. 241) at 10 s resolution. The measurements were taken from the same USW inlet used for measuring the O_2/Ar ratios using the MIMS. The optode measures the dissolved oxygen concentration based on dynamic fluorescence quenching of oxygen.

The optode's foil is a platinum porphyrin complex embedded in a foil permeable to gases. This complex acts as luminophore that, after absorbing a photon of high-energy (blue light), colloid with O_2 molecules and emit a photon of lower energy red light (Fig 2.2). Gas solubility is dependent on temperature, thus the optode measures the temperature of the water before the oxygen partial pressure is determined. The optode is placed inside a dark bottle that is connected to the USW. The dark bottle was chosen to reduce algal growth. The main advantage of this optode is that it does not consume oxygen from the water that will later be analysed using the MIMS system.

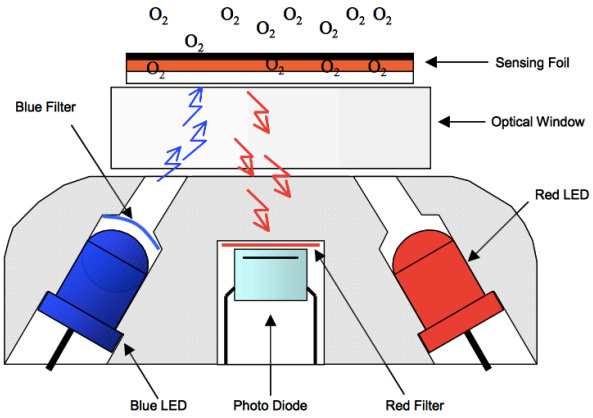

Figure 2.2. Optode's optical design (*Aanderaa* model 3830, serial no. 241), extracted from the operating manual provided by the manufacturer.

Membrane Inlet Mass Spectrometer

The membrane inlet mass spectrometer contains a semipermeable membrane that separates dissolved gases from the water phase and detects them directly with a quadrupole mass spectrometer.

The main parts of the membrane inlet mass spectrometer are:

1) The membrane that separates the dissolved gases from the seawater (Teflon AF membrane Random Technologies)
2) The quadrupole mass spectrometer QMS 200 M Prisma (Pfeiffer Vacuum Gmbh).

The membrane has a tubular shape with an inner diameter of 600 µm and 10 cm in length. The water reaches the outer part of the membrane wall and the dissolved gasses

pass through the membrane. A stainless steel tube allows those gases from the membrane to pass to the mass spectrometer (MS). The gas enters the quadrupole MS and gets ionised by a tungsten filament. The different ionised gases get separated in the flight tube and collected in a Faraday cup. The flight tube is kept under vacuum by a turbo-molecular pumping station (HiCube 80 ECO, Pfeiffer Vacuum GmbH), which keeps the flight tube at $1x10^{-6}$ mbar pressure. The vacuum facilitates the entrance of the gases into the MS. The analyzer can work with two different types of detectors, Channeltron-SEM or Faraday-detector. In this study we used the Faraday cup. The ion source is gas tight and has two tungsten cathodes, but only one is used at a time. The ion source produces an electron beam of 0.55 mA that is accelerated across the inflowing gas stream, creating positively charged ions. A quadrupole mass filter separates the charged ions based on their *m/z* value. We chose to monitor the ion currents of interest: *m*/*z* 18, 28 and 29, 32, 40, which correspond to water vapor, nitrogen, oxygen and argon respectively, although we only used oxygen and argon masses in our study. The modular application software Quadstar allowed us to record the data, display the quadrupole MS signal, tune the ion source, optimize the peak shape, create our own sequence files (e.g. displaying O_2/Ar ratio), and to do qualitative and quantitative analyses.

Setting up for continuous measurements on board

The MIMS was set up on a bench in the main lab of the ship RRS Discovery. We placed the MIMS on the bench next to the USW tap with the shortest vertical distance to the USW intake (two floors above). It is important to minimize the travel time of the water through the ship's pipes, because in the past it has been found that the concentration of the dissolved oxygen can be altered by biofouling and water warming on the way from intake to the lab (Kaiser, 2005, Juranek et al., 2010). The USW intake is located in the middle of the bow and at a nominal depth of 6 m.

The whole system could be divided in two main parts, one with the mass spectrometer and PC (dry side) and another that is more robust to water splash (wet side) that is attached to the USW inlet tap (Fig 2.3).

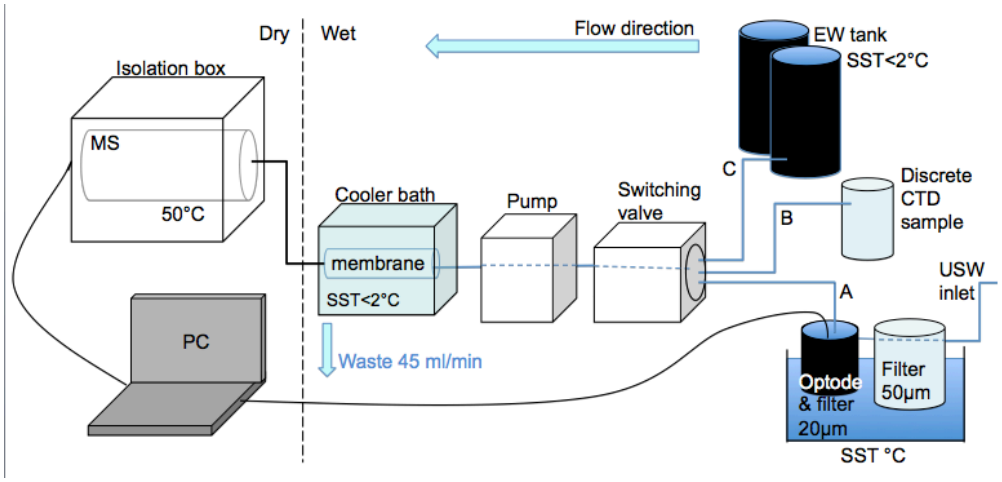

Figure 2.3. Schematic of MIMS set-up. Vertical dashed line represents division between the dry (left) and wet (right) zones. Top arrow indicates the direction of the seawater through the system. Blue lines represent the ¼" PVC Tygon tubes that carry the seawater (paths A, B and C) from various inputs to the switching valve. Black line between membrane and MS represent the stainless steel tube that carries the extracted dissolved gas.

Path (A) was used most of the time to measure dissolved gases from the sea surface (Fig 2.3). Seawater from ship's USW flows continuously through a tube to a filter cartridge (50 µm) that removes bigger particles. Then, it goes to the bottom of an open dark bottle that overflows and fills the bucket, surrounding both the bottle and the filter; this way, the overflowing seawater keeps this part of the circuit at sea surface temperature (SST). The open bottle does not build backpressure and helps to release any big bubbles before entering the closed circuit.

Inside the dark bottle there is an optode, which measures the dissolved oxygen concentration from the USW. Inside the dark bottle there is also a tube with a surrounding felt sock. Both filters, the 50 µm and the felt, need to be regularly checked and cleaned when necessary to avoid biofouling or clogging. Up to this point the pressure from the USW tap controls the flow into the system. A pump that is placed just after the switching valve is used to move the water from here towards the MIMS. We can only analyse one sample at the time, but can switch to another sample thanks to a four-port switching valve. The intensity of the signal in the mass spectrometer (which is proportional to the amount of gas) is sensitive to the changes in temperature and to flow

rate fluctuations. Sensitivity to these fluctuations can be minimised by normalising N_2 and O_2 to Ar, which can eliminate 80% of the fluctuations (Craig and Hayward, 1987). For this reason, a frequency inverter controlled pump permits adjustment of the flow rate (45 ml min^{-1} in this study). The temperature in the water flow was maintained at 1 to 3 ºC below sea surface temperature to avoid degassing. Inside the cooler bath (Thermo Neslab RTE10), the tube that contains the seawater sample is coiled to extend the cooling time. This bath also keeps the membrane at a constant temperature. In the membrane box, a fraction of the dissolved gasses will be separated from the water, which is discarded into the lab's sink. The dissolved gases will be ionized in the ion source then go through the flight tube to the detector and the electrical signal will be sent to the computer. Flowmeter, optode and MIMS signals can all be monitored at the same time by the computer with three different software packages: Tracer DAQ, OxyView and Quadstar 32-bit respectively.

Path (B) can be used to measure dissolved gases of discrete samples from CTD or other experiments. Changing between path A and B is done with the electronic switching valve, that should not allow any bubble into the equipment if set up correctly, by filling up the tube ports. This is crucial because bubbles dramatically affect the signal in the MIMS. At the entrance of the cooler bath, the tube has an easily accessible inner mesh. This mesh is necessary because discrete samples are directly connected to the switching valve without previous filtering; therefore after a few samples (typically 5-7) this mesh needs cleaning to avoid further clogging. The rest of the analytical procedure is identical to the one used for the USW path (A).

Path (C) is used to measure standards, which are seawater equilibrated with the atmosphere, called equilibrated water (EW) from now. The EW standard was prepared by filling two 1 L glass tanks with 0.2 μm-filtered seawater, in order to remove biological organisms. The water was then bubbled with air and stirred constantly for about 24 hours, until the water reached air saturation and then sampled. Because the saturation concentration of gases depends on temperature, a water jacket from the cooler bath kept the two tanks at the same temperature. Therefore, the USW supply and the equilibrated water standard were kept under the same conditions of salinity and temperature. Duplicate standards were measured every day during cruise time. O_2/Ar

measurements on EW helped us to detect any bias in the instrument precision as well as for further calibration of USW data.

The most important and time-consuming step of working with a MIMS is setting up the equipment. After the MIMS has been correctly assembled and tested, the maintenance during the cruise is minimal if properly managed.

Modifications

The measured signal intensities are sensitive to changes in temperature in the mass spectrometer, and for that reason, I did a series of tests to improve temperature stability before going to sea.

To keep the temperature of the water constant I placed the filter cartridge and the optode in a bucket with seawater, used foam insulation on the carrying tubes, and submerged the membrane in a controlled temperature bath. To keep the temperature of the gases constant I modified the MS environment. Originally, there was only a heating tape surrounding the flight tube. But after several tests, I found that the best strategy to keep a constant and homogeneous temperature (50 ºC) was to thermally isolate the fight tube and the heating tape from the environment using an aluminium box lined with foam. Inside the box we placed a fan in order to maintain thermal homogeneity. Keeping the fan covered at the back, to avoid the influx from the room's air gave the most stable temperature (Figure 2.4).

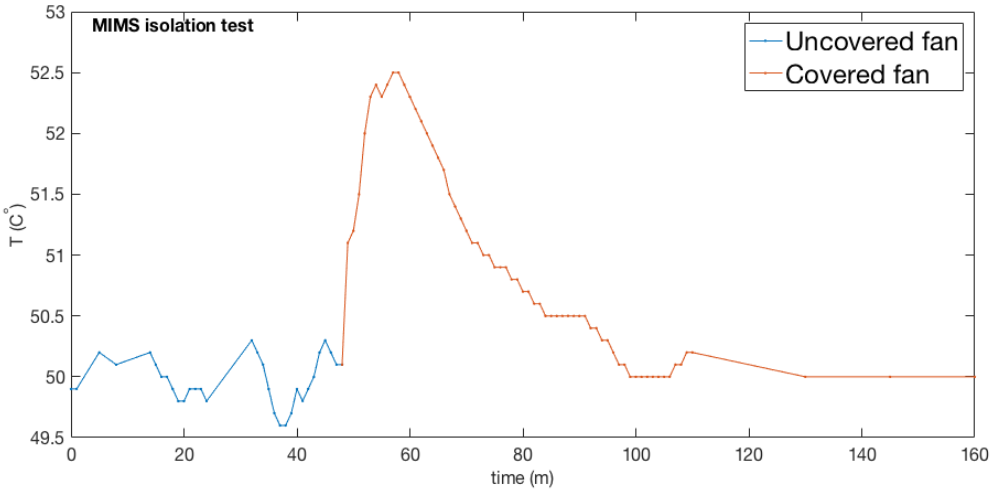

Figure 2.4. MIMS' isolation test. The blue line represents temperature oscillation inside the MIMS isolation box with the back of the fan in contact with the air in the room. The red line represents temperature oscillation after isolating the fan from the room's air.

2.3 Winkler method for oxygen determination and CTD calibration

The CTDs oxygen sensors were calibrated by automatic Winkler titration of discrete water samples with photometric or potentiometric endpoint detection (Culberson, 1991, Grasshoff, 2007) depending on the instrument available.

The Winkler method is an iodometric titration in which oxygen in the seawater sample quantitatively oxygenates iodide ions to from iodine. This is a multi-step oxidation, using manganese oxide as a transfer medium. The dissolved oxygen concentration of seawater is defined as the number of micromoles of oxygen gas per kilogram of seawater (µmol kg^{-1}). The accuracy of oxygen titration depends on standardization of the thiosulfate reagent used in the titration and the ability of the analyst to follow the protocol meticulously. A thiosulfate solution ($Na_2S_2O_3$) of about 0.2 mol L^{-1} was used. The standardization is accomplished by titrating a solution of potassium iodate of known normality (KIO_3 0.1 N). The error during standardization was between 0.02 and 0.003 %. Corrections for the contribution of reagents need to be done. Because of that

we measure a blank every two or three days. The blank results from redox species apart from oxygen in the reagents, and it can be calculated using the expression $V_{blank} = V_2 - V_1$. Here V_1 and V_2 are the volumes of $Na_2S_2O_3$ used to titrate the first and second aliquots of the KIO_3 standard.

The correlation between Winkler samples and CTD sensor values was always considered good (0.95 – 1; R^2) (Fig. 2.5), with a constant offset between CTD and Winkler measurements. I noticed that major errors during the analysis are due to the movement of the ship, which directly affects the accuracy of the photometric method. For that reason, the titrations were done during calm weather days when possible. There were no such problems when using the potentiometric method.

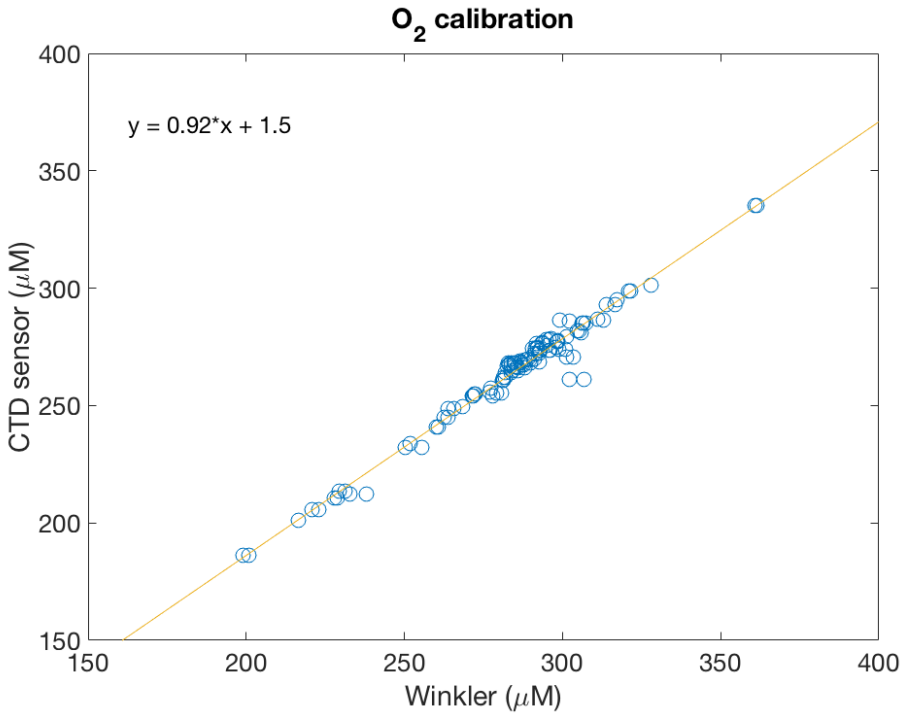

Figure 2.5. Oxygen calibration of CTD sensor by the Winkler method. A linear regression gives CTD sensor = 0.92 * Winkler + 1.5 (blue circles and line; $R^2 = 0.98$).

Calibration of the optode using the Winkler method and water from the underway system was done randomly, using triplicate samples and shows an error between 2 - 0.02%. The highest error was assumed to be due to the change in the concentration of oxygen from slightly different water masses when the ship was moving. Comparisons between Winkler samples from Niskin bottles fired at the surface and Winkler samples taken from the non-toxic supply at the same time agreed well. That means that the non-

toxic underway sea water supply was in good working condition and the Winkler method was measuring consistently during the cruise.

2.4 Stable isotope analysis by Dual Inlet Isotope Ratio Mass Spectrometry (IRMS)

Isotope ratio mass spectrometry is considered the most precise isotopic measurement method but samples require more preparation, in this case, extraction of dissolved gases and purification as explained in section 2.4.1. Before using isotopic data for the calculation of biological oxygen production we need to do corrections and calibration inherent to the method, such us mass imbalance correction, nitrogen correction, dry air calibration and the correction for the gas partition between the headspace and water as explained in the sections 2.4.2 and below.

2.4.1 Dissolved gas sample extraction and purification

Collected sea water samples for the analysis of triple oxygen isotopes and O_2/Ar analyses were stored at room temperature until further analysis. To ensure that the headspace gases are in equilibrium with the seawater sample, the bottle needs to be left to equilibrate for at least 24 hours (Luz and Barkan, 2000). The dissolved gases were always extracted after the cruise and within one month from the end of the cruise.

Extraction of dissolved gases

To extract the dissolved gases from the seawater sample first I drained the water from the side arm, then washed it with distilled water, followed by ethanol, and finally dried it. Then, the bottles with seawater were weighed, and the weight of the empty and sample filled bottle were used to calculate the volume of the sample, the ratio of sample / headspace, and the distribution of gases and isotopes between the headspace and water *(Q*). The value of *Q* will be later used in the calculation of O_2/Ar ratios (see section 2.4.7). After weighing the bottles, most of the seawater was sucked out of the bottles and leaving headspace gases only. The water phase was removed by first; inverting the

bottle, and connecting the side arm, to a 15 L container that is constantly kept under vacuum (about 25 mbar) using a rotary vane pump (Fig. 2.6). By closing the stopcock just before all the water is drained out, we safely keep the gas sample and remove 99 % of the degassed water. The 1 % water left in the bottle does not affect the final isotopic mass balance composition (Sarma et al., 2003).

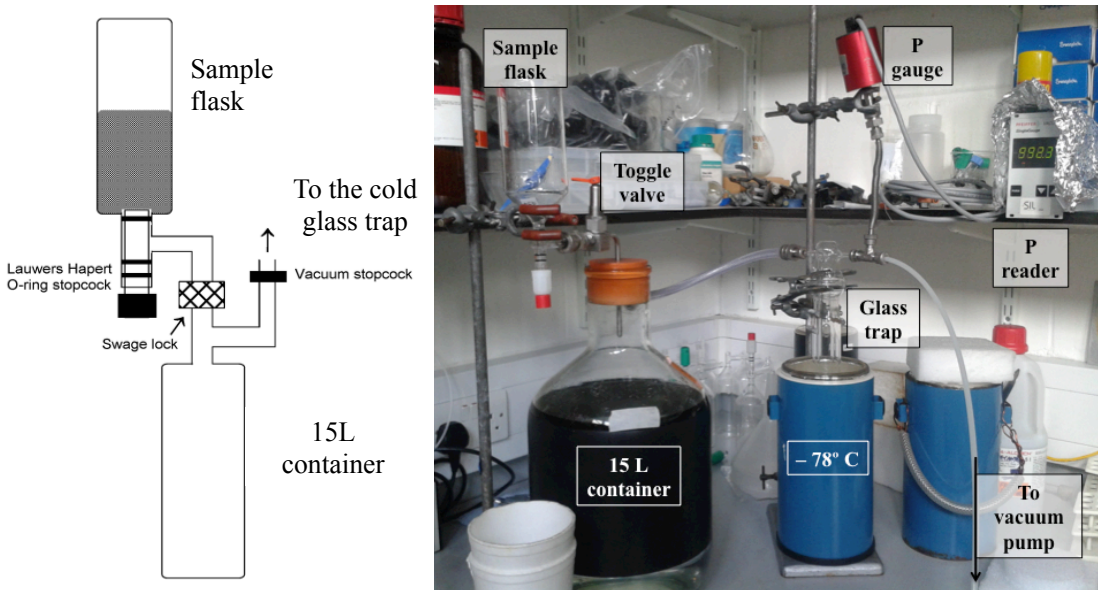

Figure 2.6. Modified schematic diagram of sample extraction unit from Sarma et al. (2003) on the left and real set up in the laboratory on the right (including 15L container, cold trap and pressure gauge).

Next, the bottles are connected to an extraction line where the gas sample is dried at liquid nitrogen temperature, then transferred and stored in a flame-sealed glass tube (Fig 2.7). After draining most of the water, the sample bottle is connected, using the side arm, to the extraction line, that is constantly kept under vacuum (3.7×10^{-7} mbar) using a high vacuum pumping station (HiCube 80, Pfeiffer Vacuum Gmbh). The sample bottle is also immersed in ethanol/dry ice mixture (-78°C), to freeze the remaining water in the bottle and thus to prevent large amounts of water vapour from the bottle entering the line (blue Dewar in figure 2.7). After the water is frozen in the bottle and high vacuum was achieved up to the isolation valve on the bottle, the line was isolated from the vacuum pump and the gases from the glass bottle were expanded into the extraction line. The gas was first expanded into a large volume trap immersed in liquid nitrogen (-196 °C), which was used to remove any water vapour and carbon dioxide that might be present in the gas sample (black Dewar in figure 2.7). Pyrex glass tubes with 10

molecular sieve pellets (5Å 1/16 inch diameter) were used to collect the sample. These tubes are attached to the line on the port to the right of the liquid nitrogen Dewar, degassed using a low temperature flame and evacuated to 10^{-7} mbar before freezing the gas sample, by freezing it at liquid nitrogen temperature. At least 99.7% of the gas sample was frozen into the tube before isolating the sample from the line by flame sealing using a small hand torch. Previous tests done by postgraduate students ((Gloël, 2012), (GonzáLez-Posada, 2012) and (Van Der Meer, 2015)) during their studies showed that there is no significant fractionation or contamination of the gas samples when extracting them in this way. For a more exhaustive description of each step, go to appendix A.

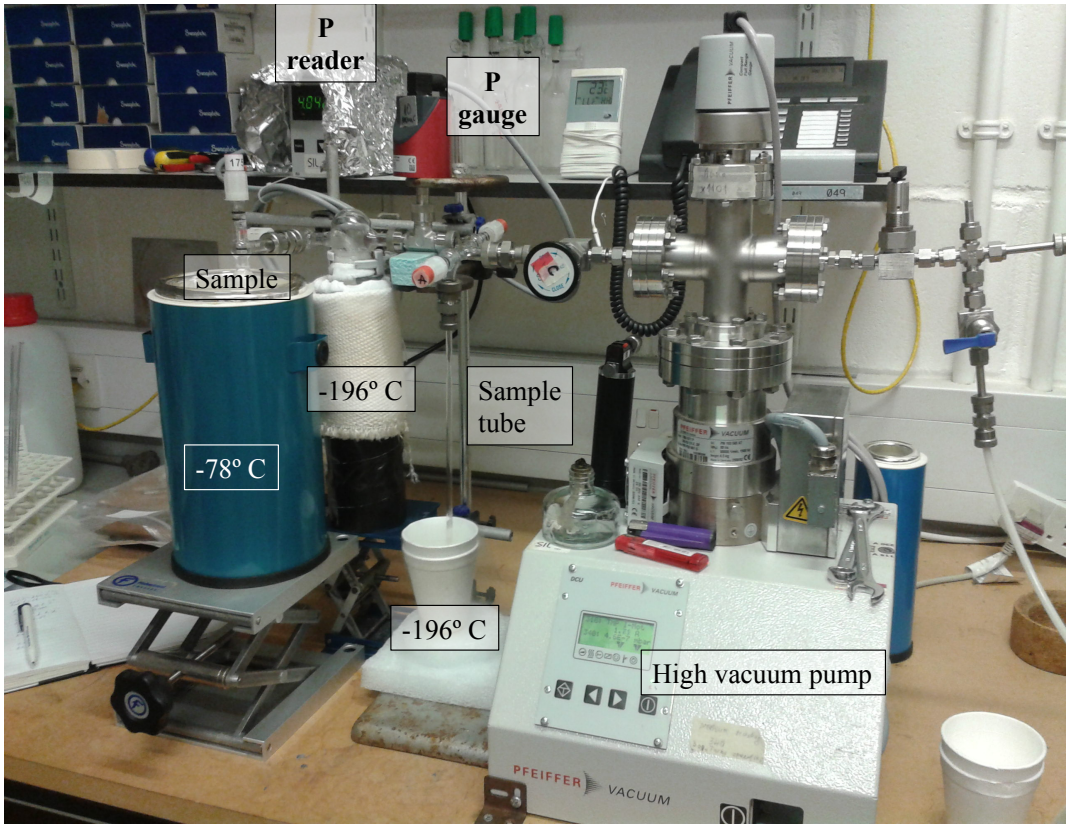

Figure 2.7. Extraction line set up.

Separation line

For the triple isotope analysis only the oxygen and the argon gases are needed, and these two components need to be pure (free from CO_2, N_2 and water traces). When measuring the triple isotopic composition of oxygen using the IRMS, isotopic species of *m*/*z* 32, 33 and 34 are monitored. If N_2 is present in the gas used for this isotopic

analysis it can create isobaric interferences, and the signal intensities measured will not be representative of oxygen molecules alone (NO can form in the ion source, and some of its isotopologues are of identical masses to some of the O_2 isotopologue masses) (Bender et al., 1994). For this reason, all samples and dry air standards were purified using our in-house designed and built separation line. This line was built by Gloël (2012) and GonzáLez-Posada (2012) during their PhD study following the work published by Reuer et al. (2007), Barkan and Luz (2003), Emerson et al. (1995) and Abe (2008) with some modifications. The schematic of the separation line is shown in Fig. 2.8.

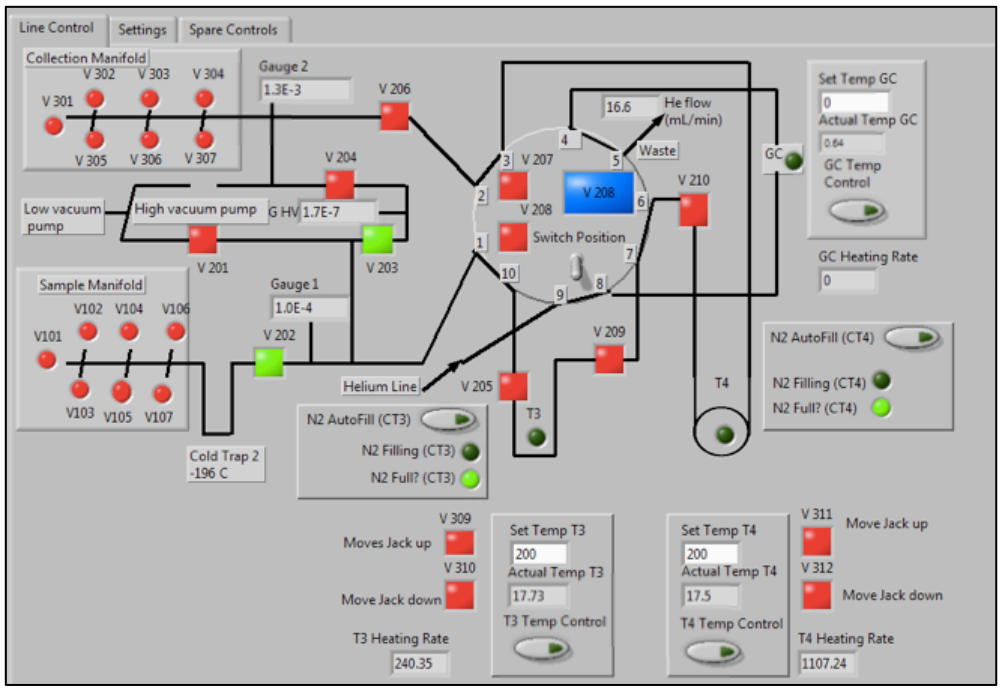

Figure 2.8. Schematic diagram showing the separation line for dissolved gases as seen with the LabVIEW 2013 software.

Sample manifold: Flame-sealed glass tubes containing the gas samples are scored and then attached to the line using tube crackers. Tube crackers are a combination of Cajon Ultra Torr fittings, along with convoluted, flexible stainless steel tubing (Fig 2.9).

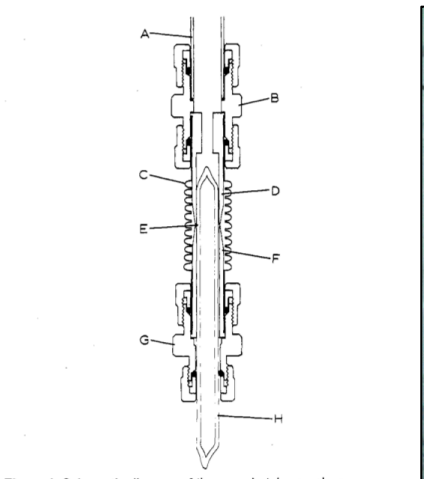

Figure 1. Schematic diagram of the sample tube cracker

(A) $\frac{3}{8}$-in. o.d. tube leading to vacuum system. (B) $\frac{3}{8}$-in. Cajon Ultra Torr union, No. SS-6-UT-A-6. (C) $\frac{3}{8}$-in. o.d. Cajon flexible tubing, No. 321-6-X-1. (D) Upper stainless steel cone. (E) Notch in glass tube. (F) Lower stainless steel cone. (G) $\frac{3}{8}$-in. to $\frac{1}{4}$-in. Cajon Ultra Torr reducing union, No. SS-6-UT-A-6-4. (H) 6-mm or $\frac{1}{4}$-in. o.d. Pyrex or quartz sample tube

Figure 2.9. (Left) Schematic diagram of a tube cracker extracted from Desmarais and Hayes (1976), and (right) dry air standard flask and six glass tube samples loaded on crackers and connected to the inlet manifold of the separation line .

The line: With the exception of the helium flow path and the gas chromatographic (GC) column, the rest of the line is evacuated to high vacuum using a turbo-molecular pumping station (HiCube 80, Pfeiffer Vacuum GmbH) (labeled G HV in the diagram), until the pressure reaches about 2 x 10^{-7} mbar. Two pressure gauges (labeled Gauge 1 and Gauge 2) allow us to monitor the pressure in the line when a gas sample is expanded in those parts of the line. Trap 2 is an empty Pyrex spiral tube immersed in liquid nitrogen that will freeze any water vapor and CO_2 left in the sample. Traps (T3 and T4) are made of stainless steel tubing (¼' o.d. and 4 mm i.d.) and are used for freezing the gases of interest at various times during the separation and purification procedure. Because the gases that need freezing will not freeze in liquid nitrogen, both traps contain ten 5Å molecular sieve pellets inside. Before use, these traps are first baked at up to 200° C for half an hour under continuous pumping to facilitate degassing. It is also recommended to do it for longer when the line hasn't been used for extended time periods or has been exposed to atmospheric air or water vapor.

The GC column: The stainless steel packed GC column (Supelco, 13074-U) is 2.74 m long, 2.1 mm i.d. containing 45/60 mesh 5Å molecular sieve. The GC column is used to separate the analyte oxygen and argon gas from the nitrogen gas. It runs at a temperature close to 0°C, by keeping it immersed in a water and ice bath an hour prior

to processing samples and for the entire duration of the sample processing day. The GC system uses helium as carrier gas (flow rate 14 mL min^{-1}).

Automation: The line runs under LabVIEW 2013 software control, developed in house, and based on National Instruments units. The software allows user defined control parameters and the sample processing is fully automated. When required, traps 3 and 4 are submerged in liquid nitrogen by automatically lifting glass Dewar flasks mounted on pneumatic actuators. The 10-port two-position valve (Valco, A4L10UWM) in the middle of the line creates two different paths depending on its position: In one position (V 208, current position in the diagram 2.8), the sample manifold is connected to T3, which allows gases from the Pyrex tubes to be collected into this trap, while the GC column is continuously flushed with He going to waste. In the second position (V 207) this valve connects the GC column to the collection manifold, allowing the oxygen and argon gases to be collected into one of the tubes.

Collection manifold: The collection manifold is a set of seven ¼" o.d. stainless steel tubes filled with molecular sieve pellets, each fitted with a pneumatically actuated isolation valve. The manifold is kept submerged in liquid nitrogen for the entire duration of the sample preparation day. Six of the tubes are used for freezing purified samples, and one will contain a dry air internal standard. The separation and purification procedure takes about 1 h 20 min per sample; therefore six samples and one standard of dry air can be separated per day. These are measured on the mass spectrometer the following day.

2.4.2 Dual inlet isotope ratio mass spectrometer (IRMS)

All dissolved oxygen samples were measured using a dual inlet isotope ratio mass spectrometer - Thermo Finnigan MAT252. The goal is to determine the oxygen isotopic composition and the oxygen/argon ratio in the gas samples, by measuring the species of m/z 32, 33, 34 and 40.

The measurements were done against a working reference gas, which is a mixture of Ar (4.7 %) and O_2, which are similar proportions to what is expected to find in the samples.

The oxygen isotopic species ^{16}O, ^{17}O, and ^{18}O in the sample gas are measured relative to the same species in the working reference gas.

One hour prior the measurement, the sample manifold used on the separation line the previous day, is warmed up with hot water (about 100 °C) to facilitate unfractionated desorption of oxygen and argon gases from the molecular sieve pellets. This is done while this manifold is connected to the sample side of the inlet system of the MAT 252 and the manifold is pumped to high vacuum up to the isolation valve of the sample tubes.

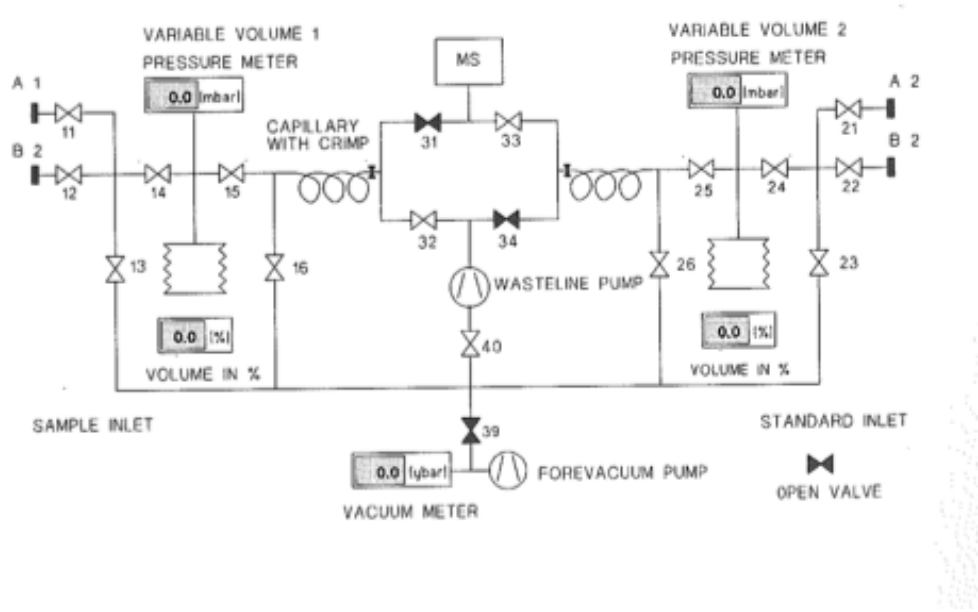

Figure 2.10. Schematic diagram of the Dual Inlet System from the 252 MAT operating manual.

The depletion rates of the reference and sample gases were also kept as matched as possible by equalising the amount of reference gas admitted to the reference bellow to that of the sample amount. This was achieved by adjusting volume of the reference bellow prior to loading the reference gas needed to measure each sample (Stanley et al., 2010). The amount of sample is roughly known before the isotopic measurement because the pressure of the gas prior to freezing in the sample tube of the collection manifold is measured. It was always admitted the sample gas while the sample bellow was fully expanded (100 %) and adjusted the reference bellow to match the reference volume to the samples. Sample and reference gases are expanded into the inlet for one

minute, then close the inlet valves (11 and 21, Fig. 2.10) and expand the reference bellow to 100 % to end up with the similar pressure on both sides. The rest of the measurement procedure is automated.

The bellows are connected to a change over valve through metal capillaries constringed with adjustable crimps. These crimps ensure that sample and reference gas flow at the same rate. The crimps also ensure viscous flow rather than molecular flow (to avoid fractionation). Samples were measured in 3 cycles, each consisting of 30 sample-reference pairs. Reference and sample gas were measured alternately thanks to a changeover valve. To avoid mixture of both gases there is a time (idle time) to evacuate the remaining gas.

The gas is ionised by bombardment with electrons released from a hot tungsten filament (75 V) source. Extraction plates focus the ions to create a beam. This beam passes through a 0.2 mm or 0.5 mm fixed width tantalum entrance slit that is the primary control of mass resolution. Reducing the width increases the resolution, but narrower window also means that part of the primary beam gets out of the slit reducing ion transmission and thus less sensitivity (Eiler et al., 2013). On the flight tube, the electromagnetic field deflect the ions in proportion to their m/z.

The IRMS has triple collectors (Faraday cups), so the masses of ionised gas can be electrically detected simultaneously (output voltage 2.5 for m/z 32, trap current 0.7 mA). Each cup is connected to amplifiers whose gain is defined by the resistor according to the isotopic abundances: m/z 32 is measured in cup 3 with a feedback resistor of 3×10^8 Ω, m/z 33 in cup 5 (1×10^{12} Ω), and m/z 34 in cup 6 (1×10^{11} Ω). The collector slit (1.5 mm) is several times the width of the ion beam. This provides a flat peak shape that is more insensitive to drift. At the end of the 3 measurements, the intensity of the Ar (m/z 40) and N_2 (m/z 28) were also measured by peak jumping. The N_2 concentration (measured as voltage) was used to correct the oxygen isotopic composition, or to detect unusual leak problems in the mass spectrometer. Samples that have shown a 1 V signal for N_2 were considered contaminated and discarded, while an intensity of 0.2 V normal, which was the case for the majority of the samples.

The whole process is 1 h and 25 min. The Dixon criterion (Dixon, 1950) is applied to the data automatically, hence the ratios that strongly deviated (outliers) are excluded from the delta calculations. The alternation of sample and reference gas and the triple Faraday cups make the IRMS more precise than sequential measurements. The main source of drift is temperature variation, because of that the temperature in the lab was kept constant.

Zero enrichment

Each day, prior to measuring samples, a zero enrichment measurement is performed. A zero enrichment measurement is a measurement for which the same gas is loaded into both sample and reference bellows. This measurements should retrieve delta values of 0 ‰. The standard deviations using aliquots of the working reference gas was 0.03 ‰ for $\delta(^{17}O)$ and 0.04 ‰ for $\delta(^{18}O)$. If values are outside of normal standard deviation it may mean technical problems (i.e. imbalance) that should be addressed before measuring any samples.

2.4.3 Mass imbalance correction

To reduce instrumental artefacts and ensure highest accuracy and precision of isotopic measurements, in theory it is necessary to have identical gas depletion rates throughout the measuring period for the sample and laboratory working standard, when measurements are done in dual inlet mode. In practice it is not possible to have totally matched depletion rates, because it is not possible to load absolutely identical amount of the two gases in the sample and reference bellows. This, coupled with the fixed step adjustment of the bellows, could create slight mismatches in the depletion rates of the two gases (called imbalance). To overcome these shortcomings, we assessed the magnitude of the impact of the imbalance on the isotopic compositions measured.

Thus I ran a series of experiments where I manually adjusted the pressure of the two gases such that the reference side was kept at a m/z 32 of 2.5 V and the sample side was

adjusted in steps of about 0.05 V up to a maximum of 0.25 V in both directions around the 2.5 V beam intensity (similar to the experiments performed by Bender et al. (1994)).

During the normal measurements runs, the pressure of the sample and working reference gas are adjusted to a signal intensity of 2.5 V. Normally the two sides are balanced to better than ± 0.03 V, but for the imbalance experiment, we chose to do measurements for a wider interval of imbalance.

Data for imbalance tests done on six different occasions (between April 2014 and May 2015) are shown in figure 2.16. In all the experiments there was a linear response in the measured delta values with respect to the size of the imbalance (measured as the difference between the signal intensity of the sample and that of the reference gas). However, these relationships are not constant over long periods, probably due to the normal wear of the filament and slit with time. Therefore, these tests were done regularly and samples analysed around that period were corrected accordingly.

Each sample is measured 3 times on the mass spectrometer and the correction due to imbalance is done for each individual cycle using the slope of the linear equations for $\delta^{17}O$ and $\delta^{18}O$ as:

$$\delta\,{}^{i}O_{true} = \delta\,{}^{i}O_{raw} - [U(32,SA) - U(32,ST)] \times m({}^{i}O) \tag{2.1}$$

where superscript i represents 17 or 18 (for delta), $U(32,SA)$ is the voltage of mass 32 the sample side, $U(32,ST)$ in the standard side and m is the slope found in the relationship of the imbalance with the $\delta^{17}O$ or $\delta^{18}O$. The slope $m(^{17}O)$ varied between -0.4 and -0.5 during the course of this project and the slope $m(^{18}O)$ varied between 1.5 and 1.7. Each individual measurement cycle was corrected for imbalance the average of the three values was calculated for each sample.

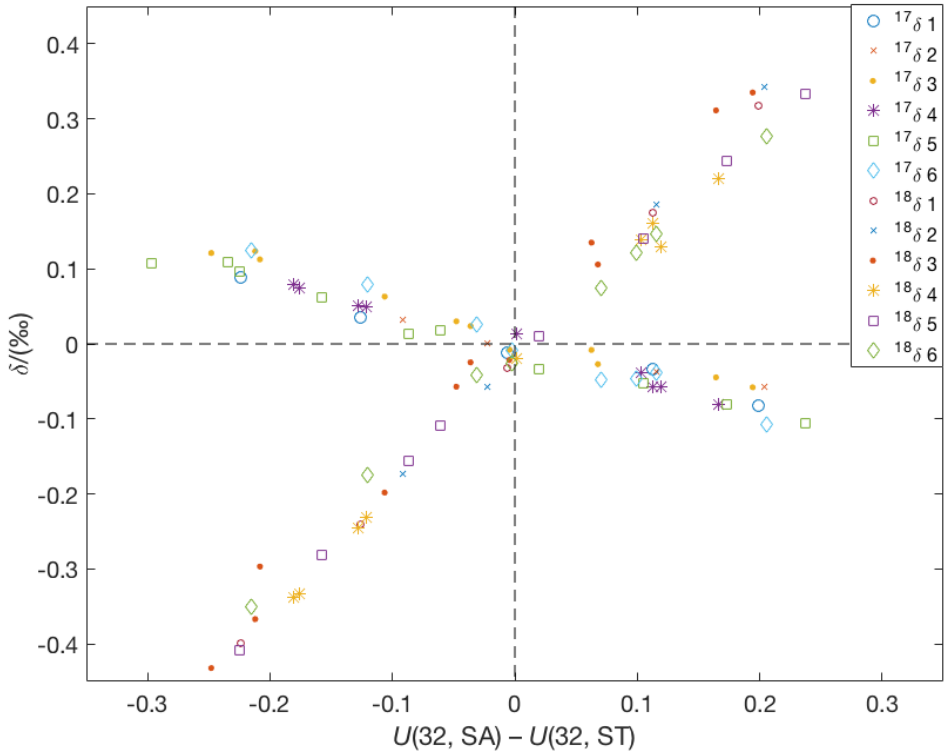

Figure 2.11. Results of six imbalance tests. The x-axis is the differences between sample and reference signal intensity (V). The y-axis is the measured $\delta^{17}O$ and $\delta^{18}O$. Numbers 1 to 6 represent the order in which the tests were done between April 2014 and May 2015.

2.4.4 Nitrogen correction

Isobaric interferences can also affect the measured oxygen isotopic composition, due to the presence of other gases in the sample gas and formation of ions with the same mass as the ionic species of interest in the ion source of the mass spectrometer. For example, when measuring the isotopic composition of oxygen, isotopic species of *m*/*z* 32, 33 and 34 are measured. If the oxygen sample gas contains traces of nitrogen, then NO^+ ions can form in the source, with *m*/*z* ranging from 30 to 33, thus interfering with some of the ionic species of interest for oxygen.

The dissolved gases in the seawater samples consist of oxygen, nitrogen, carbon dioxide, argon, etc. and prior to the mass spectrometric measurement the oxygen and argon gases are separated from the rest but the final gas sample could still have traces of

nitrogen. To assess the contribution of nitrogen traces to the measured oxygen isotopic composition, I tested how different amounts of N_2 would affect to the measured $\delta^{17}O$ and $\delta^{18}O$, using nine different concentrations of N_2, ranging from 0.05 to 0.5 %. Other authors had reported a positive relationship only in $\delta^{18}O$ (Quay et al., 1993, Emerson et al., 1999), and Abe and Yoshida (2003) found that both $\delta^{17}O$ and $\delta^{18}O$, increase with increasing N_2 amounts. We found that $\delta^{17}O$ increases with N_2 but not $\delta^{18}O$ (see Fig 2.12). This observation is also in agreement with tests perfomed previously by other scientists using the same type of IRMS, which implies that the sentitivy to N_2 seems to be instrument dependant.

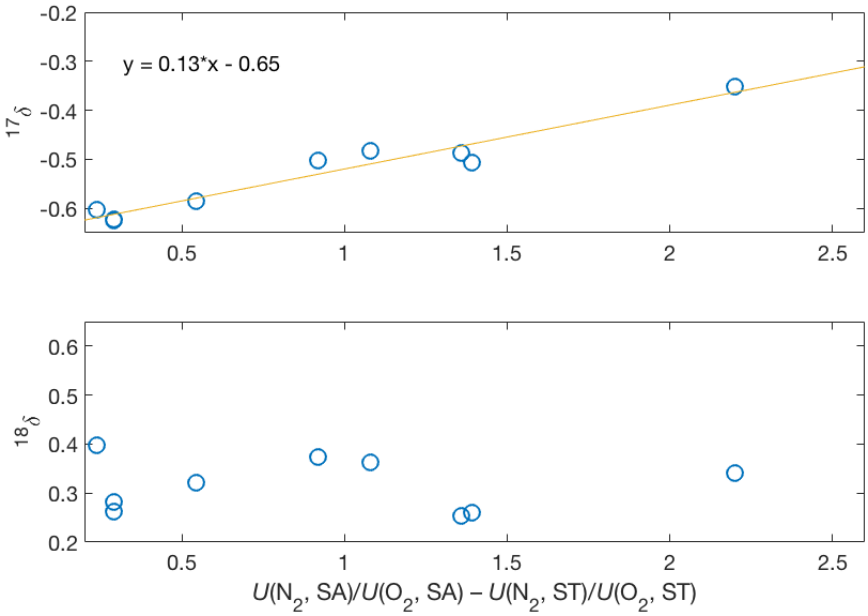

Figure 2.12. Results of nine tests done by adding different amounts of nitrogen to aliquots of oxygen and argon mixtures. The x-axis represents the differences in nitrogen amount between the sample and the reference gas, expressed as the difference in the ratio of the m/z 28 and 32 intensities (signal intensities are measured in Volts). The y-axis represents the measured $\delta^{17}O$ and $\delta^{18}O$.

At the end of the three measurement cycles for each sample, *m/z* 28 is measured. This allowed me to correct for the effect of the nitrogen amount on the measured delta values, using the slope from the linear regressions shown in figure 2.12:

$$\delta^{17}O = \delta^{17}O_{true} - [U(N_2, SA)/U(O_2, SA) - U(N_2, ST)/U(O_2, ST)] \times 0.13 \quad (2.2)$$

All raw measurements were corrected for the effects due to the amount of nitrogen present in the gas, by using equation 2.2 (see above), where $\delta^{17}O_{true}$ represents the average $\delta^{17}O$ for the three measurements, which were already corrected for the imbalance effects. Generally, the average nitrogen amount in the gas samples was approximately 0.6 V, translating to an average correction of about 0.005 ‰.

2.4.5 Dry air calibration

Every day, samples were processed on the separation line; an internal dry air standard was prepared and measured on the IRMS. These dry air samples have been purified on the separation line in the same way as the samples of dissolved gases extracted from seawater samples (see section 2.4.1) and then measured on the mass spectrometer. We also used them to check if the separation line was working properly. The mean values and standard deviations when measuring dry air (DA) samples are: $\delta^{17}O$ (-0.493 ± 0.03) ‰, $\delta^{18}O$ (-0.905 ± 0.04) ‰, $^{17}\Delta$ (-24.42 ± 9.7) ppm and $\Delta(O_2/Ar)$ (133 ± 0.9) ‰, with respect to the O_2/Ar working reference gas. The use of atmospheric oxygen (here called dry air) as reference material, is a common practice for dissolved O_2 in seawater samples and has been endorsed by the Commission on Isotopic Abundances and Atomic Weights (Wieser and Berglund, 2009). These values were used to normalise our seawater sample as follow:

$$^{17}\Delta_{nor} = \frac{^{17}\Delta - {}^{17}\Delta_{DA}}{1 + {}^{17}\Delta_{DA}} \tag{2.3}$$

where subscript *nor* means normalised and DA means dry air. The same normalization was applied to δ and $\Delta(O_2/Ar)$. For more detailed protocol steps for measuring samples, zero enrichment, imbalance or nitrogen tests see Appendix A.

2.4.6 Correction for the gas partition between the headspace and water (*Q*)

As mentioned in section 2.2.1, seawater samples were collected in pre-evacuated bottles, in order to measure the isotopic composition of the dissolved oxygen but also O_2/Ar during the peak jumping. ΔO_2/Ar values from discrete samples were calculated in the same way as from continuous measurements by the MIMS (Eq. 1.6 $\Delta(O_2/Ar) = [c(O_2)/c(Ar)]/[(c_{sat}(O_2)/c_{sat}(Ar)] - 1$), where c_{sat} was obtained from laboratory experiments detailed in next section 2.5. However, correction needs to be applied to dissolved gases for the partition between the water phase and the headspace, and the small fraction of the gases that will remain in the water phase. To correct for that, we have to know the exact volume of the bottle, seawater sample, and headspace.

Prior the sampling sea water and also before preparing the sampling bottles for a cruise, we calculated the exact volume of the bottle (Culberson, 1991) by first weighing each bottle empty, then weighing each bottle filled with distilled water. Using these two weights I calculated the mass of the water in the bottle volume, according to equation 2.4:

$$m_{water} = 1.00105 \times (W_{full} - W_{empty}) \tag{2.4}$$

where 1.00105 represents the buoyancy correction due to differences in air or in vacuum weight and W_{full}, W_{empty} are the weights of the bottle when full and empty. Using the density of water, and correcting for the glass volume expansion at the lab temperature, I calculated the exact volume of the bottle using equation 2.4 that is finally corrected for glass volume expansion due to temperature differences:

$$V_{bottle} = m_{water} \times [1 + 10^{-5} (t_{lab}/^{o}C - 20)] \tag{2.5}$$

where t_{lab} is the temperature of the lab at the time of weighing the bottles.

When calculating the volume of the gas sample I followed the same calculation protocol. First I calculated the weight of the seawater in the bottle using the weight of the bottles containing the water sample from which I subtracted the weight of the empty bottle, and corrected it for the density of the seawater. The dissolved gasses were partitioned mainly in the head space of the sampling bottle, thus the volume of head space will be the difference between the volume of the bottle and the volume of the water that it contains.

Using these calculated volumes, I then calculated the volume ratio f = (water sample volume / headspace volume) and the factor Q (Luz et al., 2002).The Q factor takes into account the distribution of the O_2 and Ar gases between seawater and headspace, which also depend on the slightly different Ostwald solubility coefficients of oxygen e.g ($\alpha(O_2)$ = 27.14 ml L^{-1}) and argon (α(Ar) = 29.89 ml L^{-1}) at 20 °C and salinity 35.

$$Q = \frac{1 + \alpha(O_2)\, V_w / V_h}{1 + (\alpha Ar)\, V_w / V_h} \tag{2.5}$$

where V_w is the volume of the water phase and V_h is the volume of the head space. Because our sample volume was always greater than the headspace and the solubility of oxygen is smaller than argon, our Q values will be always close but smaller than 1.
These values were used to correct our $\Delta(O_2/Ar)$ value as follow:

$$\Delta(O_2/Ar)_{final} = Q \times (1 + \Delta(O_2/Ar)) - 1 \tag{2.6}$$

2.5 Equilibrated water with the atmosphere (EW)

For the calculation of fluxes, we need to know the air-equilibrated water (EW) values of ΔO_2/Ar and $^{17}\Delta$ (Luz and Barkan, 2000, Craig and Hayward, 1987) (see sections 1.5 and 1.6). Other authors have measured it in the lab, but numbers do not agree well (Juranek and Quay, 2005, Luz and Barkan, 2009, Reuer et al., 2007, Stanley et al., 2010). Therefore, the value of $^{17}\Delta$ of air-equilibrated water is still in debate (Juranek and Quay,

2013). For this reason, I run seven experiments of water equilibrated with the atmospheric air.

The set-up is similar to Emerson et al. (1999) and Hamme and Emerson (2004) but our system is open to the lab's atmosphere. We used three 2 L glass Erlenmeyer flasks, which hold enough volume of water to prepare 4 replicates of EW per flask (Fig. 2.13). The 2 L flasks were bubbled with air through 1 mm i.d. tubes connected to an air pump. The flasks with air bubbled through the water were continuously stirred to kept the water well mixed. For the first four experiments we used distilled water and for the last three experiments seawater poisoned with $HgCl_2$ left from the samples collected at sea. The temperature of the lab was constant during each experiment but we tried various water temperatures in different experiments (between 13.5 – 25.5 ºC). We also tried different equilibration times for bubbling (24 – 96 h). After this time interval, the equilibrated water was transferred to sampling bottles in the same way as the seawater samples were taken on the cruise ship. Then, the dissolved air in the water sample was left to reach equilibrium with the headspace for 48 h in all seven experiments.

The final isotopic values reported here were calculated using the average values for EW from the last three experiments. During those experiments the temperature was more carefully controlled and – either because of this or improved operator practice - results showed better agreement with the published literature.

Figure 2.13. Equilibrated water experimental set-up (on the left) and 4 bottles containing EW samples (on the right).

All our EW samples are reported against dry air. Our mean $^{17}\Delta$ is (13.4 ±1.9) ppm (n = 15) or $^{17}\delta$ = (0.373±0.006) ‰, $^{18}\delta$= (0.695±0.011) ‰. Unceratainties are ± standard error here for comparison with reported values with other authors. The mean and standard deviation are in figure 2.14, been those values within the normal range of long term instrument precision. Luz and Barkan (2009) reported $^{17}\Delta$ = (16 ± 2) ppm, Juranek and Quay (2005) (18 ± 3) ppm and Sarma et al. (2006) (18 ± 2) ppm, however Reuer et al. (2007) and Stanley et al. (2010) found much lower values (8 and 7 ppm, respectively). Therefore, our value 13 ppm is within the range of reported values and uncertainty.

Mean ΔO_2/Ar is -96.1 ‰ (Fig 2.15) and has a mean standard deviation of ± 1.2 ‰ or 0.12 % which is the same precision as found in (Emerson et al., 1999). Our values are slightly lower (0.2 %) than expected (García and Gordon, 1992, Hamme and Emerson, 2004). I used different temperatures, salinities, and length of equilibration, but this didn't reduce the scatter of results between experiments; neither did I find a relationship between these parameters and $^{17}\Delta$ or ΔO_2/Ar or the order in which the samples were taken or analysed. Like in this experiment, Hamme and Emerson (2004) didn't find any relationship with the length of time of the experiment or the order in which the O_2 and Ar samples were taken but with temperature. Luz and Barkan (2009) found a dependence with temperature for $^{17}\Delta$ that I didn't find. Acoording to Luz and Barkan (2009) I adopted the temperature parameterisation but shifting by a constant offset according to the water temperature during my experiments.

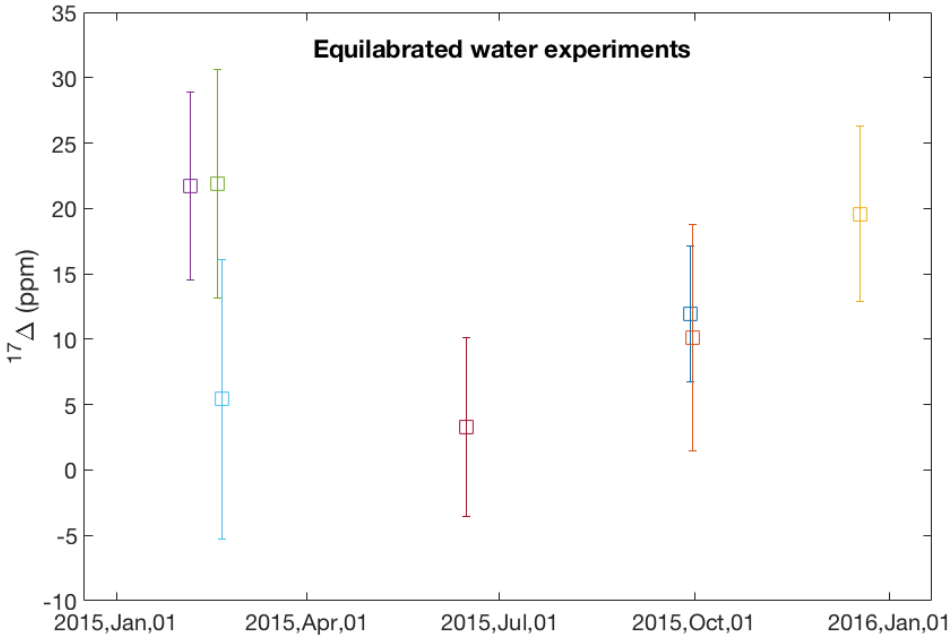

Figure 2.14. Results of seven equilibrated water experiments. The y-axis is the $^{17}\Delta$ (ppm). Squares are the mean of six samples and the bars are the standard deviation.

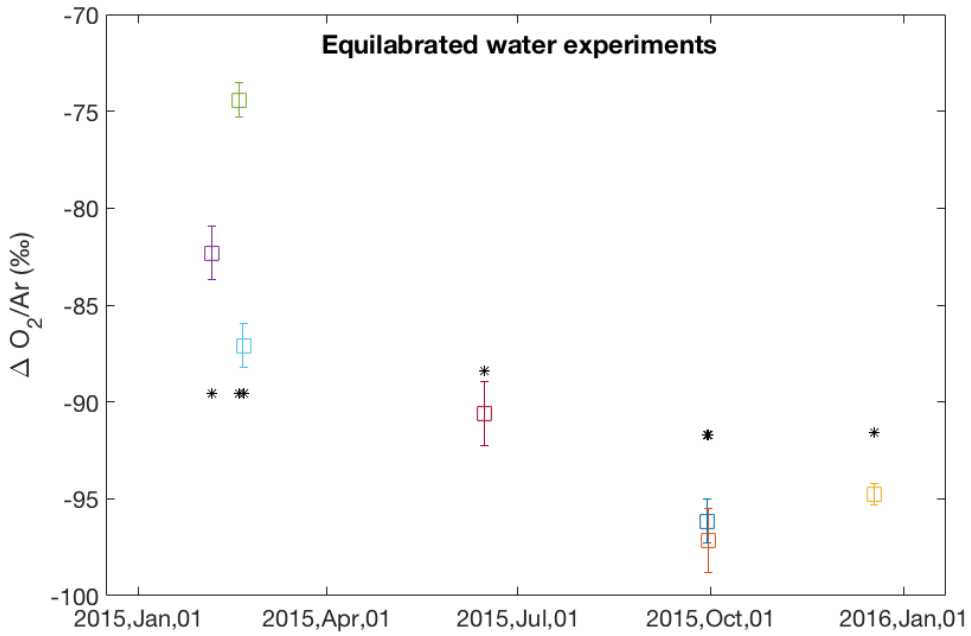

Figure 2.15. Results of seven equilibrated water experiments. Black (*) shows the expected values according to (Hamme and Emerson, 2004, García and Gordon, 1992). The y-axis is the ΔO_2/Ar (‰). Squares are the mean of six samples and the bars are the standard deviation. Each colour is a different experiment.

2.6 O_2/Ar analysis by Membrane Inlet Mass Spectrometer (MIMS)

For every cruise, the way in which the data was processed and calibrated should be the same. Only in exceptional cases due to instrument faults, the data will need to be calibrated or re-checked against other parameters.

I present the ΔO_2/Ar as the deviation of O_2/Ar from the air-saturation value. Discrete samples of equilibrated water were analysed also with the MIMS. Because EW samples are measured approximately every 24 h and the MIMS is measuring every 10 s, we first interpolated the EW to the MIMS's time resolution. With the software Matlab I calculate ΔO_2/Ar in our 200,000 data points using eq. 1.7 (Fig. 2.16). The spikes correspond to discrete CTD samples measured with the MIMS. CTD sample data were later separated from continuous surface measurements.

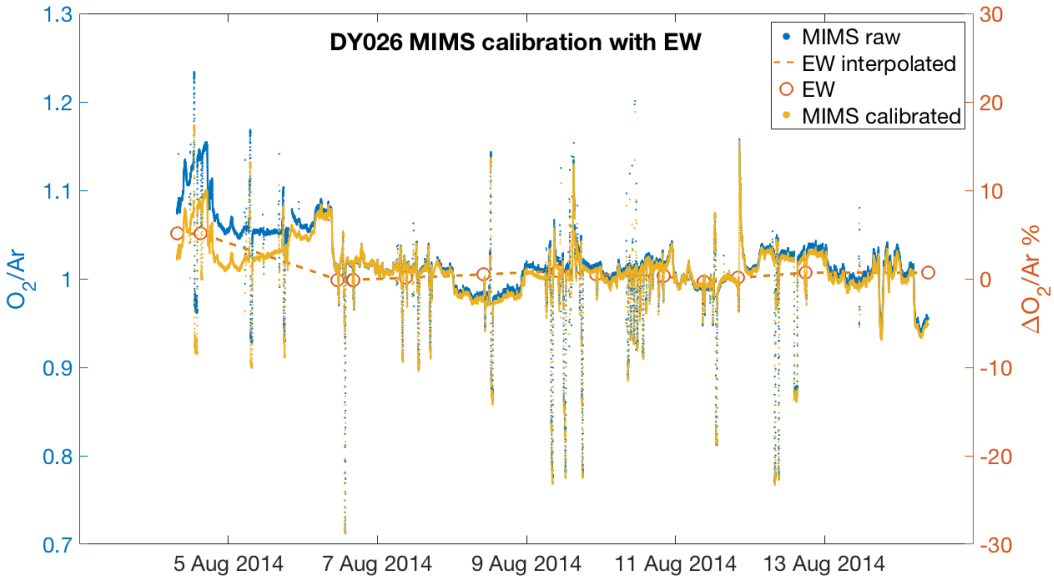

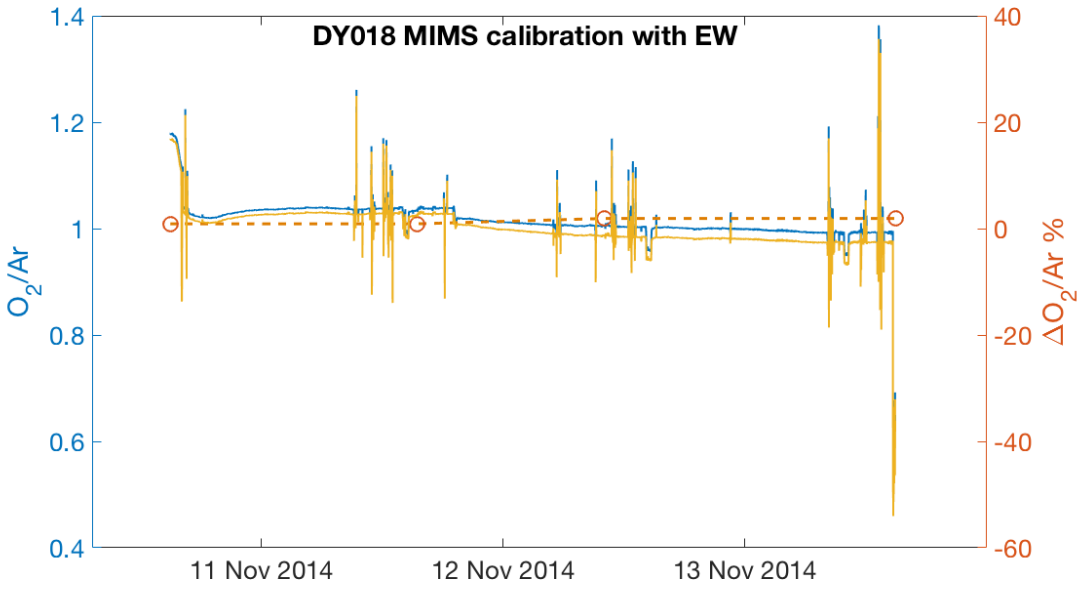
DY018 MIMS calibration with EW
1.4
1.2
1
0.8
0.6
0.4
O2/Ar
40
20
0
-20
-40
-60
ΔO2/Ar %
11 Nov 2014
12 Nov 2014
13 Nov 2014

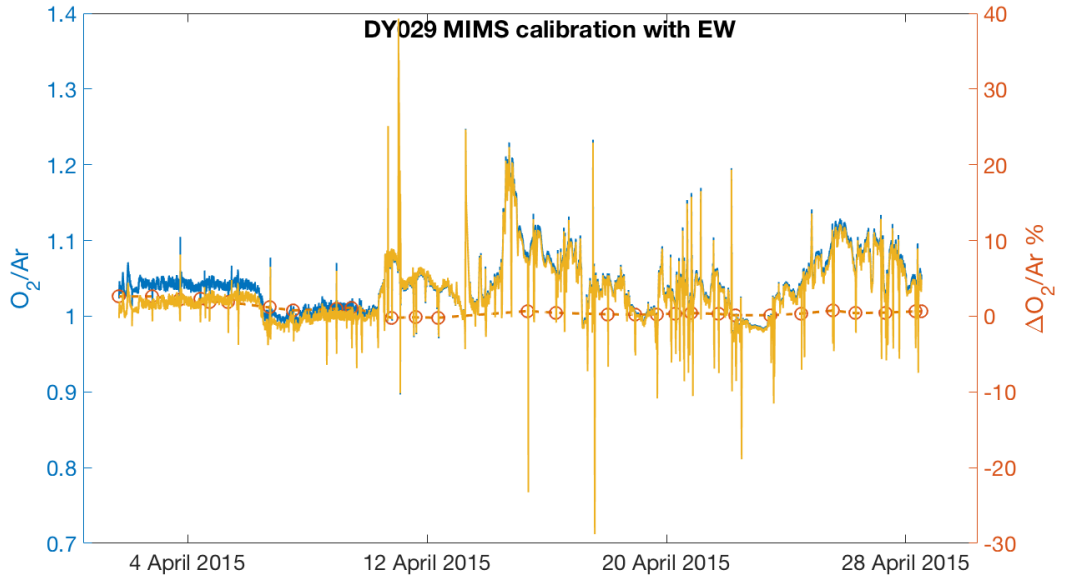
DY029 MIMS calibration with EW
1.4
1.3
1.2
1.1
1
0.9
0.8
0.7
O2/Ar
40
30
20
10
0
-10
-20
-30
ΔO2/Ar %
4 April 2015
12 April 2015
20 April 2015
28 April 2015

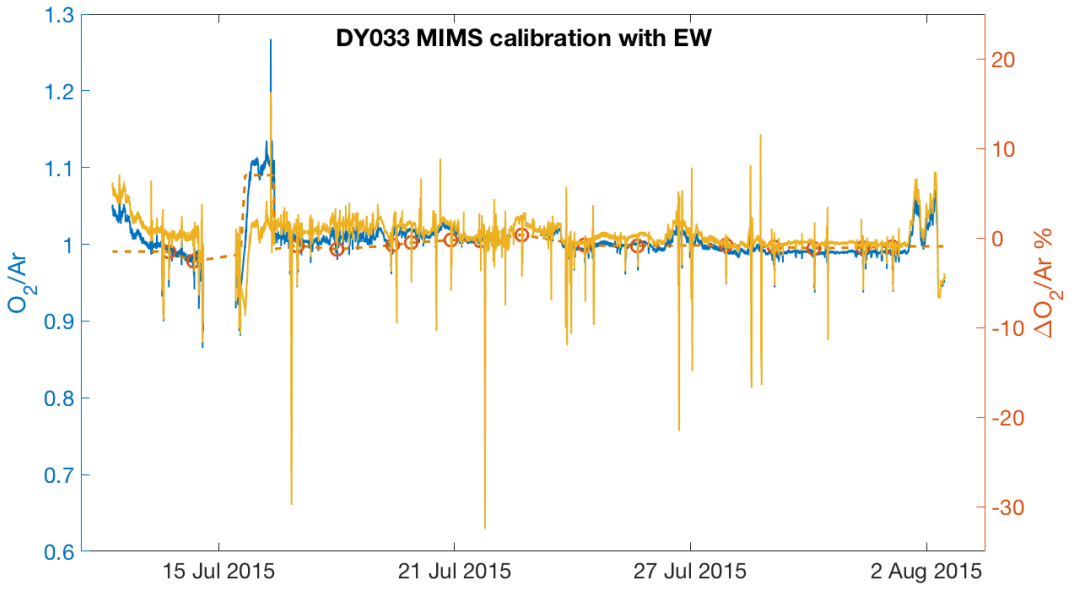

Figure 2.16. MIMS calibration with EW. In the left axis are: MIMS raw data (blue), EW interpolated (dark orange), and EW discrete values (red circles). In the right axis the MIMS data calibrated (dark yellow) against the EW interpolated values.

2.6.1 Biofouling correction

Respiratory O_2 consumption has been found in some USW pipes (Juranek et al., 2010). To avoid that, the USW pipes were treated with dilute bleach solution and flushed immediately prior to the cruise and after two weeks at sea.

There are two locations of biofouling occurring and influencing the measurements: 1) in the ship's USW pipes and 2) in the MIMS filter. I checked this by comparing $\Delta(O_2/Ar)$ discrete USW samples with CTD samples at similar depth (4 – 10 m), both measured by IRMS. These samples were not taken exactly at the same time (varied from 30 min to 4 hours) but even so did not show significant consumption or production in the ship's pipes (Fig 2.17) in cruises DY029 (April 2015) and DY033 (July 2015). During cruise DY026, I did not collect enough discrete samples from above 10 m depth, so I can only test for biofouling in the MIMS filter.

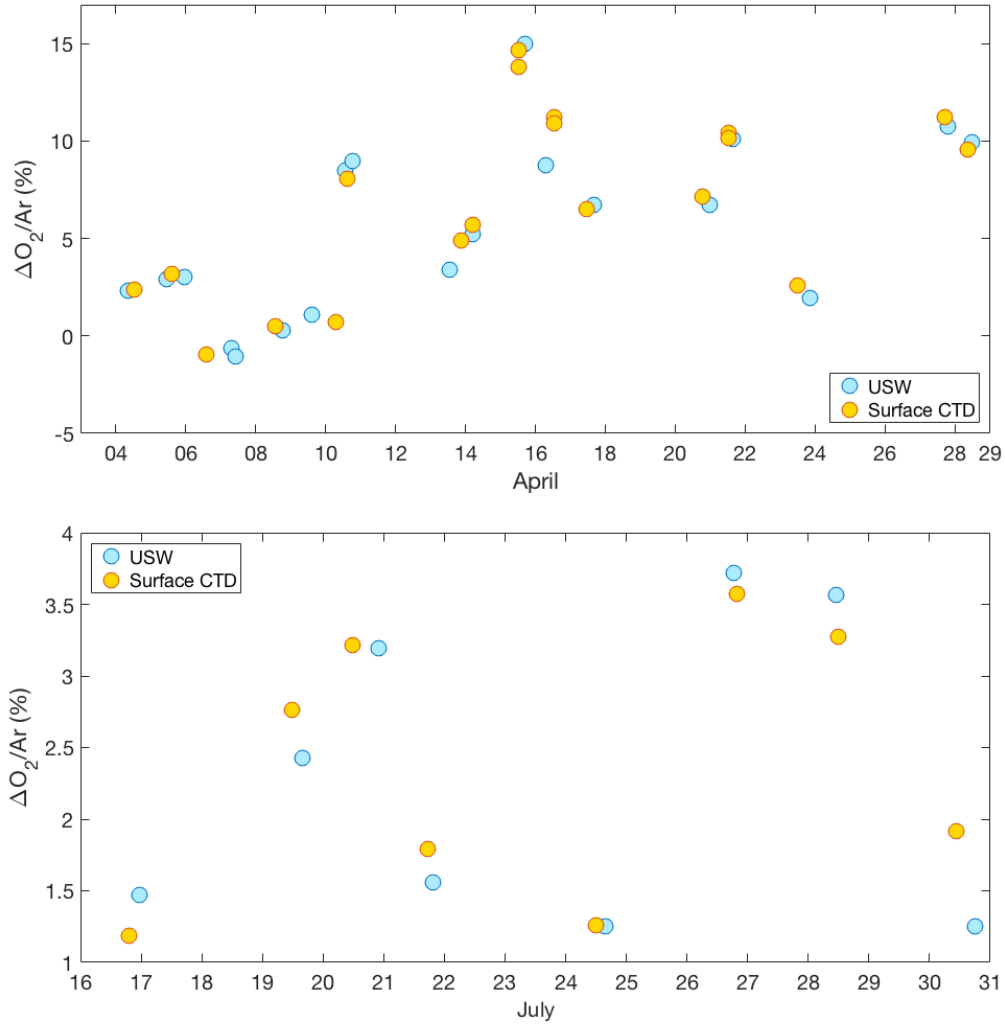

Figure 2.17. Test for biofouling effect in $\Delta O_2/Ar$ showed from no significant differences between discrete USW and near surface CTD.

However, USW samples analysed by MIMS and IRMS did not agree well. Samples analysed by MIMS are lower than the same ones measured with the IRMS ($\Delta(O_2/Ar;$ IRMS) = 1.3 $\Delta(O_2/Ar;$ MIMS) + 0.64 %) in DY029 cruise (Fig 2.18). Same analysis was done for summer cruise DY026 and DY033 and the mean residual was (2.7±1.0) % and (1.3±0.7) % respectively.

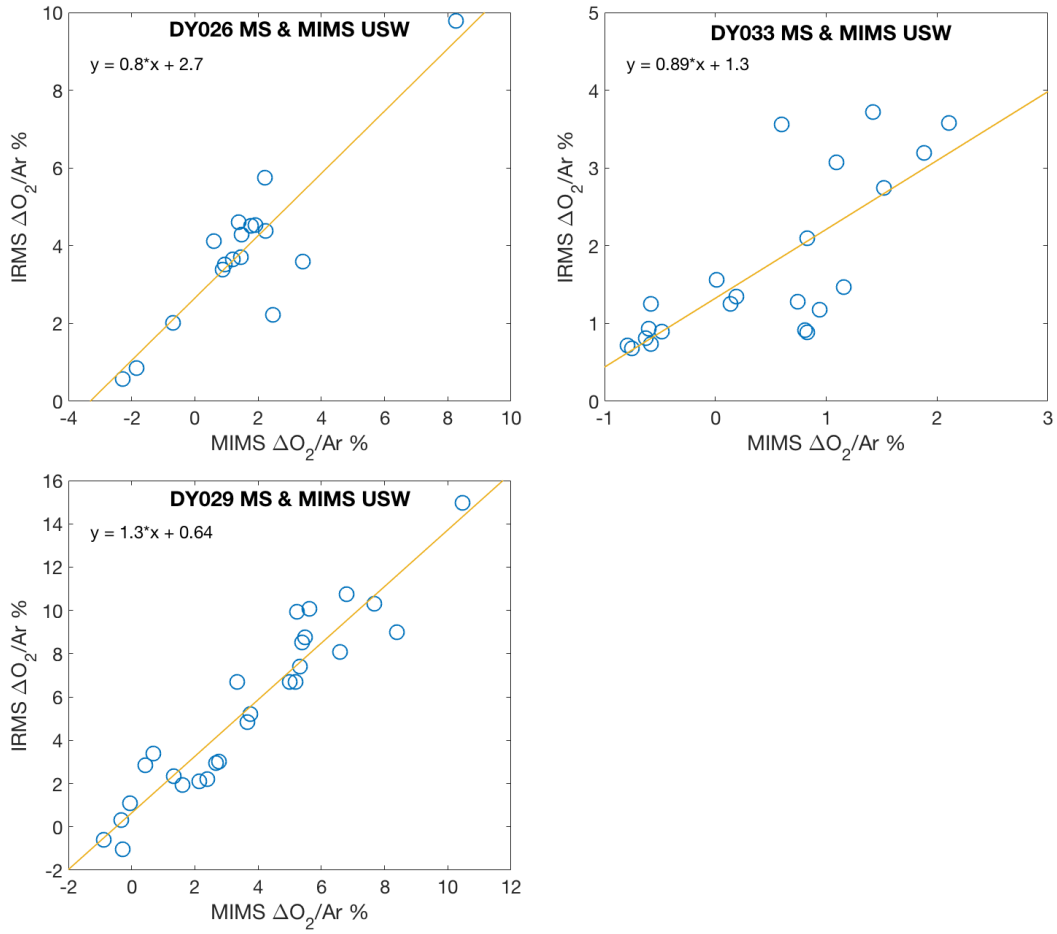

Figure 2.18. USW $\Delta O_2/Ar$ measurements with MS and MIMS on summer cruise 2014 (DY026) and 2015 (DY033), and spring cruise 2015 (DY029).

It has been already shown that there is not consumption in the ship's pipes (Fig 2.17). Therefore, the only explanation can be biofouling in the 50 µm filter at the entrance of the MIMS. I corroborate this by looking at the range in the differences of USW samples taken from before and after the filter with time and found that the differences increase until the date the filter got clogged and cleaned during DY029 cruise. After the filter was cleaned (22nd) the differences went to about 0 % and increased with the time since then (Fig. 2.19). The slopes values (represented here by the mathematical symbol α) were used to correct the continuous MIMS data. Because biofouling growth seems to be quicker after the 22nd we corrected MIMS values by two different linear regressions (α = 0.95 and α = 0.27) for spring data (Fig. 2.19 & Fig. 2.20) and one linear regression for each summer data (α = 0.08 and α = 0.24) (Fig. 2.19).

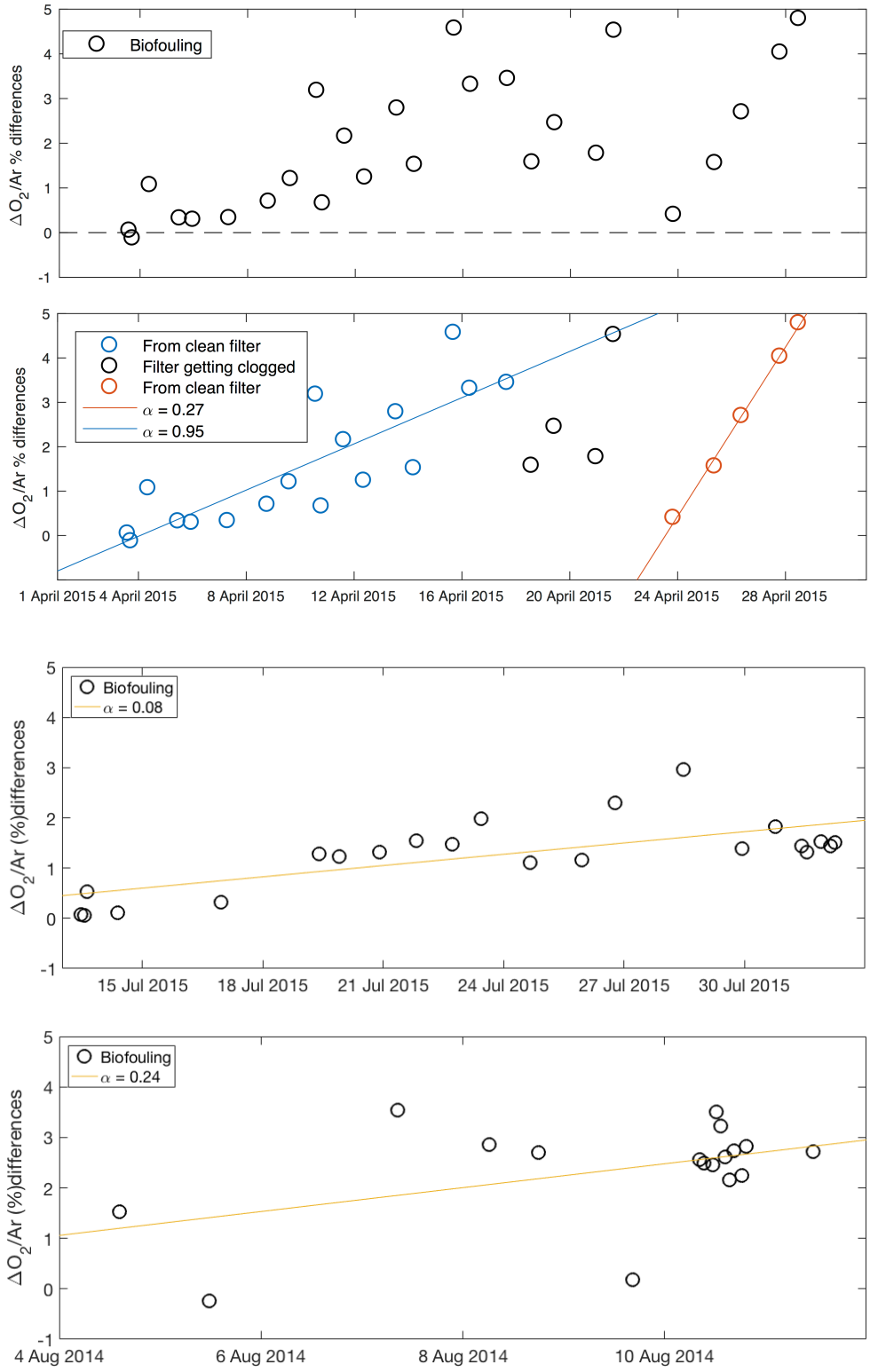

Figure 2.19. Biofouling effect in $\Delta O_2/Ar$ showed from the differences between USW samples measured before and after the 50 µm filter. Black circles show the differences along the entire cruises. April plots show the differences from the beginning of the cruise with the filter clean (blue circles), filter getting clogged (black circles) and after cleaning filter (dark orange).

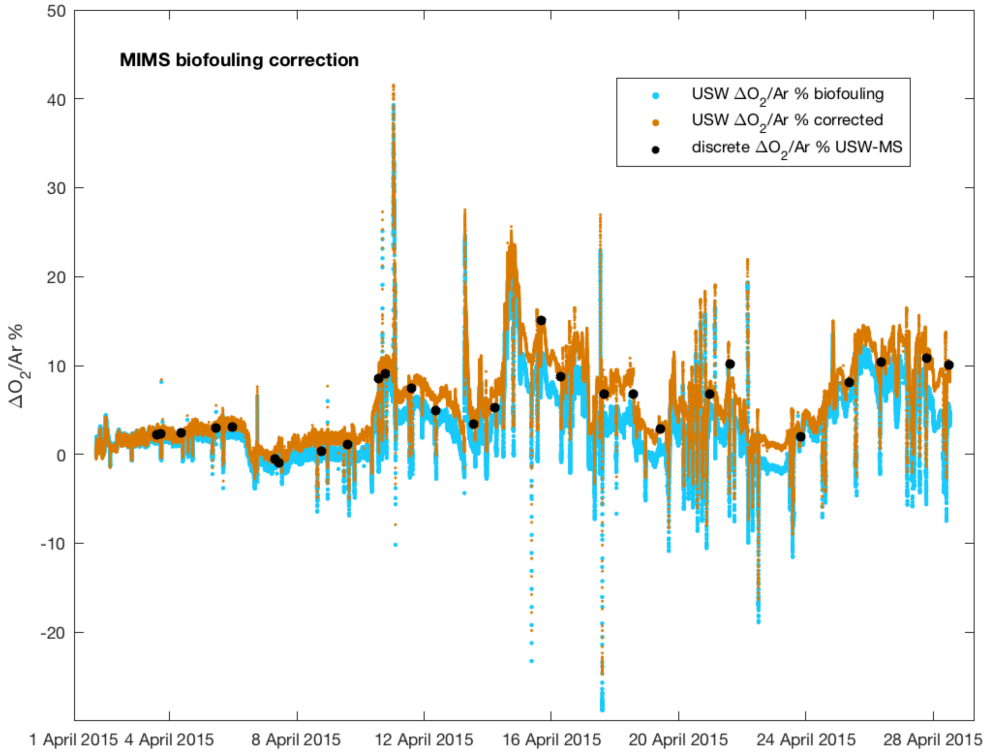

Figure 2.20. MIMS data affected by biofouling (blue), MIMS data corrected (dark orange) and discrete samples used for the calibration (black).

Once our data are calibrated and corrected for instrument deviation and biofouling, we can then use them for the calculation of net community production that is explained in the following chapter 3.

Chapter 3. Net community production and gross production calculation

3.1 Introduction

In the present chapter I explain how to calculate net community production ($N(O_2/Ar)$) from O_2/Ar ratios and gross production ($G(^{17}O)$) from triple oxygen isotopes. $N(O_2/Ar)$ was calculated from continuous and discrete samples, while $G(^{17}O)$ only from discrete ones. The combination of the two allows us to calculate the ratio of net to gross production, called f-ratio.

3.2 Net community production

$\Delta(O_2/Ar)$ can be used to assess net community production assuming steady state conditions by equating it with the biological air-sea exchange flux and neglecting mixing, but these assumptions can entail large uncertainties (Cassar et al., 2014, Jonsson et al., 2013, Nicholson et al., 2012), especially in dynamic systems like the Celtic Sea. The high frequency surface measurements performed with the MIMS combined with discrete samples at different depths will allow us to calculate high resolution $N(O_2/Ar)$ without resorting to the steady state assumption.

In the following section I will show how to combine biological oxygen fluxes due to diapycnal mixing across the base of the mixed layer (F_v), entrainment into the mixed layer (F_e), lateral advection (F_a), temporal change (F_{nss}) and production below the mixed layer (F_{bml}) with the biological air-sea exchange flux (F_{bio}) to give improved estimates of net community production ($N(O_2/Ar)$):

$$N(O_2/Ar) = F_{bio} - F_v + F_e + F_a + F_{nss} + F_{bml} \tag{3.1}$$

3.2.1 Biological air-sea exchange flux (F_{bio})

I calculate the biological air-sea exchange flux as follows:

$$F_{bio} = k\, c_{sat}(O_2)\, \Delta(O_2/Ar) \quad (3.2)$$

where k is the O_2 gas exchange coefficient calculated from a wind speed-based parameterisation (Nightingale et al., 2000) and $c_{sat}(O_2)$ is the oxygen in air-saturation concentration at a given seawater temperature, salinity and atmospheric pressure (Hamme and Emerson, 2004, García and Gordon, 1992).

3.2.2 Wind speed parameterisation for gas exchange calculation (*k*)

The value of k depends to which parameterisation is considered the most appropriate, which is still under debate (see section 1.4.1). From the parameterisations in the literature, two were considered as options for this study: Wanninkhof (2014) and (Nightingale et al., 2000). The most frequently used method is Wanninkhof (1992) but in 2014 the same author publish an updated paper based on the same method, but using updated global ocean ^{14}C inventories, improved wind speed (at 10 m, u_{10}) products and new estimates of the Schmidt number (Sc). The value a in the equation $k = a <[u_{10}/(m/s)]^2> (Sc/660)^{-0.5}$ changed from 0.31 cm h^{-1} in Wanninkhof (1992) to 0.251 cm h^{-1} in Wanninkhof (2014). The accuracy of a is crucial to reduce the uncertainty of k. The uncertainty using Wanninkhof (2014) is estimated to be 20 %.

Nightingale et al. (2000) used a dual tracer experiment in the North Sea to calculate the k dependence on wind speed. He proposed the following equation:

$$k/(cm\ h^{-1}) = 0.222 <[u_{10}/(m/s)]^2> + 0.333 <u_{10}/(m/s)> (Sc/600)^{-0.5} \quad (3.3)$$

I will use this parameterization for our calculations because gas exchange rates can vary from global parameterizations to shelf seas. The area of study is strongly related to the conditions in this dual-tracer experiment (e. g. intensity of the winds, temperature) and close geographically. For that reason I prefer (Nightingale et al., 2000) for the calculations of k but note that the difference to Wanninkhof (2014) is small (Fig. 3.1). For the calculation of the Sc number, I used Wanninkhof (2014) in both cases. The two parameterisations differ slightly at higher wind speeds, but the mean difference is less than 2 %, which is a negligible uncertainty.

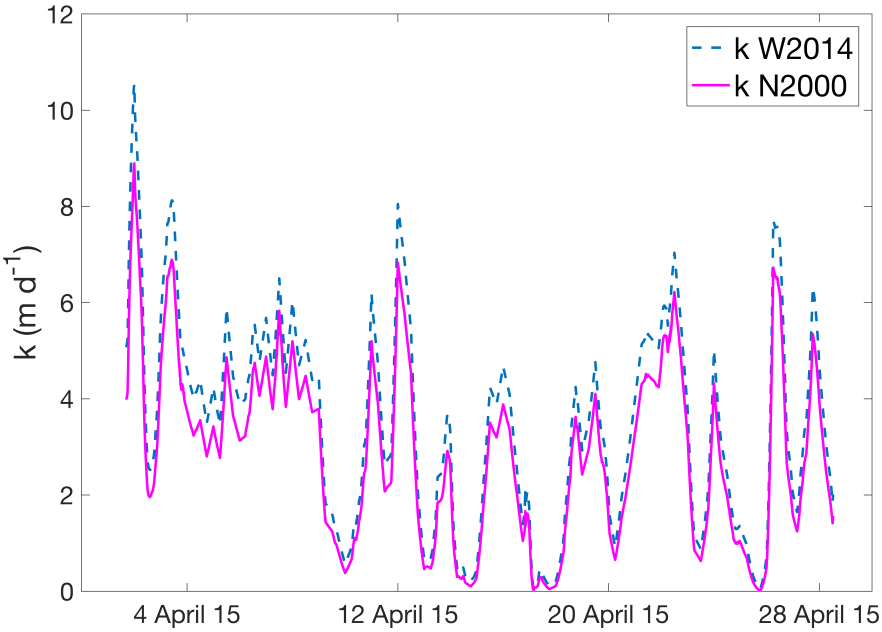

Figure 3.1. Gas exchange coefficients based on wind speed parameterisations according to Wanninkhof (2014) (W2014) and Nightingale et al. (2000) (N2000).

Wind speeds can be measured directly from the ship, on buoys or with satellites. In theory, wind speeds measured in situ by the ship's anemometer should be the most accurate and relevant for the flux calculations. Buoys also provide in situ measurements but maybe outside the sampling area. Satellites derive wind speeds from microwave radiometer remote sensing.

Satellite wind products can be calibrated with in situ observations using a Variational Analysis Method (VAM) to produce high-resolution gridded analyses. Here I compared a wind product and ship measurements and found that winds measured directly by the ship compared with CCMP winds, appeared to be (1.5±2.0) m s^{-1} higher on average (Fig. 3.2). It is known that ship wind measurements can be biased by the ship's superstructure (Moat et al., 2005). For this reason I have not used the ship's winds in the present analysis. Instead, I use Cross Calibrated Multi Platform (CCMP) wind speeds at 0.25° and 6 h resolution (http://www.remss.com/measurements/ccmp) for the calculation of the gas exchange velocities.

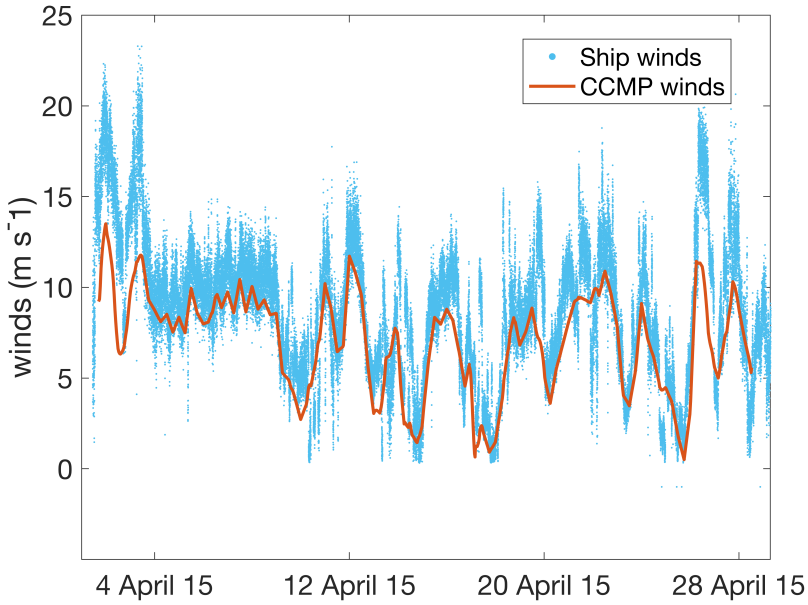

Figure 3.2. Wind speed (m s^{-1}) comparison between ship's winds and CCMP winds during cruise time.

A comparison of CCMP winds with anemometer measurements at the Met Office ODAS buoy positioned in the centre of the Celtic Sea showed that they agreed to within (0.2±0.2) m s^{-1} (Fig. 3.3). Ship, buoy and wind product observations are referenced to a height of 10 meters.

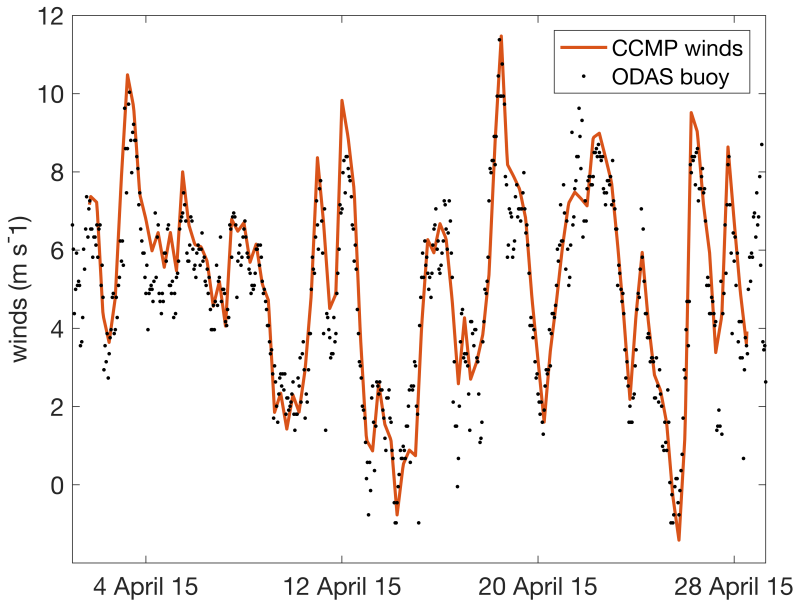

Figure 3.3. Wind speed comparison between CCMP winds and ODAS buoy at the CCS station during the same period as the cruise.

Instantaneous winds have been used to calculate k here. However, Reuer et al. (2007) proposed a weighted gas transfer coefficient (k_w) to account for wind speed variability (Eq. 3.4). Other authors have also followed this type of calculation (Stanley et al., 2010, Bender et al., 2011).

$$k_w = \frac{\sum_{t=1}^{n} k_t \, \omega_t}{(1-\omega_n) \sum_{t=1}^{n} \omega_t} \tag{3.4}$$

where the $(1-\omega_n)$ term accounts for the residual unventilated portion of the mixed layer and n are the days prior the sampling. This calculation is not possible when using ship's winds because of its retrospective nature, but it is possible with satellite wind products and buoy observations. The weighting factors (ω_t) account for the ventilation of the mixed layer during the residence time of O_2. The gas exchange time or residence time of gases is calculated as the ratio of mixed layer depth and gas exchange coefficients. Although the gas exchange coefficients can be calculated prior the sampling period, the mixed layer depth has to be assumed constant. However, the mixed-layer depth actually varies a lot in the Celtic Sea, at least for the period sampled in spring. For the transition from winter to spring, I expect changes in water column stratification, and assumption of a fixed mixed layer depth is likely to be incorrect. Moreover, since the overturning time of O_2 in the mixed layer during the first two weeks of the spring bloom is relatively short (1 – 2 weeks) I use instantaneous wind-speeds here. Main uncertainties from the air-sea exchange fluxes arise from analytical uncertainties when O_2 value is close to equilibrium, and from gas exchange coefficient calculation when O_2 value is large (Reuer et al., 2007). Therefore, as O_2 at the beginning of the cruise was close to equilibrium (Fig 2.20), the contribution of this uncertainty in the gas exchange coefficient to the uncertainty in F_{bio} is relatively small. However, for comparison, I also calculated the weighted-mean gas exchange coefficients over the month prior to the sampled period, March 2015. This shows a k_w value of 1.6 m d^{-1}, which is less than the mean k (2.1 m d^{-1}) with instantaneous winds.
Our production values will be compared in the next chapter 4 with other studies in the Celtic Sea, and none of those studies used weighted winds (e. g. Robinson et al. (2009) use in situ winds in their calculations). Further explanations of how suitable are k or k_w depending on the season will be addressed in chapter 5 (Seasonality in the Celtic Sea).

3.2.3 Diapycnal diffusion

The contribution of diapycnal diffusion across the base of the mixed layer (F_v) was calculated according to the following equation

$$F_v = K_z c(O_2) \frac{d \ln \frac{c(O_2)}{c(Ar)}}{dz} \tag{3.5}$$

where K_z is the vertical diffusivity coefficient, $c(O_2)$ is the oxygen concentration from the CTD oxygen sensor and the third term is the O_2/Ar gradient across the base of the mixed layer. I haven't estimate K_z but I took a value of (3±2) × 10^{-5} m^2 s^{-1} from the literature for the area of our study (Simpson and Sharples, 2012, Osborn, 1980, Palmer et al., 2013).

The calculation of diffusion depends on the definition of the mixed layer base. The mixed layer depth (z_{mix}) is typically calculated from changes in density, but it can be defined as changes in nutrients or oxygen. The mixed layer depth was defined as the depth where the absolute oxygen concentration difference exceeded 0.5 % with respect to the surface, as recommended for gas exchange studies (Castro-Morales and Kaiser, 2012). For comparison I also calculated F_v based on a density-difference based mixed layer depth using a 0.01 kg m^{-3} threshold (Fig. 3.4). F_v calculated from every profile was linearly interpolated over time before applying to MIMS data.

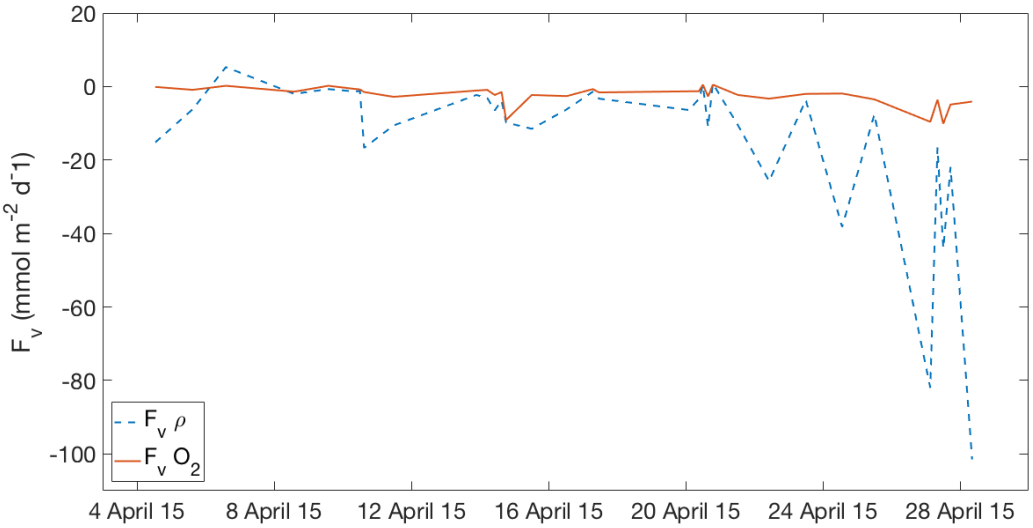

Figure 3.4. Diapycnal diffusion based in different definitions of mixed layer depth (density in blue and oxygen in orange).

3.2.4 Entrainment

Entrainment occurs when the depth of the mixed layer increases ($\Delta z_{mix} > 0$). Entrainment events will decrease oxygen concentration due to mixing with deeper waters, which typically have lower oxygen concentrations than surface waters. When $\Delta z_{mix} < 0$ there is no entrainment, no change in O_2/Ar concentration and therefore this term is not applied to the calculation of $N(O_2/Ar)$. The entrained concentration (F_e) can be approximated by the concentration gradient at the base of the mixed layer and the increase in mixed layer depth Δz_{mix}:

$$F_e = -\frac{1}{2}\, c(O_2)\, \frac{(\Delta z_{mix})^2}{\Delta t}\; \frac{\mathrm{d}\ln\left(\frac{c(O_2)}{c(Ar)}\right)}{\mathrm{d}z} \tag{3.6}$$

½Δz_{mix} is the entrainment length scale (Gruber et al., 1998, Castro-Morales et al., 2013) and Δt is the number of days in between samplings.

3.2.5 Temporal changes

Temporal non-steady state changes in the oxygen mass balance are taken into account by the term F_{nss} (Eq 3.7):

$$F_{nss} = z_{mix}\, c(O_2)\, \frac{\mathrm{d}\ln\frac{c(O_2)}{c(Ar)}}{\mathrm{d}t} \tag{3.7}$$

where z_{mix} is the shallower mixed layer depth from different moments, and the third term is the O_2/Ar differences over time. I use depth profiles to calculate the z_{mix}. O_2/Ar changes over time are derived from continuous MIMS measurements.

3.2.6 $N(O_2/AR)$ below the mixed layer

By measuring temporal changes in O_2/Ar, it is possible to measure $N(O_2/Ar)$ below the mixed layer. However, it was not possible to calculate horizontal transport, and deep currents can be strong (Palmer et al., 2013), therefore there is some uncertainty in our calculation of this term. The contribution of F_{bml} to the final oxygen mass balance will also depend on the thickness of the layer between z_{mix} and z_{eu}. The production below the mixed layer (F_{bml}) is not affected by gas exchange and is only relevant within the euphotic zone (z_{eu}). Therefore, I calculated production below the mixed layer only when z_{eu} was deeper than z_{mix} ($z_{eu} > z_{mix}$). The depth of the euphotic zone (1 % of incident light) was determined from photosynthetically active radiation (PAR) profiles during daytime CTD casts. The contribution of $N(O_2/Ar)$ below the mixed layer depth was calculated in the same way as F_{nss} (i.e. $\Delta(\int c(O_2)dz) / \Delta t$).

3.2.7 Differences in O_2 and Ar solubilities

There is a small difference between O_2 and Ar solubilities. To account for that I use the Schmidt numbers Sc and O_2 and Ar gas exchange coefficients:

$$F_{Sc} = k\, c(O_2)\, (\Delta O_2 - \Delta O_2/Ar)\, [1 - (\frac{Sc(O_2)}{Sc(Ar)})^{0.5}] \quad (3.8)$$

where the term $1-(Sc/Sc')^{0.5}$ is about 0.042 (Wanninkhof (2014) Sc parameterisation) or 0.044 (Keeling et al. (1998) Sc parameterisation). Here I used Wanninkhof (2014).

3.3 Gross production

The triple oxygen isotope ratios ($^{17}O/^{16}O$ and $^{18}O/^{16}O$) of dissolved O_2 can be used to estimate gross oxygen production integrated in the mixed layer at steady state. Initial work used an approximated equation based on the ^{17}O excess, $\Delta(^{17}O)$ (Luz and Barkan, 2000) (see section 1.3.1; Chapter 1). Here I use the improved dual-isotope approach to calculate $G(^{17}O)$ (Kaiser, 2011b, Kaiser and Abe, 2012):

$$G_{ss}(^{17}\mathrm{O}) = k(\mathrm{O}_2)c_{sat}(\mathrm{O}_2)\frac{(1+{}^{17}\varepsilon)\frac{{}^{17}\delta - {}^{17}\delta_{sat}}{1+{}^{17}\delta} - \gamma(1+{}^{18}\varepsilon)\frac{{}^{18}\delta - {}^{18}\delta_{sat}}{1+{}^{18}\delta} + s({}^{17}\varepsilon - \gamma\,{}^{18}\varepsilon)}{\frac{{}^{17}\delta_P - {}^{17}\delta}{1+{}^{17}\delta} - \gamma\frac{{}^{18}\delta_P - {}^{18}\delta}{1+{}^{18}\delta}} \quad (3.9)$$

where ε is the kinetic isotope fractionation during O_2 evasion ($^{18}\varepsilon$ = –2.095 ‰ (Knox et al., 1992) and $^{17}\varepsilon$ = –1.463 ‰ (based on a mass-dependent relationship between $^{18}O/^{16}O$ and $^{17}O/^{16}O$ fractionation with an exponent of 0.522 (Kaiser, 2011b) and δ_{sat} at the measured temperature and salinity, i.e. $^{17}\delta_{sat}$ = (0.373±0.02) ‰ and $^{18}\delta_{sat}$ = (0.695±0.04) ‰ (Luz and Barkan, 2009). $\gamma = {}^{17}\varepsilon_R / {}^{18}\varepsilon_R = 0.5179$ is the triple isotope fractionation coefficient during respiration. $^{17}\delta_P$ = –11.644 ‰ and $^{18}\delta_P$ = –22.832 ‰ are assumed as the photosynthetic end-member delta values (Kaiser, 2011b, Kaiser and Abe, 2012, Kaiser, 2011a). Prokopenko et al. (2011) proposed a similar approach to the dual-delta method of Kaiser (2011b); the only difference being that they omitted the isotopic fractionation during gas exchange (ε) and the biological O_2 supersaturation $s = \Delta(O_2/Ar)$. The dual delta method has been used by a number of authors to calculate gross production rates (Castro-Morales et al., 2013, Hamme et al., 2012, Nicholson et al., 2012, Juranek et al., 2012, Palevsky et al., 2016).

The above equation 3.10 is valid for steady-state conditions (Kaiser, 2011b). In the following section I will show how to calculate diapycnal mixing across the base of the mixed layer (F_v), entrainment into the mixed layer (F_e), lateral advection (F_a), temporal changes in the oxygen mass balance (F_{nss}) and production below the mixed layer (F_{bml}), which – together with steady state $G_{ss}(^{17}O)$ estimates – give $G(^{17}O)$.

3.3.1 Diapycnal diffusion

The diffusion across the base of the mixed layer from a more O_2 concentrated layer to the other ($d \ln[(1+{}^{17}\delta) / (1+{}^{18}\delta)^{\gamma}] / dz \neq 0$) was calculated according to the following equation:

$$F_v = k_z c(O_2)\left[\frac{\frac{d\ln\left(\frac{(1+{}^{17}\delta)}{(1+{}^{18}\delta)\gamma}\right)}{dz}}{\frac{{}^{17}\delta_P - {}^{17}\delta_{ml}}{1+{}^{17}\delta_{ml}} - \gamma\frac{{}^{18}\delta_P - {}^{18}\delta_{ml}}{1+{}^{18}\delta_{ml}}}\right] \quad (3.10)$$

were k_z is the same value as in equation 3.5, subscripts ml stands for mixed layer, γ is the triple isotope fractionation coefficient during respiration (0.5179) and δ_P is the photosynthetic end-member delta values stated in equation 3.9.

3.3.2 Entrainment

The calculation of entrainment is equivalent to $\Delta O_2/Ar$: changes of δ with deepening of the mixed layer ($d\ \ln[(1+{}^{17}\delta) / (1+{}^{18}\delta)^{\gamma}] / dz \neq 0$). Δ_{zmix} is the thickness of the entrainment, Δt are differences from the first and second sampling:

$$F_e = -\frac{1}{2}\, c(O_2)\frac{(\Delta_{zmix})^2}{\Delta t}\left[\frac{\frac{d\ln\left(\frac{(1+{}^{17}\delta)}{(1+{}^{18}\delta)\gamma}\right)}{dz}}{\frac{{}^{17}\delta_P - {}^{17}\delta_{ml}}{1+{}^{17}\delta_{ml}} - \gamma\frac{{}^{18}\delta_P - {}^{18}\delta_{ml}}{1+{}^{18}\delta_{ml}}}\right] \quad (3.11)$$

3.3.3 Temporal changes

Combining ${}^{17}\delta$ and ${}^{18}\delta$ changes over time I arrive to the following equation 3.12 (Kaiser, 2011b):

$$F_{nss} = z_{mix} c(O_2)\left[\frac{\frac{d\ln\left(\frac{(1+{}^{17}\delta)}{(1+{}^{18}\delta)\gamma}\right)}{dt}}{\frac{{}^{17}\delta_P - {}^{17}\delta_{t1}}{1+{}^{17}\delta_{t1}} - \gamma\frac{{}^{18}\delta_P - {}^{18}\delta_{t1}}{1+{}^{18}\delta_{t1}}}\right]$$

(3.12)

where z_{mix} is the same value as used for O_2/Ar, t_1 and t_2 are dates of sampling, and the third term is the δ differences over time (d ln[$(1+^{17}\delta) / (1+^{18}\delta)^{\gamma}$] / d$t \neq 0$).

3.3.4 GP below the mixed layer

The isotopic composition below the mixed layer will change only due to production, as it will not be affected by air exchange signal with time. The equation is exactly the same as per equation 3.12 above but using delta values measured below the mixed layer (Kaiser, 2011b).

3.4 Calculation of ƒ-ratio

The combination of net oxygen community production and gross oxygen production allow us to calculate the efficiency of the biological pump or *f*-ratio:

$$f(O_2) = N(O_2/Ar) / G(^{17}O) \tag{3.15}$$

To calculate net community production in carbon equivalents, $N(O_2/Ar)$ was converted using a photosynthetic quotient of 1.4 (Laws, 1991):

$$N_C = N(O_2/Ar) / 1.4 \tag{3.16}$$

Similarly, to convert $G(^{17}O)$ and to make it compatible with conventional ^{14}C-labelled 24 hour-incubations, I used (Marra, 2002):

$$P_C(^{14}C; 24\ h) = G(^{17}O) / 2.7 \tag{3.17}$$

These conversions were then used to calculate the "historic" *f*-ratio

$$f_C(\text{historic}) = N_C / P_C(^{14}C; 24\ h)$$

(3.18)

However, this value is not constant. Therefore, for comparison I also used Hendricks et al. (2004) equation:

$$G_C(^{17}O) = N(O_2/Ar) / 1.4 + [0.8\ G(^{17}O) - N(O_2/Ar)] / 1.1$$

(3.19)

which uses photosynthetic quotients of 1.4 for "new" production (assumed to equal net community production) and 1.1 for "regenerated" production. The factor of 0.8 corrects for water-to-water cycling reactions such as the Mehler reaction, which produce O_2 with the oxygen isotope signature of photosynthetic O_2 and consume O_2 with ambient δ values, without associated C fixation. These conversion was then used to calculate the *f*-ratio in terms of carbon equivalents (Hendricks et al., 2004):

$$f_C(O_2) = N_C / G_C(^{17}O)$$

(3.20)

Chapter 4. High-resolution net and gross biological production during a Celtic Sea spring bloom

4.1 Introduction

This introduction has been shortened from the publication version to avoid repetition within the thesis.

In the last 15 years, considerable efforts have been made in developing and improving techniques to measure marine biological productivity (Tortell, 2005, Kaiser et al., 2005, Cassar et al., 2009, Juranek and Quay, 2013). There are different terms and metrics in use to express marine biological productivity (or production), in particular gross and net primary production (GPP, NPP) and net community production (NCP), either expressed in terms of C or O_2 equivalents. GPP, here measured as $G(^{17}O)$, represents the total photosynthetic O_2 production by autotrophs. NCP, here measured as $N(O_2/Ar)$, is GPP minus community respiration by autotrophs and heterotrophs. NPP is GPP minus autotrophic respiration, an approximation of which is derived from 24 hour ^{14}C incubations, here designated $P(^{14}C; 24\ h)$.

Despite spatio-temporal limitations during a research cruise and inherent uncertainties to any productivity determination, the non-incubation methods based on dissolved oxygen-to-argon (O_2/Ar) ratios and triple oxygen isotopes (^{16}O, ^{17}O, ^{18}O) provide an improved way to derive estimates of net and gross biological production (Juranek and Quay, 2013, Quay et al., 2012). These two methods together can be used to estimate the efficiency of the carbon pump (Palevsky et al., 2016, Haskell et al., 2017), based on the ratio of $N(O_2/Ar)$ to $G(^{17}O)$, or $f(O_2)$.

Here, we use the biogeochemical O_2/Ar method to derive mixed layer net community production rates from continuous membrane inlet mass spectrometry (MIMS) measurements (Kaiser et al., 2005), which resolves variability at sub-km scale resolution. Using the measured O_2/Ar supersaturation and wind-speed based air-sea gas exchange parameterisations, we calculate biological O_2 air-sea fluxes (F_{bio}), correct them for diapycnal diffusion and disequilibrium terms to estimate mixed layer net community production rates. These measurements are combined with shore-based analyses of discrete samples for oxygen triple isotope ratios to derive gross O_2 production rates (Luz et al., 1999). Our combined approach results in high-resolution in

situ estimates of primary production during the spring bloom in the Celtic Sea. Such measurements can serve to validate satellite ocean colour productivity estimates, and feed models of the carbon pump to predict the impact of climate change. This will improve our understanding of primary production variability and potential impacts of human activities in the temperate shelf seas.

4.2 Material and Methods

This section has been shortened from the publication version to avoid repetition within the thesis.

4.2.1 Study area

The temperate Celtic Sea comprises an area of the North Atlantic Ocean and is part of the northwest European shelf. Throughout the Celtic Sea, the spring bloom typically initiates in April when the water column becomes stratified, and can last anywhere from weeks to two months (Rees et al., 1999, Sharples et al., 2006). The barotropic M_2 tide is responsible for the predominant currents in this region, which are considered weak and spatially variable compared with the adjacent areas of the European Shelf Sea (Holt et al., 2001). We sampled during the DY029 "spring cruise" in April 2015, as part of the NERC Shelf-Sea Biogeochemistry (SSB) programme. MIMS O_2/Ar data collection started in the English Channel and continued almost uninterrupted for 28 days in the Celtic Sea, focussing on repeat transects between Celtic Deep (station A) and Shelf Edge (stations CS2 and Fe). Discrete samples were taken from Niskin bottles attached to a CTD rosette water sampler at all stations (Fig. 4.1).

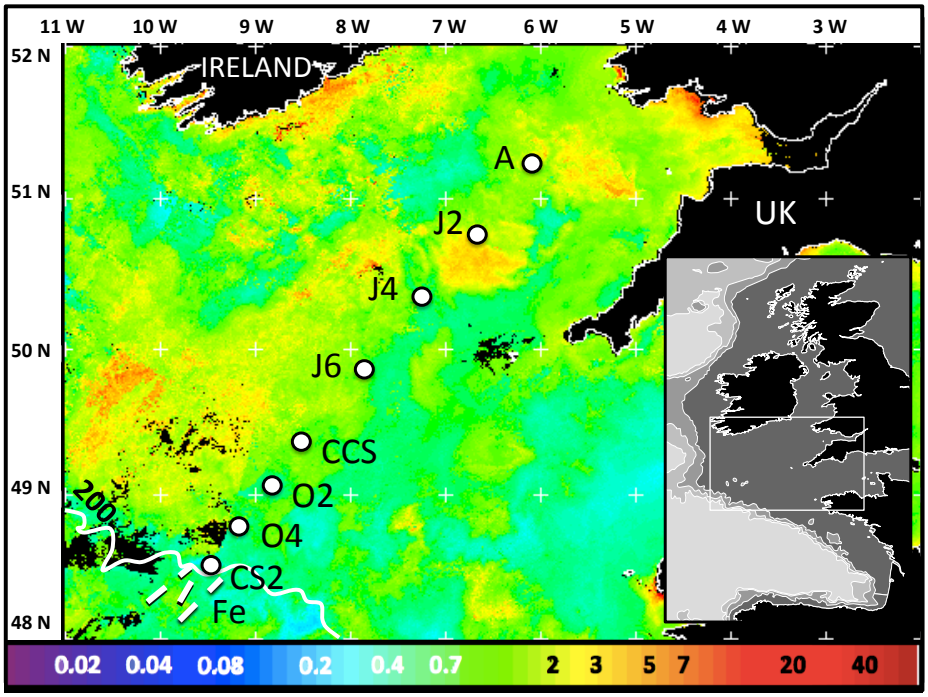

Figure 4.1. Area of study in the Celtic Sea, with Ireland in the north and Great Britain in the east. White circles, superimposed on a chlorophyll *a* concentration (in mg m^{-3}) composite image from VIIRS Chlorophyll OC5 (11^{th} to 19^{th} of April; courtesy of NEODAAS), indicate the approximate station locations (A, J2, J4, J6, CCS, O2, O4, CS2). Straight white blocks represent multiple stations outside the shelf (Fe). The curved white line between CS2 and Fe indicates the shelf-edge, represented by the 200 metre isobath. The contextual wider area map (grey inset) was plotted using QGIS software.

4.2.2 Methods

Along-track O_2/Ar ratios were determined using a shipboard MIMS connected to the ship's non-toxic underway seawater (USW) intake. We also collected discrete samples for triple oxygen isotopes that were subsequently analysed with a dual-inlet isotope ratio mass spectrometer (IRMS Finnigan MAT 252) in the Stable Isotope Laboratory at the University of East Anglia.

Continuous sampling

The USW intake was located in the middle of the bow at a nominal depth of 6 m, and plumbed to the main laboratory. To avoid biofouling (Juranek et al., 2010), the USW

pipes were treated with dilute bleach solution and flushed immediately prior to the cruise and after two weeks at sea. Comparison between samples collected from near-surface Niskin bottles and USW samples, measured by IRMS, showed no consumption or production of oxygen in our ship's pipes.

The MIMS was set-up according to Kaiser et al. (2005), but with the vacuum on the inside of the membrane and modified flow (45 ml/min) and temperature control. Before entering the membrane inlet, a small open flask (500 ml) was used to smooth fluctuations in the pumped seawater delivery (1 L min^{-1}). The flow to the membrane inlet was delivered by a gear pump (*Micropump*) controlled by a frequency inverter (*Allen-Bradley*). The USW circuit in the lab and the membrane (Teflon AF membrane, Random Technologies) were maintained at 1 to 3 ºC below sea surface temperature, to avoid degassing. The temperature of the mass spectrometer flight tube was kept constant at 50 °C using an insulated box with an electric heater and fan inside. Standards of 0.2 µm-filtered seawater, aerated and stirred for 24 hours to reach air-saturation were used for daily calibration. Standard error in O_2/Ar of 0.09 %. O_2/Ar ion current ratios were measured with a quadrupole mass spectrometer QMS 200 M Prisma (*Pfeiffer Vacuum*) with Faraday cup and recorded every ten seconds. The analyser was at a constant pressure of 1.0×10^{-6} mbar.

The shipboard MIMS calibration was cross-checked against O_2/Ar ratios derived from discrete samples extracted and analysed as described in the next paragraph. Both calibrations gave identical results, with a mean difference of $\Delta(O_2/Ar)$ between discrete and continuous measurements of (0.0±0.6) % (1σ; $R^2 = 0.98$, $n = 142$).

Discrete sampling

We also took discrete samples from 33 CTD Niskin casts at six different depths (three in the surface mixed layer and three below) and measured their O_2/Ar ratio with the MIMS. During analysis of these samples, flow was alternated between continuous USW supply and discrete samples using a six-port valve (*Valco Cheminert*).

Further discrete samples from the same CTD casts as mentioned above were taken to measure oxygen triple isotopes and O_2/Ar ratios from three depths, (surface, near the bottom of the surface mixed layer, and below the surface mixed layer), using evacuated 330 ml-glass sampling bottles with Viton O-rings stopcocks (*Louwers Hapert*) that were treated with 100 µl saturated $HgCl_2$ solution (7 mg $HgCl_2$) before sampling (Emerson et al., 1995). Samples were carefully drawn into the vessel by overflowing the

side-neck, to avoid atmospheric oxygen contamination, filling the vessel up to about 55 % by volume (range: 40 to 69 %), slightly below the optimum fill level of 85 % that is required to extract the maximum fraction of O_2 (Seguro et al., 2017). Samples were prevented from leaking by filling the side-necks with water and capping (Luz et al., 2002). Within one month of the end of the cruise the gas from all samples was extracted and stored in sealed glass tubes with molecular sieves. We extracted the gas samples and removed water vapour, CO_2 and N_2 by cryogenic trapping and gas chromatography before measuring O_2/Ar and O_2 isotopologue ratios ($^{16}O^{17}O/^{16}O_2$, $^{16}O^{18}O/^{16}O_2$) using a Finnigan MAT 252 isotope ratio mass spectrometer. The standard error for standard samples was 0.03 ‰ for $\delta(^{17}O)$ and 0.05 ‰ for $\delta(^{18}O)$. Our purification line was based on the method of Barkan and Luz (2003) and Abe (2008). Tests with artificial O_2/Ar mixtures showed that there was no isotopic fractionation of the gas sample during extraction and purification.

4.2.3 Calculation of net community production, $N(O_2/Ar)$

The O_2/Ar method is based on the similar solubility and diffusivity properties of the dissolved oxygen and argon. Only dissolved O_2 is affected by biological production and consumption processes. The relative difference between sample O_2/Ar and calculated saturation O_2/Ar ratio can therefore be used to express the magnitude of the biological O_2 supersaturation (Craig and Hayward, 1987, Kaiser et al., 2005): $\Delta(O_2/Ar) = [c(O_2)/c(Ar)]/[(c_{sat}(O_2)/c_{sat}(Ar)] - 1$, where c is the dissolved gas concentration and c_{sat} is the air-saturation concentration at a certain temperature, salinity and atmospheric pressure.

$\Delta(O_2/Ar)$ reflects the biological processes affecting mixed layer oxygen concentrations (production and respiration), but is not significantly affected by physical processes such as heat and freshwater fluxes or bubble injection and exchange. In combination with estimates of gas exchange rates (usually based on wind-speed), $\Delta(O_2/Ar)$ can be used to calculate biological O_2 fluxes (F_{bio}): $F_{bio} = k(O_2)c_{sat}(O_2)\Delta(O_2/Ar)$, where $k(O_2)$ is the O_2 gas exchange coefficient calculated from a wind speed-based parameterisation (Nightingale et al., 2000) and $c_{sat}(O_2)$ is the oxygen in air-saturation concentration at a given seawater temperature, salinity and atmospheric pressure (Hamme and Emerson,

2004, García and Gordon, 1992).

F_{bio} can be used to estimate net community production, where the second derivative of oxygen concentration $c(O_2)$ with respect to time is 0, and the effects of horizontal and vertical mixing on the O_2/Ar ratio are negligible (Kaiser et al., 2005). In shelf seas, these conditions are often not met, and we apply corresponding corrections for non steady-state conditions here.

For $k(O_2)$, we compared the parameterisation of Nightingale et al. (2000) to that of Wanninkhof (2014), but prefer the former because it is based on two experiments in European shelf seas and because its use was recommended for winds at intermediate speed (3.5-15 m s^{-1}), which cover the range we encountered in the Celtic Sea. However, F_{bio} calculated using the Wanninkhof (2014) parameterisation or other recent wind-speed gas-exchange parameterisations (e.g. Ho et al., 2006; Sweeney et al., 2007) would change $k(O_2)$ by <5 %, which is a negligible uncertainty. The gas exchange coefficient is scaled to the in situ Schmidt number of O_2 by multiplication with the factor $(Sc(O_2)/600)^{-0.5}$. The calculation of the Schmidt number is based on Wanninkhof (2014). We use Cross Calibrated Multi Platform (CCMP) wind speeds at 0.25° and 6 h resolution (http://www.remss.com/measurements/ccmp) for the calculation of the gas exchange velocities. A comparison of CCMP winds with anemometer measurements at the Met Office ODAS buoy positioned in the centre of the Celtic Sea showed that they agreed to within (0.2±0.2) m s^{-1}. Winds measured directly by the ship were also compared with the CCMP winds, and appeared to be (1.5±2.0) m s^{-1} higher. Ship wind measurements can be affected by the ship's hull geometry (Moat et al., 2005) and for this reason have not been used in the present analysis.

Correction for non-steady state conditions, entrainment into the mixed layer and diapycnal mixing across the base of the mixed layer

Entrainment of water from below the mixed layer and diapycnal mixing across the base of the mixed layer need to be taken into account for accurate biological oxygen production calculations (Quay et al., 2012, Luz and Barkan, 2000, Quay et al., 2010, Nicholson et al., 2012, Palevsky et al., 2016). The O_2/Ar gradient will determine if F_{bio} over- or underestimates production in the mixed layer. The contribution of vertical

mixing across the base of the mixed layer (F_v) was calculated according to the following equation 3.5, chapter 3. $K_z = (3\pm2) \times 10^{-5}$ m^2 s^{-1} (Simpson and Sharples, 2012, Osborn, 1980, Palmer et al., 2013) is the vertical diffusivity coefficient.

During the period of our study, no sustained increases in mixed-layer depth (entrainment) occurred. Entrainment events, deepening of the mixed layer ($\Delta z > 0$), make a significant contribution only two times (Fig. B.2, Appendix C).

According to Ruiz et al. (submitted) there were no upwelling events in this region, thus the influence of vertical advection was not explored further.

Lateral advection was not considered either since (a) its calculation requires O_2/Ar measurements in two places at the same time and (b) we did not expect to find strong currents or gradients perpendicular to the transect. Surface currents were weak at <1 km d^{-1} (0.01 m s^{-1}) during spring 2015 (M. P. Humphreys and E. Ruiz-Castillo, pers. comm., January 2017) and previous studies have shown fronts in the Celtic Sea only in waters below the mixed layer (Brown et al., 2003, Sharples et al., 2013).
Temporal non-steady state changes in the oxygen mass balance are taken into account by the term F_{nss} (equation 3.7)

This gives the following combined equation for the calculation of $N(O_2/Ar)$:

$$N(\mathrm{O_2/Ar}) = F_{bio} + F_{nss} - F_v$$
$$= k(\mathrm{O_2})c(\mathrm{O_2})\Delta(\mathrm{O_2/Ar}) + c(\mathrm{O_2})\left[z_{mix} \frac{\mathrm{d}\ln\frac{c(\mathrm{O_2})}{c(\mathrm{Ar})}}{\mathrm{d}t} - K_z \frac{\mathrm{d}\ln\frac{c(\mathrm{O_2})}{c(\mathrm{Ar})}}{\mathrm{d}z} \right] \quad (4.1)$$

The mixed layer depth (z_{mix}) is typically defined using density (Kara et al., 2000). However, here we use a criterion based on the O_2 concentration gradient (Fig B.1, Appendix B), which is expected to more reliably define the depth of active mixing, which is relevant for gas exchange (Castro-Morales and Kaiser, 2012).
In order to asses if primary production values could be higher for times when z_{eu} was deeper than z_{mix}, the depth of the euphotic layer (z_{eu}) (1 % of incident light) determined from daytime CTD casts was used to assess to what extent mixed-layer production

reflects the overall productive zone. The contribution of $N(O_2/Ar)$ below the mixed layer depth was calculated as $\Delta(\int c(O_2)dz) / \Delta t$ at stations A, J2, J4, J6, CCS and CS2 because these were the only stations where we had frequent repeated vertical profiles (n = 25).

4.2.4 Calculation of gross production, $G(^{17}O)$

Oxygen has three naturally occurring isotopes (Hoefs, 2004). The triple oxygen isotope ratios ($^{17}O/^{16}O$ and $^{18}O/^{16}O$) of dissolved O_2 can be used to estimate gross oxygen production in the mixed layer. Initial work used an approximated equation based on the ^{17}O excess, $\Delta(^{17}O)$ (Luz and Barkan, 2000). Here we use the improved dual-isotope approach with the equation 3.9 (Kaiser, 2011b, Kaiser and Abe, 2012). The specific inputs of this equation are: ε is the kinetic isotope fractionation during O_2 evasion ($^{18}\varepsilon$ = –2.095 ‰ (Knox et al., 1992) and $^{17}\varepsilon$ = –1.463 ‰ (based on a mass-dependent relationship between $^{18}O/^{16}O$ and $^{17}O/^{16}O$ fractionation with an exponent of 0.522 (Kaiser, 2011b) and δ_{sat} at the measured temperature and salinity, i.e. $^{17}\delta_{sat}$ = (0.373±0.02) ‰ and $^{18}\delta_{sat}$ = (0.695±0.04) ‰ (Luz and Barkan, 2009). $\gamma = {}^{17}\varepsilon_R / {}^{18}\varepsilon_R$ = 0.5179 is the triple isotope fractionation coefficient during respiration. $^{17}\delta_P$ = –11.644 ‰ and $^{18}\delta_P$ = –22.832 ‰ are assumed as the photosynthetic end-member delta values (Kaiser, 2011b, Kaiser and Abe, 2012, Kaiser, 2011a).

Prokopenko et al. (2011) proposed a similar approach to the dual-delta method of Kaiser (2011b); the only difference being that they omitted the isotopic fractionation during gas exchange (ε) and the biological O_2 supersaturation $s = \Delta(O_2/Ar)$. The dual delta method has been used by a number of authors to calculate gross production rates (Castro-Morales et al., 2013, Hamme et al., 2012, Nicholson et al., 2012, Juranek et al., 2012, Palevsky et al., 2016).

The equation 3.9 is valid for steady-state conditions ($G_{ss}(^{17}O)$) (Kaiser, 2011b). Similar corrections therefore have been applied for non steady-state conditions: diapycnal diffusion ($d\ln[(1+{}^{17}\delta) / (1+{}^{18}\delta)^{\gamma}] / dz \neq 0$) in all the stations and ($d\ln[(1+{}^{17}\delta) / (1+{}^{18}\delta)^{\gamma}] / dt \neq 0$) where there are $\Delta(^{17}O)$ gradients for the mixed layer and below the mixed layer until the euphotic zone (F_{bml}), as well as entrainment

$(\mathrm{dln}[(1+{}^{17}\delta) / (1+{}^{18}\delta)^{\gamma}] / \mathrm{d}z \neq 0)$ where $\Delta z > 0$ for the stations sampled repeatedly (Kaiser, 2011b).

4.2.5 Calculation of *f* ratio

The combination of net oxygen community production and gross oxygen production allow us to calculate the efficiency of the biological pump or *f*-ratio: $f(O_2) = N(O_2/Ar) / G(^{17}O)$.

To calculate net community production in carbon equivalents, $N(O_2/Ar)$ was converted using a photosynthetic quotient of 1.4: $N_C = N(O_2/Ar) / 1.4$ (Laws, 1991). Similarly, to convert $G(^{17}O)$ and to make it compatible with conventional ^{14}C-labelled 24 hour-incubations, we used $P_C(^{14}C; 24\ h) = G(^{17}O) / 2.7$ (Marra, 2002). These conversions were then used to calculate the "historic" *f*-ratio $f_C(\text{historic}) = N_C / P_C(^{14}C; 24\ h)$.

However, this value is not always constant. Then, for comparison we also used $G_C(^{17}O) = N(O_2/Ar) / 1.4 + [0.8G(^{17}O) - N(O_2/Ar)] / 1.1$ which uses photosynthetic quotients of 1.4 for "new" production (assumed to equal net community production) and 1.1 for "regenerated" production. The factor of 0.8 corrects for water-to-water cycling reactions such as the Mehler reaction, which produce O_2 with the oxygen isotope signature of photosynthetic O_2 and consume O_2 with ambient δ values, without associated C fixation. These conversion was then used to calculate the *f*-ratio in terms of carbon equivalents, i.e. $f_C(O_2) = N_C / G_C(^{17}O)$ (Hendricks et al., 2004).

4.3 Results

4.3.1 Metabolic balance

Continuous O_2/Ar measurements showed a metabolic balance corresponding to net autotrophic conditions ($\Delta(O_2/Ar) > 0$) for the whole month of April (Fig. 4.2), with a mean of (6±4) %. During the two days of transect from the western English Channel (50° N 2° W) to station CCS (49.4° N 8.6° W), then south to CS2 and back to CCS on 10th of April, $\Delta(O_2/Ar)$ values remained relatively constant at (1.8±1) % (Figs. 4.2 – transit 1 & 3a). $\Delta(O_2/Ar)$ began to increase substantially from April 11th whilst the ship

remained at CCS. The highest $\Delta(O_2/Ar)$ values were recorded on 15th April (up to 26 %) moving south from A to CCS. The cruise track followed the same transect (51.2° N 6.1° W to 48.1° N 10° W) on two occasions (numbers 1 and 2 in figure 4.2) and partially a third one at the end of the cruise. The first complete transect covered pre-bloom, bloom and the bloom-peak according to the $\Delta(O_2/Ar)$ recorded values (1st - 15th April). The second (15th – 27th) and third (27th – 29th) transects recorded similar values in the inner shelf of about 12 % (Fig 4.2). Outside the shelf, southwest of CS2, waters were undersaturated or at lower saturation than on the shelf, presumably due to Atlantic waters with lower $\Delta(O_2/Ar)$ values mixing with shelf waters in the less stratified water column.

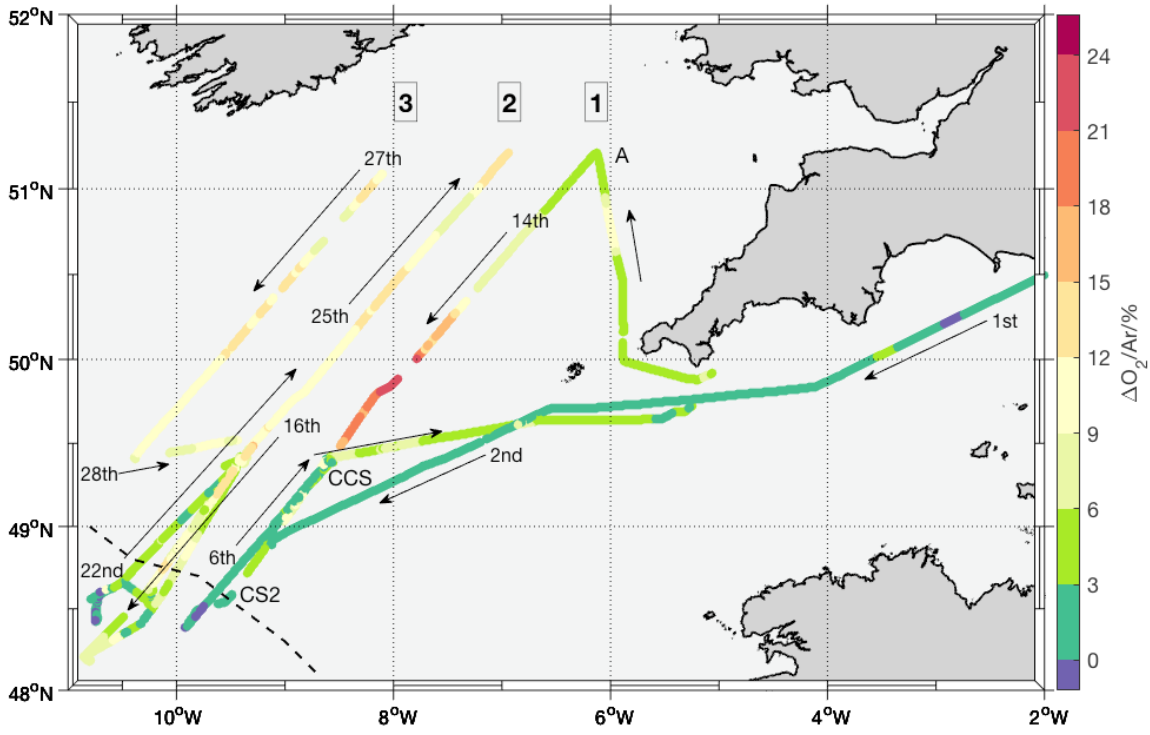

Figure 4.2. $\Delta(O_2/Ar)$ along the cruise track in the Celtic Sea and English Channel. Numbers 1, 2, 3 shows the first (1st – 15th April), second (15th – 27th) and third transect (27th – 28th), respectively. For clarity, transects 2 and 3 have been displaced by 0.9 and 1.9 ° W to the west, respectively. A, CCS, CS2, indicate approximate location of the inner, central and outer stations, arrows shows direction of traveling and approximate date, and dashed line indicates the shelf edge.

4.3.2 Biological oxygen sea-air fluxes from continuous sampling

Biological oxygen fluxes between surface waters and the atmosphere for the entire cruise were calculated from $\Delta(O_2/Ar)$ (Fig. 4.3a). The resulting F_{bio} values from two wind-speed gas exchange parameterisations, Wanninkhof (2014) and Nightingale et al. (2000), are shown in Figure 3b. Both parameterisations give virtually indistinguishable results except during the strongest winds (> 9 m s^{-1}; corresponding to k > 5 m d^{-1}; Fig 4.3a). For low and intermediate wind speeds the differences in F_{bio} with different parameterisations were negligible. Mean F_{bio}(N2000) was (56±32) mmol m^{-2} d^{-1}, but was higher after 11 April when the spring bloom started. The combination of O_2 supersaturation in the surface layer during the spring bloom and stronger winds resulted in the highest F_{bio} values during spring bloom decay (Fig. 4.3b).

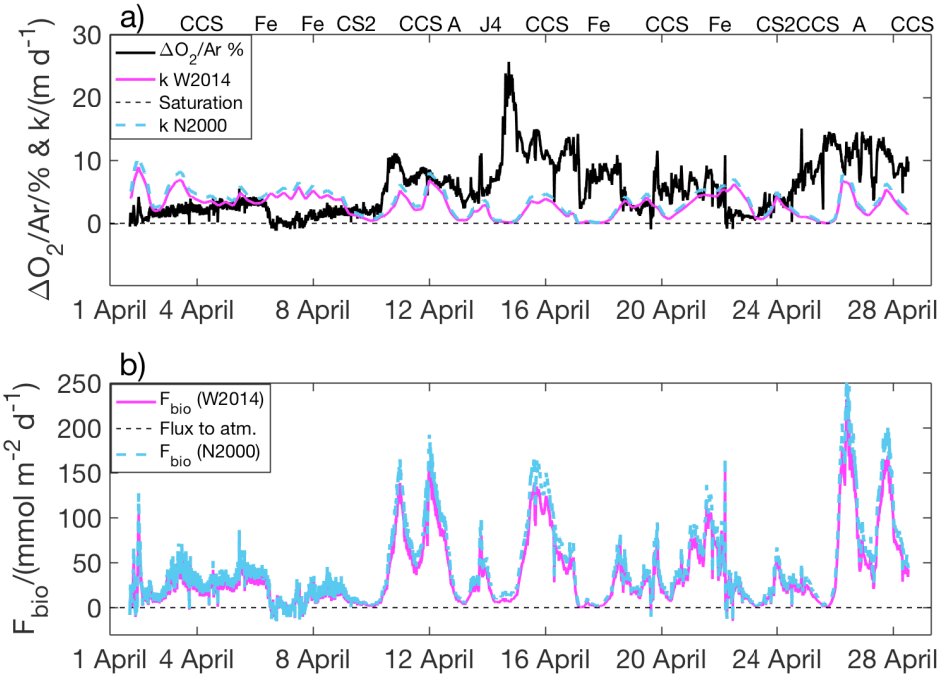

Figure 4.3. (a) O_2/Ar supersaturation ($\Delta(O_2/Ar)$) from the USW during April 2015. Negative values mean undersaturation. Gas exchange coefficients based on wind speed parameterisations according to Wanninkhof (2014) shown in pink (W2014); according to Nightingale et al. (2000) in dashed blue (N2000). (b) Biological sea-to-air O_2 fluxes (F_{bio}) are >0, air-to-sea fluxes are < 0.

4.3.3 Net community production, diapycnal diffusion and temporal changes

To evaluate how well F_{bio} approximates net community production, we considered the influence of vertical transport due to diapycnal diffusion and temporal non-steady state.

Diapycnal diffusion

Diapycnal diffusion, F_v, was calculated when the ship was on station and linearly interpolated over time (Fig. 4.4). The mixed layer depth was generally shallow, around 20 m. F_v was generally negative throughout, which corresponds to loss of oxygen from the mixed layer to below; consequently, subtracting negative F_v values from F_{bio} result in higher $N(O_2/Ar)$ values. Values of F_v ranged from +0.5 to -10.1 mmol m^{-2} d^{-1}. The average F_v (K_z = (3±2) × 10^{-5} m^2 s^{-1}), –3.7 ± 2.5 mmol m^{-2} d^{-1}, accounts for about 6.7 % of F_{bio}, thus diapycnal diffusion made a small contribution to $N(O_2/Ar)$.

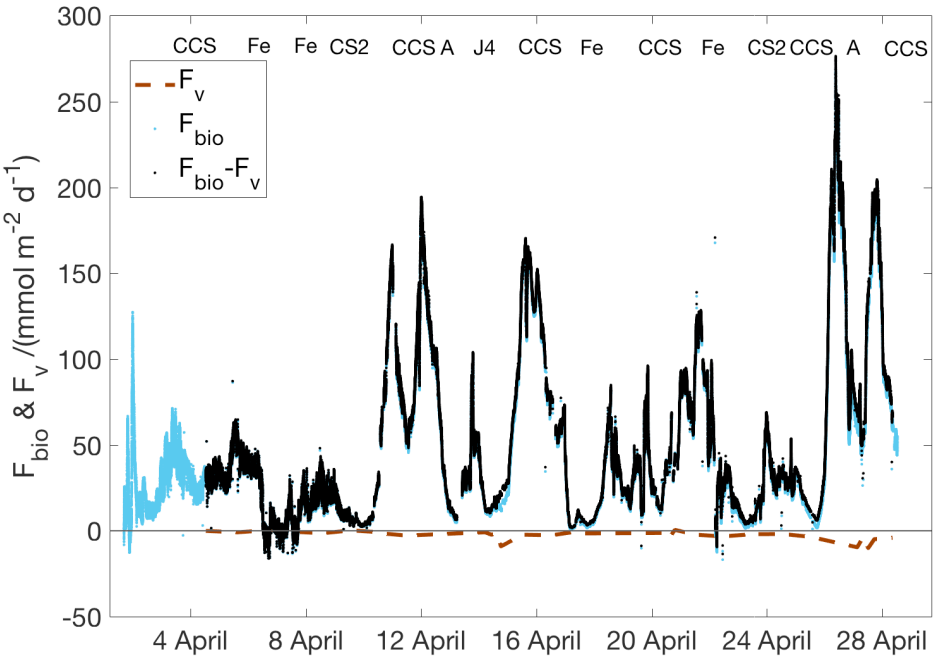

Figure 4.4. Time variations in F_{bio} accounting for diapycnal diffusion. Diapycnal diffusion (F_v) calculated from oxygen based mixed layer depth (differences of 0.5 % with the near-surface concentration) in dashed brown. $F_{bio} - F_v$ in black.

Temporal non-steady state changes

The temporal change term, F_{nss}, was calculated as the change in $\Delta(O_2/Ar)$ over the time interval between repeat occupations of the transects 1 and 2 (Fig. 4.2 & 4.5). Transect 3 was not used for the calculation of F_{nss} as there is not significant change in $\Delta(O_2/Ar)$ in respect to transect 2. F_{nss} was mainly negative from the central to the southern part of the transect (Fig. 4.6), meaning a loss of oxygen with time. From 50.2° N, F_{nss} was positive, corresponding to a biological oxygen gain. Overall, values of F_{nss} ranged from +61 to -56 mmol m^{-2} d^{-1}. The average F_{nss}, -2 mmol m^{-2} d^{-1}, accounted for about -3.6 % of F_{bio}. In the calculation of $N(O_2/Ar)$, F_{nss} was added to the mean $F_{bio} - F_v(O_2)$ for the main transect.

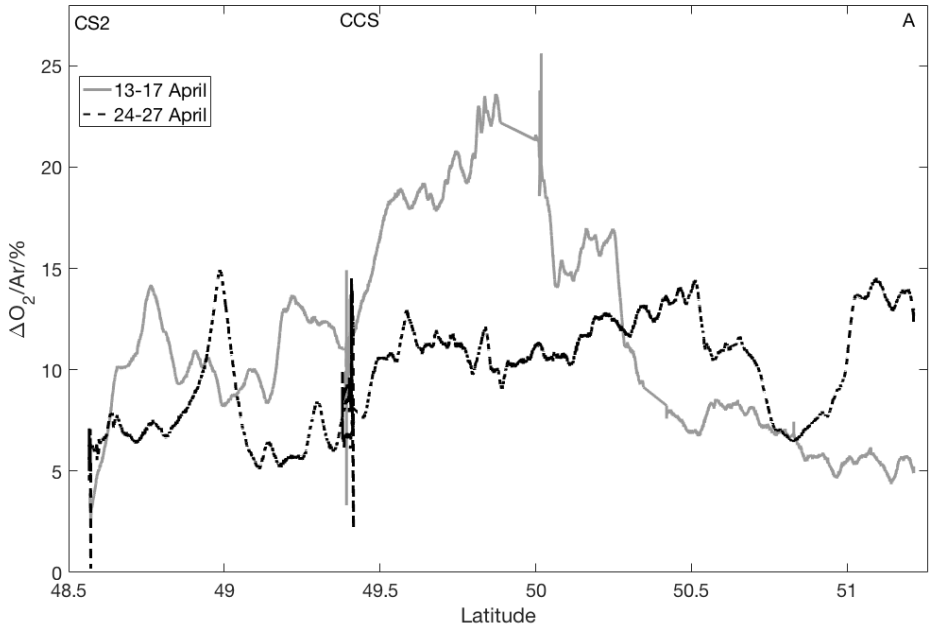

Figure 4.5. $\Delta(O_2/Ar)$ time variation for the 13-17 April transect from station A to CS2 (grey line) and the 24-27 April transect from CS2 to A (dashed black) between 48.5° N and 51.5° N. The approximate locations of stations A, CCS and CS2 are also indicated on the plot.

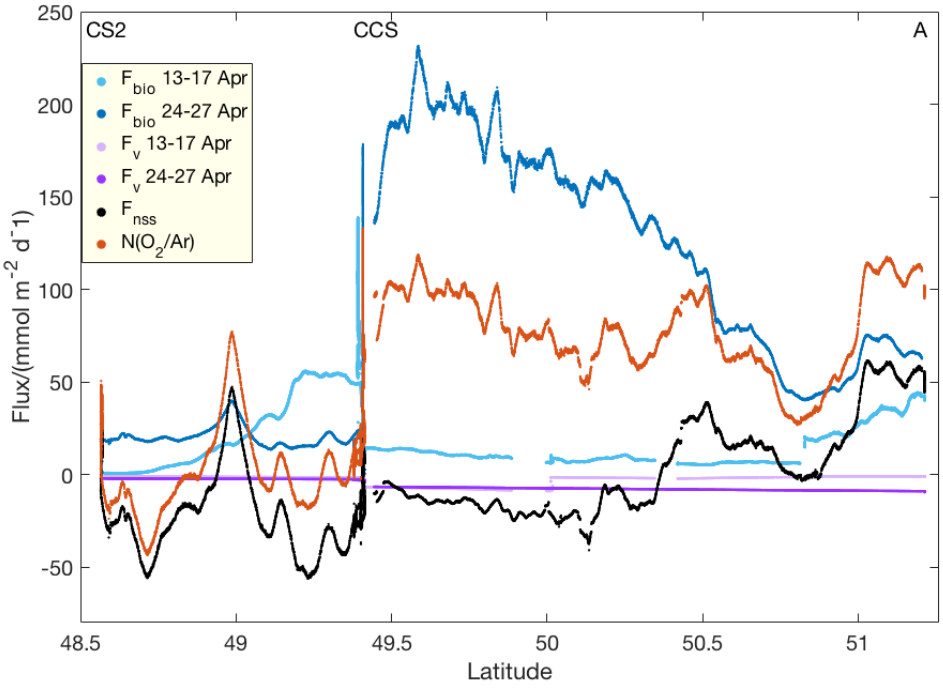

Figure 4.6. Net community production, diapycnal diffusion and temporal non-steady state oxygen fluxes during the first transect (13 to 17 April; light blue and purple) and the second transect (24 – 27 April; dark blue and purple). F_{nss} (in black) and $N(O_2/Ar)$ (in orange) correspond to the period between first and second transect.

Net community production, $N(O_2/Ar)$, represents the combination of the biological oxygen fluxes, diapycnal diffusion and temporal changes. The average value was (33±41) mmol m^{-2} d^{-1}, thus the Celtic Sea was net autotrophic (see Fig. 4.7). The highest $N(O_2/Ar)$ values were found at stations CCS and A, 133 and 117 mmol m^{-2} d^{-1} respectively (Figs. 4.6 & 4.7). However, from CCS to the CS2, the Celtic Sea appeared very patchy in its southern part with some negative $N(O_2/Ar)$ values, accordingly this section was net heterotrophic. Therefore, our $N(O_2/Ar)$ calculations show that at high spatial resolution the Celtic Sea is heterogeneous during the spring bloom.

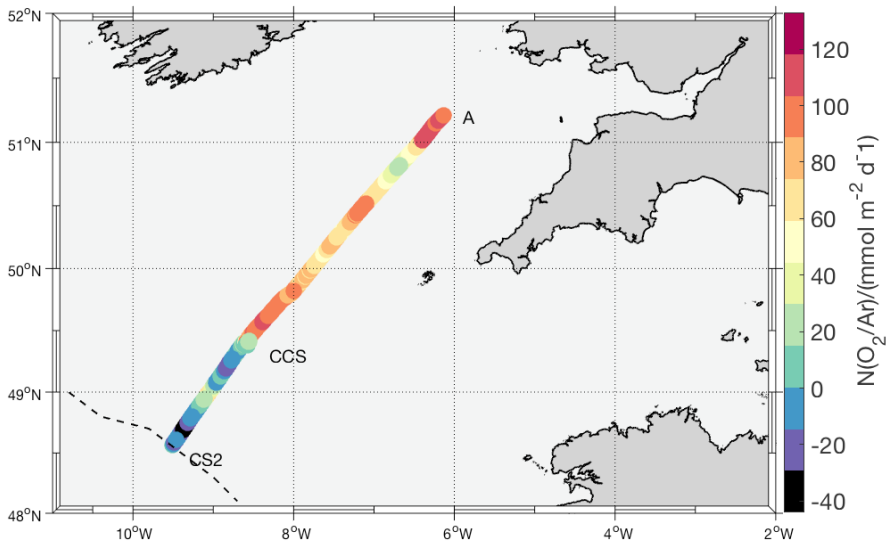

Figure 4.7. Zonal variations of net community oxygen production ($N(O_2/Ar)$) along the Celtic Sea as a composite of first and second transect, calculated using equation 5. The approximate location of the main stations A, CCS and CS2 is also indicated on the plot. Dashed line indicates the shelf edge.

4.3.4 Net community production, gross production and *f* ratio from discrete samples

Gross oxygen production is calculated from *in situ* discrete CTD samples and calculated using the dual-delta method. $G(^{17}O)$ also shows that the Celtic Sea appeared very patchy with an average value of 225 mmol m^{-2} d^{-1}, ranging from 0 to 424 mmol m^{-2} d^{-1} (Fig. 4.8). Values of $F_v(^{17}O)$ ranged from +20 to -21 mmol m^{-2} d^{-1}. The average $F_v(^{17}O)$, -5.4 mmol m^{-2} d^{-1}, accounts for about 2.6 % of G in steady state, thus diapycnal diffusion made a small contribution to $G(^{17}O)$. $F_{nss}(^{17}O)$ was mainly negative during the peak of the bloom, meaning a loss of photosynthetic oxygen over time. Before and after the peak of the bloom F_{nss} was positive, corresponding to a biological oxygen gain. Overall, values of F_{nss} ranged from +217 to -201 mmol m^{-2} d^{-1}. The average F_{nss}, 36.4 mmol m^{-2} d^{-1} or 18 % of G in steady state, made more significant contribution to $G(^{17}O)$. Euphotic zone deeper than the mixed layer depth occurred seven times (Fig B.1, Appendix B). Only in two of them, before the peak of the bloom, F_{bml} was positive (63 and 22 mmol m^{-2} d^{-1}), meaning gross production below the mixed layer. Entrainment made an

important contribution (291 mmol m^{-2} d^{-1}) only at CCS at the end of the sampling period.

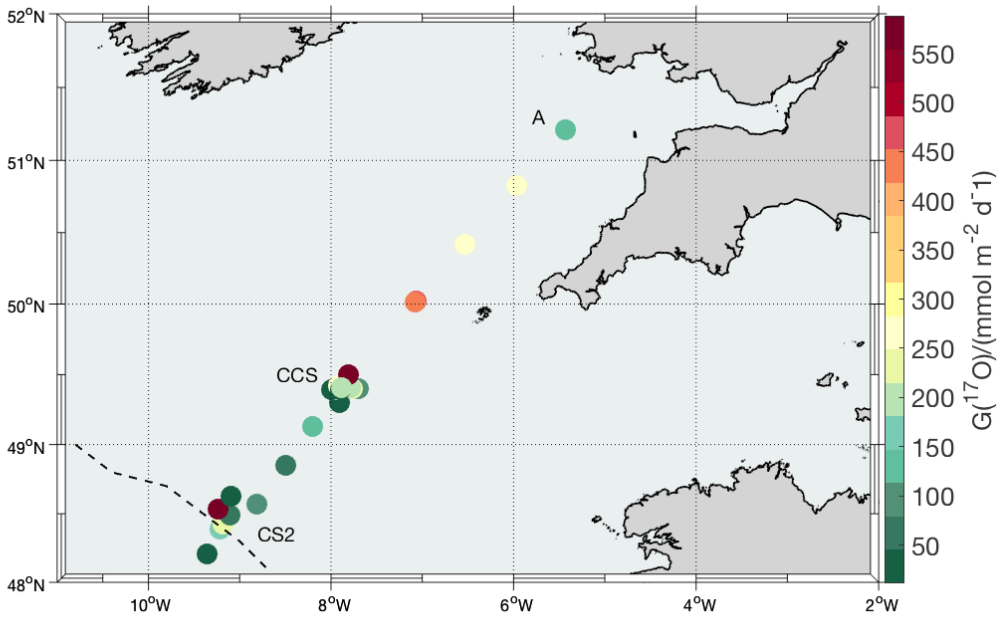

Figure 4.8. Zonal variations of gross oxygen production ($G(^{17}O)$) based on oxygen triple isotopic measurements from CTD along the Celtic Sea and calculated using equation 6. The approximate location of the main stations A, CCS and CS2 is also indicated on the plot. Dashed line indicates the shelf edge.

From the same discrete samples, $N(O_2/Ar)$ values were obtained. These samples have been corrected in the same way as $G(^{17}O)$ measurements. The average of F_v, F_{nss}, F_{bml}, and F_e was -1, 19, 3 and 8 mmol m^{-2} d^{-1} respectively (Table 4.1). Using F_v, F_{nss}, F_{bml}, and F_e terms for the calculation of $N(O_2/Ar)$ and $G(^{17}O)$ we found a correlation (R^2 = 0.22, n = 11, p < 0.001). The $f(O_2)$-ratio was determined by linear regression of $N(O_2/Ar)$ against $G(^{17}O)$ as (0.14±0.09) for the stations that we sampled multiple times, therefore, not including two of the stations on shelf neither the station out of shelf. To calculate $f(O_2)$ for the entire sampled area (on and off shelf) and from the beginning to the end of the sampled period, we used a more simple mass balance approach by using the F_v as non steady-state term only. We found a good correlation between $N(O_2/Ar)$ and $G(^{17}O)$ values (R^2 = 0.58, n = 33, p < 0.001). $f(O_2)$-ratio for the entire sampled area was (0.18±0.03) (Fig. 4.9), similar to the more complex approach value of (0.14±0.09). However, interestingly $f(O_2)$ yielded different correlations and slopes for samples taken

on or off the shelf. The $f(O_2)$ ratio slope corresponding to the samples off the shelf was notably lower (0.07±0.02, R^2 = 0.69) than from the samples on the shelf (0.25±0.02, R^2 = 0.91) regardless of the time. In terms of carbon equivalents and for comparison with historical data (i.e. the ratio N_C / $P_C(^{14}C$; 24 h), see Method section 2.5), f_C(historic) for off and on the shelf was 0.13 and 0.49, respectively. $f_C(O_2)$ in terms of carbon according to Hendricks et al. (2004) (i.e. the ratio N_C / $G_C(^{17}O)$, see Method section 2.5), for off and on the shelf was 0.06 and 0.25 respectively.

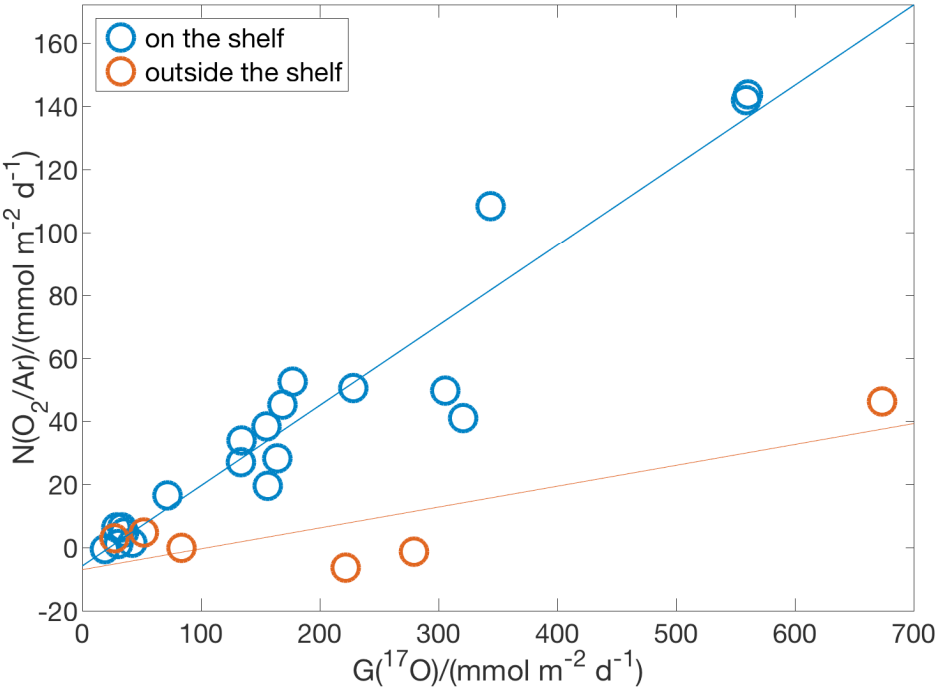

Figure 4.9. Net oxygen community production ($N(O_2/Ar)$) vs. gross oxygen production ($G(^{17}O)$) from CTD water samples in the Celtic Sea. A linear regression for samples on the shelf gives $N(O_2/Ar)$ = (0.25±0.02) $G(^{17}O)$ - (5.7±4.5) mmol m^{-2} d^{-1} (blue circles and line; R^2 = 0.91). The regression for samples from outside the shelf gives $N(O_2/Ar)$ = (0.07±0.02) $G(^{17}O)$ – (6.9±6.9) mmol m^{-2} d^{-1} (orange circles and line; R^2 = 0.69).

Table 4.1. Net community production at steady-state or biological O_2 fluxes (F_{bio}), gross production at steady-state ($G_{ss}(^{17}O)$), diapycnal diffusion (F_v) and $f(O_2)$ for all stations visited. Temporal non-steady state term (F_{nss}), production below the mixed layer (F_{bml}) and entrainment (F_e) for the stations visited repeatedly (units: mmol m^{-2} d^{-1} of O_2 equivalents). Stations on the first column as per order sampled. Hyphens mean there is no sample.

	$N(O_2/Ar)$					$G(^{17}O)$					
	F_{bio}	F_v	F_{nss}	F_{bml}	F_e	$G_{ss}(^{17}O)$	F_v	F_{nss}	F_{bml}	F_e	$f(O_2)$
CCS	20	0	78	13	-4.9	153	-2	86	13	2	0.1
CCS	37	-1	40	0		-	-	-	-		-
Fe08	-6	0				225	3				0.0
Fe11	-2	-1				277	-2				0.0
Fe14	0	0				65	-18				0.0
CS2	1	-1	18	0		41	-1	214	0		0.0
O4	16	0				75	4				0.2
O2	43	-2				159	-10				0.3
CCS	35	-3	58	10		152	-2	217	10		0.2
A	28	0	15	0		164	0	113	0		0.2
J2	5	0	4	0		32	-3	40	0		0.1
J4	6	0	18	0	0	27	-6	19	0	1	0.2
J6	0	1	29	0	-1	16	-3	-29	0	5	0.0
J6	138	-4				541	-18				0.3
CCS	64	-2	-35	-5		227	-4	-72	-10		0.3
CCS	5	-1			0	32	-4			0	0.2
CS2	1	0	13	3		21	-9	-69	3		0.0
Fe01	4	1				22	-5				0.1
CCS	19	-1	19	5		120	-3	81	-42		0.2
CCS	27	-1				128	-2				0.2
CCS	34	3				276	-17				0.1
CCS	70	8				345	-14				0.2
CCS	52	5				264	20				0.2
CCS	126	-2				675	-11				0.2
Fe17	45	-2				664	-9				0.1
Fe20	6	2				67	15				0.1
CS2	27	0				129	-5				0.2
CCS	4	-3	-34	7	48	20	-9	-201	7	291	0.2
A	45	-7				157	-21				0.3
J2	39	-2				307	-13				0.1
J4	101	-7				335	-9				0.3
J6	140	-4				550	-11				0.3
CCS	48	-3				221	-7				0.2

4.4 Discussion

Our MIMS-based approach has shown that within a relatively short period during the spring bloom, $\Delta(O_2/Ar)$ can increase very rapidly (e.g. 15 % in less than 6 hours). In the following, we discuss the dynamic changes during the spring bloom period, to what extent the steady state assumption can be used when relating biological oxygen air-sea fluxes to net community production and what the implications of the observed changes in $f(O_2)$ are for organic carbon export.

4.4.1 Evolution of the spring bloom

Low winds 10th-11th April on the outer part of the shelf (between the shelf edge (CS2) and CCS) led to z_{mix} shoaling above the euphotic depth (z_{eu}), which led to an increase in the biological oxygen production, $\Delta(O_2/Ar)$ (Fig 4.3a & Fig B.1, Appendix B). During transitting (13th- 16th) we covered the inner part of the shelf (stations A to CCS) when lower wind speed seemed to trigger the highest $\Delta(O_2/Ar)$ values of the spring bloom on the 15th. This was also considered the peak of the spring bloom by independent primary production experiments using ^{14}C uptake (Poulton et al. submitted, García-Martín et al., 2017). This period is also coincident with the maximum in Chl-*a* as observed by satellite (Fig B.2, Appendix B) On this occasion z_{mix} was very shallow and generally coincident with z_{eu}. After two days in CCS, we continued the transect in the direction of CS2. Net community production decreased further south with values of oxygen supersaturation close to 0 % or below on some areas out of the shelf. This could be due to the fact that the water column tends to stratify later at the shelf edge than on the shelf (Joint et al., 2001) and therefore mixing with the deeper Atlantic undersaturated waters (Nolan and O'boyle, 2011). Although, this could be due to the timing of the bloom being later off of the shelf than on shelf, the chlorophyll satellite observations of the last week of the cruise does not show the same high values of chlorophyll off shelf than in the previous two weeks on shelf. Nevertheless, we cannot assume that other regions would not exhibit a peak in biological activity after our period of sampling.

Back at CCS, average $\Delta(O_2/Ar)$ remained almost constant on 20 and 21 April. This suggests that spatial variability is greater than temporal variability after the peak of the bloom (Fig 4.3a). From the 25th to the end of the sampling period on 29th of April, we

passed the same transect on the inner shelf twice. During this time, $\Delta(O_2/Ar)$ was quite constant. In general, higher values occurred on the inner shelf and lower ones on the outer shelf. The differences in $\Delta(O_2/Ar)$ for stations occupied repeatedly shows that the shelf sea is a dynamic and heterogeneous system. To assess if it is due to: a) the timing of the bloom varying across the study region and that the cruise captured different phases of the bloom in different areas, or b) if the spring bloom is really more intense in some areas we used chlorophyll maps at different times of the bloom (Fig B.2, Appendix B). Based on it, we can say that the later is true, and the Celtic Sea is very heterogeneous, and that the short-lived peak in biological oxygen supersaturation (e.g. an increase of 15 % in $\Delta(O_2/Ar)$ over less than 6 hours and a distance of 20 km) was captured during the spring bloom. This shows the importance of high-resolution techniques for biological production measurements under the studied seasonal and geographical conditions.

What triggered the spring bloom should be a combination of light, water column stratification and the availability of nutrients (Simpson and Sharples, 2012). As expected prior to the spring bloom, surface nutrient concentrations were at their annual peak (Ruiz-Castillo et al. in this issue). The water column became more stratified after the 10th of April due to lower winds (Fig. 3a), which would probably have triggered the beginning of the spring bloom. The peak of the bloom occurred around the 15th. From the beginning of the bloom, the water column was well stratified. But from the 14th to the 16th, the mixed layer shoaled in response to weaker winds. Moreover, z_{eu} was coincident with z_{mix} (Fig B.1, Appendix B). This condition of shallower mixed layer, with nutrients and light available may have triggered the peak values of the spring bloom. After the peak of the bloom, $\Delta(O_2/Ar)$ showed oversaturation, to a lesser degree, until the end of the cruise. Only on the last day, a decrease in $\Delta(O_2/Ar)$ oversaturation was recorded (Fig. 4.2 & Fig. 4.3a). That could be an early observations of the decay of the bloom, perhaps triggered by nutrient depletion, grazing or coagulation (Tiselius and Kuylenstierna, 1996).

4.4.2 Biological production in the Celtic Sea

For comparison, we converted previous studies that measured biological production in the Celtic Sea during springtime to O_2 equivalents (Table 4.2). However, different

techniques do not measure the same quantity even if they all measure "biological production", making the comparison between techniques very difficult (Juranek and Quay, 2013). Incubation times can vary from one study to another, leading to recycling of ^{14}C, and dissolved organic carbon fluxes are often ignored. For example, ^{14}C with incubation time of 24 hours approximates to net primary production (gross primary production minus autotrophic respiration), while incubation times between 2 and 6 hours are considered to get results closer to gross primary production.

With these caveats in mind, we compared our gross and net values with previous studies in the Celtic Sea spring bloom (Table 4.2). Our production estimates are within the range of previous studies, mainly because the range of previous studies is very large. Studies conducted in summer in the Celtic Sea show $P_C(^{14}C$, 2–4 h) between 38 to 88 mmol m^{-2} d^{-1} (Hickman et al., 2012) and $P_C(^{14}C$; 24 h) from 63 to 180 mmol m^{-2} d^{-1} (Poulton et al., 2014). Incubation experiments gave spring bloom $P_C(^{13}C$; 24 h) values of 31 to 310 mmol m^{-2} d^{-1} in a relatively close North Atlantic temperate shelf sea area (Daniels et al., 2015), showing that our values are in the same order of magnitude of adjacent spring bloom events.

We compared our values with other studies that assumed steady state or integrated over the euphotic zone instead of the mixed layer. To asses for the contribution of production below the mixed layer, we calculated its contribution for times when z_{eu} was deeper than z_{mix}, but calculation of production below the mixed layer did not show a significant contribution to our $N(O_2/Ar)$ estimation (see section 2.3). To test for the difference between steady and non-steady state with high spatio-temporal resolution measurements, we calculated the diapycnal diffusion and the temporal changes. In general, diapycnal diffusion (F_v) was less than 4 mmol m^{-2} d^{-1}, and the temporal non-steady state change flux F_{nss} was 2 mmol m^{-2} d^{-1}. This is a small contribution to the F_{bio}; then, the steady state assumption could be valid to represent the net community production when considering the Celtic Sea transect as a whole and assuming we are always sampling the same water mass. However, the magnitude of F_{nss} varies from positive to negatives values (+61 to -56 mmol m^{-2} d-1). This suggests that although the time resolution is very fine (every 10 s), the time resolution inherent to cruise track (time between transect 1 and 2) may not be enough to fully capture all of the changes in this dynamic system. From station J6 to the shelf edge the contribution of F_{nss} is mainly negative, greatly contributing to the heterotrophic conditions, while in the inner area of

the shelf, from station A to J4 (51.5º N to 50.5º N), F_{bio} was 41 mmol m^{-2} d^{-1}, but with the contribution of F_v and F_{nss} to the final $N(O_2/Ar)$ it is 74 mmol m^{-2} d^{-1} and clearly showing this area as net autotrophic. Therefore, the steady state assumption could underestimate daily primary production in the northern Celtic Sea by up to 55 %.

Table 4. 2. Summary of previous results on biological production during the Celtic Sea spring bloom in comparison to the present study (units: mmol m^{-2} d^{-1} of O_2 equivalents). Different methods are shown in brackets. *G* stands for gross production; *P* for primary production, which is expected to be closer to *N* for 24 h. *N* stands for net community production.

References	***G*(^{17}O)**	***G*(^{18}O)**	***G*(O_2)**	***P*(^{14}C 24 h)**	***N*(O_2)**	***N*(O_2/Ar)**
Present study	225±115					33±41
(Robinson et al., 2009)		58-2400	37-840	22-496	16-760	
(Joint et al., 2001, Rees et al., 1999)				168		
(Joint, 1986)				11-91		

4.4.3 Carbon export efficiency of the shelf sea during the spring bloom

During winter, nutrients in the mixed layer are used incompletely. Primary production fuelled by nitrate is called new production (Eppley and Peterson, 1979). The ratio of new production to total production is called *f* ratio, which, indicates the efficiency of the biological pump. Many factors can affect the efficiency of the biological pump: the structure of the plankton community, zooplankton vertical migration, phytoplankton size and taxa, and physical forcing of surface waters (Lutz et al., 2007).The combination of $N(O_2/Ar)$ and $G(^{17}O)$ shows the portion that had not been used for respiration and therefore the proportion that is available for export in O_2 terms (Laws et al., 2000).

Our samples show two different $f(O_2)$ ratios, with values much higher on the shelf sea than off the shelf. This indicates that off shelf the majority of the organic matter gets recycled in the mixed layer likely due to either, or a combination of, physical or

biological processes like a community shift: increase in grazing pressure, smaller autotrophic cell community, larger representation of bacterial heterotrophic activity (Haskell et al., 2017, Rees et al., 1999). $f(O_2)$ ratios were 0.18±0.03 for the whole Celtic Sea and 0.25±0.02 on shelf. It is in agreement with biogeographic controls of transfer efficiency suggested in the global forecast of annual export (Lutz et al., 2007) and values found in autotrophic areas of the Southern Ocean (Reuer et al., 2007). Slightly higher values (0.35±0.06) has been found during the spring bloom in the subpolar N. Atlantic (Quay et al., 2012) and in the N. Pacific coast (~ 0.50) (Haskell et al., 2017). Robinson et al. (2009) measured plankton production in the Celtic Sea with different incubation techniques in April 2002. Although their experiment doesn't include $f(O_2)$ ratio estimations, we calculated it from their Table 4.2 for comparison ($G(O_2)$ / $NCP(O_2)$ = 0.37±0.07), where production values were not obtained from triple oxygen isotopes but from oxygen evolution from incubations. Our $f(O_2)$ ratio is still higher than the most globally observed values of 0.10 to 0.20 (Juranek and Quay, 2013). Some studies tried to find GOP (gross oxygen production) : G_C (gross carbon production; 3 – 6 h ^{14}C incubation) ratio that would allow to scale between the two techniques, but the reported values typically vary from 1.7 to 7.6 (Munro et al., 2013, Juranek and Quay, 2013, Luz et al., 2002). Recently, an experiment that compare $G(^{17}O)$: G_C ratio found a value of 1.2±1.1 which they conclude is not a definitive value and further studies are needed (Jurikova et al., 2016). With this caveats on mind, we followed Hendricks et al. (2004) to convert $G(^{17}O)$ in G_C and Laws (1991) to convert $N(O_2/Ar)$ to N_C using the photosynthetic quotient of 1.4. Our average $f_C(O_2)$ ratios (0.25±0.02) for the on shelf are comparable with average $f_C(O_2)$ ratios found by Prokopenko et al. (2011) in the spring bloom on the Bering Sea shelf. In addition, to make our values comparable to the more common f_C(historic) ratio, we divided our $G(^{17}O)$ by 2.7 (Marra, 2002) in order to convert our values to ^{14}C production $P_C(^{14}C; 24$ h). This robust relationship has been widely used for comparison with historical ^{14}C and satellite-based estimates (see Juranek and Quay (2013) for more extensive discussion) and still in use (e.g. Palevsky et al. (2016)). To convert $N(O_2/Ar)$ to N_C we still using the photosynthetic quotient of 1.4 (Laws, 1991). Here, we study f in terms of carbon, as f_C(historic) = N_C / $P_C(^{14}C; 24$ h) represents the probability of using carbon for new production and therefore, an approximation of total primary production that is available for carbon export, whereas 1 – f would be the fraction of carbon used for regenerated or

recycled production (Eppley and Peterson, 1979). Importantly, new production requires net inorganic carbon uptake while regenerated production does not. Our f_C(historic) ratios were 0.34±0.06 for the whole Celtic Sea. These are not the highest values recorded (Laws et al., 2000), but still higher than values found in open ocean, e.g. the equatorial Pacific (0.12 ±0.12) (Hendricks et al., 2005) or the global average of 0.20 (Laws et al., 2000).

Only two studies calculated *f* ratios in the Celtic Sea, specifically in the shelf edge, during the spring bloom: Rees et al. (1999) and Joint et al. (2001); they calculated *f* ratios of 0.8 from nitrate assimilation for samples close to the shelf edge. This values are much higher than those found in our study. This discrepancies with nitrate *f* ratios has been also found before (Hendricks et al., 2004). Moreover, we think that a comparison is complicated here because we would need a conversion factor C : N, but Rees et al. (1999) found highly variable C : N ratios (2.5 – 9) in their study. Therefore, converting nitrate assimilation *f* ratios to C or O_2 *f* ratios, will not give an appropriate comparison with our study.

Large microphytoplankton cells (20-200 μm) that are typical of the spring bloom are associated with higher *f* ratios (Tremblay et al., 1997). However, the phytoplankton community found on during the spring bloom was dominated by nanoplankton (2-20 μm) (Hickman et al. this issue), which thus may explain the lower values found in this study. Rees and Joint studies found that the spring bloom was dominated by large cells and higher *f* ratios when larger phytoplankton dominated the assemblage. In addition, experiments had demonstrated that phytoplankton communities dominated by small cells are more sensitive to changes in carbon concentrations (Richier et al., 2014), and the shift to smaller size-cell population, reduces the export efficiency, which could indicate an effect of climate change (Palevsky et al., 2016).

Compared to the on-shelf values, the f_C(historic) values off the shelf seems implicate three times less particulate organic carbon (POC) export than the shelf edge.

On average, our f_C(historic) ratios suggest that about 35 % of the total production is available for export and 65 % for remineralisation. It is in good agreement with annual global estimation of coastal margin carbon sequestration (Muller-Karger, 2005), because although our study does not represent annual carbon export, the spring bloom is typically the most productive season. To calculate annual carbon export requires further

studies during other seasons (Palevsky et al., 2016), which will be presented in a follow-on paper.

Therefore, our *f* ratio is comparable, albeit sometimes slightly lower than those reported previously in other shelves, but higher than the global average, indicating that the Celtic Sea is indeed a highly productive region of the northwest European Shelf.

4.5 Conclusions

This is one of the first data sets of net community (N) and gross production (G) rates during a Celtic Sea spring bloom at high resolution. Our results apply to the mixed layer and below up to the euphotic zone.

We find net community production rates based on continuous membrane-inlet mass spectrometry measurements of oxygen-to-argon ratios, $N(O_2/Ar)$, of up to 144 mmol m^{-2} d^{-1} in April 2015, with an average of (33±41) mmol m^{-2} d^{-1}. Biological air-to-sea oxygen fluxes (F_{bio}) were the dominant term in the $N(O_2/Ar)$ calculation. The diapycnal diffusion term (F_v) was negligibly small (< 4 mmol m^{-2} d^{-1}). The disequilibrium term (F_{nss}) contributed between –50 and +50 mmol m^{-2} d^{-1} at specific locations, but had a negligible effect when considering the Celtic Sea as a whole. In other words, for measurement of net community production at high spatial resolution in dynamic shelf-sea environments, good temporal resolution and repeat occupations of transects are required. The assumption of steady state (i.e. assuming $N(O_2/Ar) = F_{bio}$) may lead to errors of 50 % or more. In turn, when integrating over larger areas, F_{bio} may present a faithful representation of the metabolic balance of the Celtic Sea as a whole.

Gross production rates based on oxygen triple isotopologues in discrete samples, $G(^{17}O)$, were up to 424 mmol m^{-2} d^{-1} and (225±115) mmol m^{-2} d^{-1} on average. Calculating net community production just for these discrete samples gave an average of $N(O_2/Ar)$ = (55±34) mmol m^{-2} d^{-1}. $f(O_2)$ ratio for the entire shelf was 0.18±0.03, or f_C(historic) = 0.34±0.06 in carbon equivalents. f(C) ratio is more than four times higher on the shelf than on the shelf edge. The average of nearly 0.34 for the Celtic Sea is expected to lead to a large organic carbon export flux.

The observed heterogeneity in the continuous $N(O_2/Ar)$ estimates as well as the variability of discrete $G(^{17}O)$ values along the cruise transect demonstrate the virtue of

high-resolution techniques. Our results could help improve the validation of remote sensing algorithms and ecosystem models.

Chapter 5. Interannual and seasonal variability of gross biological production and net community production in the Celtic Sea

5.1 Introduction

Europe's population is increasing in coastal areas and the prediction is that it will continue in the future, (Neumann et al., 2015). An increasing population leads to an expansion in land use, industry, shipping and pollution affecting coastal areas (e.g. changes in community composition) (Painting et al., 2017). The northwest European shelf seas are of high importance for recreational, artisanal and industrial fisheries industry (Sharples et al., 2013). They are also the interface between the northwest European coastal zones and the Atlantic waters (Fig 1.1).

At the base of the shelf sea ecosystem are phytoplankton providing food source for plankton that support key marine services like fisheries (Sharples et al., 2013, Sharples et al., 2009). The phytoplankton is responsible for the vast majority of biological production: the synthesis of organic matter from inorganic compounds by aquatic photosynthesis. This process fixes inorganic carbon. A fraction of this fixed organic carbon sink to the seabed, reducing the amount of CO_2 in the sea surface and enabling more CO_2 to be taken from the atmosphere. The shelf seas are responsible for up to 30 % of ocean biological production (Muller-Karger, 2005). Therefore, quantifying biological production is essential to understanding the role of the shelf seas in CO_2 uptake and carbon export.

Temperate shelf sea areas have been extensively sampled because of their economic and ecologic importance. However, these areas are heterogeneous and dynamic systems that require higher temporal and spatial resolution than the open ocean and snapshots sampling usually fails to capture their variability. Satellite observations provide high spatial and temporal coverage, but algorithms used to estimate net biological production and carbon export from satellite images need to be validated with in situ measurements. Currently, different ways of estimating biological production have large uncertainties

associated with methodological artefacts, photosynthetic quotients or integration times (Cullen, 2001, Robinson et al., 2009), which makes it more difficult to create a coherent story or calibrate satellite data accurately. Thus, our understanding of the seasonal and spatial variability of biological production in temperate shelf seas is still incomplete.

Phytoplankton activity is determined by a combination of different variables (nutrients, light, turbulence, temperature, etc.) (Seguro et al., 2015). These variables change seasonally. The seasonal cycle is expected to change in a climate change scenario (Henson et al., 2013). It is therefore important to quantify and understand spatial and seasonal variations in biological production to be able to preserve or improve the quality of these highly productive waters and to help predict the impacts of future changes due to growth of population and climate change.

Here I use oxygen species to obtain estimates of biological production without incubation. Oxygen is produced by phytoplankton during photosynthesis, but is also affected by physical processes such as air-sea gas exchange and mixing. I can quantify net community production (gross production minus respiration) by measuring oxygen supersaturation and using argon as a tracer ($\Delta O_2/Ar$) to separate physical from biological oxygen (Craig and Hayward, 1987).

Moreover, the isotopic signal of oxygen produced during photosynthesis is different from that of atmospheric O_2 added to the water by gas exchange. This is due to the anomalous enrichment of stratospheric O_3 in ^{17}O and its transfer to CO_2, leading to a corresponding depletion in O_2, compared with O_2 produced by photosynthesis (Luz and Barkan, 2000). Using the other heavy stable oxygen isotope, ^{18}O, as additional constraint allows eliminating the simultaneous effect of respiration. These differences in isotopic signature make it possible to quantify gross biological production by measuring the isotopic composition of dissolved oxygen.
Gross biological production and net community production can be converted to carbon-based quantities using photosynthetic stoichiometric quotients (Laws, 1991, Marra, 2002).

The data combines high frequency underway observations of $\Delta(O_2/Ar)$ and discrete triple oxygen isotopes and provides unprecedent seasonal gross production and net community production in the Celtic Sea using in situ observations. The budget calculations account for production in the euphotic zone, air-sea gas exchange, diapycnal fluxes from below the mixed layer and entrainment. I estimate seasonal variations in biological production based on data from four cruises, spanning spring, summer and autumn. The results show that the biological pump in the Celtic Sea makes this area a net carbon sink.

5.2 Material and Methods

5.2.1 Area of study

The temperate Celtic Sea is part of the northwest European shelf and connects with the Northeast Atlantic Ocean. Temperate seas are characterised by changes in temperature (Fig. 5.1), winds and irradiance during 4 seasons. Usually, the spring bloom starts in April when the water column becomes stratified, and lasts up to two months leading to summer when the mixed layer is still stratified. Autumn starts with deepening of the mixed layer due to changes in winds and temperature, leading to a fully mixed water column in the winter season (Simpson and Sharples, 2012).

The barotropic M_2 tide is responsible for the predominant currents in this region and circulation is driven by winds. These currents are considered weak and spatially variable compared with the adjacent areas of the European Shelf Sea, especially in spring-summer when the winds are weaker than in autumn-winter (Holt et al., 2001). I sampled during three seasons (two summers, one autumn and one spring) on the DY026 cruise in August 2014, DY018 November 2014, DY029 April 2015 and DY033 in July 2015 in the context of the NERC Shelf-Sea Biogeochemistry (SSB) programme (Chapter 2, table 2.1).

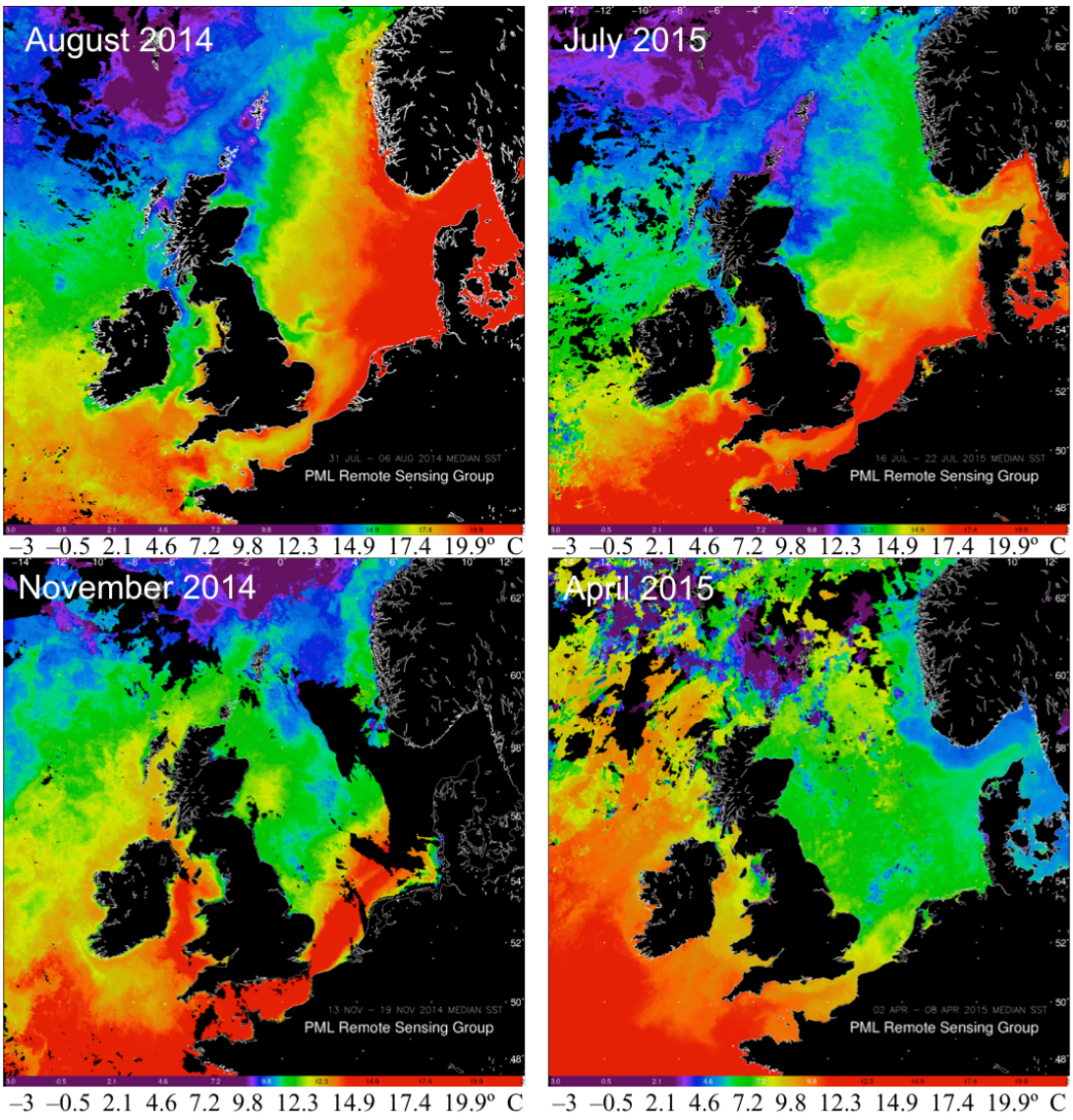

Figure 5.1. Sea surface temperature (ºC) (SST) of the west European shelf. Land is shown in black patches with white edge. Black patches over the sea are cloud coverage. One week composite images from AVHRR (1.1 km): 31st July to 6th of August 2014; 16st to 22nd of July 2015; 13th to 19th of November 2014; 2nd to 8th of April 2015. Note that the colours in the scales vary from image to image. Images downloaded from NEODAAS webpage: http://www.neodaas.ac.uk

5.2.2 Methods

Continuous measurements

Continuous O_2/Ar measurements were taken with a MIMS on board of RRS Discovery

during three cruises (DY026, DY029 and DY033). O_2/Ar data collection started in the English Channel and continued almost uninterrupted on all cruises, apart from DY018 cruise when the MIMS stop working at the beginning of the cruise. I calibrated each O_2/Ar MIMS cruise measurements with EW samples from each specific cruise to calculate biological supersaturation (ΔO_2/Ar %) as explained in chapter 2; section 2.6.

Discrete measurements

Discrete samples were taken from Niskin bottles attached to a CTD rosette water sampler on every station. At least 3 stations have been sampled on all cruises: Celtic Deep (station A), Central Celtic Sea (station CCS) and Shelf Edge (station CS2). Analytical precision based on ΔO_2/Ar duplicates was ±0.2 %.

$\Delta(O_2/Ar)$ discrete samples taken from the CTD were measured by MIMS and IRMS. The mean offset was (1.1±1.4), (0.1±0.6), and (0.8±1.7) % for the DY026, DY029 and DY033 respectively (Fig. 5.2). Therefore, there are no systematic differences between MIMS and IRMS because the mean differences between the two instruments are within the uncertainty. Four of 149 samples where considered outliners due to sampling error in DY029 (Fig. 5.2).

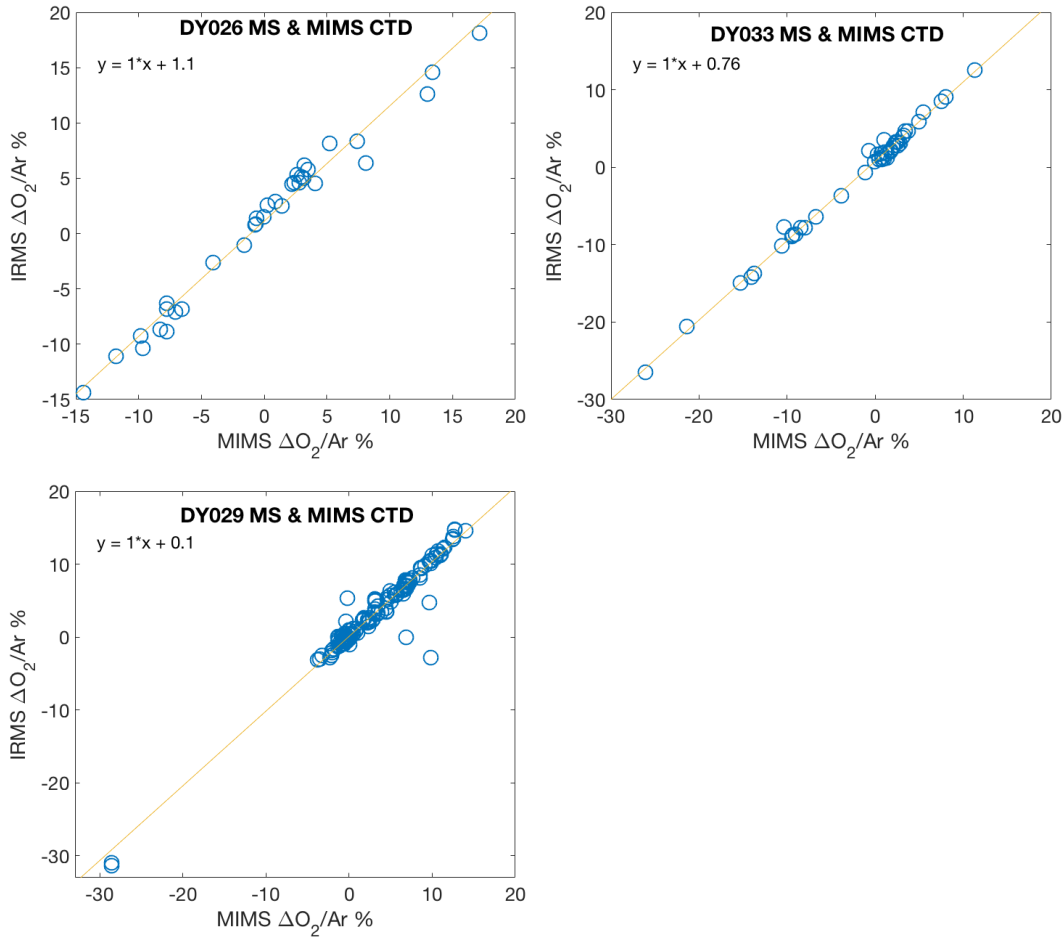

Figure 5.2. $\Delta O_2/Ar$ samples from the CTD cast measured by MS and MIMS on summer cruises 2014 (DY026) and 2015 (DY033), and spring cruise 2015 (DY029).

Discrete samples were also taken to test if there is oxygen consumption or production in the USW pipes. The MIMS samples where calibrated against IRMS ones to correct for biofouling in the filter (see also Chapter 2,section 2.6.1).

Ancillary data (oxygen concentration, chlorophyll and photosynthetic active radiation) was measured with the sensors attached to the CTD frame.

Net community and gross biological production calculation in the mixed layer and the euphotic zone

To calculate net community production $N(O_2/Ar)$ and gross production $G(^{17}O)$ in the mixed layer and the euphotic zone, it is necessary a sampling strategy that meet some conditions:

1) For F_v, samples at depths above and below the euphotic zone depth (z_{eu}) are required to calculate the gradient across the base of the euphotic zone.
2) For F_e, samples at depths above and below the mixed layer depth (z_{mix}) are required to calculate the effect of entrainment, where the mixed layer is deeper than z_{eu}.
3) For the calculation of F_{nss} and F_{bml}, samples have to be collected at different times at the same place to calculate the rate of change.

These constraints apply to the calculation of $G(^{17}O)$ in mixed layer and euphotic zone. Here I will calculate mixed layer gross biological production ($G_{ml}(^{17}O)$) as $G_{ml}(^{17}O) = G_{ss} - F_v(^{17}O)$, and compare it with a euphotic zone gross production calculated as $G_{eu}(^{17}O) = G_{ss} - F_v(^{17}O) + F_{nss}(^{17}O) + F_{bml}(^{17}O) + F_e(^{17}O)$.

Due to different sampling schedules, not all cruises allowed revisiting the same station and calculation of $F_{nss}(^{17}O)$ and $F_{bml}(^{17}O)$. However, in all cases, it is possible to calculate the biological oxygen fluxes, F_{bio} and G_{ss}, which is often used to estimate mixed layer productivity (Juranek and Quay, 2005, Kaiser et al., 2005, Stanley et al., 2010, Luz and Barkan, 2009, Palevsky et al., 2013).

The same approach will be used for $N(O_2/Ar)$ and mixed layer net community production ($N_{ml}(O_2/Ar)$), as $N_{ml}(O_2/Ar) = F_{bio} - F_v + F_{nss}$. The term F_{nss} can be included in the calculation of $N_{ml}(O_2/Ar)$ because the MIMS meets condition (3) in the mixed layer in all the cruises. The net community production in the euphotic zone was calculated as: $N_{eu}(O_2/Ar) = F_{bio} - F_v + F_{nss} + F_{bml} + F_e$.

Detailed description of each calculation is presented in chapter 3.

Uncertainty quantification

The uncertainty in the seasonal $N_{eu}(O_2/Ar)$ and $G_{eu}(^{17}O)$ for the whole Celtic Sea was calculated by error propagation from the independent errors of each term used in the calculation.

Instrument uncertainty

Instrument uncertainty was determined based on the standard deviation of dry air samples. The IRMS performance changed over time and therefore the variability in every season is slightly different. Instrument uncertainty (mean±sd) of standard gas (dry air) against working reference gas (mixture of Ar and O_2) were: $s(^{17}\Delta)$ = (-6.4±8.1) ppm and $s(\Delta O_2/Ar)$ = (133±1.03) ‰ in autumn; $s(^{17}\Delta)$ = (-24.4±9.7) ppm and $s(\Delta O_2/Ar)$ = (133±0.9) ‰ in spring; and $s(^{17}\Delta)$ = (–23.1±4.5) ppm and $s(\Delta O_2/Ar)$ = (132±0.8) ‰ in summer 2015. Instrument variability in summer 2014 was slightly higher at $s(\Delta O_2/Ar)$ = (133±1.15) ‰ and $s(^{17}\Delta)$= (–3±11) ppm.

Therefore, gross production data from summer 2014 should be interpreted with caution.

Reproducibility of samples

$\Delta O_2/Ar$ measurements from the MIMS were calibrated against IRMS, therefore the instrument uncertainty is the same as mentioned above, $s(\Delta O_2/Ar)$ = (133±1.03) ‰ in autumn, (133±0.9) ‰ in spring, (132±0.8) ‰ in summer 2015, and (133±1.15) ‰ in summer 2014.

The uncertainty related to the reproducibility of actual samples is calculated by the standard deviation of duplicates or triplicates taken randomly on each cruise, and gave a mean standard deviation of $s(^{17}\Delta)$ = 9 ppm and $s(\Delta O_2/Ar)$ = 1 ‰ which is very similar to instrument uncertainty and can probably be attributed to that. All the samples where taken around midday to avoid the possibility of diurnal variability that could affect the values.

Gas transfer velocity uncertainty

Mean *k*, gas transfer velocity, in summer 2014, autumn, spring and summer 2015 were 5, 2, 3, 4 m d^{-1}, respectively. The parameterisation of winds by Nightingale et al. (2000) has an estimated uncertainty of about 20 %. Some studies (Reuer et al., 2007), use a weighted mean accounting for the time residence of oxygen in the water before the

sampling period. The weighted-mean piston velocity calculation of Reuer et al. (2007) assumes steady-state for $\Delta(O_2/Ar)$, δ values and constant mixed layer depth. Here, I explicitly include non-steady state terms, making these assumptions unnecessary. Moreover, a mean change of 30 m was measured in the MLD from summer to autumn season (August to November 2014) in the Celtic Sea, therefore, the fixed mixed layer depth assumption in the weighted k calculation at that time would likely entail some additional uncertainty to our measurements.

The uncertainty in the calculation of $c_{sat}(O_2)$ originates from temperature and salinity variations, and is expected to be small < 0.5 μmol l^{-1}.

G_{eu} and N_{eu} propagated uncertainty

Propagated absolute uncertainty in summer 2014, autumn, spring and summer 2015 for the calculation of G_{ss} is (295, 116, 69, 94) mmol m^{-2} d^{-1}, and the relative uncertainty is (25, 71, 35, 28) % respectively. For F_{bio} the absolute uncertainty is (9, 2, 7, 4) mmol m^{-2} d^{-1} in summer 2014, autumn, spring and summer 2015, and the relative uncertainties are 20 % in all seasons (Table 5.1).

From the non-steady state term calculated from triple oxygen isotopes, mean $F_{nss}(^{17}O)$ uncertainties in autumn, spring and summer are (17, 6, 11) mmol m^{-2} d^{-1}, respectively.

$F_v(^{17}O)$ has the highest uncertainty (13, 3, 14) mmol m^{-2} d^{-1}, mainly due to the larger uncertainty (67 %) in the vertical diffusivity coefficient (K_z). K_z was not estimated directly but previous studies had measured K_z in the Celtic Sea (3±2) × 10^{-5} m^2 s^{-1} (Simpson and Sharples, 2012, Osborn, 1980, Palmer et al., 2013). Although the relative uncertainty is big, the diffusivity is one of the smallest terms in the estimation of $G_{eu}(^{17}O)$ and therefore absolute uncertainty is small (Table 5.1).

The uncertainty in $F_{bml}(^{17}O)$ is the same as in F_{nss} but there is also uncertainty derived from the possibility of horizontal transport due to strong deep currents (Palmer et al., 2013) that was not possible to calculate because of lack of two samples taken at the same time in two different locations.

Absolute uncertainty in the entrainment calculation $F_e(^{17}O)$ is (8, 13, 6) mmol m^{-2} d^{-1} in winter, spring and summer 2015 data.

Then, the propagated relative uncertainties in summer 2014, autumn, spring and summer 2015 for $G_{eu}(^{17}O)$ are (94, 232, 482) mmol m^{-2} d^{-1}, respectively, showing that the added terms (F_{bml}, F_{nss}, F_e, F_v) added half or more than half of the total uncertainty.

From the terms adding uncertainty in the calculation of $N_{eu}(O_2/Ar)$, F_{nss}, F_e, F_v, contribute each only with ~1% each of them, and F_{bml} 12 %. Then, the propagated uncertainty for $N_{eu}(O_2/Ar)$ is almost 71 % in all the seasons.

Table 5.1. Absolute uncertainty (σ), and relative uncertainty σ % of each term in the calculation of G_{ss}, F_{bio}, $G_{eu}(^{17}O)$, $N_{eu}(O_2/Ar)$

	DY026 (summer)		DY018 (autumn)		DY029 (spring)		DY033 (summer)	
	σ (mmol m^{-2} d^{-1})	σ %	σ (mmol m^{-2} d^{-1})	σ %	σ (mmol m^{-2} d^{-1})	σ %	σ (mmol m^{-2} d^{-1})	σ %
g	**0.2**	14	**0.1**	68	**0.1**	28	**0.1**	20
$\Delta(O_2/Ar)$	**0**	0.6	**0**	0.8	**0**	0.7	**0**	0.6
k	**1.0**	20	**0.8**	20	**0.4**	20	**0.6**	20
$c_{sat}(O_2)$	**0.5**	0	**0.5**	0	**0.5**	0	**0.5**	0
$\boldsymbol{G_{ss}}$	**295**	25	**116**	71	**69**	35	**94**	28
$\boldsymbol{F_{bio}}$	**9**	20	**2**	20	**7**	20	**4**	20
			DY018 (autumn)		DY029 (spring)		DY033 (summer)	
$F_v(^{17}O)$	-	-	**13**	87	**3**	85	**14**	84
$F_{nss}(^{17}O)$	-	-	**2**	33	**6**	29	**11**	26
$F_{bml}(^{17}O)$			**11**	33	**1**	29	**42**	26
$F_e(^{17}O)$	-	-	**8**	30	**13**	23	**6**	19
F_v	-	-	**5**	67	**0**	67	**0**	67
F_{nss}	-	-	**0**	0.8	**0**	0.7	**0**	0.6
F_{bml}	-	-	**1**	12	**1**	12	**1**	12
F_e	-	-	**0**	0.8	**0**	0.7	**0**	0.6
$\boldsymbol{G_{eu}(^{17}O)}$	**-**	**-**	**94**	125	**232**	103	**482**	98
$\boldsymbol{N_{eu}(O_2/Ar)}$	**-**	**-**	**16**	71	**39**	71	**4**	71

5.3 Results

5.3.1 Interannual and seasonal cycle of $\Delta O_2/Ar$ and biological fluxes

Discrete and continuous O_2/Ar measurements were carried out on three cruises (DY026, DY033, DY029) and only discrete ones on cruise DY018. All cruises followed similar transects. In summer 2014 (DY026), continuous O_2/Ar measurements showed net autotrophic conditions ($\Delta O_2/Ar$ = (4±2) %) (Fig.5.3). In summer 2015 (DY033), continuous O_2/Ar measurements showed net autotrophic conditions again but half of the supersaturation of 2014 (2±1) %. In autumn 2014 (DY018), conditions were inverted and the discrete surface samples showed net heterotrophic state ($\Delta O_2/Ar$ = (–1±0.8) %). Higher $\Delta O_2/Ar$ values were recorded in spring 2015 (DY029), with a mean of (6±4) %. Discrete surface samples measured by IRMS has been superimposed over continuous ones measured by MIMS (Fig.5.3).

A recurrent feature of lower $\Delta O_2/Ar$ values was observed in the English Channel, with heterotrophic conditions east of 4º W in both summers and values near equilibrium in spring. SST satellite images show a change in water mass temperature in this area, suggesting the collision of two different water masses in the English Channel that could explain the sharp change in $\Delta O_2/Ar$ (Fig. 5.1). There are no data for the English Channel in autumn.

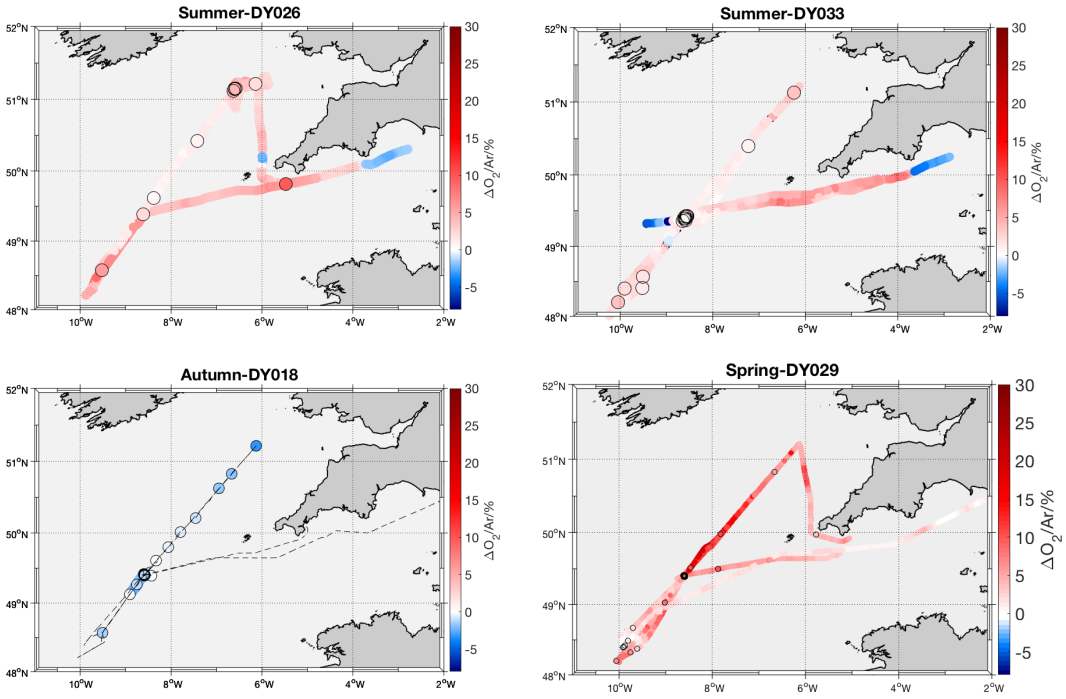

Figure 5.3. USW $\Delta O_2/Ar$ by MIMS in summer 2014 (DY026), summer 2015 (DY033), autumn 2014 (DY018) and spring 2015 (DY029). Back edge circles superimposed on the cruise track are surface $\Delta O_2/Ar$ by MS. Red colour shows autotrophic conditions and blue heterotrophic. Dashed line indicates the cruise track in DY018.

F_{bio} ranged from 20 to 117 and from -1 to 119 mmol m^{-2} d^{-1} in summer 2014 and 2015, respectively (Fig 5.4). However, the mean value was higher in 2014 (46±31) than in 2015 (19±23). Mean G_{ss} is also higher in summer 2014 (1195±861; n = 10) mmol m^{-2} d^{-1} than in 2015 (331±341; n = 24) mmol m^{-2} d^{-1} (Fig 5.5). One reason for the differences between the two summers is the unusual average stronger winds in 2014 (k = 5 m d^{-1}) than in 2015 (k = 3 m d^{-1}) (data not shown). Another explanation for the high values in 2014 is that the data from this cruise showed the highest instrument uncertainty. Finally, because both F_{bio} and G_{ss}, are higher in 2014 there appear to be real biological differences between the two summers.

Minimum (-58 mmol m^{-2} d^{-1}) and maximum (140 mmol m^{-2} d^{-1}) F_{bio} values occurred in autumn and spring respectively. Mean F_{bio} was (-12±15) mmol m^{-2} d^{-1} in autumn and (36±39) mmol m^{-2} d^{-1} in spring (Fig 5.4). The average value of G_{ss} was (164±158) mmol m^{-2} d^{-1} in autumn and (199±180) mmol m^{-2} d^{-1} in spring (Fig 5.5). Winds were

stronger in autumn (k = 4 m d^{-1}) as expected in this season and weaker in spring (k = 2 m d^{-1}).

In summary, G_{ss} is higher in summer and autumn and lower in spring, but greater respiration in summer and in autumn likely leads to lower F_{bio} values than in spring. The positive F_{bio} values show biological O_2 fluxes from the sea to the atmosphere in spring and summer, while fluxes of O_2 from atmosphere to the sea would occur in autumn.

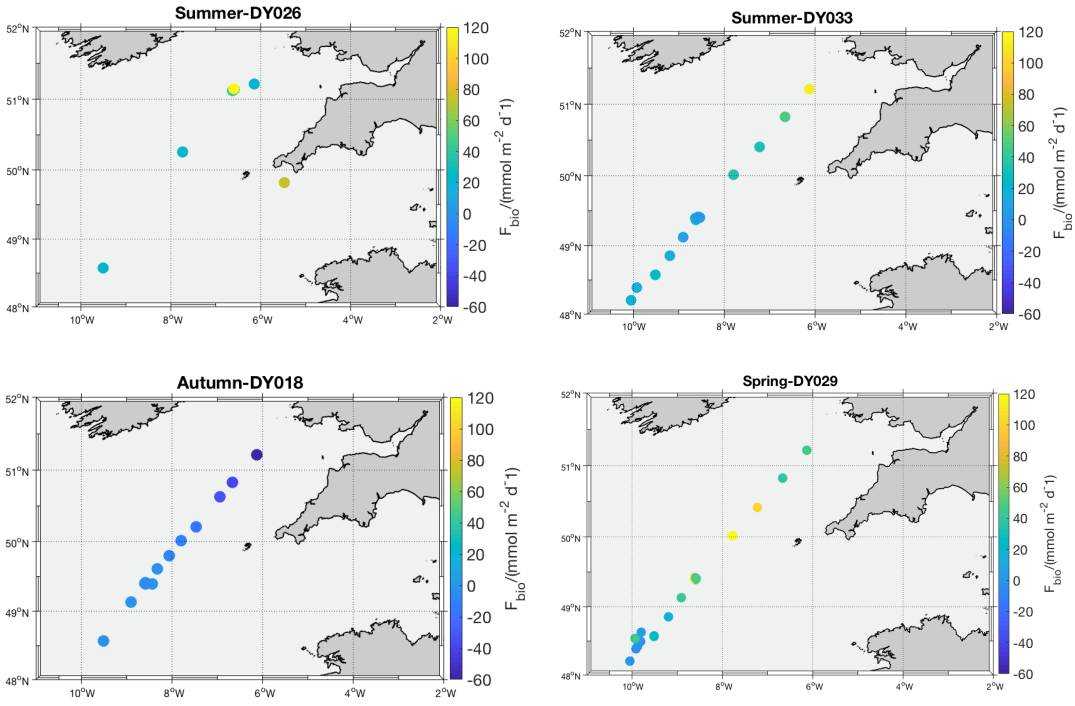

Figure 5.4. Zonal variations of biological fluxes (F_{bio}) at steady state from CTD discrete samples taken in summer 2014 (DY026), 2015 (DY033), autumn 2014 (DY018) and spring 2015 (DY029).

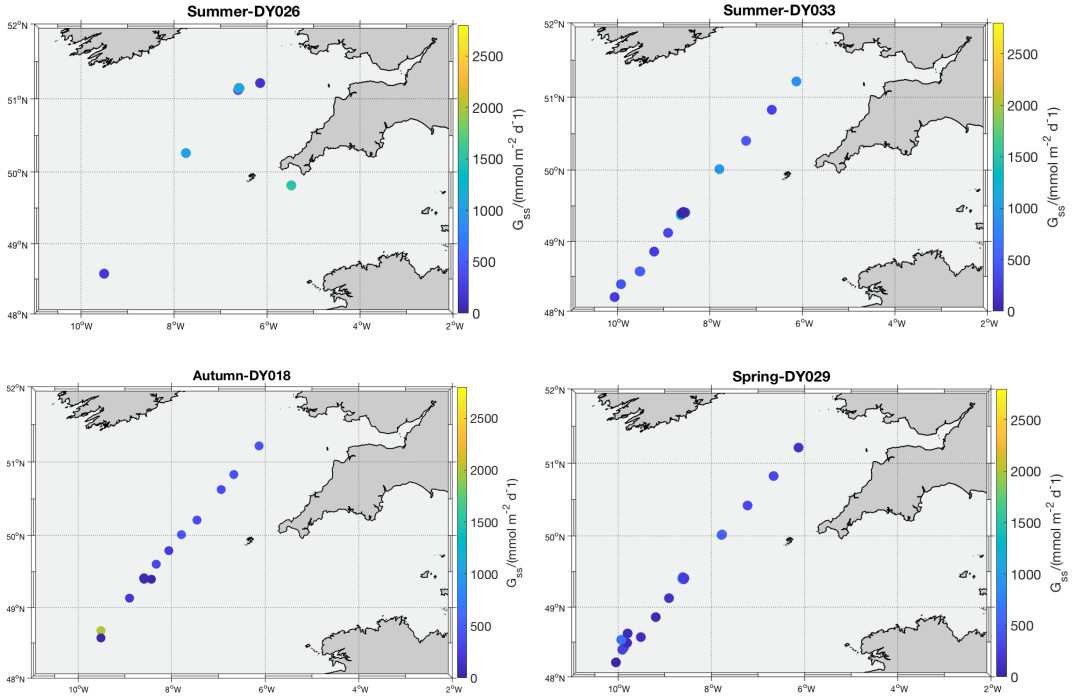

Figure 5.5. Zonal variations of gross oxygen production at steady state (G_{ss}) from CTD discrete samples taken in in summer 2014 (DY026), 2015 (DY033), autumn 2014 (DY018) and spring 2015 (DY029).

5.3.2 Seasonal gross production and net community production

Euphotic zone vs. mixed layer depth

To evaluate how well biological production in the mixed layer captures biological production in the euphotic zone (euphotic zone depth: z_{eu}), the influence of vertical transport due to diapycnal diffusion (F_v), temporal changes (F_{nss}), entrainment (F_e) and production below the mixed layer (F_{bml}), but within the euphotic zone were considered for each season.

The MLD was shallow in summer and spring, around 20 m; and deeper, around 50 m, in autumn, with less variation between stations (Fig 5.6). z_{eu} was around 50 m in summer and autumn and shallower, around 40 m, in spring. Generally, z_{eu} seems to be controlled geographically. The most inland stations (A, J2, J4, J6 and CCS) show shallower z_{eu}, while stations closer to the shelf edge and off shelf (O4, O2, CS2 and Fe) show deeper z_{eu}. Taking the central Celtic sea (CCS) station as a reference point, z_{eu} follows an annual cycle from summer 2014 when z_{eu} at CCS is 40 m, gets deeper in

autumn and finally being shallowest in spring. The summer 2015 shows the deepest z_{eu} showing stronger interannual than annual variability (Fig 5.6). Regardless of the annual variability, the MLD is always shallower than the z_{eu} in both summers, or in other words, photosynthesis can happen in the mixed layer and below. In autumn the MLD goes deeper reaching the z_{eu} or even deeper, which means that at the end of the sampling period in November 2014, the whole mixed layer was not exposed to enough light to support photosynthesis. In spring, ML and z_{eu} shoal being generally similar in depth and therefore, the whole mixed layer is exposed to light that allows photosynthesis.

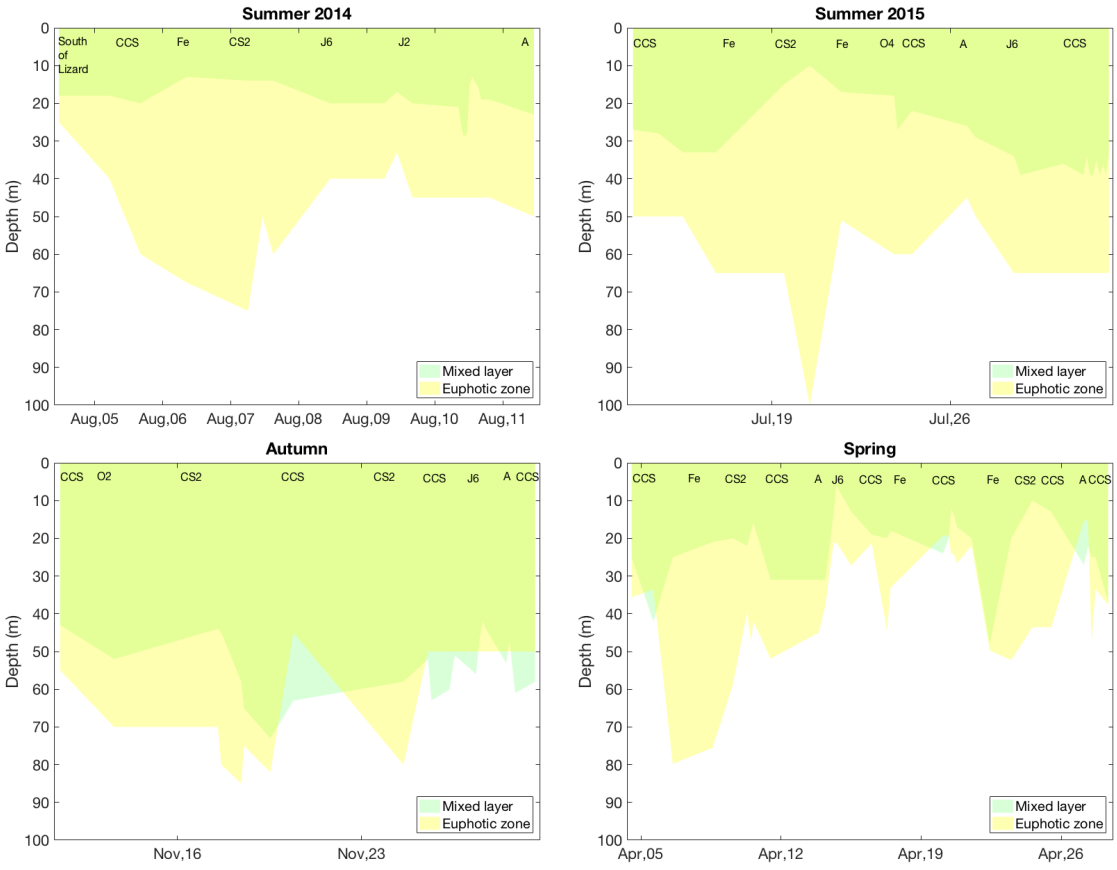

Figure 5.6. Time variations of mixed layer (green) and euphotic zone (yellow) during summer 2014 and 2015, autumn and spring. Guiding stations label in the top axis.

Net community production seasonally

Net community production in the mixed layer at high spatial resolution $N_{ml}(O_2/Ar)$ represents the combination of the biological oxygen fluxes, temporal changes in the mixed layer and diapycnal diffusion (Fig. 5.7, 5.8 & 5.9 top plots). In autumn, due to a lack of continuous measurements, F_{nss} was ignored and $N_{ml}(O_2/Ar)$ only represents

biological fluxes and diapycnal diffusion. The average $N_{ml}(O_2/Ar)$ value was (-14±28) mmol m^{-2} d^{-1}, thus the Celtic Sea was net heterotrophic (Fig. 5.7, top). The lowest values were found at stations CCS (49.4º N 8.6º W) and O2 (49.1º N 8.9º W), -97 and -70 mmol m^{-2} d^{-1} respectively. Although the Celtic Sea appears mainly heterotrophic, there are positive $N_{ml}(O_2/Ar)$ values up to 20 mmol m^{-2} d^{-1} that indicate autotrophic conditions also in autumn. Net community production until the end of the euphotic zone $N_{eu}(O_2/Ar)$ represents the combination of the biological oxygen fluxes, diapycnal diffusion, changes over time, entrainment and production below the mixed layer (Fig. 5.7, 5.8 & 5.9 bottom plots). In autumn, the average $N_{eu}(O_2/Ar)$ value in CCS was (-18±63) mmol m^{-2} d^{-1}, ranging from -90 to 28 mmol m^{-2} d^{-1}. At CS2 (48.6N 9.5W) $N_{eu}(O_2/Ar)$ value was -31 mmol m^{-2} d^{-1} (Fig. 5.7, bottom & Fig. 5.13), thus the Celtic Sea still appeared net heterotrophic in autumn even when including production below the ML. Both, $N_{ml}(O_2/Ar)$ and $N_{eu}(O_2/Ar)$ were calculated from discrete CTD samples.

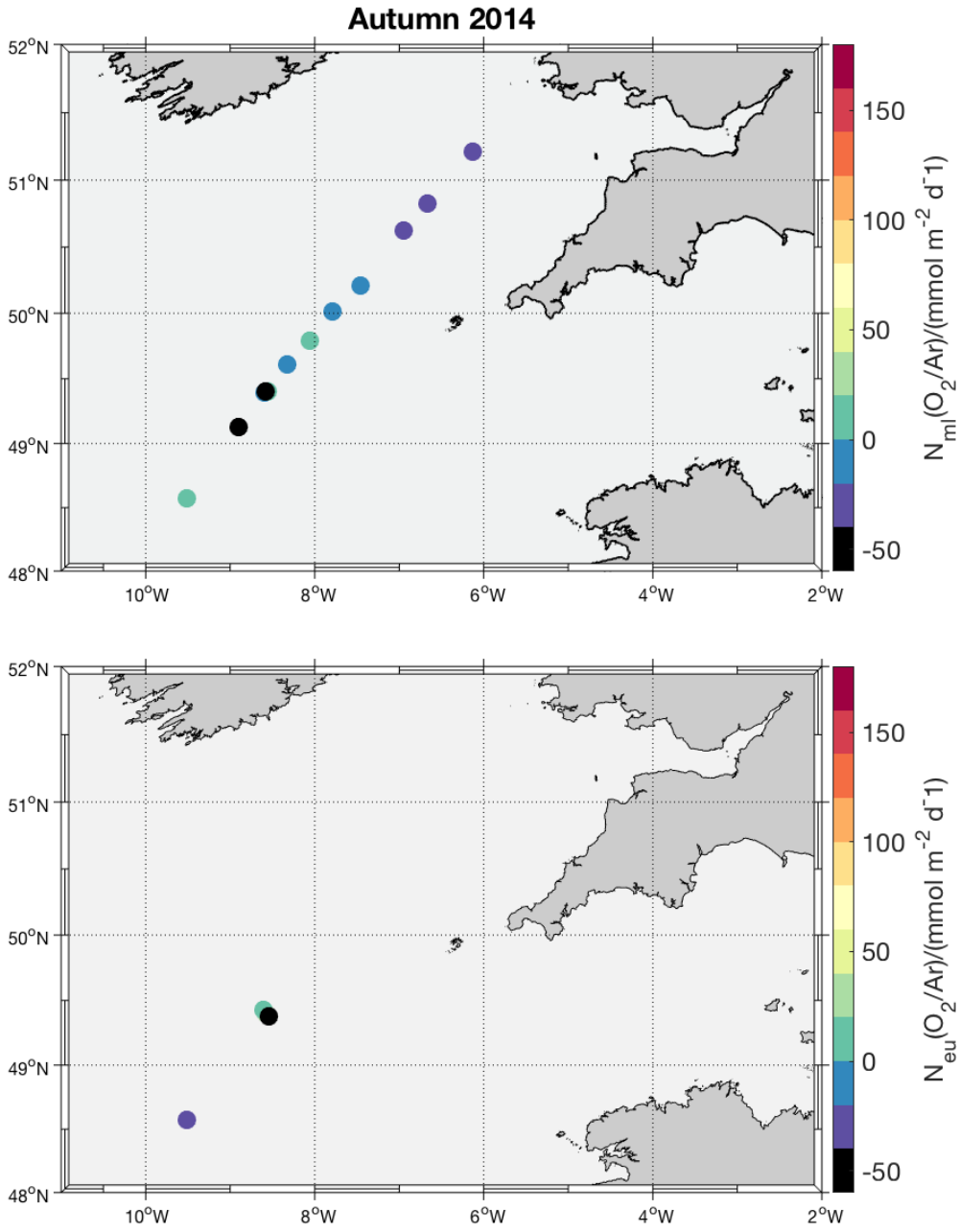

Figure 5.7. Zonal variations of $N_{ml}(O_2/Ar)$ (top) and $N_{eu}(O_2/Ar)$ (bottom) samples taken in autumn 2014 (DY018).

In spring 2015, $N_{ml}(O_2/Ar)$ was calculated using O_2/Ar from continuous MIMS measurements and therefore including temporal changes in the mixed layer at high spatial resolution. The average was (33±41) mmol m^{-2} d^{-1}, thus the Celtic Sea was net autotrophic (Fig. 5.8, top). The highest $N_{ml}(O_2/Ar)$ values were found at stations CCS and A (51.2º N 6.1º W), 133 and 117 mmol m^{-2} d^{-1} respectively. However, from CCS to

the CS2, the Celtic Sea appeared very patchy in its southern part with some negative $N_{ml}(O_2/Ar)$ values, accordingly this, that section was net heterotrophic. The average $N_{eu}(O_2/Ar)$ value for the 6 stations (A, J2, J4, J6, CCS, CS2) was (55±34) mmol m^{-2} $d^{-}1$, ranging from 2 to 100 mmol m^{-2} d^{-1}. At CS2 $N_{eu}(O_2/Ar)$ values were (25±7) mmol m^{-2} d^{-1} (Fig. 5.8, bottom & Fig. 5.13), thus the Celtic Sea still appearing net autotrophic in spring even including production below the mixed layer but missed the heterotrophic areas detected at high resolution.

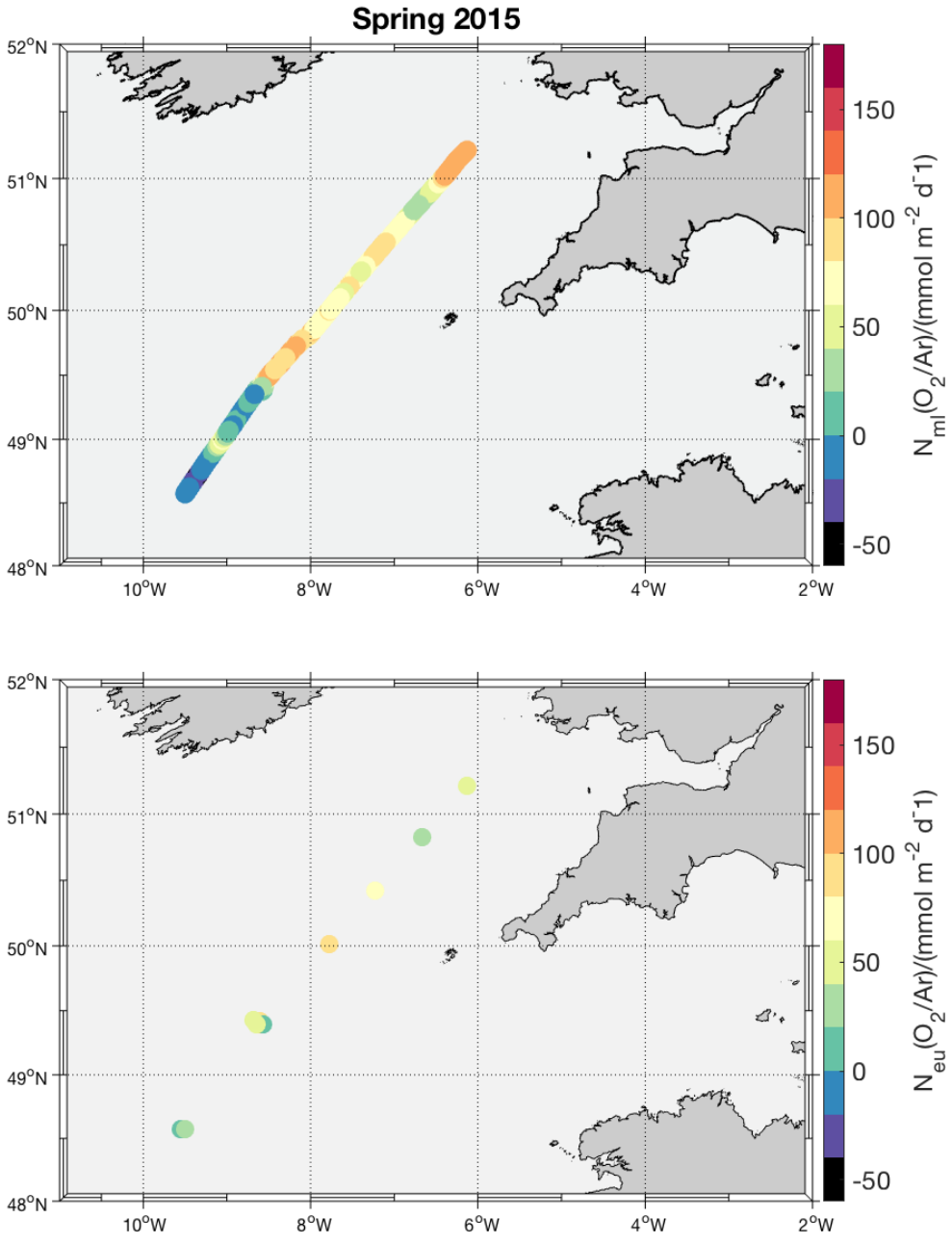

Figure 5.8. Zonal variations of $N_{ml}(O_2/Ar)$ (top) and $N_{eu}(O_2/Ar)$ (bottom) samples taken in spring 2015 (DY029).

The samples collected in summer 2014 do not allow the calculation of F_{nss}, F_e and F_{bml}, and therefore the data is not included here. In summer 2015, the $N_{ml}(O_2/Ar)$ values were also calculated using O_2/Ar from continuous MIMS measurements and therefore including temporal changes. The average was (33±24) mmol m^{-2} d^{-1}, thus the Celtic Sea was net autotrophic (Fig. 5.11, top). The highest $N_{ml}(O_2/Ar)$ value (171 mmol m^{-2} d^{-1}) was found at station J2 (51.0º N 6.5º W). For the majority of the shelf, values are between 0 and 50 mmol m^{-2} d^{-1}. The lowest value is -6 mmol m^{-2} d^{-1} but it last very short time (~ 5 minutes) and therefore is not visible in the plot. The average $N_{eu}(O_2/Ar)$ value for the 3 stations CCS, CS2 and Fe (48.4º N 9.8º W) was (-11±39), 19 and 23 mmol m^{-2} d^{-1} respectively (Fig. 5.9, bottom & Fig. 5.13), thus the Celtic Sea still appearing net autotrophic (5±29 mmol m^{-2} d^{-1}) in summer even including production below the ML but missed the highly autotrophic areas detected in the inner part of the shelf.

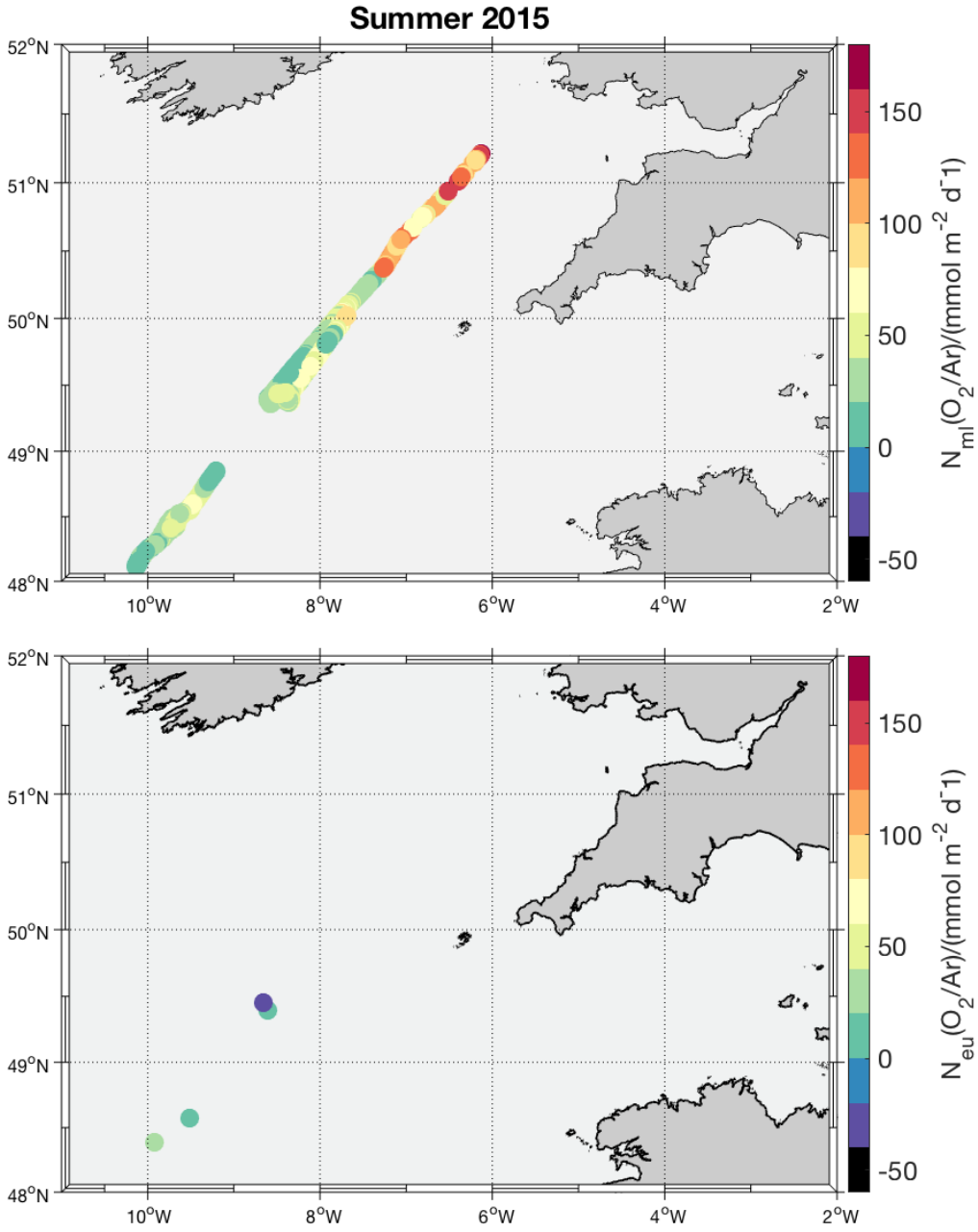

Figure 5.9. Zonal variations of $N_{ml}(O_2/Ar)$ (top) and $N_{eu}(O_2/Ar)$ (bottom) samples taken in summer 2015 (DY033).

Gross production seasonally

Gross production in the mixed layer, $G_{ml}(^{17}O)$, represents the combination of the biological oxygen fluxes and diapycnal diffusion (Fig. 5.10, 5.11 & 5.12 top plots). The average $G_{ml}(^{17}O)$ was (181±167) mmol m^{-2} d^{-1} during autumn. The $G_{ml}(^{17}O)$ values

show a gradual decrease towards the shelf edge, showing higher values (~400 mmol m^{-2} $d^{-1)}$ from station A to J6 and decreasing to ~100 mmol m^{-2} d^{-1} at the shelf edge (CS2). Although this spatial trend is generally clear, winds play an important role in autumn fluxes. Consequently, the maximum $G_{ml}(^{17}O)$ occurred also in CS2 favoured by strong winds (k = 7 m d^{-1}; 2021 mmol m^{-2} d^{-1}). Gross production in the euphotic zone at lower spatial resolution $G_{eu}(^{17}O)$ represents the combination of gross oxygen fluxes, diapycnal diffusion, changes over time, entrainment and production below the mixed layer (Fig. 5.10, 5.11 & 5.12 bottom plots). As for autumn $N_{eu}(O_2/Ar)$, our spatial resolution is constrained to stations CCS and CS2. The mean $G_{eu}(^{17}O)$ value was (75±151) mmol m^{-2} d^{-1} (Fig. 5.10, bottom & Fig. 5.13). Therefore, the average value is half of $G_{ml}(^{17}O)$, mainly due to the lack of samples in the inner part of the shelf. Moreover, the information of the gradient from inland to off shelf is missed with $G_{eu}(^{17}O)$ calculations.

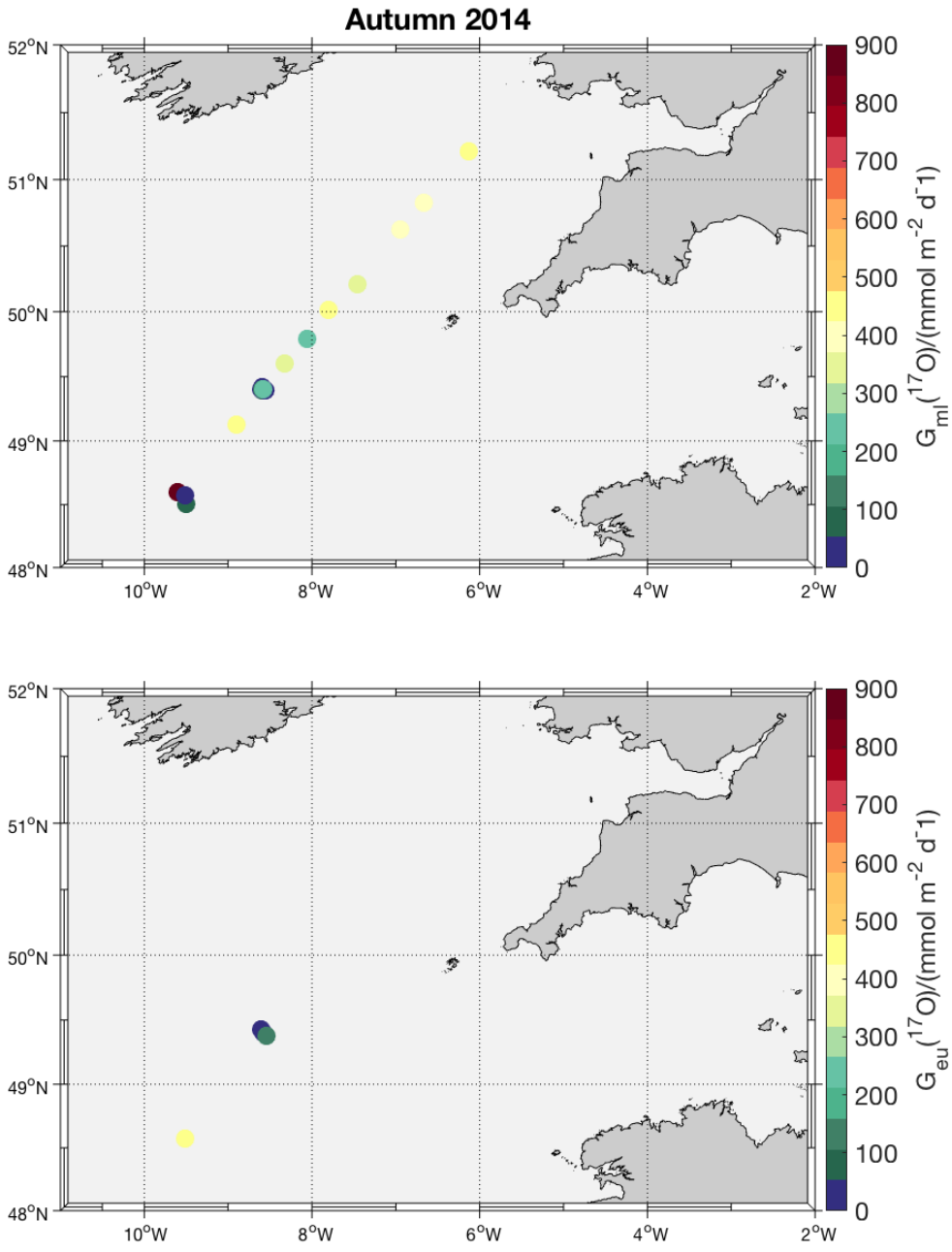

Fig 5.10. Zonal variations of $G_{ml}(^{17}O)$ (mmol m^{-2} d^{-1}) (top) and $G_{eu}(^{17}O)$ (bottom) samples taken in autumn 2014 (DY018).

In spring, $G_{ml}(^{17}O)$ shows that the Celtic Sea appeared very patchy with an average value of 192 mmol m^{-2} d^{-1}, ranging from 19 to 673 mmol m^{-2} d^{-1} (Fig. 5.11, top). As seen in the spring $N_{ml}(O_2/Ar)$ values, the shelf could be spatially divided into two, with higher production from stations A to CCS and generally lower production from CCS to Fe. Surprisingly, I find the maximum $G_{ml}(^{17}O)$ in the shelf edge, but as happened in

autumn, this flux was mainly raised by the strongest winds (k = 6 m d^{-1}) during the spring sampling period. The sampling strategy during the spring cruise allowed a good spatial resolution also using $G_{eu}(^{17}O)$ calculations. The mean $G_{eu}(^{17}O)$ value (225±115) mmol m^{-2} d^{-1} is similar to the one obtained with $G_{ml}(^{17}O)$ (Fig. 5.11, bottom). A subtle but clear decrease from 284 mmol m^{-2} d^{-1} at station A to 162 mmol m^{-2} d^{-1} at CS2 is seen in $G_{eu}(^{17}O)$. Therefore, the $G_{eu}(^{17}O)$ model allowed to calculate production until the z_{eu} without compromising spatial resolution information in this occasion.

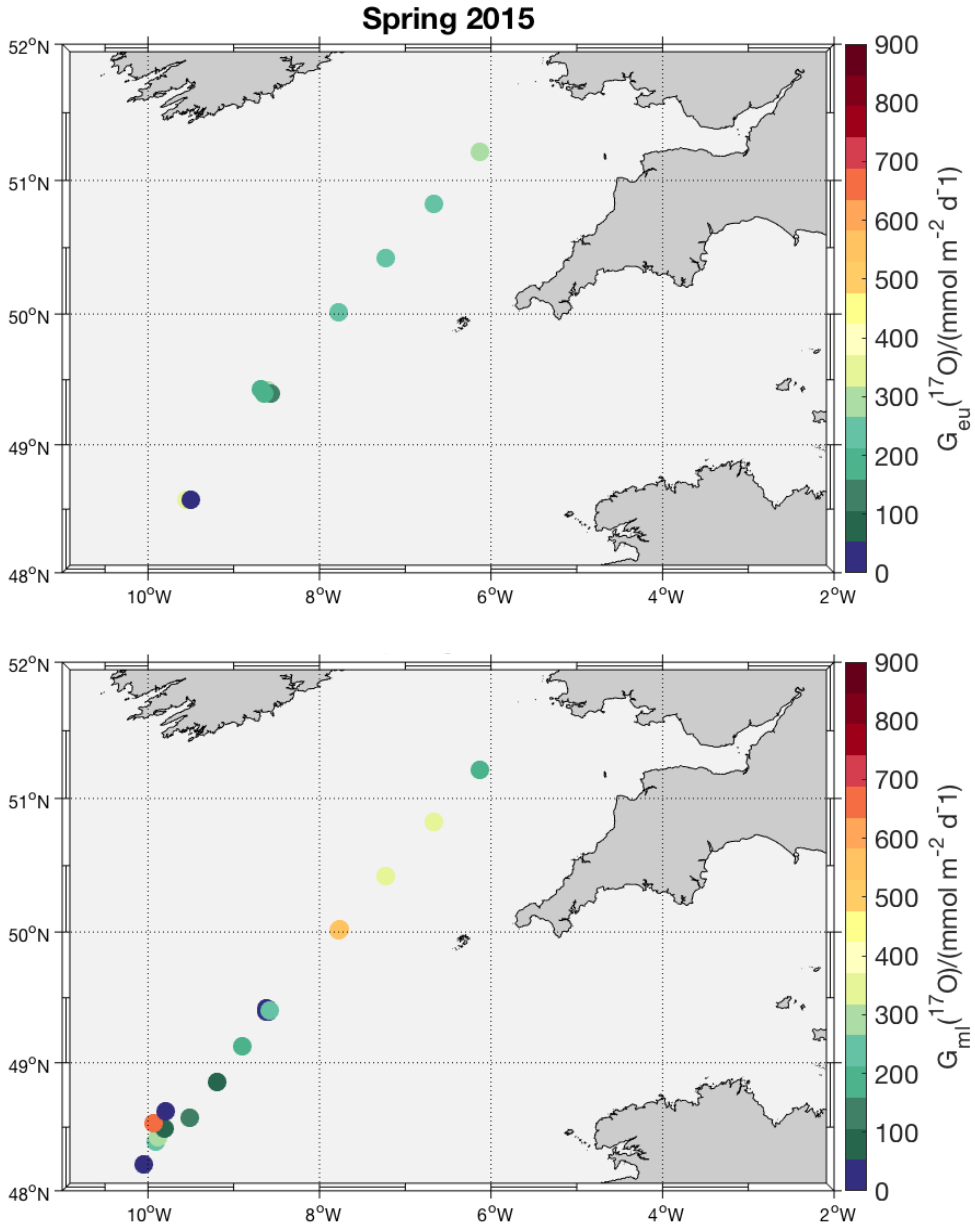

Figure 5.11. Zonal variations of $G_{ml}(^{17}O)$ (mmol m^{-2} d^{-1}) (top) and $G_{eu}(^{17}O)$ (bottom) samples taken in spring 2015 (DY029).

During summer, $G_{ml}(^{17}O)$ appeared very patchy, with an average value of 494 mmol m^{-2} d^{-1}, ranging from 139 to 1367 mmol m^{-2} d^{-1} (Fig. 5.12, top). This value is double $G_{ml}(^{17}O)$ during the spring cruise. Nevertheless, $N_{ml}(O_2/Ar)$ values during summer suggest that respiration was stronger than in spring. The average $G_{eu}(^{17}O)$ value for the 3 stations CCS, CS2 and Fe was (493±497), 335 and -42 mmol m^{-2} d^{-1} respectively (Fig. 5.12, bottom & Fig. 5.13). The negative value at station Fe is the result of the sum of negative values from two non steady state production terms of gross production calculated both in the same way ($d^{17}\Delta/dt$) but one referring to the mixed layer (F_{nss}) and the other below (F_{bml}) (-84 an -217 mmol m^{-2} d^{-1}). It is worth noticing that G_{ss} cannot be negative. Negative gross production is physiologically impossible. The negative value is probably an artefact due to horizontal processes like different water mass on the second sampling. This suggest that during summer $G_{eu}(^{17}O)$ calculation budget seems to be affected by deep currents from Atlantic waters with a lower photosynthetic oxygen signal.

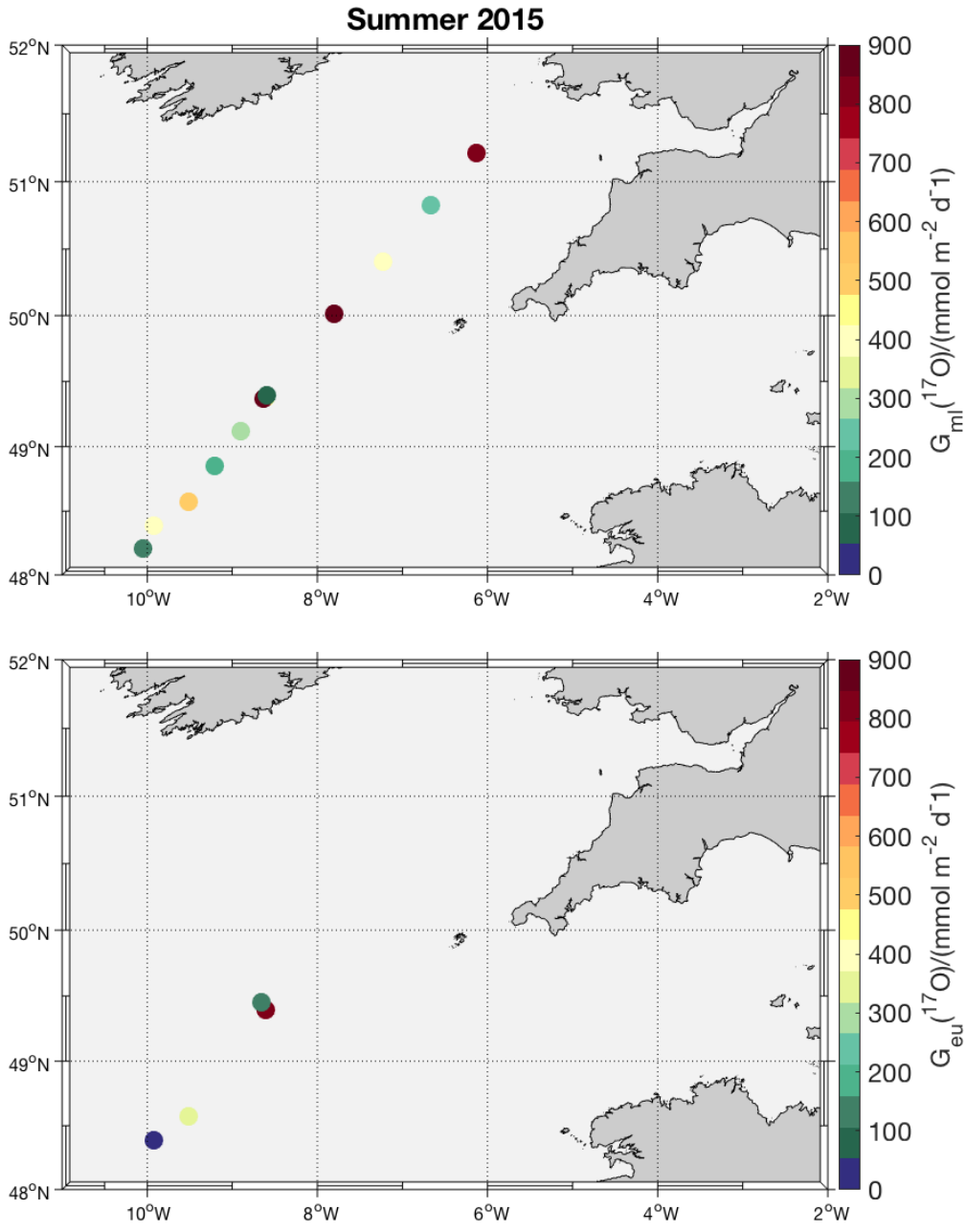

Figure 5.12. Zonal variations of $G_{ml}(^{17}O)$ (mmol m^{-2} d^{-1}) (top) and $G_{eu}(^{17}O)$ (bottom) samples taken in spring 2015 (DY033).

Mean values of net and gross production are presented in table 5.2. Seasonally, the Celtic Sea shows higher net production in spring, higher gross production occurs in summer and respiration exceeding production in autumn (Table 5.2). These net, gross and respiration characterisations of the three seasons are true regardless of the

calculation used for net (F_{bio}, $N_{ml}(O_2/Ar)$ or $N_{eu}(O_2/Ar)$) and gross (G_{ss}, $G_{ml}(^{17}O)$ or $G_{eu}(^{17}O)$) production.

Note that for the discussion on the contribution of the each parameter it is necessary to compare calculations at the same spatial resolution. The next section on "CCS and CS2 seasonality" will cover that.

Table 5.2. Seasonal representation (mean±sd) of F_{bio}, $N_{ml}(O_2/Ar)$, $N_{eu}(O_2/Ar)$, G_{ss}, $G_{ml}(^{17}O)$, $G_{eu}(^{17}O)$, R, R_{ml}, R_{eu} (mmol m^{-2} d^{-1}) in the Celtic Sea.

	F_{bio}	$N_{ml}(O_2/Ar)$	$N_{eu}(O_2/Ar)$	G_{ss}	$G_{ml}(^{17}O)$	$G_{eu}(^{17}O)$	R	R_{ml}	R_{eu}
Autumn	**-12**	**-14**	**-22**	**164**	**181**	**75**	**275**	**293**	**144**
	±15	±28	±52	±158	±167	±151	**±159**	**±169**	**±160**
Spring	**36**	**33**	**55**	**199**	**192**	**225**	**163**	**159**	**170**
	±39	±41	±34	±180	±179	±115	**±184**	**±183**	**±120**
Summer	**19**	**13**	**5**	**331**	**494**	**493**	**312**	**481**	**488**
	±23	±11	±29	±341	±370	±497	**±342**	**±370**	**±497**

5.3.3 CCS and CS2 seasonality

The Celtic Sea can be divided into three regions, inner shelf (A), central shelf (CCS) and shelf edge (CS2). For the calculation of $G_{eu}(^{17}O)$ and $N_{eu}(O_2/Ar)$ it is necessary to sample the water column at least two times. The stations that fitted this condition were the CSS and CS2. The inner shelf was only revisited in the spring cruise. In figure 5.13 the value of each term are presented separately to show their contribution to $G_{eu}(^{17}O)$ and $N_{eu}(O_2/Ar)$. Based in the mean production values, station CCS represents the Celtic Sea as a whole better than station CS2. z_{eu} is deeper at CS2 than at CCS, regardless of the season, while the opposite is true for the MLD (Fig. 5.13). That makes z_{mix} closer to z_{eu} in CCS than in CS2. Entrainment (Δz_{mix}) occurs at all seasons in CCS but it doesn't at CS2.

The largest terms contributing to $N_{eu}(O_2/Ar)$ vary between stations and season, but in general it were F_{nss} and F_{bml} terms. In contrast, the largest term contribution to $G_{eu}(^{17}O)$ is G_{ss} at any season or station. Negative values of F_{nss} with triple oxygen isotopes in CCS are always associated to negative values of F_{bml} and F_e, suggesting an influence of the different deep-water masses to the mixed layer budget during entrainment (see further explanation in the discussion below). F_v is generally weak (<10 mmol m^{-2} d^{-1})

especially in spring (Fig. 5.13), and therefore, the least significant term. In summer, diffusion direction is from below the mixed to the mixed layer at both stations, suggesting subsurface maximum production, which is a common feature in summer. G_{ss} only represents $G_{eu}(^{17}O)$ values at CS2 in summer, but differs in other seasons. Equally, summer F_{bio} approximates to $N_{eu}(O_2/Ar)$ only at this station. Therefore, steady state fluxes (G_{ss} and F_{bio}) approximate $N_{eu}(O_2/Ar)$ and $G_{eu}(^{17}O)$ at station CS2 during summer only (Fig. 5.13).

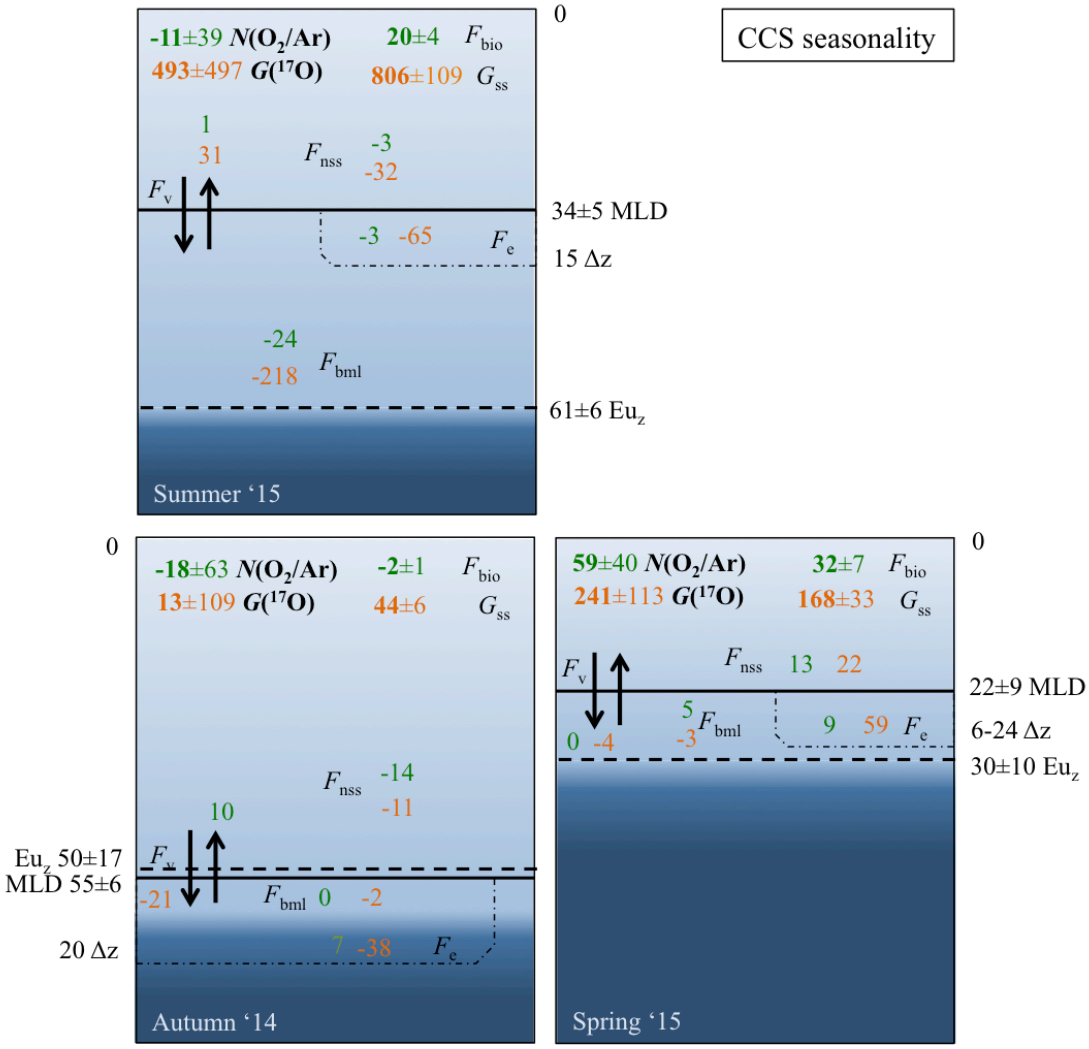

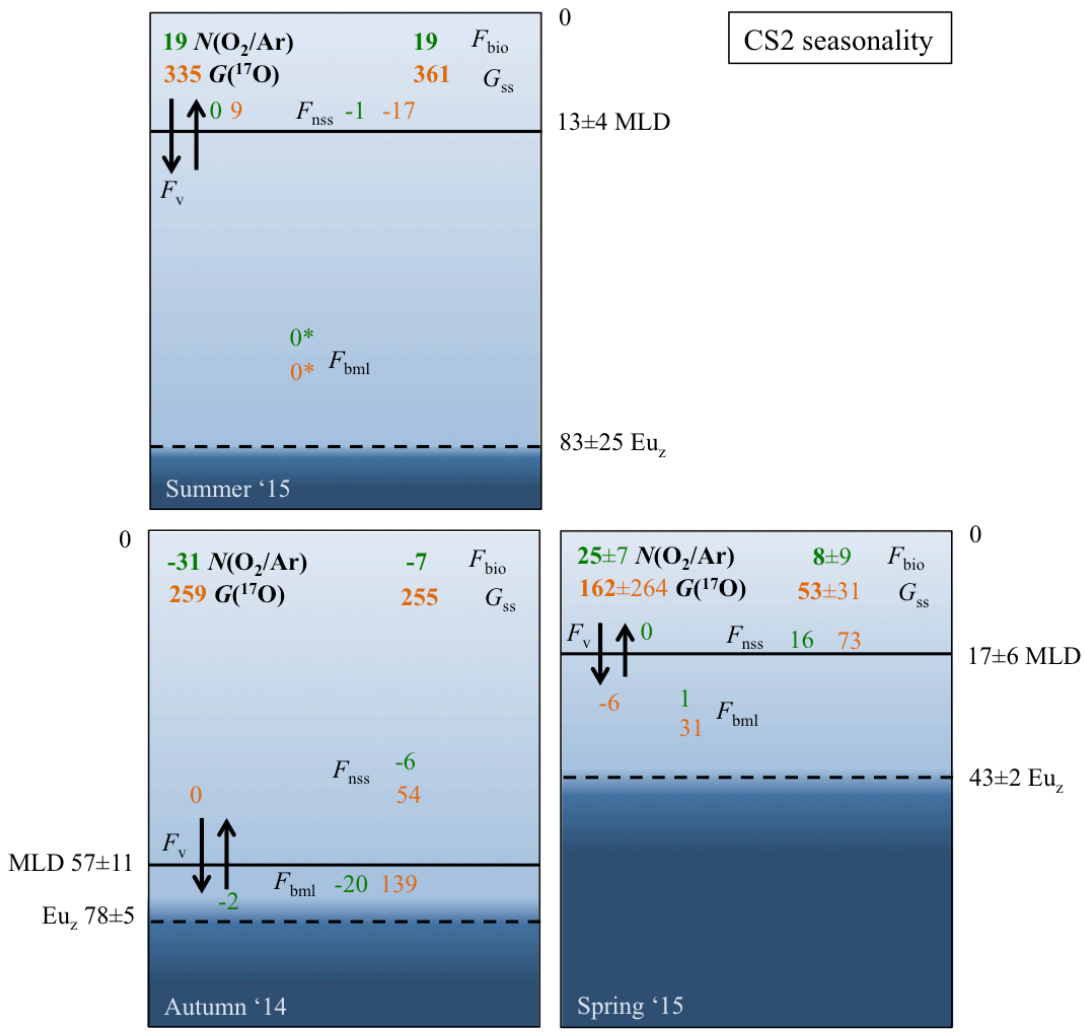

Figure 5.13. Water column representation in station CCS (top) and CS2 (bottom) during summer 2015, autumn 2014 and spring 2015. Depth values of mixed layer depth (MLD) (−), euphotic zone limit (z_{eu}) (--), and deepening of the ML (Δz_{mix}) (-·-) are shown outside the profiles (mean±sd). Gradient blue colour represents extinction of light with depth. Values of F_{bio} and G_{ss} correspond to steady state production until the mixed layer depth. $N(O_2/Ar)$ and $G(^{17}O)$ correspond to non-steady state production until the z_{eu}. Non-steady state terms (F_v, F_{nss}, F_{bml}, F_e) calculated from O_2/Ar in green and from triple oxygen isotopes in orange. (*) Show data removed due to large uncertainty.

5.3.4 Seasonal variations of $^{17}\Delta$ and $\Delta O_2/Ar$ in the water column.

The $^{17}\Delta$ values depth profiles change in every season. The highest surface values occur in spring and summer. In spring, $^{17}\Delta$ values are higher at the surface and decrease with depth. $^{17}\Delta$ values in summer are similar to spring ones in the surface but increase sharply with depth creating a subsurface maximum below the mixed layer and decreasing rapidly over the next 10 m below. $^{17}\Delta$ values in autumn are lowest near the surface and increase with depth. In contrast to the spring depth profile, in autumn the maximum value is at the bottom and the lowest value at the surface.

$\Delta O_2/Ar$ values generally decrease with depth. Depth profiles of $\Delta O_2/Ar$ follow similar patterns than $^{17}\Delta$ in spring and summer, higher values in the mixed layer in spring and subsurface maximum in summer. However, $\Delta O_2/Ar$ and $^{17}\Delta$ pattern are inverted in autumn. Surface values are close to 0 and decrease with depth to negative values. Overall, $\Delta O_2/Ar$ values are higher in spring, followed by the summer and minimum in autumn (Fig. 5.14).

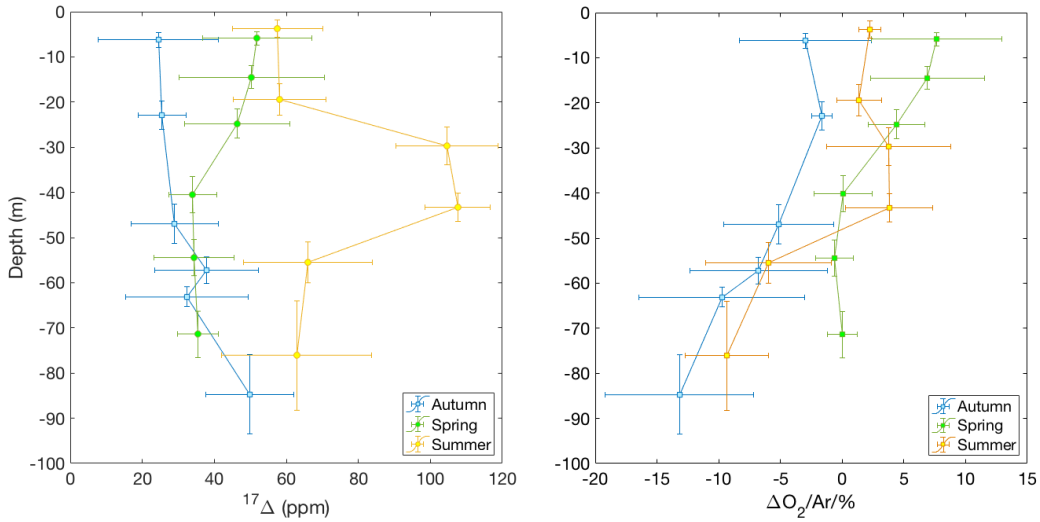

Figure 5.14. $^{17}\Delta$ and $\Delta O_2/Ar$ depth profiles at CCS in spring (yellow), summer (orange) and autumn (blue). Horizontal error bars depicted the standard deviation from the mean value at certain range of depth indicated by the vertical bars.

5.3.5 Seasonal *f* ratio

The $f(O_2)$-ratio was determined by linear regression of F_{bio} against G_{ss} (Fig 5.15). I used F_{bio} and G_{ss} instead of $N_{eu}(O_2/Ar)$ and $G_{eu}(^{17}O)$, because the former does not allow to represent the entire sampled area (on and off shelf), neither from the beginning to the end of the sampled period. Similar but weaker relationship (mainly in summer) was found when using $N_{ml}(O_2/Ar)$ and $G_{ml}(^{17}O)$ (Fig 5.16).

In chapter 4, I showed different correlations and slopes (α) for samples taken on or off the shelf during the spring season. There was no similarly strong correlation in the other two seasons (Fig 5.15). Positive correlation was found in summer 2015, with similar slopes in samples on and off the shelf (R^2 = 0.42, α = 0.045 and R^2 = 0.39, α = 0.030 respectively). Samples from summer 2014 show high scatter and therefore a weak relationship (R^2 = 0.04), but has been plotted together with samples from summer 2015 to show the general agreement between both summers. A negative correlation was found in autumn, with similar slopes in samples on and off the shelf (R^2 = 0.54, α = -0.071 and R^2 = 0.23, α = -0.080 respectively). In spring, a positive correlation was found with different slopes on and off the shelf (R^2 = 0.90, α = 0.23 and R^2 = 0.64, α = 0.060 respectively). To get an approximation of total biological production that is available for carbon export F_{bio} and G_{ss} where converted to carbon as f_C(historic) = N_C / $P_C(^{14}C;\ 24\ h)$ (Marra, 2002, Laws, 1991) or $f_C(O_2)$ = N_C / $G_C(^{17}O)$ (Hendricks et al., 2004, Laws, 1991). In summer, the f_C(historic) and $f_C(O_2)$ for the whole shelf were(0.10±0.08) and (0.05±0.04) respectively. In autumn the f_C(historic) was (-0.13±0.14) and $f_C(O_2)$ (-0.07±0.07). In spring the f_C(historic) for the whole shelf was (0.34±0.23) and $f_C(O_2)$ was (0.17±0.12).

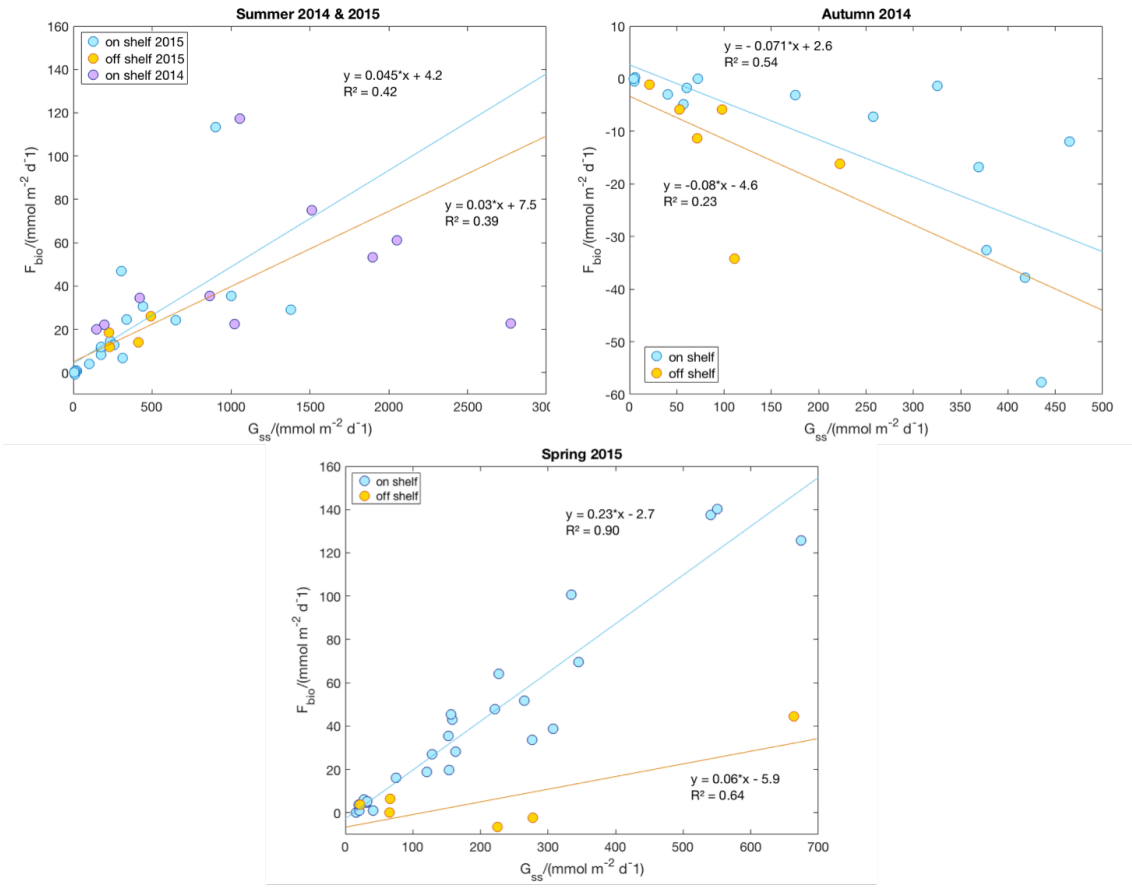

Figure 5.15. F_{bio} vs. G_{ss} from CTD samples in summer 2014 and 2015, autumn 2014, and spring 2015. Summer 2014 & 2015: Linear regressions for samples on the shelf (blue circles and line; $R^2 = 0.42$) and off the shelf (orange circles and line; $R^2 = 0.39$) in summer 2015. Violet circles are on shelf samples in summer 2014. Autumn 2014: Linear regressions for samples on the shelf (blue circles and line; $R^2 = 0.54$) and off the shelf (orange circles and line; $R^2 = 0.23$). Spring 2015: Linear regressions for samples on the shelf (blue circles and line; $R^2 = 0.90$) and off the shelf (orange circles and line; $R^2 = 0.64$).

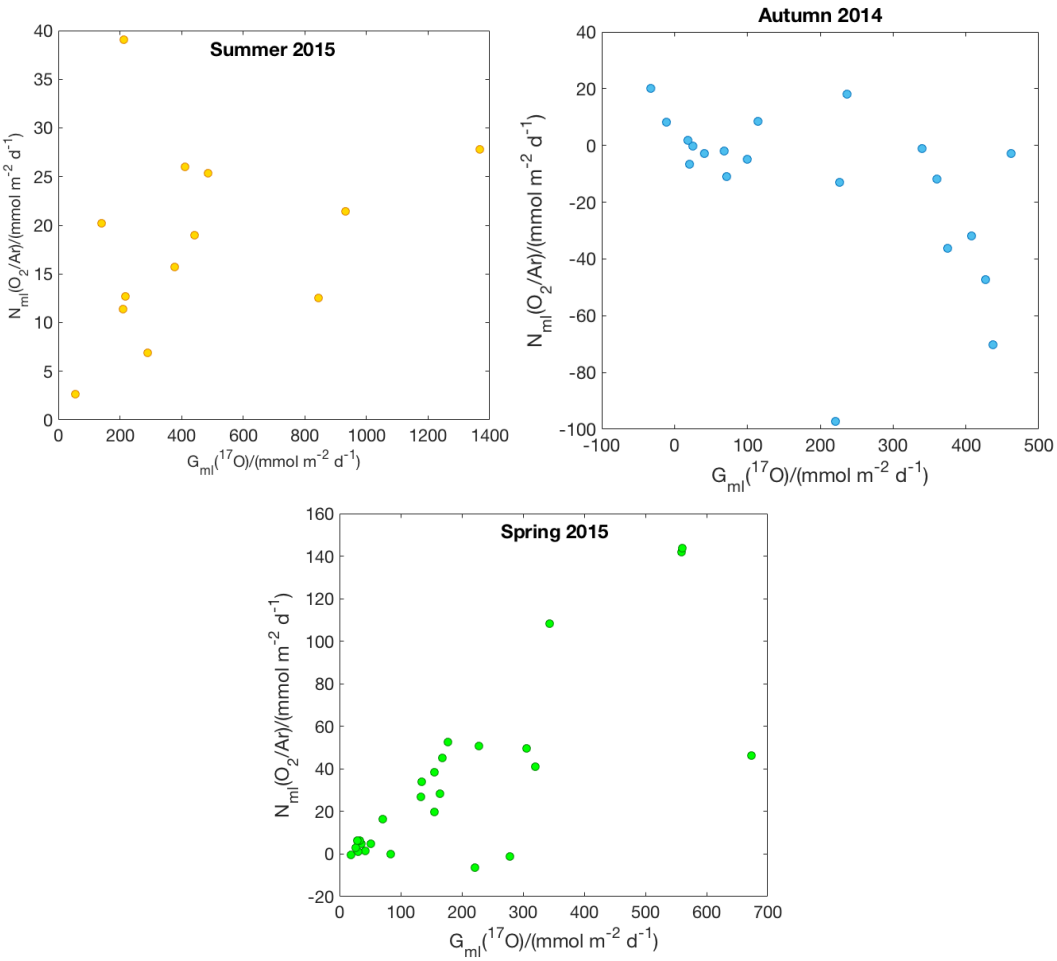

Figure 5.16. $N_{ml}(O_2/Ar)$ vs. $G_{ml}(^{17}O)$ from CTD samples in summer 2014 and 2015, autumn 2014, and spring 2015.

5.4 Discussion

5.4.1 Seasonality of biological production patterns

From $^{17}\Delta$ and $\Delta O_2/Ar$ depth profiles, it is possible to get information about the seasonal variations in biological production in the shelf sea. The autumn decrease in $^{17}\Delta$ in the surface suggests that strong winds ventilate the surface, bringing the $^{17}\Delta$ signal closer to atmospheric equilibrium values. $^{17}\Delta$ below the mixed layer is higher than at the surface because of the absence of air-sea gas exchange and gross production remaining

"trapped" below the mixed layer. Gross production in deeper layers is possible when the euphotic zone is deep enough to permit photosynthesis in deep waters rich in nutrients.

ΔO_2/Ar tells us how much of this biological oxygen remains in the water column after respiration. In autumn, surface respiration is greater than production, showing heterotrophic conditions. The effect of respiration increases with depth, because of the absence of surface ventilation. Therefore, autumn waters in the Celtic Sea are clearly net heterotrophic. The water column was not fully mixed during the sampling time, but less stratified. Previous studies shows that the water column gets fully mixed in winter (Sharples et al., 2013).

In spring, the water column became more stratified, due to solar surface irradiance and weakening of wind stress. The spring bloom was reflected by the highest surface $^{17}\Delta$ signal. Coming from heterotrophic conditions, the $^{17}\Delta$ increase is the result accumulating gross production. Winter nutrients available permit optimum conditions for photosynthesis. These can be seen by the ΔO_2/Ar positive values that decrease. A subsurface Chl *a* maximum below the mixed layer shown by the CTD fluorometer (Figure 5.17) was clearly detected by the $^{17}\Delta$ biological signal in summer. Surface and deep $^{17}\Delta$ values are very similar, only slightly lower in the surface due to ventilation (Wilhelm et al., 2004) that doesn't affect deep samples below the mixed layer. Interestingly, respiration seems to be stronger in summer than in spring or even winter, especially in the deeper layer. This was also found by Haskell et al. (2017) at the beginning of summer in another coastal areas the Southern California Bight. ΔO_2/Ar was lower than in spring but still autotrophic for the majority of the water column and heterotrophic below the subsurface oxygen maximum.

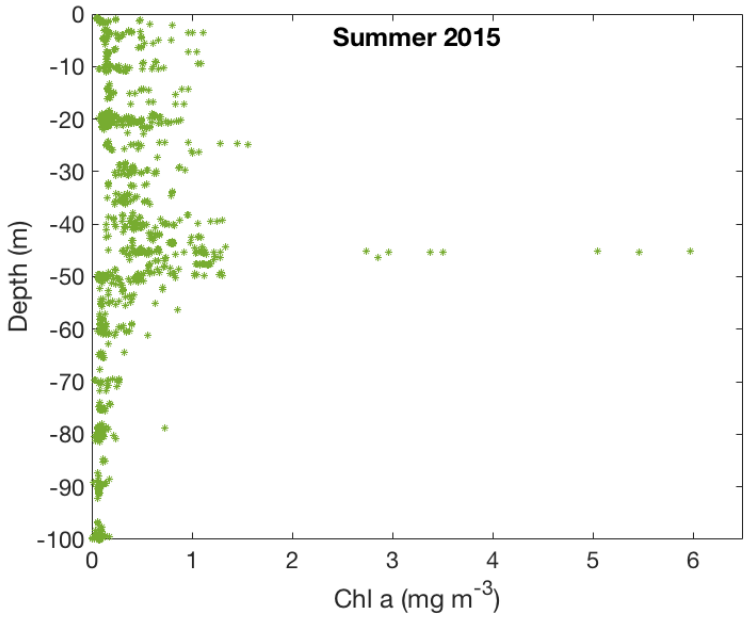

Fig 5.17. Vertical profiles of chlorophyll (Chl *a*) during summer 2015 showing subsurface Chl a maximum around 45 m depth.

5.4.2 Production rates in shelf seas

Although winds and non steady state terms can strongly alter quantitatively the calculation of production rates, the general seasonal patterns seen in $^{17}\Delta$ and $\Delta O_2/Ar$ are conserved well. The calculation for the euphotic zone is the more complete one, but reduces the spatial resolution. The remaining uncertainty in the calculation of production until the euphotic zone comes from the lack of horizontal advection calculation and current velocity measurements. Therefore, when logistically possible, (e.g. revisiting the same station two times and/or doing parallel sampling) biological production should be better characterised by including production in the euphotic zone when it is deeper than the mixed layer depth.

During this study, it was not possible to sample the same station twice on the inner shelf Celtic Sea during summer and autumn. However, for the autumn season, biological production in the Celtic Sea is actually well reflected by mixed layer depth-based productivity rates because z_{eu} and z_{mix} are almost coincident. This calculation also has the advantage of reduced measurement uncertainties compared with $G_{eu}(^{17}O)$, albeit may have higher systematic uncertainties because of the omission of certain terms in the

calculation. In summer, z_{eu} was deeper than the z_{mix}. Therefore, $G_{eu}(^{17}O)$ and $N_{eu}(O_2/Ar)$ should be used,. However, the lack of horizontal transport could have dramatically affected our apparent production measurements below z_{mix}. Apparent negative values of gross production highlight the likely influence of horizontal transports. Such negative values have also been found recently by Haskell et al. (2017). In Haskell's study, the main reason for these negative values was associated to entrainment, transport between layers and change in isotopic composition between samplings.

For the present study there are two plausible hypothesis: 1) the influence of different water mass due to strong currents below the mixed layer that would change the isotopic composition and 2) bias during sampling. The first hypothesis agrees with Haskell et al. (2017) as I also found association of entrainment with lower isotopic signal waters (represented by F_{bml}) in negatives values of F_{nss} during autumn and summer seasons. The second hypothesis applies specially to the summer sampling. The calculation of gross production below the mixed layer is challenging because, while any sample within the mixed layer should have the same value, samples taken below the mixed layer don't. A gradual decrease in Chl *a* and oxygen concentrations just from below the mixed layer depth is normally seen in winter and spring profiles, but not in summer when a peak in Chl *a* and oxygen below the mixed layer was found. This peak is not always constant with time and depth, and sometimes only one or two meters wide. Discrete samples taken from 20 L-Niskin bottles collect water from a specific depth but at a resolution of about 2 m. That means that a high photosynthetic isotopic signal from thin layers may be missed by taking samples just one meter below the peak and therefore the measured values would be "diluted" by a low photosynthetic signal during the sampling process. $^{17}\Delta$ from this sample would still have a $^{17}\Delta$ value above equilibrium, but because the non steady state terms are $d^{17}\Delta/dt$, if the first sample is taken at the subsurface maxima and the second not exactly there or under the influence of a difference water mass, it is possible to obtain negative gross production values as seen here and in Haskell et al. (2017). Entrainment would mix this low production signal to the mixed layer, which its isotopic composition is also affected by ventilation.

A few studies have measured biological production in the Celtic Sea, using ^{14}C, ^{13}C, ^{18}O, O_2 incubation methods and FRRf as *in situ* technique (Robinson et al., 2009, Rees

et al., 1999, Joint et al., 2001, Hickman et al., 2012, Poulton et al., 2014, Daniels et al., 2015, Joint, 1986). (Robinson et al., 2009) made an exhaustive comparison of 8 biological production estimation methods and found great discrepancies between them. As far as I am aware, there are no other publications of biological production measured with triple oxygen isotopes and O_2/Ar in the Celtic Sea, therefore, further comparison with other methods should be taken with care. Values measured from other studies in mg of C have been converted to mmol of O_2 for comparison with this study and are detailed below.

Net community production and gross production during the spring season are within the wide range of values reported for the European shelf (Daniels et al., 2015, Robinson et al., 2009, Rees et al., 1999, Joint et al., 2001, Joint, 1986). Net community production during the summer season is lower than recent values measured around the Celtic Sea (63 to 180 mmol m^{-2} d^{-1}) measured by Poulton et al. (2014) and one order of magnitude higher for gross production compared to estimates from Hickman et al. (2012) (38 to 88 mmol m^{-2} d^{-1}). As mentioned above, this can be due to discrepancies between methods or due to changes in the efficiency of the biological pump that suggest higher gross production and respiration in summer than in previous years. In summer 2005 and 2011, years in which Poulton et al. (2014), Hickman et al. (2012) studies were conducted, sea surface temperature was about 13 to 14º C, while for this study (summer 2015) SST was about 16º C. A recent experiment has shown that an increase in temperature can increase carbon fixation and bacterial respiration (Arandia-Gorostidi et al., 2016). Field summer data from this study compared to previous ones seems to be consistent with the lab experiment of Arandia-Gorostidi et al. (2016), although more years of data would be needed to corroborate a change in the Celtic Sea biological pump due to specific changes in temperature, nutrients, etc.

5.4.3 Seasonal *f*-ratio

The efficiency of the biological pump can be expressed by the *f* ratio, which is a metric of the carbon fraction that is available for export.

F_{bio} and G_{ss} from the three cruises can be used to evaluate the efficiency of seasonal export from the mixed layer. The uncertainty in the F_{bio} and $G_{ss}(^{17}O)$ calculation that comes from the wind speed parameterisation do not affect to the ratio (F_{bio} / $G_{ss}(^{17}O)$) because it uses the same wind parameterization in both terms, therefore $f(O_2)$ is independent of the wind uncertainty. $f(O_2)$ in summer, autumn and spring clearly show that the efficiency of the biological pump changes seasonally. Higher values of f_C(historic) in spring suggests that in this season respiration is low and therefore a large proportion (34 %) of organic matter is available for export. As seen in chapter 4, there were two different $f(O_2)$ ratios in spring, with values much higher on the shelf sea than on the shelf edge. This feature was not found in the other two seasons.

In autumn, biological production is more homogeneous geographically. Therefore, it is not surprising to have the same $f(O_2)$ on and off the shelf.

However, in summer, when I detected geographic heterogeneity, similar $f(O_2)$ values on and off the shelf could be an artifact due to undersampling bias, because there were only four samples off the shelf and all values are very close to the axis origin. Although the summer 2014 $f(O_2)$ values display high scatter, they follow a similar relationship as the summer 2015 $f(O_2)$ values suggesting little biological interannual variability. f_C(historic) values in summer show that the amount of carbon available for export is 1/3 less than in spring, suggesting that 90% of the gross production is supported by remineralised organic matter in the mixed layer.

In autumn, $f(O_2)$ was negative, showing that respiration was more intense in zones where there was more gross production. This is in agreement with the vertical profiles of $^{17}\Delta$ and ΔO_2/Ar in autumn, where the oxygen accumulated in the deep layer is rapidly respired likely due to the absence of light. Subsequently, the f_C(historic) shows that there is no carbon available for export in autumn and any production is supported by recycled organic matter.

$f(O_2)$ values of this study were compared with the North Pacific values, obtained by using the same method (Palevsky et al., 2016). The $f(O_2)$ values were higher in spring for the Celtic Sea but lower in summer and autumn compared to the North Pacific

values (0.13 – 0.20 in autumn, 0.8 – 0.11 in spring, 0.9 – 0.15 in summer). This shows that the biological carbon pump in shelf seas can potentially export more carbon than the open ocean during the spring bloom, which is in agreement with the global carbon sink distribution (Muller-Karger, 2005).

$f(O_2)$ values during the spring bloom are not the highest recorded in coastal zones. Goldman et al. (2015) measured $f(O_2)$ values (0.25 – 0.60) in Antarctic coastal zones that are double those found here (0.23). Slightly higher values (0.35) were estimated in the subpolar North Atlantic near Iceland (Quay et al., 2012). Seasonal $f(O_2)$ values in a coastal upwelling region were also higher than those reported here (Haskell et al., 2017). Juranek et al. (2012) estimated $f(O_2)$ on two spring and summer North Pacific meridional transects. Their values were similar to those found here, spanning from 0.03 to 0.20. Seasonality seems to be more pronounced in the Celtic Sea and other coastal regions than in the open ocean, and generally follows the same pattern of highest photosynthetic energy conversion by phytoplankton in spring, less in summer and lowest in autumn/winter (Haskell et al., 2017, Quay et al., 2010).

5.5 Conclusion

The spring and the summer seasons were net autotrophic, while autumn was net heterotrophic. Although the sampling programme didn't cover the whole year, the variability between seasons was well characterised and the magnitude of the values measured suggests that the Celtic Sea is a net autotrophic system on an annual basis. Different ways of calculating net fluxes generally agree and are of the same order of magnitude. Nevertheless, the differences and statistical measurement uncertainties increase when I include terms other than air-sea exchange fluxes in the calculations.

Steady-state mixed layer fluxes ($G_{ss}(^{17}O)$ and F_{bio}) can deviate by up to 50 % from estimates that cover the euphotic zone and that account for non-steady state inventory changes, entrainment and vertical eddy diffusion, depending on season and conditions. These discrepancies are due to two main reasons: 1) the biological spatial heterogeneity of the Celtic Sea requires high-resolution measurements. Reducing the sampling area to the Central Celtic Sea and shelf edge underestimates the total biological production

generated in the entire shelf. 2) More complete calculations entail higher overall measurement uncertainty and widen the confidence intervals for the final values, while at the same time approaching the values based on steady-state approximations.

Interestingly, the seasonal variations are consistent regardless of the calculation used. Net community production is highest in spring and gross production is highest in summer. Both stations CCS and CS2 show net autotrophic conditions, while autumn is clearly net heterotrophic. Hence, this study characterised the seasonal biological patterns, quantified non-steady state production rates and showed that the biological pump makes the Celtic Sea a net carbon sink. Further studies in the Celtic Sea would benefit from higher temporal and spatial data coverage, in order to accurately understand the rates and efficiency of carbon export for the whole shelf.

Chapter 6. Comparing two powerful aquatic gross production techniques in physically complex waters: oxygen isotope signatures versus electron transfer rates.

6.1 Introduction

Quantifying net community production, gross production and respiration, and how they vary over space and time, underpins our capability to predict changes in the marine environment (e.g. water quality, fisheries and atmospheric CO_2 uptake from the sea). Not only do these processes fundamentally represent the "health" of the planet, but also the blue economy. As demonstrated in chapters 4 and 5, shelf seas are physically complex and highly dynamic. Improved understanding requires high resolution primary production measurements, such as in situ (or in line surface sampling) measurements through methods such as MIMS (Kaiser et al., 2005), fluorometry and bio-optics (Moore et al., 2003), or remotely through ground-truthed satellite imagery. While MIMS has been used to measure $\Delta O_2/Ar$ to estimate net community production (Kana et al., 1994, Tortell, 2005), gross oxygen production was measured by discrete samples, lacking the high time resolution of MIMS, fluorometry or satellite imagery. Since Luz and Barkan (2000) first described the approach for estimating gross production of photosynthetic oxygen, based on the isotopic ^{17}O excess ($^{17}\Delta$) of dissolved oxygen (DO) of seawater, numerous studies have used their approach. Isotopic excess of delta 17 oxygen is an indicator of oxygen produced during the photosynthesis, and when accounting for gas transfer velocities and at steady state, is equal to gross oxygen production $G(^{17}O)$ (mmol m^{-2} d^{-1}). It is possible to infer gross production in terms of carbon by applying a photosynthetic quotient (PQ), defined as the ratio of CO_2 uptake to O_2 production (Marra, 2002, Hendricks et al., 2004). This technique is been increasingly used as it is free from incubation biases (see Chapter 2, section 2.4), however, it has the limitations of discrete sampling. Continuous measurement would cover better the variation in physically complex waters.

As explained in section 1.1 primary production occur through phytoplankton photosynthesis, which direct product is gross primary production. The photosynthesis reaction needs the presence of light to produce O_2. This process involves a series of photochemical reactions in the light harvesting complex. The first complex is the photosystem II (PSII). In the PSII, the energy of light is used on the O_2 evolving complex to split or oxidize the water molecule. During the splitting of H_2O, O_2 is released and four electrons are extracted and passed down to the electron transport chain that fuel the photosynthesis. Therefore, an alternative method for measuring gross O_2 production is through active fluorometry, and notably Fast Repetition Rate fluorometry (FRRf) (Kolber et al., 1998). This bio-optical technique specifically yields electron transport rates (ETR) of PSII at frequencies of seconds with unprecedented high spatial and temporal resolution (Kolber and Falkowski, 1993). Numerous studies have compared FRRf-based ETR with corresponding measurements of carbon uptake, but few have compared them with O_2 evolution (Suggett et al., 2009, Sarma et al., 2005, Suggett et al., 2001, Hancke et al., 2015, Robinson et al., 2009). Comparisons studies with carbon uptake have shown that ETR derived from FRRf can be converted to carbon fixation rates (C_{uptake}) if the electron requirement for carbon fixation (K_c) is known, where K_c = ETR / C_{uptake}. The calculation of K_c has led to different values (Kolber and Falkowski, 1993, Suggett et al., 2001, Suggett et al., 2009). More recent studies show that discrepancies could be due to the dependency of K_c on environmental variables, but the reasons for this variability remain unclear (Zhu et al., 2016), highlighting the need for more studies. The most recent study suggests that there is a co-variability between K_c and light availability (R^2 = 0.70 – 0.81) when including size of phytoplankton groups in the algorithms for the calculation of K_c (Zhu et al., 2017). However, these authors concluded that additional physico-chemical conditions needs to be included to effectively improve the robustness of the models.

In spite of the interests in reconciling FRRf with carbon-based measures of productivity, few studies have attempted to reconcile FRRf with gross production measurements, which should more directly scale with the ETRs. Numerous processes act to decouple ETRs from C-uptake (e.g. Suggett et al. 2009) whereas fewer processes, e.g. cyclic flow around PSII, act to decouple ETRs from gross O_2 production. Sarma et al. (2005) compared gross production from FRRf and triple oxygen isotopes for a few

discrete samples and found similar tendencies between both. Lefebvre et al. (2007) found a linear relationship between classical oxygen evolution and ETR in single diatom culture experiment. Fujiki et al. (2008) attempted to estimate in situ daily gross oxygen production from an underwater profiling buoy system, but no relationship with independent production measurements was found. There appear to be no studies on ETR requirements for gross oxygen production in physically complex systems like shelf seas.

The aim of this study is to determine if K_{O2} (e^- requirement for carbon fixation) can be calculated from $^{17}\Delta$ and ETR by establishing a relationship between two free-from-incubation gross production methods using profile samples taken in a European shelf sea during the spring season of 2015. Understanding how the environment regulates K_{O2} would therefore facilitate estimates of gross production using FRRf technique as a tool to provide the same spatial resolution as performed with the MIMS and similar accuracy as with the isotopic oxygen method. We explored the relationship of ETR against $G(^{17}O)$ in order to calculate the first *in situ* K_{O2} algorithm.

6.2 Material and methods

6.2.1 Study area

The sampling area for this study was the Celtic Sea, as described in previous chapters. Samples were collected from 27 CTD casts on board of the RRS Discovery during the DY029 cruise, as part of the NERC Shelf-Sea Biogeochemistry (SSB) programme. Sampling was conducted in April 2015 to coincide with the spring bloom. As seen in chapter 5, the Celtic Sea was much more heterogeneous during the spring period than during autumn or summer. As such, this season potentially provided the broadest range of environmental conditions to examine the dependence of K_{O2} on combinations of different environmental variables.

6.2.2 Methods

Gross oxygen production estimated from photosynthetic isotopic signatures

Sampling and calculation of the isotopic method is briefly described here. Full details are given in Chapters 2 and 3, respectively. Discrete samples were collected from Niskin bottles fired within and below the mixed layer. Following Emerson et al. (1995), 330 ml glass vessels (Louwers Hapert) with Viton O-rings stopcocks were evacuated and poisoned with 100 µl of $HgCl_2$ saturated solution before sampling. Samples were carefully drawn into the vessel by overflowing the side-neck, to avoid atmospheric oxygen contamination, filling the vessel up to about ~ 66% full. Samples were prevented from leaking by filling the side-necks with water and capping (Luz et al., 2002). All samples were extracted and stored in sealed glass tubes with molecular sieves within one month from the end of the cruise. We extracted the samples and removed N_2O, CO_2, and water vapour by gas chromatography before measuring $^{16,17,18}O$ in the mass spectrometer (Barkan and Luz, 2003).

6.2.3 Calculation of $^{17}\Delta$ & G(^{17}O)

$G(^{17}O)$ was calculated via analysis of triple oxygen isotopes (^{16}O, ^{17}O and ^{18}O) from samples measured by spectrometry. Initial work used an approximated equation based on the ^{17}O excess, ($^{17}\Delta$) (Luz & Barkan, 2000). Chapter 3, provides a discussion of the advantages of using a more rigorously derived expression using $\delta^{17}O$ and $\delta^{18}O$ directly (Kaiser, 2011b). However, for the comparison of every ETR value against oxygen isotopic signal, I choose $^{17}\Delta$ instead of the two end-members $^{17}\delta$ and $^{18}\delta$, as the former provides a more manageable single value for comparisons.

$^{17}\Delta$ relates to $^{17}\delta$ and $^{18}\delta$ as $^{17}\Delta \equiv {}^{17}\delta * \gamma\ {}^{18}\delta$ (Thiemens et al., 1995b), where γ is fractionation slope = (0.5179 ± 0.0006) (Luz and Barkan, 2005) (see Chapter 1, section 1.3.1).

As explained in Chapter 1 section 1.5, I used $^{17}\delta$ and $^{18}\delta$ to constrain the $G(^{17}O)$. However, $G(^{17}O)$ can be directly determined from $^{17}\Delta$ according to Luz and Barkan (2000) as $G(^{17}O) = k\, c_{sat}\, (^{17}\Delta - {}^{17}\Delta_{sat})/(\,{}^{17}\Delta_P - {}^{17}\Delta)$, where k is the gas transfer velocity,

C_{sat} is the oxygen in the water at saturation, $^{17}\Delta$ is the measured value and $^{17}\Delta_{sat}$ and $^{17}\Delta_P$ are the values at saturation concentration and the maximum photosynthetic value respectively.

6.2.4 Gross oxygen production estimation by fast repetition rate fluorometry

Measurements were made from discrete water samples collected from the same CTD casts as for triple oxygen isotopes. The discrete water samples were stored in the dark for at least 30 minutes at sea surface temperature to allow for the relaxation of quenching. For sample analysis, each bottle was gently shaken and a cuvette was rinsed twice before filling with 1.5 ml of sample. Samples were measured in order from the deepest to shallowest sampling depths.

A FastOcean (Chelsea technologies group Ltd) FRR fluorometer with an integrated FastAct bench-top unit (CTG), hereafter referred to as FRRf, was used to acquire active fluorescence data and derived physiological parameters. These samples were collected from the same Niskin as those for the oxygen analysis. FastPro 8 (v1.0.55) software (Chelsea technologies Group) was used to program the induction curves and fit the physiological model to parameterise phytoplankton physiology and derive ETRs. The FRRf was programmed with a single turnover protocol to deliver a saturation induction curve of 100 flashlet sequences of 1 μs duration and 1 μs interval. Each induction curve was delivered at 150 ms intervals and the final result recorded was the mean of the sequential induction curves.

Each sample analysed was subject to a rapid light curve (RLC) analysis, which lasted 40 minutes and consisted of 15 light steps ranging from 0 to 1551 μmol photons m^{-2} s^{-1} preceded by an initial 'dark' measurement. The sample was stirred using the FastAct mixer unit every 20s. Filtered seawater samples were measured for each RLC on the FRRf to allow for the correction of background fluorescence. The FastOcean has a water jacket to keep it at similar temperature to the seawater. Lenses were periodically inspected and cleaned with deionised water to avoid biofouling. The calculation of physiological parameters F_o, F_m, σ_{PSII}, and F_v/F_m (see table 6.1) were based on the KPF fitted model (Kolber et al., 1998) and and based on the light chamber data.

Samples were collected in conjunction with other scientist. I used the physiological parameters provided (e.g. Initial fluorescence yield in the dark chamber (F_o) to calculate electron transport rates.

Table 6.1. Definitions of photosynthetic parameters derived from FRRf measurements. Every parameter is for light chamber.

Physiological parameter	Definition
F_o	Initial fluorescence yield in light chamber
F_m	Maximum fluorescence yield in light chamber
σPSII	Effective absorption cross section of PSII in light chamber
F_v/F_m	Potential photochemical efficiency of open reaction centres
α	Initial slope of ETR vs. E
E (µmol photons m^{-2} s^{-1})	Instantaneous irradiance
E_k (µmol photons m^{-2} s^{-1})	Irradiance that represents inflexion from α to saturation E
ETR (µmol photons m^{-3} s^{-1})	Electron transport rate through PSII
K_{O2} (µmol photons mol O_2)	Quantum electron requirement for oxygen
K_d (m^{-1})	Light extinction coefficient
ζ (m)	Optical depth
$^{17}\Delta$ (ppm)	^{17}O isotopic excess

6.2.5 Calculation of ETR & K_{O2}

The absolute ETR was calculated in each sample and for each in situ PAR depth as follows (Suggett et al., 2006):

$$ETR = \alpha E_k \ (1-\exp^{(-E/Ek)}) / 1.567 \ \exp(-0.037\zeta) \quad (6.1)$$

where the numerator is calculated according to the mathematical model of a exponential relationship between E and depth (Webb et al., 1974), $\zeta = K_d$ * depth, represents the optical depth calculated from the light extincion coefficient (K_d) obtained from the model of Beer–Lambert: K_d = Ln (E_0) − Ln (E_z), where E_z is the irradiance at certain depth, E_0 is the irradiance in the surface water.

The $^{17}\Delta$ values within the mixed layer represents the whole mixed layer, therefore to be able to compare ETR and $^{17}\Delta$ values I calculated the integrated ETR (ETR_{int}) at the mixed layer depth (MLD) as $\int ETR dz$, where dz is the differences in depth between samples. Once a relationship between $^{17}\Delta$ and ETR has been found, we can finally calculate the quantum electron requirement for oxygen as:

$$K_{O2} = ETR_{int}/G(^{17}O). \quad (6.2)$$

6.2.6 Statistical analysis

Linear regression analyses were performed with ETR, $^{17}\Delta$, $G(^{17}O)$, Chl *a*, DO, and PAR. To examine for possible relationships between different stations and environmental variables (salinity, temperature, ammonium (NH^+_4), nitrite (NO^-_2), nitrate (NO^-_3), silicate (SiO_4^{4-}) and phosphate (PO_4^{3-}), chlorophyll (Chl *a*), MLD and photosynthetic active radiation (PAR). I performed a multivariate analysis similar to the analytical approach followed by Zhu et al. (2017). Nutrient data were collected and provided by Malcolm Woodward, another project member of the SSB programme. First, a Bray–Curtis similarity matrix was calculated between stations of Log(X+1) transformed environmental variables. Significant groups of samples at a $p < 0.05$ level were determined by the SIMPROF routine. A non-metric multidimensional scaling (nMDS) ordination plot was constructed using the same similarity matrix. SIMPROF groups were indicated on the same plot. Spearman rank order correlations were drawn to infer relationships between the environmental variables and the station location ordination plot. Multivariate analyses were performed using the statistical package PRIMER 6 (Plymouth Marine Laboratory, UK).

6.3 Results

6.3.1 Physicochemical state in the Celtic Sea during the study period

The spring water column was characterised by thermal stratification, with temperatures ranging from 10 to 12º C at the surface and about half degree less below the mixed layer (Fig. 6.1, I). Salinity varied between 34.7 and 35.6, and was vertically homogeneous at the majority of the stations (Fig. 6.1, II). The northern station A was characterised by the lowest salinity (34.7) and was the only station to exhibit salinity stratification. Stratification of the water column during the sampling period was mainly as a result of temperature rather than salinity differences. Chl *a* concentrations were generally high (from 1 to 20 mg m^{-3}) within the mixed layer (22 ± 9 m) (Fig. 6.1, III). One of the profiles went up to 20 mg m^{-3} (green one). This data is not shown because the *x*-axis is set to up 8 mg m^{-3} for the clarity of other profiles. The mean euphotic depth (1% of incident light) (36 ± 16) m was shallower at inner stations due to higher levels of turbidity (data not shown) (Fig 6.1, IV).

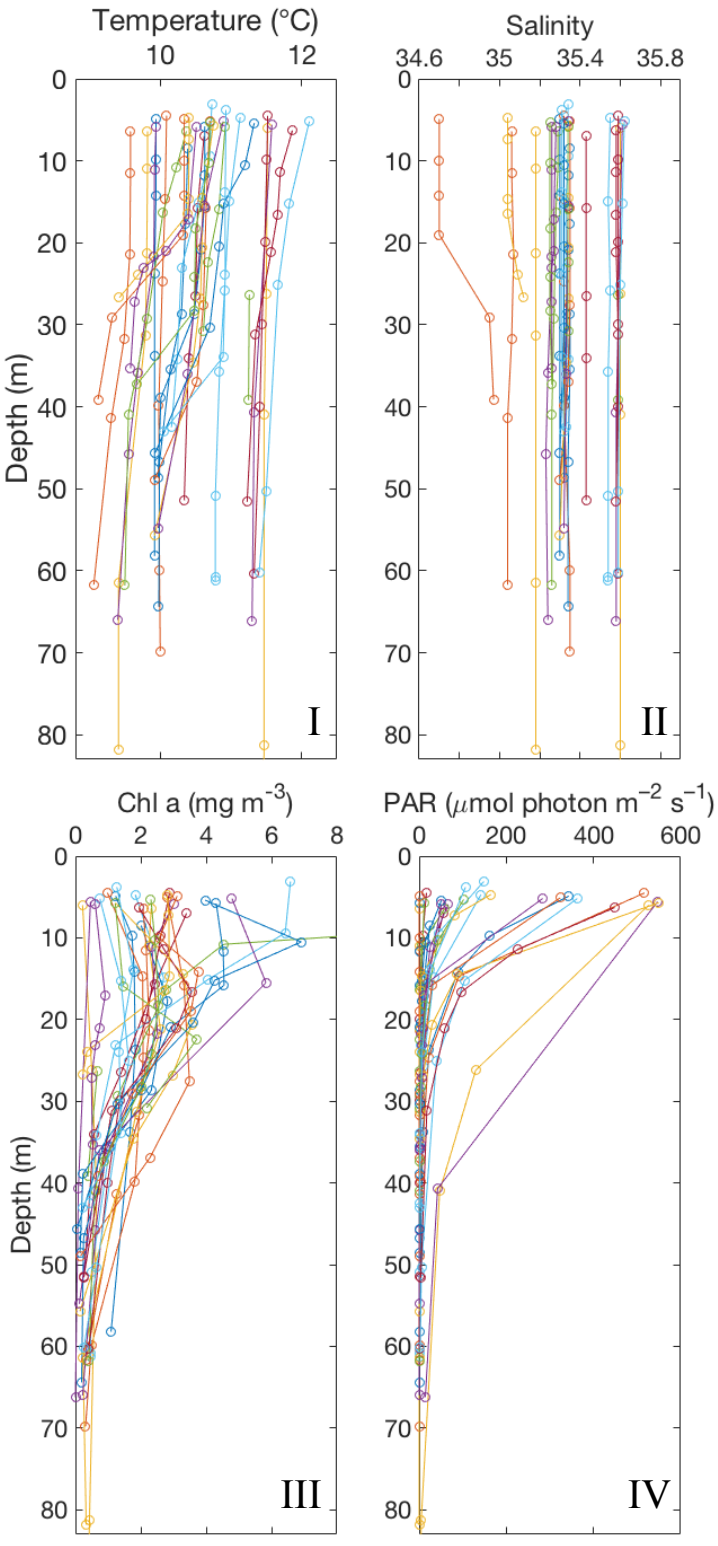

Figure 6.1. Vertical profiles of temperature (I), salinity (II), chlorophyll (III), and photosynthetic active radiation (IV) from 27 stations in the Celtic Sea. Different colours represent different profiles.

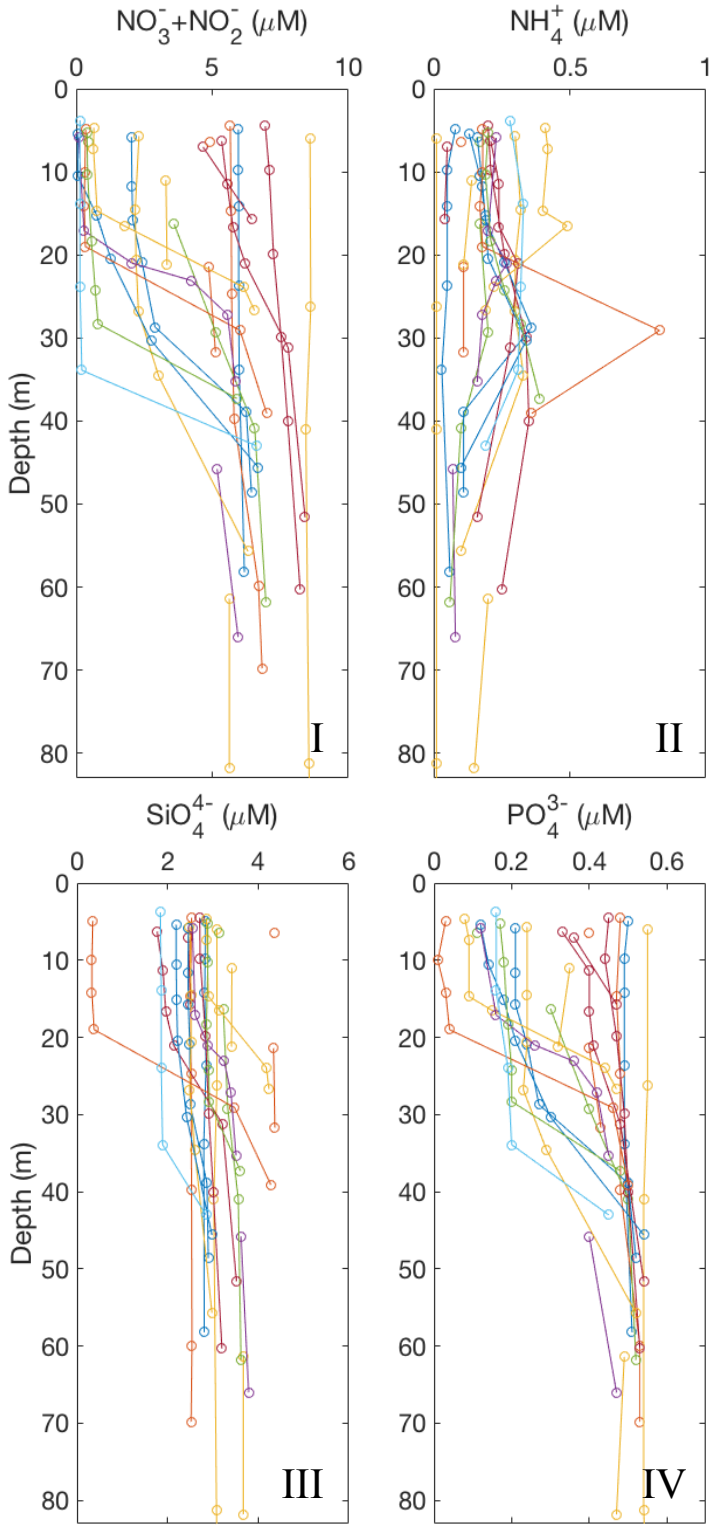

Figure 6.2. Vertical profiles of nitrate + nitrite (I), ammonium (II), silicate (III), and phosphate (IV). The colours represent different profiles.

Inorganic nutrients concentrations (NO^-_3 + NO^-_2, SiO_4^{4-}, and PO_4^{3-}) showed higher values below the mixed layer (Fig. 6.2, I-II-III), while NH^+_4 generally showed the higher concentrations around the mixed layer depth (Fig. 6.2, IV). Mean whole profile concentrations are (4.4 ± 2.8), (0.2 ± 0.1), (2.8 ± 0.8), and (0.4 ± 0.2 µM) for NO^-_3 + NO^-_2, NH^+_4, SiO_4^{4-}, and PO_4^{3-} respectively.

6.3.2 Relationship of FRRf and triple oxygen isotopes with environmental variables

Across all samples, a positive linear relationship ($R^2 = 0.36$) was found between $^{17}\Delta$ and Chl *a*, indicating that across-sample differences in gross production could be generally examined by changes in phytoplankton pigment biomass. We also found a positive relationship, although with some scatter ($R^2 = 0.31$), between $^{17}\Delta$ and DO (Fig. 6.3). This indicates that the biological processes like photosynthesis incorporate oxygen to the water and the scatter reflects physical incorporation, short-term events of low or high production or respiration.

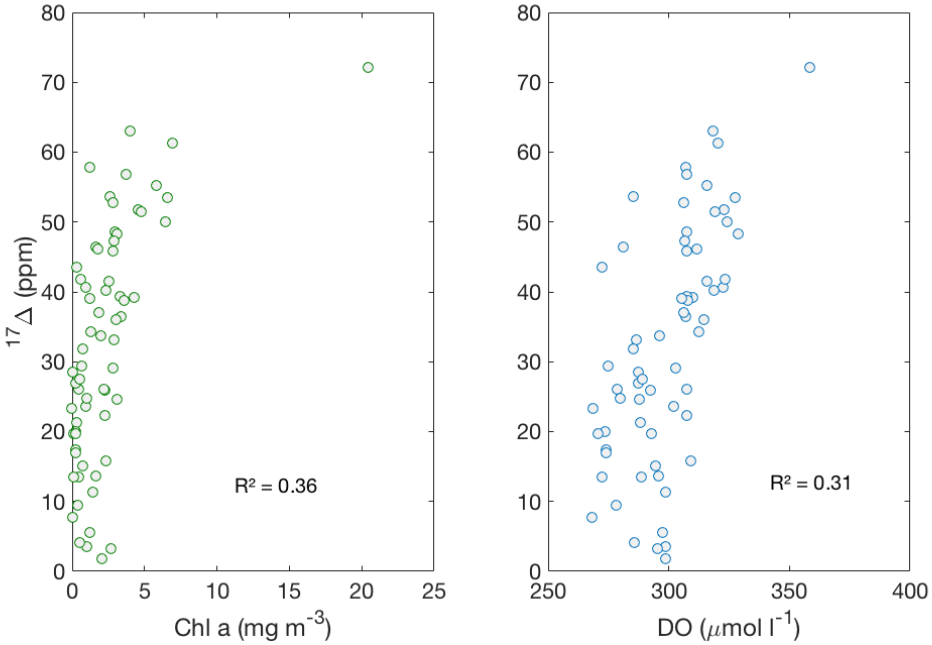

Figure 6.3. Relationship of $^{17}\Delta$ (ppm) with Chl *a* (mg m^{-3}) and DO (µmol l^{-1}).

In contrast to $^{17}\Delta$, ETRs did not vary in a positive (linear) manner with Chl *a* (R^2 = 0.04), and no relationship was observed between ETR and DO (Fig. 6.4). In all cases,

the data point with the higher Chl *a* and DO values deviate from the general relationships.

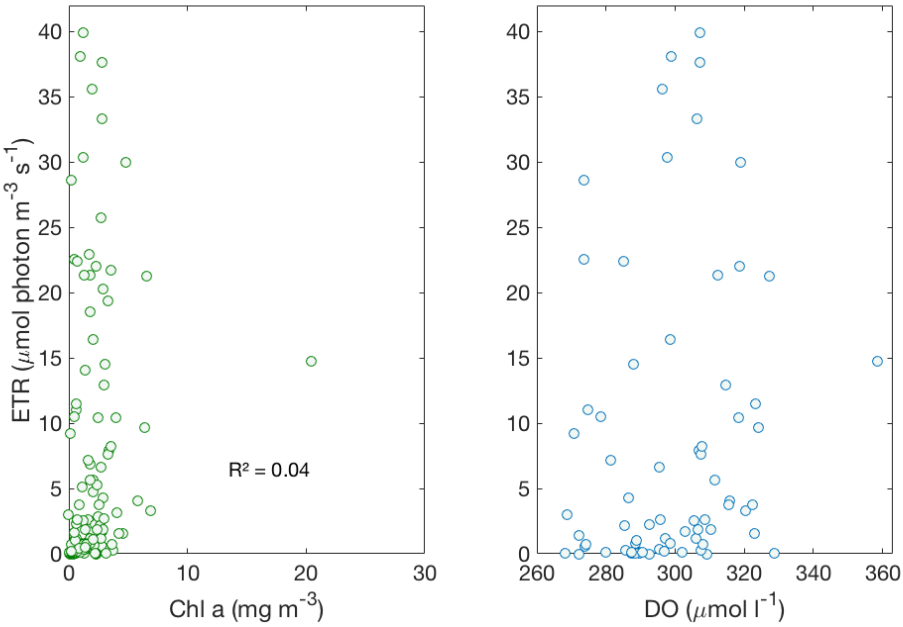

Figure 6.4. Relationship of ETR with Chl *a* (mg m^{-3}) and DO (μmol l^{-1}).

6.3.3 Variability of K_{O2}

Comparison of ETR and $^{17}\Delta$ from all the stations sampled in the Celtic Sea similarly did not yield a significant positive relationship (Fig. 6.5). Since the ratio of ETR and $^{17}\Delta$ gives the electron requirement for gross O_2 evolution (K_{O2}), the lack of trends highlights that no single factor for K_{O2} was apparent for the data set.

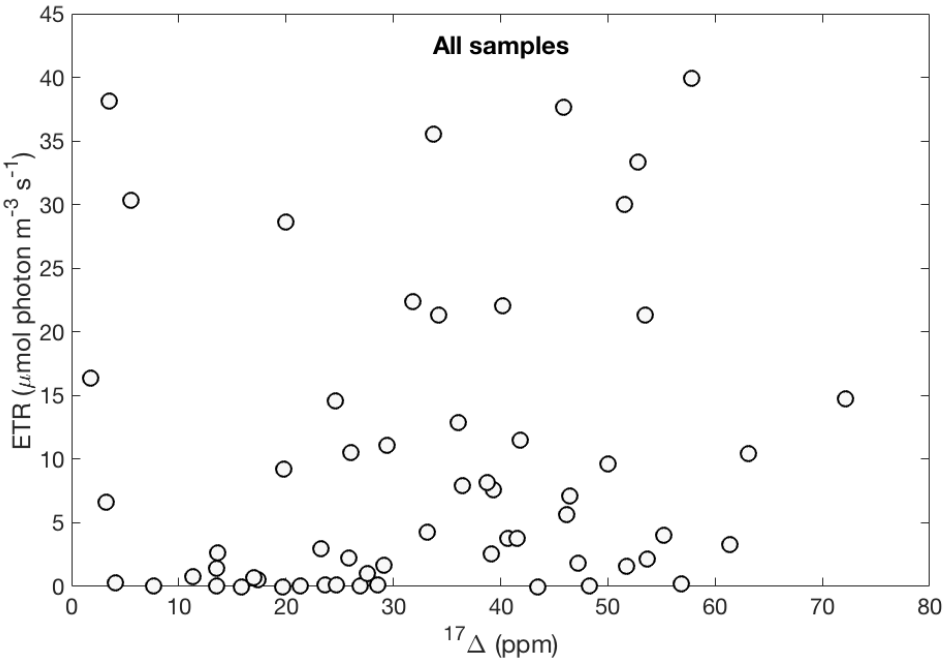

Figure 6.5. ETR µmol photons m^{-3} s^{-1} against $^{17}\Delta$ ppm. Each sample was taken from the same Niskin bottle.

Previous studies comparing ETR and ^{14}C have shown that binning data into common biogeographic conditions enables improved reconciliation between the two measurements (Lawrenz et al., 2013). However, binning the data from this study into different stations (represented by different colours) did not improve the correlation (Fig. 6.6).

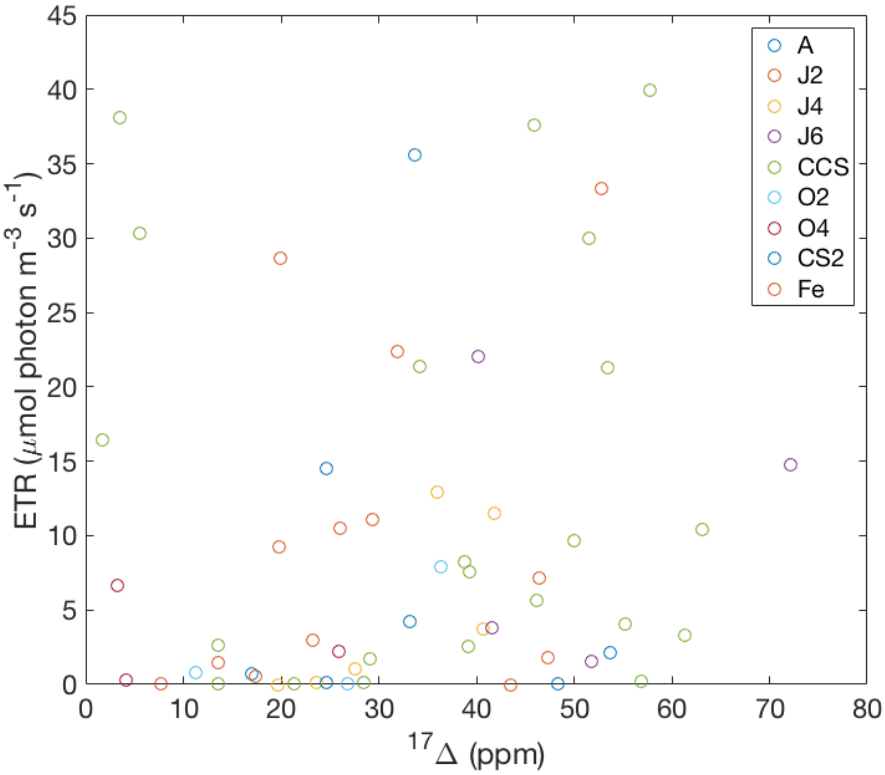

Figure 6.6. Mean ETR µmol photons m^{-3} s^{-1} against $^{17}\Delta$ ppm. The colour represent each sampling station. Each sample was taken from the same Niskin bottle.

To examine why these variables did not reconcile, the data were binned according to time of day. As expected, ETRs are weighted by the available light intensity and hence exhibit a diurnal pattern with highest values around midday. However, $^{17}\Delta$ seems to be almost independent of the time of the day sampled. Higher values are around midday but data is very scattered during dawn and dusk. This is also relatively expected as the $^{17}\Delta$ values represent average production over the residence time of oxygen in the water and short time variations would be "diffused". All samples from all depths are included here (Fig. 6.7).

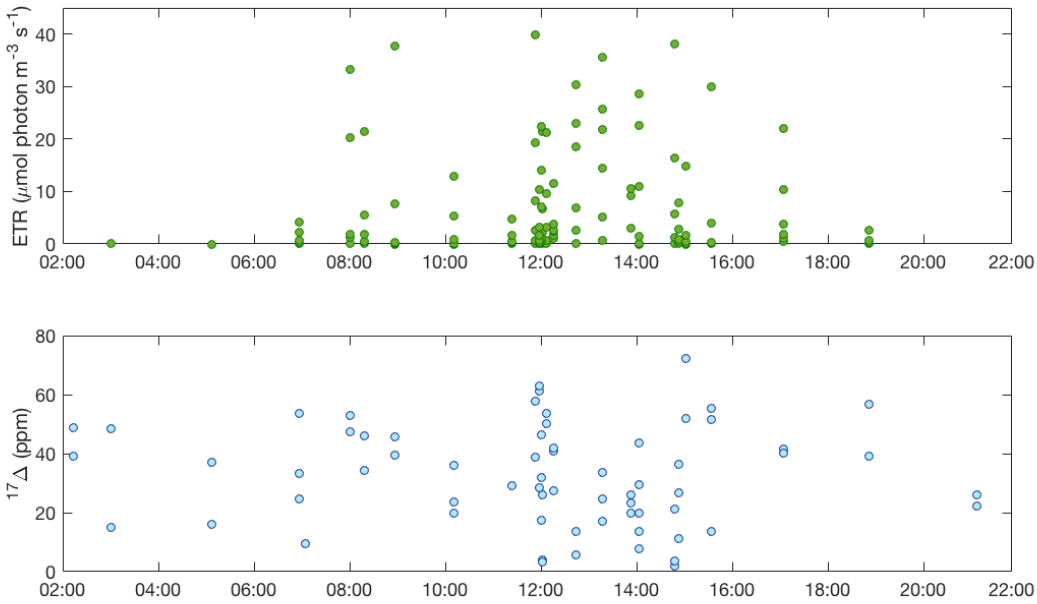

Figure 6.7. ETR µmol photons m^{-3} s^{-1} and $^{17}\Delta$ ppm per time of the day.

Other studies had found a good relationship between ETR and PAR (Zhu et al., 2016). We also made the relationship between ETR and PAR for every sample and depth and found a relationship of R^2 = 0.71 (Fig. 6.8). In contrast no relationship was observed between integrated $^{17}\Delta$ and integrated PAR (data not shown).

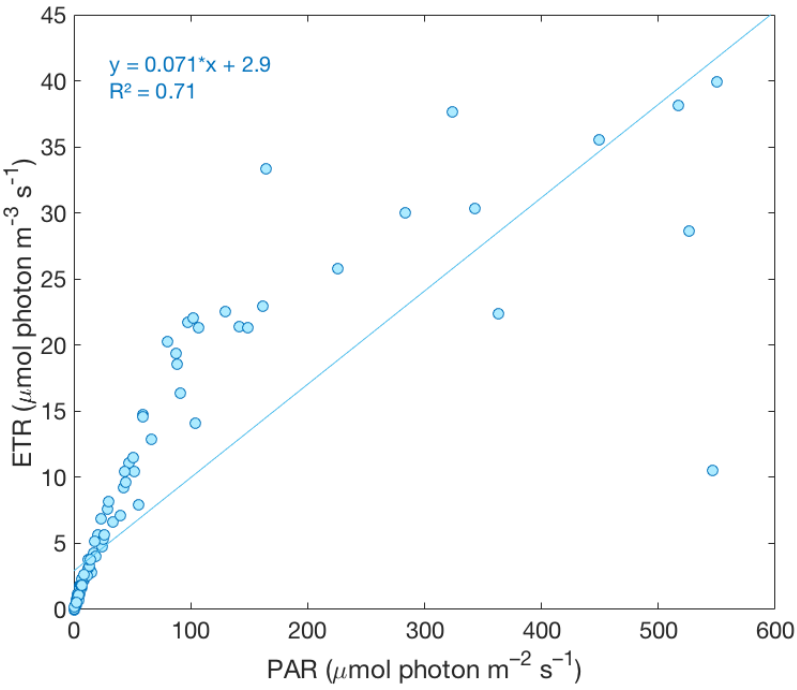

Figure 6.8. ETR_{int} µmol photons m^{-3} s^{-1} against PAR µmol photons m^{-2} s^{-1} at each depth.

The water column showed clear physicochemical differences above and below the MLD (Fig 6.1 & Fig 6.2). However, again further testing to whether K_{O2} variability was driven by depth by considering the mean ETR and $^{17}\Delta$ from the mixed layer only did not yield a significant relationship (Fig. 6.9).

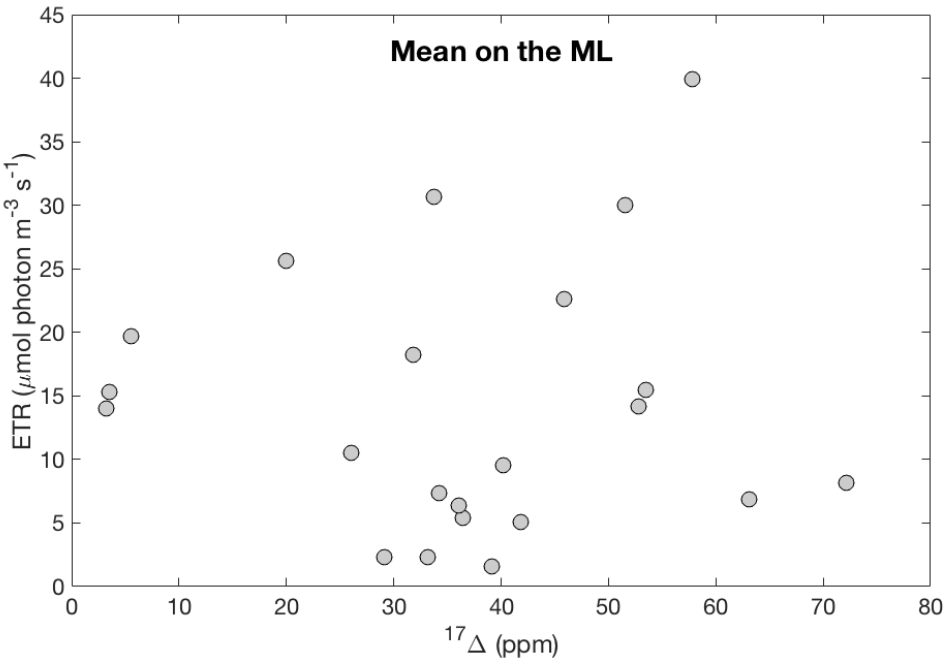

Figure 6.9. Mean values of ETR µmol photons m^{-3} s^{-1} against $^{17}\Delta$ ppm in the mixed layer (ML).

Given the good relationship between ETR and PAR when integrating our samples over the mixed layer (Fig. 6.8), I subsequently integrated ETR measurements over the mixed layer and applyed equation 6.2 to the isotopic oxygen measurements to calculate gross production measurements, also integrated production in the mixed layer. However, these depth integrated values did not improve the relationship between ETR_{int} and $G(^{17}O)$ (Fig. 6.10).

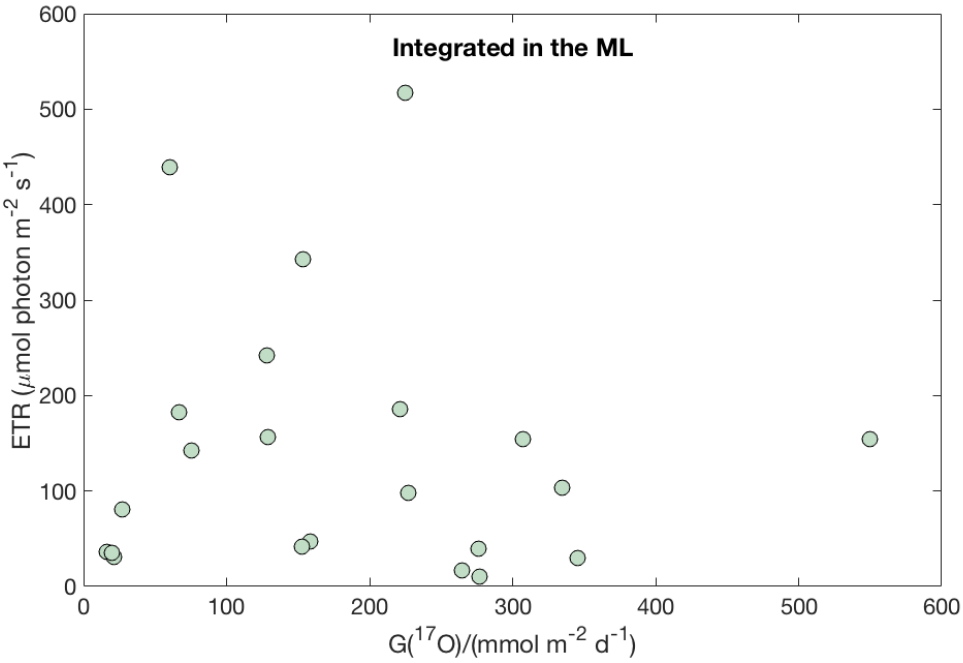

Figure 6.10. ETR_{int} µmol photons m^{-2} s^{-1} against $G(^{17}O)$ mmol m^{-2} d^{-1} in the mixed layer (ML).

Finally, to test if the variability of K_{O2} was a result of evolution of the spring bloom, ETR_{int} and $G(^{17}O)$ were plotted along the cruise dates. ETR_{int} showed a maximum at the beginning of the cruise while $G(^{17}O)$ showed the opposite trend (Fig 6.11).

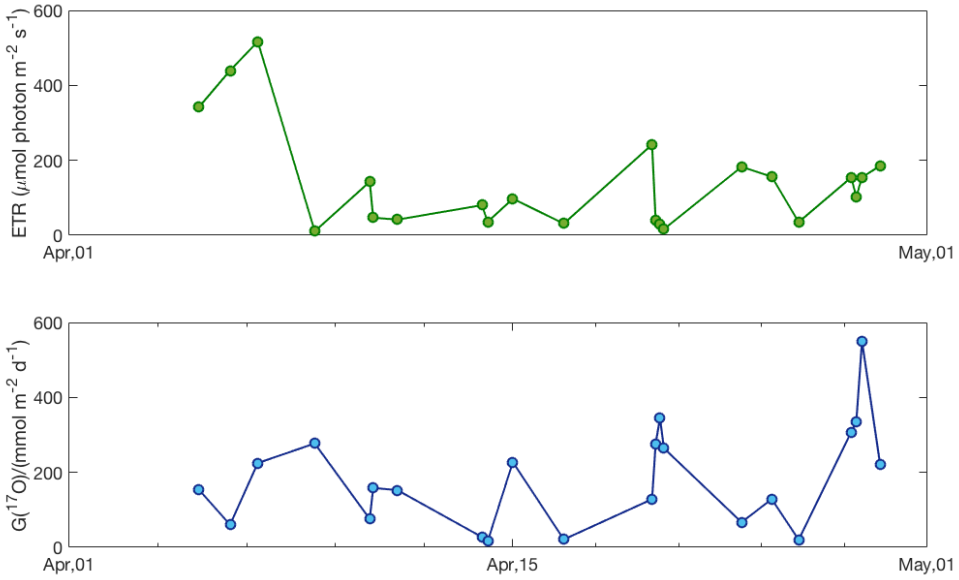

Figure 6.11. ETR_{int} µmol photons m^{-2} s^{-1} and $^{17}\Delta$ ppm per date of the cruise.

6.3.4 The Celtic Sea assemblages during the spring bloom

In table 6.2 I present the mean values of physicochemical parameters in the mixed layer. Stations are presented in the north to south order. Some of the stations were visited several times, CCS was visited five times (CCS1, CCS2, CCS3, CCS4, CCS5), and J6 and CS2 two times (J6, J6b, CS2, CS2b). Mean MLD was shallow (22 ± 9 m) during the entire sampled period. A subtle salinity gradient was present along the cruise transect from 34.7 in stations A (inner station) to 35.6 in station Fe08 (off the shelf). Temperature in the mixed layer generally increased with time, whereby the repeat visited station CCS shows a general increase from 9.9 to 11.3 ºC over 3 weeks time. Mean K_d and Chl *a* do not show clear trends with place or time; average values are (0.12 ±0.08 m) and (3.05 ± 2.93 mg m^{-3}). However, nutrients concentrations in the mixed layer showed different patterns. $NO_3^- + NO_2^-$ increased toward off shelf, from 0.3 to 8.6 μM. NH^+_4 concentrations were generally low (0.2 ± 0.1 μM) and slightly decrease toward off shelf. SiO_4^{-4} show a relative constant mean value of (2.4 ± 0.7 μM) along transect. PO_4^{3-} varies randomly along transect with a mean of (0.3 ± 0.2 μM). It is noteworthy that all nutrients show a decrease in concentration with time in the repeatedly visited stations CCS and CS2. ETR_{int} (149 ± 162 μmol m^{-2} s^{-1}) and $G(^{17}O)$ (9 ± 5 μmol m^{-2} s^{-1}) do not show clear patterns, greatly varying from place to place.

Table 6.2. Mean values on the mixed layer of salinity (S), temperature (T), light extinction coefficient (K_d), chlorophyll a (Chl *a*), nitrate and nitrite ($NO_3^- + NO_2^-$), silicate (SiO_4^{4-}), phosphate (PO_4^{3-}), electron transport rate (ETR), and gross oxygen production ($G(^{17}O)$). The name of the stations is in geographical order north to south.

Stations	Date	MLD (m)	S	T (ºC)	K_d (m^{-1})	Chl *a* (mg m^{-3})	$NO_3^- + NO_2^-$ (µM)	NH^+_4 (µM)	SiO_4^{4-} (µM)	PO_4^{3-} (µM)	ETR (µmol m^{-2} s^{-1})	$G(^{17}O)$ (µmol m^{-2} s^{-1})
A	27/04	27	34.7	10.3	0.0	3.2	0.3	0.2	0.3	0.0	0.0	1.8
J2	27/04	22	35.0	10.4	0.3	2.8	1.0	0.4	2.9	0.1	154.1	3.6
J4	20/04	25	35.3	10.2	0.1	0.7	1.7	0.2	2.8	0.2	103.1	3.9
J6	14/04	13	35.3	10.3	0.2	12.5	0.5	0.2	3.1	0.1	35.9	0.2
J6b	27/04	25	35.3	10.6	0.1	2.4	0.5	0.2	2.9	0.2	154.6	6.4
CCS	04/04	25	35.3	9.9	0.1	1.6	6.0	0.1	2.8	0.5	342.3	1.8
CCS2	05/04	42	35.3	10.0	0.1	1.7	5.7	0.0	2.5	0.5	439.6	0.7
CCS3	20/04	24	35.3	10.6	0.0	4.5	2.1	0.2	2.5	0.2	0.0	0.0
CCS4	20/04	12	35.3	10.7	0.2	1.2	2.3	0.3	2.5	0.2	39.9	3.2
CCS5	25/04	13	35.3	11.3	0.1	5.4	0.1	0.1	2.2	0.1	35.0	0.2
CCS6	26/04	37	35.3	10.9	0.1	1.4	0.2	0.3	1.9	0.2	185.4	2.6
O2	10/04	16	35.4	10.6	0.1	2.9	5.6	0.0	2.5	0.4	46.9	1.8
CS2	17/04	20	35.6	11.5	0.1	2.6	7.1	0.2	2.8	0.5	31.1	0.2
CS2b	24/04	10	35.6	11.8	0.1	2.3	5.4	0.2	1.8	0.4	156.4	1.5
Fe08	06/04	25	35.6	11.5	0.1	0.4	8.6	0.0	3.1	0.6	516.9	2.6

In order to address whether K_{O2} variance was from the complex changes in environment over both space and time, we adopted an approach recently considered by Zhu et al. (2017) as to whether these various stations can be grouped based on similar physicochemical parameters. SIMPROF analysis of the groups averages dendrogram plot using PAR, sea surface temperature, and nutrients cannot identify groups with less than 85% similarity from the cluster analysis (Fig. 6.12, I & Fig. 6.13, I) and therefore, the contribution of some variables that don't vary regionally could be camouflaging the possible diverse biogeographic regions. Exchanging PAR for K_d (to include differences in turbidity instead of light) and including salinity didn't create significantly ($p < 0.05$) different groups although this re-analysis did reveal different clusters at high 90 % similarity (Fig. 6.12, II & Fig. 6.13, II). Performing the same analysis but only with K_d and nutrients created three clusters of 70 % similarity and station A separately (Fig. 6.12, III & Fig. 6.13, III). Including the ML depth didn't create clusters with less similarity (Fig. 6.12, IV & Fig. 6.13, IV). Other combinations, like including Chl *a* did not show clusters better differentiated than combination III (data not shown).

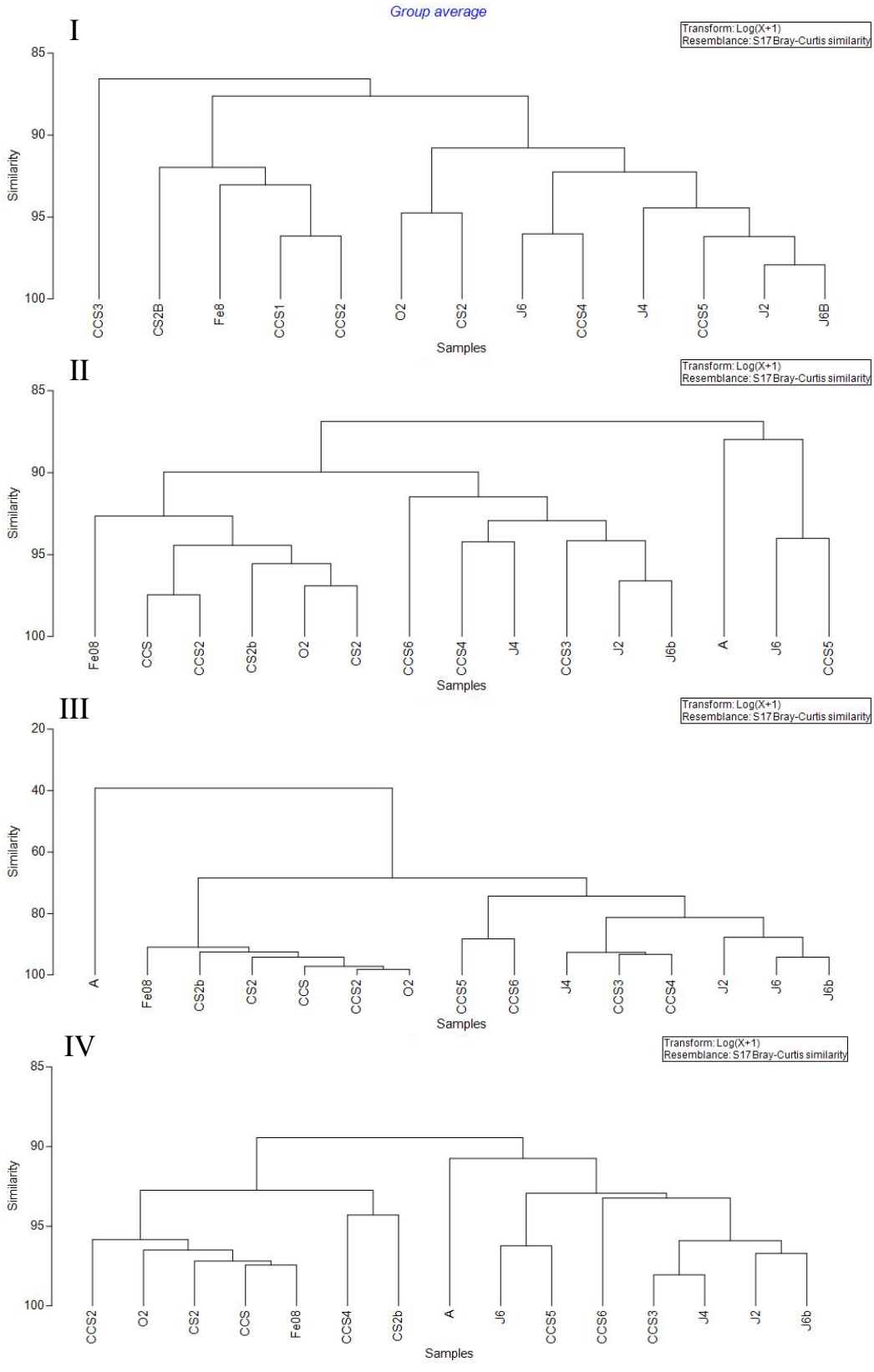

Figure 6.12. SIMPROF dendogram of a Bray–Curtis for the analysis of similarity based in a matrix of physicochemical parameters transformed with Log (X+1).

The cluster obtained based on the environmental variables trying to demonstrate that the

dependence of K_{O2} cannot be explained by individual relationship with single variables. These clusters plotted over nMDS plot enable us to explain which variables contribute more to the formation of different groups. Non-metric MDS ordination plot III showed a spatial gradient on the horizontal axis separating station A from in the inner shelf from Fe08 off shelf, placing the stations in between in geographical order (J2, J4, J6, CCS, O2, and CS2). On the vertical axis, there is no clear separation. The length of the parameters vectors represents the strength of the parameter in forming the clusters and the orientation its correlation with horizontal and vertical axis. Nutrients show the stronger correlation with the horizontal axis separating inner from outer stations, while K_d it does with the vertical one. The blue circle in plots I and II help to visualize the vectors length. $NO_3^- + NO_2^-$ and PO_4^{3-} length show that those nutrients predominantly control assemblages formation.

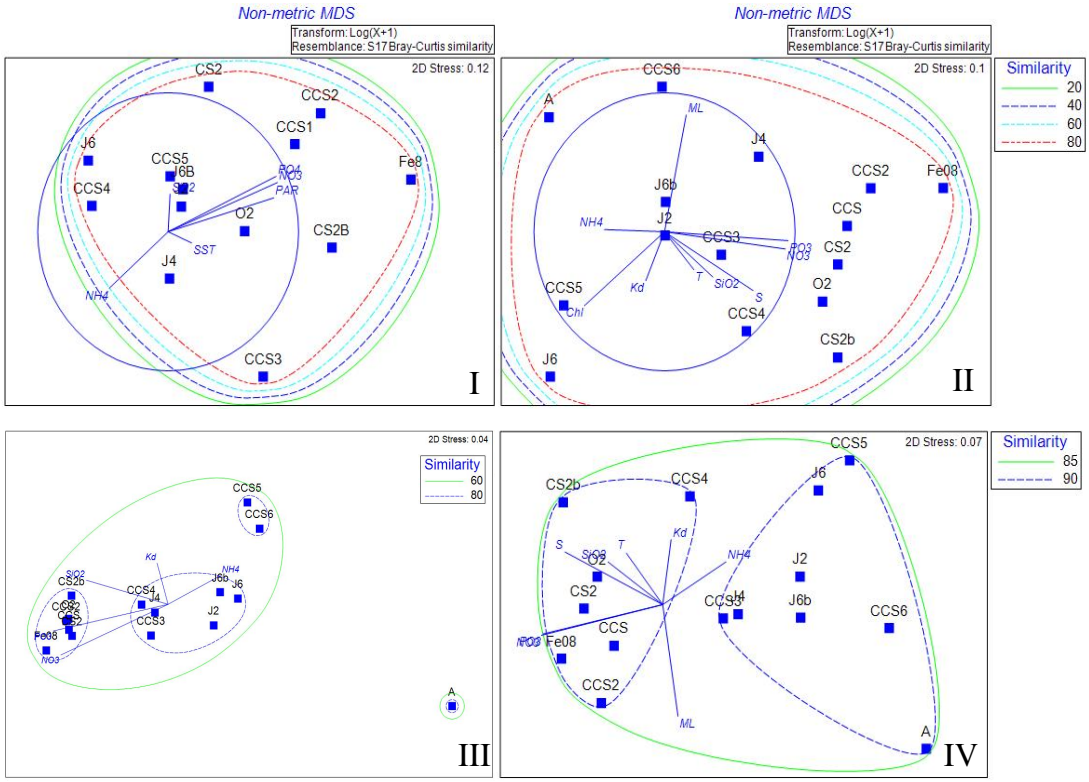

Figure 6.13. nMDS plot of a Bray–Curtis similarity matrix of Log (X+1) transformed environmental variables (mixed layer depth, salinity, temperature, PAR, K_d, Chl *a* and nutrients) along the stations in the Celtic Sea for the mixed layer depth during the spring bloom (Stress: 0.12). Circles indicate possible groups at 20, 40, 60 and 80% similarity level derived from cluster analysis. Vectors indicate direction and relative magnitude of Spearman correlation with the plot axes of the most relevant environmental variables.

Based in the groups formed in analysis III I re-plotted K_{O2} against $NO_3^- + NO_2^-$ and PO_4^{3-} to evaluate K_{O2} variability due to those nutrients, but we didn't find any relationship, nor a relationship against PAR (data not shown). But we found a positive relationship between ETR and $G(^{17}O)$ when using the data divided in three clusters (R^2 = 0.2, 0.5 and 1)

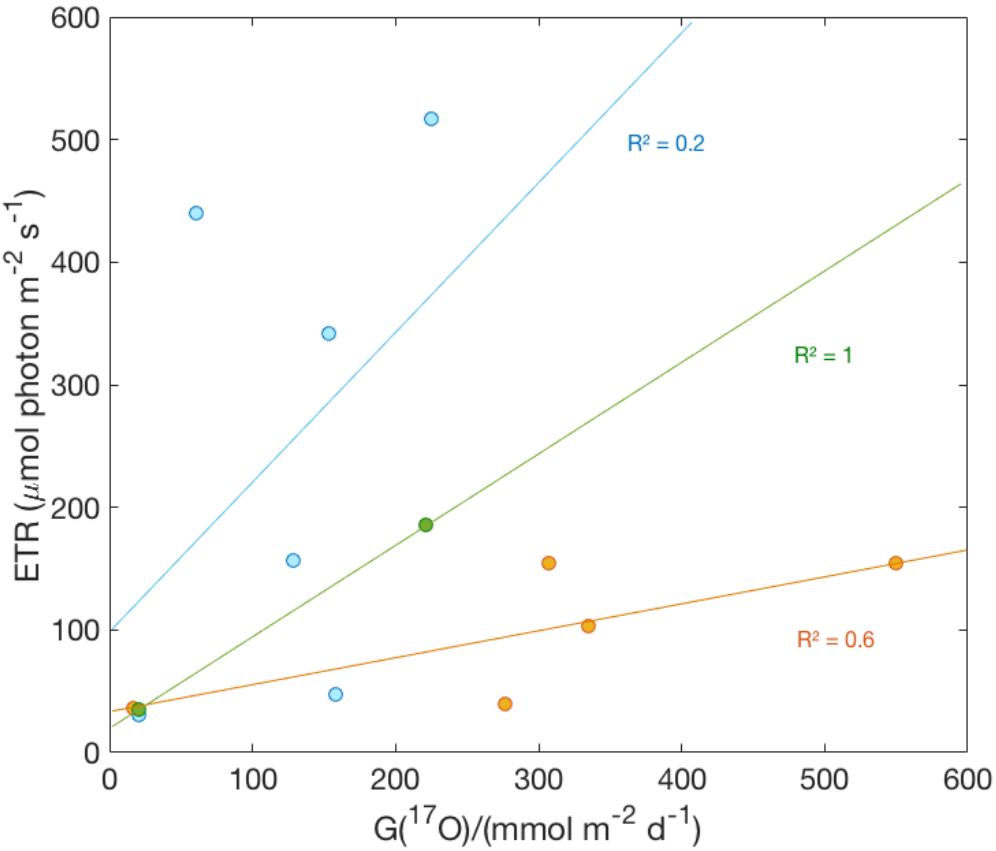

Figure 6.14. Integrated values of ETR µmol photons m^{-2} s^{-1} against $G(^{17}O)$ mmol m^{-2} d^{-1} in the mixed layer (ML) separated in three groups according to cluster based in nutrients and light contribution.

6.4 Discussion

In theory, the calculation of K_{O2} to obtain gross production values should be more straightforward than the calculation of K_C to obtain net production, because ETR is more closely related to the rate of gross O_2 evolution, and less directly to the later production of ATP and NADPH used for carbon fixation (Lawrenz et al., 2013). While

"wall effects" can affect primary production calculated from incubation techniques, non-invasive direct measurements should not, and therefore FRRf and triple oxygen isotopes should both represent true gross primary production.

Previous studies have found a good relationship between ETR and C uptake (Zhu et al., 2017, Suggett et al., 2009, Schuback et al., 2015), although the ratio of the two shows different values depending the study and region (Lawrenz et al., 2013, Suggett et al., 2009). The results here do not show a clear ETR/$G(^{17}O)$ relationship. I explore here the reasons of the discrepancies that would help to improve the search for a future K_{O2} algorithm.

Analysis of gross production discrepancies

The nMDS analysis of the present study shows biogeographic regions based on mixed layer nutrient concentrations. Lawrenz et al. (2013) does an analysis of 14 studies in 12 marine regions and describes as something surprisingly the inclusion of PO_4^{3-} with the creation of biogeographic regions associated to K_C rather than with NO_3^-. However, we also found that the contribution of PO_4^{3-} in the formation of different clusters is the strongest followed by NO_3^-+ NO_2^- (Fig 6.13). Our data was re-grouped according to the results of the clusters to perform new multiple linear regressions of ETR against $G(^{17}O)$. However, from the ETR/$G(^{17}O)$ multiple linear regression plot, only one group shows a significant correlation (R^2 = 0.6, n = 5), the other two show large scatter (R^2 = 0.2, n = 6) and not enough data points (R^2 = 1, n = 2), therefore it was concluded that the present study did not offer enough significant correlation to calculate K_{O2}.

Some studies have already examined some of the reason why we are still finding discrepancies in the calculation of primary production from FRRf (Zhu et al., 2017, Lawrenz et al., 2013), but many focused on the discrepancies with the ^{14}C method. For our oxygen method and to avoid assumptions, we didn't apply the photosynthetic quotient in the conversion of O_2 to CO_2 and worked with O_2 units directly for the calculation of ETR and gross production relationship, nor the assumption of the photosynthetic unit size n_{PSII} was included. Errors related to sample handling and processing have been discarded for $G(^{17}O)$ values as those have shown to match well

with independent production indicators such as concentrations of dissolved oxygen and chlorophyll *a*. Provided FRRf data have to be assumed correct as handling, calibration and processing cannot be further investigated. Provided nutrients have been already published in García-Martín et al. (2017) and therefore are also assumed as correct here. Systematic errors in the ETR calculations would affect comparisons with other studies, but would not affect finding patterns in the regression lines, which is the objective of the present work. Recently, Zhu et al. (2017) found a relative good relationship of ETR and ^{13}C including a size fractionated phytoplankton community. Unfortunately, taxonomic data was not available for this research. However, we assume that environmental variables would also influence in different phytoplankton community composition, and therefore our results may also show the presence of different phytoplankton communities (Lawrenz et al., 2013). The main source of discrepancy is most likely the differences in both methods timescales. While the FRRf technique measure in a time scale of μseconds, the $G(^{17}O)$ method represent production over the resident time of oxygen in the water. FRRf would measure rapid changes of photoacclimation and physiology variability, while these changes will be "diluted" in the $G(^{17}O)$ values. The high space-temporal variability of shelf seas together with the special rapid conditions of productivity and nutrients during the spring bloom, have probably aggravated the timescale differences between methods. Episodes of cloud coverage have shown a decrease in gross production derived from FRRf (Fujiki et al., 2008), that again would not be detected in daily $G(^{17}O)$. In further research we recommend FRRf measurement time series that could be integrated to the time residence of oxygen in the water. That would probably represent better the relationship between the two gross production approaches. This could be very time consuming with discrete samples but the efforts could be minimized by attaching a second Fast Ocean to the underway system and complement the measurement in depth with discrete samples. Including community structure would probably also increase the accuracy in the calculations of a K_{O2} algorithm (Zhu et al., 2017). The nutrient data was also not available for all the stations where we did the sampling, minimising the number of data points that can be used in the multiple linear regression (e.g. one of the cluster groups only contained two data points). Although other analytical analysis (e.g. principal components analysis or PCA) could be done, it will not save the limitations of the sampling strategy, and therefore further studies with a better sampling strategy as

explained above are necessary to analyse ETR and $G(^{17}O)$ relationship in order to develop appropriate K_{O2} algorithms.

6.5 Conclusion

Conversion of ETR to $G(^{17}O)$ is not currently possible, probably due to differences in the time frame used to calculate primary production by each technique. $G_{ss}(^{17}O)$ can be considered to be a time-integrated estimated over the residence-time of oxygen in the mixed layer, whereas the more complete calculations going into $G(^{17}O)$ are limited by the number of repeat occupations of the same location required to estimate the inventory change. The O_2 residence time in the mixed layer was between 2 and 14 days, whereas ETR is instantaneous and represents better what happens in seconds, but not necesarily over the residence time of oxygen in the mixed layer.

The Celtic sea is quite heterogeneous in terms of production in space and time during the spring season, but this is partly due to measurement uncertainty, especially in case of $G(^{17}O)$. The same heterogeneity is not reflected by other environmental variables (mixed layer depth, salinity, temperature, PAR, K_d, Chl *a* and nutrients), which in spring show 70 % similarity. K_{O2} does show a statistically significant dependence on environmental variables, but the limited amount of data makes it difficult to find different hydrographic regions that could drive different K_{O2} values for the whole cruise. Importantly, this study provides a methodology for future data collection and defined time integration to improve K_{O2} algorithms.

Chapter 7. Conclusions and future work

Conclusions

This thesis presents estimates of shelf-sea gross and net production from triple oxygen isotopes and oxygen-argon ratios, as well as an attempt to relate them to FRRf-based measurements of phytoplankton physiology.

The three main chapters lead to the following conclusions:

Chapter 4 presents net community and gross production rates during a Celtic Sea spring bloom at high resolution. Separate results are presented for the mixed layer and euphotic zone.

I found $N(O_2/Ar)$ values of up to 144 mmol m^{-2} d^{-1} in April 2015, with an average of (33±41) mmol m^{-2} d^{-1}. Biological air-to-sea oxygen fluxes (F_{bio}) were the dominant term in the $N(O_2/Ar)$ calculation. The diapycnal diffusion term (F_v) was negligibly small (< 4 mmol m^{-2} d^{-1}). The disequilibrium term (F_{nss}) contributed between –50 and +50 mmol m^{-2} d^{-1} at specific locations, but had a negligible effect when considering the Celtic Sea as a whole. In other words, for measurement of net community production at high spatial resolution in dynamic shelf-sea environments, good temporal resolution and repeat occupations of transects are required. The assumption of steady state (e.g. assuming $N(O_2/Ar) = F_{bio}$) may lead to errors of 50 % or more. In turn, when integrating over larger areas, F_{bio} may present a good representation of the metabolic balance of the Celtic Sea as a whole because the disequilibrium terms cancel out in the absence of net advective transport.
Gross production rates, $G(^{17}O)$, were up to 424 mmol m^{-2} d^{-1} and (225±115) mmol m^{-2} d^{-1} on average. Calculating net community production just for these discrete samples gave an average of $N(O_2/Ar)$ = (55±34) mmol m^{-2} d^{-1}. $f(O_2)$ ratio for the entire shelf was 0.18±0.03, or f_C(historic) = 0.34±0.06 in carbon equivalents. The f(C) ratio is more than four times higher on the shelf than on the shelf edge. The average of nearly 0.34 for the Celtic Sea is expected to lead to a large organic carbon export flux.

The observed heterogeneity in the continuous $N(O_2/Ar)$ estimates as well as the variability of discrete $G(^{17}O)$ values along the cruise transect demonstrate the virtue of high-resolution techniques. Our results can be used to improve remote sensing algorithms and ecosystem models, using biogeochemical oxygen-based estimates of biological production rates.

Chapter 5 analyses the seasonal variations in biological production based on data from four cruises, spanning spring, summer and autumn. Spring and summer were net autotrophic, while autumn was net heterotrophic. Although the sampling programme did not cover each month of the year, seasonal variability was well captured and the magnitude of the values measured suggests that the Celtic Sea is a net autotrophic system on an annual basis. Different ways of calculating net fluxes generally agree and are of the same order of magnitude. Nevertheless, the differences and statistical measurement uncertainties increase when I include terms other than air-sea exchange fluxes in the calculations.

Steady-state mixed layer fluxes (G_{ss} and F_{bio}) can deviate by up to 50 % from estimates that cover the euphotic zone and that account for non-steady state inventory changes, entrainment and vertical eddy diffusion, depending on season and conditions. These discrepancies are due to two main reasons: 1) the biological spatial heterogeneity of the Celtic Sea requires high-resolution measurements. Reducing the sampling area to the Central Celtic Sea and shelf edge underestimates the total biological production generated in the entire shelf. 2) More complete calculations entail higher overall measurement uncertainty and widen the confidence intervals for the final values, while at the same time approaching the values based on steady-state approximations.

Interestingly, the seasonal variations are consistent regardless of the calculation used. Net community production is highest in spring and gross production is highest in summer. Both stations CCS and CS2 show net autotrophic conditions, while autumn is clearly net heterotrophic. Hence, this study characterised the seasonal biological patterns, quantified non-steady state production rates and showed that the biological pump makes the Celtic Sea a net carbon sink.

Chapter 6 explored the relationship of electron transfer rate (ETR) against $G(^{17}O)$ in order to calculate the first *in situ* K_{O2} algorithm. Conversion of ETR to $G(^{17}O)$ is not currently possible, probably due to differences in the time frame used to calculate primary production by each technique. $G_{ss}(^{17}O)$ can be considered to be a time-integrated estimated over the residence-time of oxygen in the mixed layer, whereas the more complete calculations going into $G(^{17}O)$ are limited by the number of repeat occupations of the same location required to estimate the inventory change. The O_2 residence time in the mixed layer was between 2 and 14 days, whereas ETR is instantaneous and represents better what happens in seconds, but not necesarily over the residence time of oxygen in the mixed layer.

The Celtic sea is quite heterogeneous in terms of production in space and time during the spring season, but this is partly due to measurement uncertainty, especially in the case of $G(^{17}O)$. The same heterogeneity is not reflected by other environmental variables (mixed layer depth, salinity, temperature, PAR, K_d, Chl *a* and nutrients), which in spring show 70 % similarity. K_{O2} does show a statistically significant dependence on environmental variables, but the limited amount of data makes it difficult to find different hydrographic regions that could drive different K_{O2} values for the whole cruise. Importantly, this study provides a methodology for future data collection and defined time integration to improve K_{O2} algorithms.

Future work

This work has shown the importance of high-resolution measurements of net and gross production in heterogeneous and dynamic areas. Further studies in the Celtic Sea would benefit from higher temporal and spatial data coverage, in order to accurately understand the rates and the efficiency of carbon export for the whole shelf.

Many studies use incubation methods or “snap shots” to estimate primary production. The production rates calculated here are within the range of values previously measured in the Celtic sea, but only because this range is very large. Previous studies have demonstrated that different primary production approaches deliver highly divergent values (Robinson et al., 2009). The main reasons seem to be due to variable incubation

times and bottle effects (Cullen, 2001). The relationships between the present method and carbon-based measures of production need to be better understood. Calculation of fluxes under natural conditions over a range of timescales can provide insight into what the differences imply about biological carbon and O_2 cycling. Further studies on the relationship between methods would allow comparison of previous data with recent O_2/Ar and triple oxygen isotope-based measurements to establish an historical context of the area of study.

This study has shown that steady state mixed layer production fluxes can deviate by up to 50 % from estimates that account for non-steady state inventory changes, entrainment and vertical eddy diffusion, depending on season and conditions. The sensitivity of the triple oxygen isotope technique has revealed the difficulties and uncertainties in the calculation of production below the mixed layer when there are summer subsurface maxima. Further studies should adapt the sampling strategy to seasonal characteristics. Moreover, the sampling strategy should meet the necessary conditions to include non-steady state inventory changes, entrainment and vertical eddy diffusion to be able to deliver accurate production rates with high temporal resolution in highly dynamic and heterogeneous areas, where the steady-state assumption is likely to be erroneous at least over small scales.

The O_2/Ar and triple oxygen isotopes approaches are globally applicable. Many areas with high productivity (e.g. high latitudes) remain undersampled. These two techniques together present an opportunity for similar studies in other oceanic or shelf seas areas. These studies would provide better estimates of the biological O_2 exchange and may be used to provide alternative parameterisations of remote-sensing based production estimates.

Gas exchange coefficient calculation remains a large uncertainty in the calculation of biological fluxes. Very low and high winds normally do not fit well in a single parameterisation. The parameterisation of winds is especially a problem for seasons or areas where the winds are changeable. The calculation of biological fluxes in areas where the sea surface is covered or partially covered by ice is still a matter of debate (Prytherch et al., 2017). However, one particular advantage of the O_2/Ar-based method

is that it is not sensitive to partitioning between diffusive and bubble-related gas exchange.

The discrepancies between the FRRf-based gross production and $G(^{17}O)$ have shown the necessity of further investigation. Future work should attempt to make comparisons on similar time scales, for example, by integrating high-frequency ETR measurements over the residence time of oxygen in the water. Sampling in seasons when the biological and climatological conditions do not change rapidly would also reduce the uncertainty and simplify the comparison. That would allow the basis for the relationship between FRRf-based gross production and $G(^{17}O)$ to be established in order to derive an *in situ* K_{O2} algorithm for the first time.

Appendix A: Protocols

I present step-by-step protocols of seawater samples for dissolved oxygen analysis and tests for the performance of the IRMS.

1. Winkler method for dissolved oxygen

The following protocol is based in Grasshoff (2007), Culberson (1991). The following steps and sketches explain and complement the original method.

Sampling

1. Check that stopper and bottle numbers match. Bottles should be clean. Prepare Tygon tubing with the right size for sampling from the CTD or UWS supply.
2. In a template sheet take note of CTD cast number, event number, date, time, and align the number of your bottles with the number of the Niskin that you want to sample. Prepare the dispensers of $MnCl_2$ or $MnSO_4$ and NaOH/NaI by flushing several times in recirculation position and then in dispenser position into a waste container until you are sure there are no trapped bubbles.
3. Bring the bottles for sampling, a thermometer, template sheet and Tygon tubing close to the place for sampling. Chemicals have to be close to you but in a protected place that we will call "the station". Let others know about the "the station" so it is safe for others to work around.
4. Connect the Tygon tubing to the Niskin or USW inlet. Pick up the bottle and Niskin as written in your sheet. Let the water flow and pinch the tube with your fingertips to remove air bubbles.
5. Invert and rinse the bottle for 10-15 seconds.

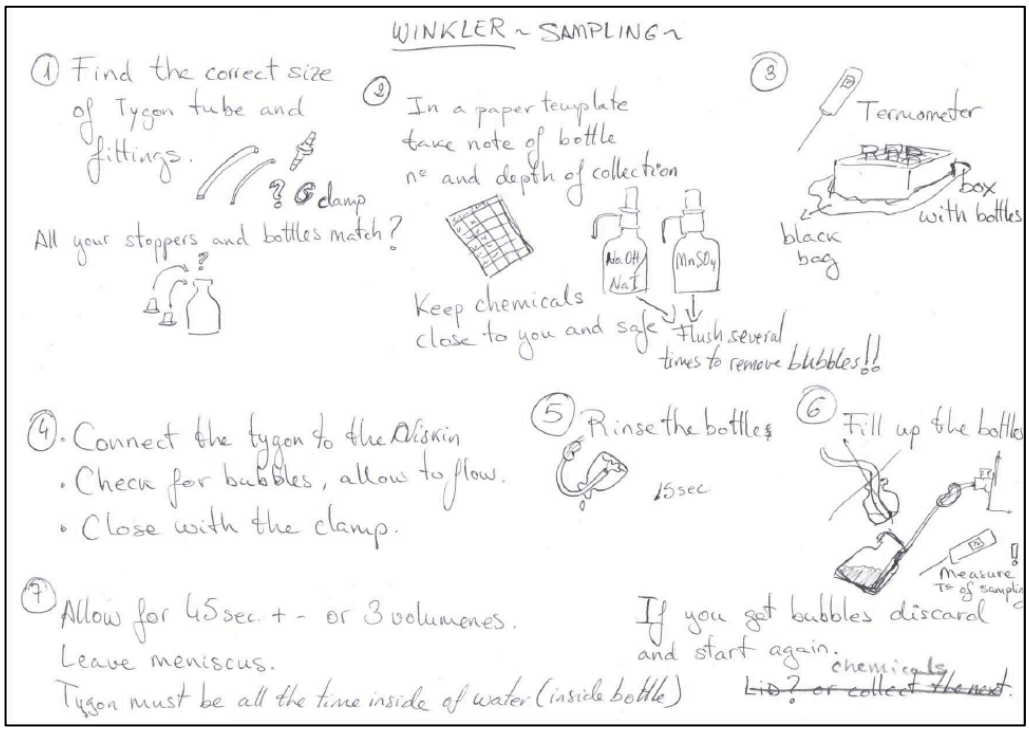

Figure A.1. Sampling of seawater from Niskin bottle. Close the clamp, turn the bottle up and slightly bend. Place the tip of the tube in the downer corner of the bottle. Slowly release the clamp to let the water flow smoothly.

6. Fill up the bottle until overflow 2-3 volumes. Check there are no bubbles stuck to the glass walls while filling up, and if so, remove them by shaking the tube inside the bottle. Holding the bottles from the neck minimise changes in water temperature. You can measure the temperature of the water while sampling or later just before fixing the sample.
7. Put the lid to the samples immediately after collecting them and minimise the time holding the sample.

Figure A.2. Sample bottles empty in a dark box.

Fixing

1. After collecting one or more replicates from one Niskin go to the station and measure temperatures with one hand (do not hold the bottle) while take note with the other. Place the temperature probe in the middle of the bottle.
2. Add the two reagents, $MnCl_2$ and NaOH/NaI, in this order, placing the dispenser tip inside the sample.
3. Close the bottle with the stopper quickly to avoid trapping bubbles. This operation will displace the excess seawater. Because a tiny amount of reagent could be present in this excess, it is recommended to put the lid and shake over a sink or at least not pointing to other people. Inverting the bottles about 20 times after addition of the two chemicals is enough to get a homogeneous sample. No second shake was done, as we didn't encounter any improvement by doing it.
4. Keep the samples inside a dark box until you finish collecting the others. Bring to a safe place in the lab.
5. Secure lids with elastic bands and submerge them in a bath with cold water. If the temperature of the lab is similar to the temperature of the water you can just add water around the neck of the bottle to make a water seal.

Standardisation of sodium thiosulfate

1. Move the thiosulfate bottle to get homogeneous concentration and flush to remove bubbles. Check there is enough volume.
2. Place electrode and dispenser in the stand.
3. Flush the thiosulfate until you cannot see any bubble. Create a big bubble to help remove little ones if necessary.
4. Set up parameters like concentration, size of burette, etc. in the software.
5. Place deionised water in an empty and clean sample bottle up to 2 cm below the neck.
6. Add 1 ml of H_2SO_4, NaOH/NaI, $MnCl_2$, KIO_3 and move gently in between each addition. Add a stirring magnet.
7. Place the bottle in the stand and immerse the electrode and the dispenser tip inside the bottle water. Pipette tips should not be pointing to the electrode directly.
8. Run the software method and take note of the thiosulfate added. Repeat 6 times.

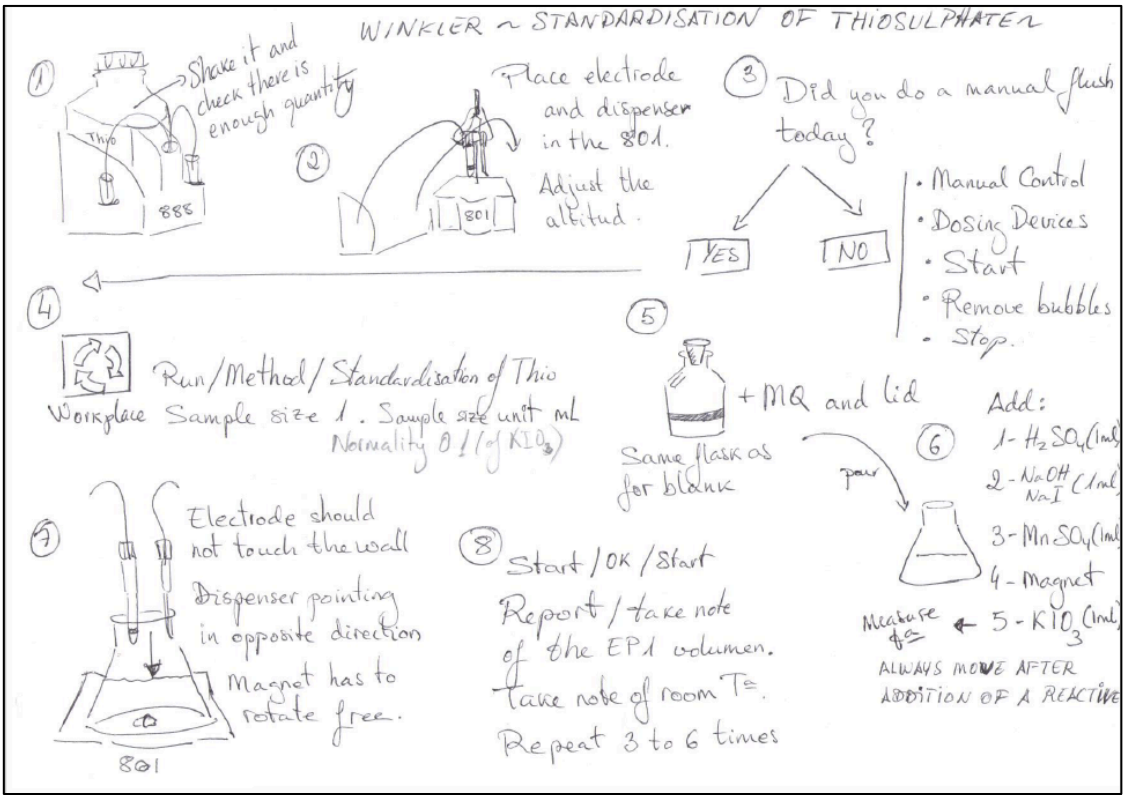

Figure A.3. Standardisation of sodium thiosulfate

Blank

1. Choose "Blank" method from the software.
2. Place deionised water in an empty and clean sample bottle up to 2 cm below the neck.
3. Add 1 ml of H_2SO_4, NaOH/NaI, $MnCl_2$, and 0.1 ml of KIO_3. Move gently in between each addition. Add a stirring magnet.
4. Flush the thiosulfate until you cannot see any bubble.
5. Place the bottle in the stand and immerse the electrode and the dispenser tip inside the bottle water.
6. Run the software method and take note of the thiosulfate volume.
7. The equipment can have a second dispenser of KIO_3 that will be added automatically or you will be asked to add it manually.
8. $V_{blank} = V_2 - V_1$. Here, V_2 and V_1 are the volumes of $Na_2S_2O_3$ used to titrate the first and second aliquots of the KIO_3 standard.

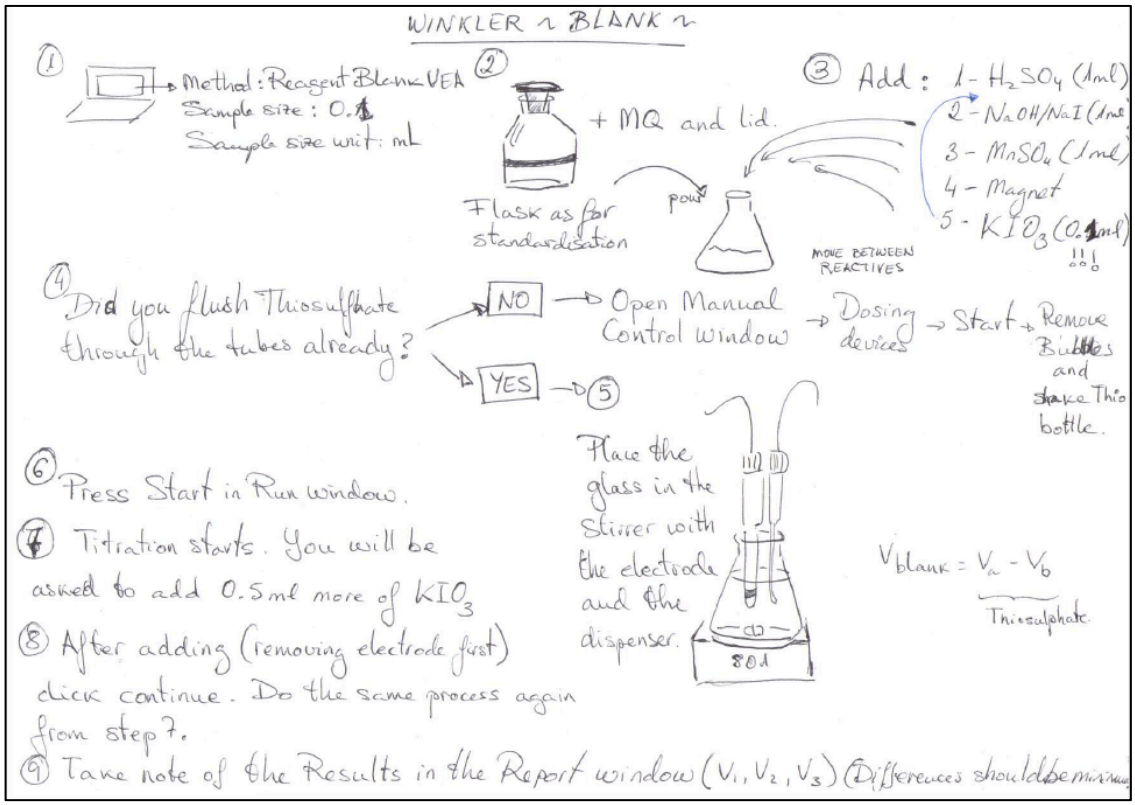

Figure A.5. Titration blank.

Sample titration

1. Add 1 ml of H_2SO_4 and stir. Add a magnet.
2. Repeat steps 4 to 6 for the titration method.
3. Take note of the thiosulfate used.
4. Repeat for every sample. Always place the pipette tip at the same high.

2. **Liquid phase displacement and extraction of dissolved gases from seawater headspace**

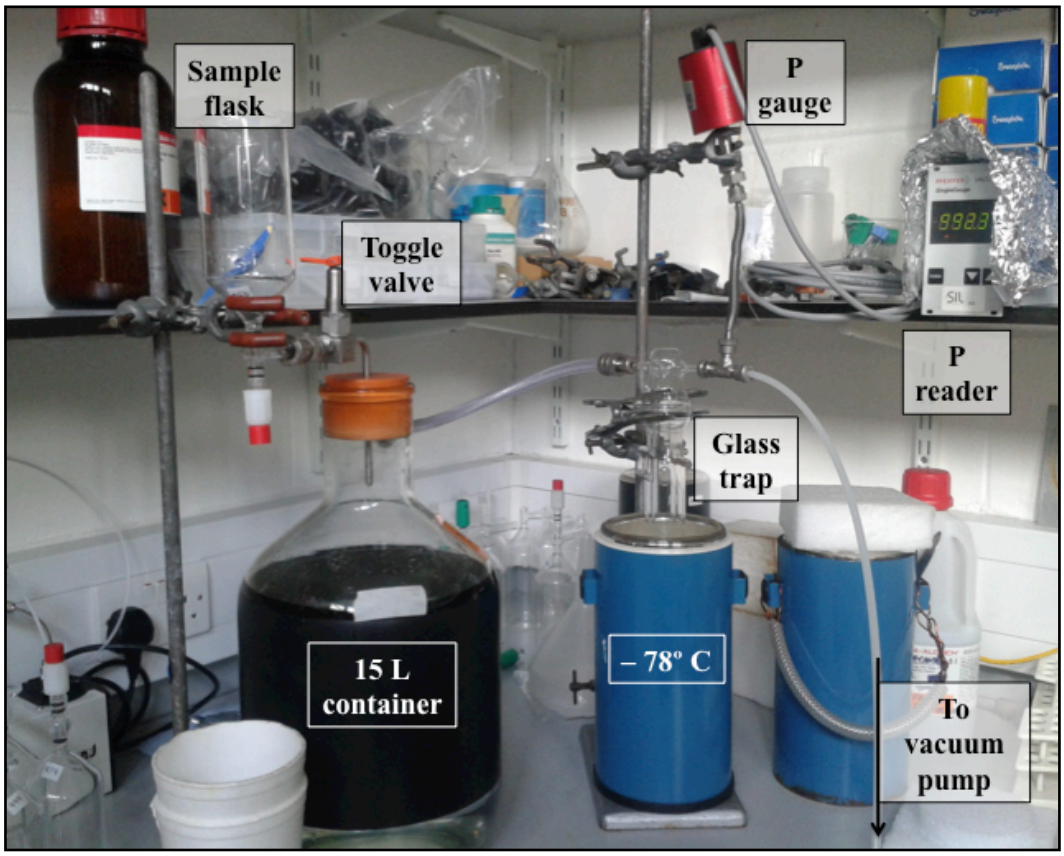

Figure A.6 Setting up of the sample extraction system.

Sample extraction

1. Prepare a dewar with ethanol (half full) and dry ice (pour it slowly until settles at the bottom). When dry ice is visible at the bottom of the dewar, then ethanol is at -78 ºC.
2. Immerse glass trap into the dewar. The trap will prevent large amounts of water vapour from the 15 L-container entering the pump.
3. Connect the cable from the pressure gauge to the pressure gauge display and set to the correct scale (1000 mbar). Select this from the measuring instrument menu[1].
4. Connect the rotary vacuum pump, the vacuum gauge and the glass trap with a T connection.

[1] Pressure gauge setting: Press the 'menu' button at the front of the vacuum measuring instrument until 'FS' is displayed, then with the up and down arrows, go up or down to change between the 10 and 1000 mbar scales.

5. Close the toggle valve that connects to the 15 L-container and switch on the vacuum pump. Prepare the sample bottles while the pressure in the system is 25 mbar or better.
6. The plastic cap from the sample flask side-arms were removed and the seawater drained away. The side-arms where then washed with distilled water to remove sea salt and dried using compressed air.
7. Sample bottles with clean and dry side-arm were weighted using a pan balance.
8. The water phase from the bottles is removed by first, inverting the bottle, making sure that there are no gas bubbles between the stopcock piston and the water above. Then the inverted bottle is connected to the container that is constantly kept under vacuum using the side-arm and 12 mm Cajon Ultra-Torr connector.
9. Open orange toggle valve.
10. Look at the pressure gauge display and make sure you notice that the pressure increases after opening the toggle valve, and then decreases (this assures that the glass trap is not blocked with ice). If pressure doesn't change, then the glass trap is blocked with ice and need to be replaced. This normally happens after processing 10-15 samples. If pressure increases significantly, and does not recover, then there is probably a leak at the connector. In this case, close toggle valve and re-fit bottle into the Cajon Ultra-Torr connector.
11. Add dry ice to the dewar if necessary.
12. Slowly open inverted sample bottle to let the water flow. Look at the pressure gauge display and check that the pressure doesn't increase. If the pressure increases, close the bottle immediately because there is a risk of air bubbles getting inside.
13. The stopcock of the sampling bottle is closed just before all the water is drained out (0.5-1 cm of water is left above the glass valve piston), thus we safely keep the gas sample while removing ~99% of the degassed water.
14. After water is drained from one sample bottle, close toggle valve, remove bottle and attach following bottle.
15. After processing all the sample bottles, close orange toggle valve, turn off vacuum pump, disconnect all components to vent the system, then thaw and dry the glass trap.

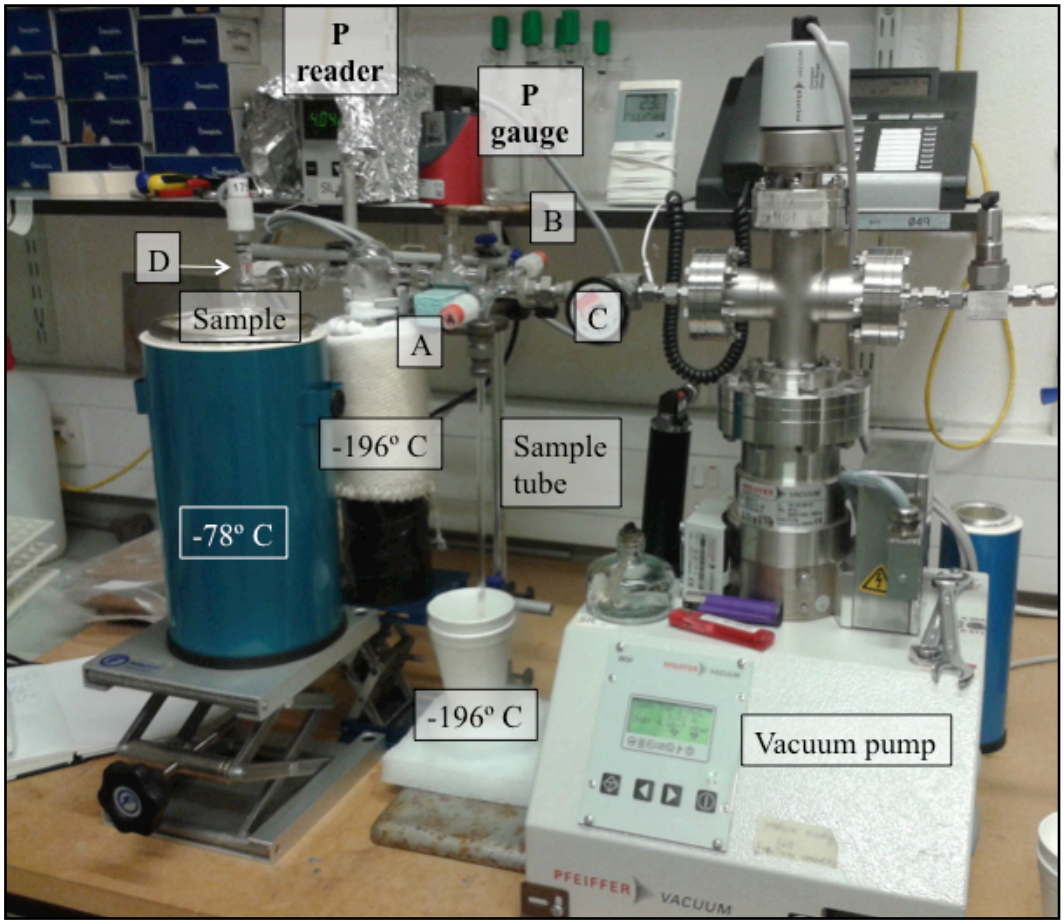

Figure A.7 Setting up of the sample extraction system.

Transferring samples to sealed tubes

1. Switch on the vacuum pumping station (preferably the day before). Open valves C and B to evacuate glass trap. Valves A and D should be closed.
2. Place a dewar with glass fibre protection shield around the glass trap and add liquid nitrogen slowly till reaches the top.
3. Connect the cable from the pressure gauge reader to the pressure gauge and set to the correct scale (10 mbar).
4. Rinse the side-arm with deionised water and ethanol, then dry with nitrogen gas from zero grade N_2 cylinder.
5. Adjust the height of the jack and immerse sample bottle in the ethanol/dry ice (blue dewar). Attach the side-arm to the line using a 12 mm Cajon Ultra-Torr connector.
6. Close valve B.
7. Expand the air volume trapped between valve D and the valve on the sample bottle by opening valve D.

8. The water vapour will freeze in the liquid nitrogen trap while we prepare the tube for collection of the sample.
9. Attach sample tube containing 10 molecular sieves pellets (5Å 1/16 inch diameter) of similar length, then slowly open valve A to remove the air from the tube until $p < 10^{-5}$ mbar.
10. Using small ethanol flame, heat the molecular sieves while watching the pressure on the pumping station. The pressure should increase. When pressure starts going down move the flame away and wait until pressure is about 10^{-6} mbar, then heat one more time. After the second flaming, wait till pressure reaches 10^{-7} mbar, then close A.

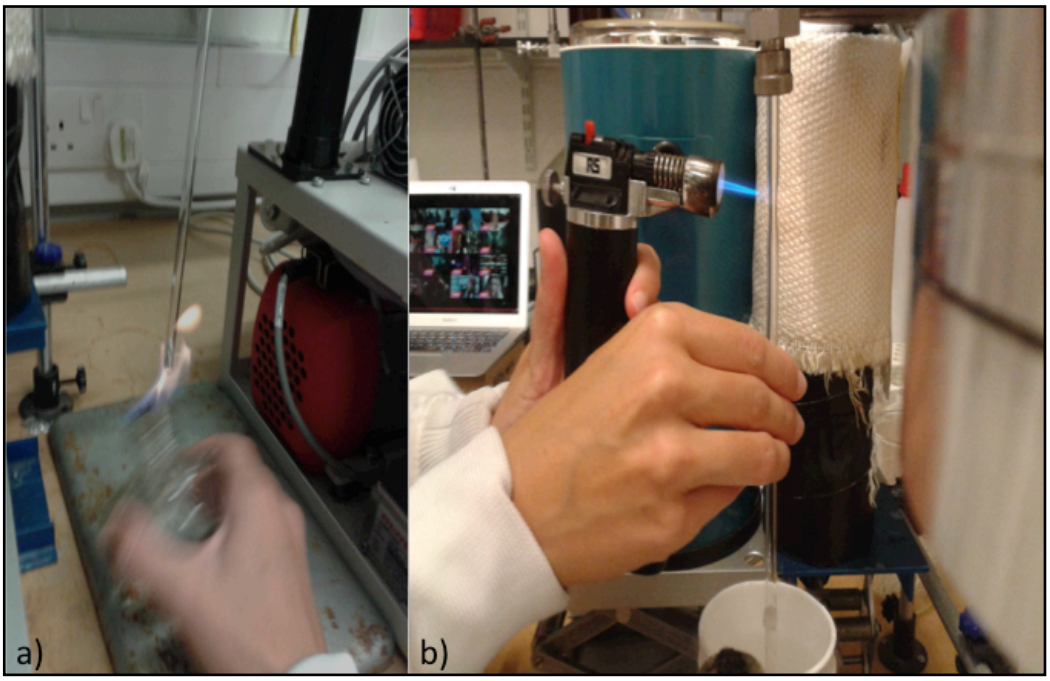

Figure A.9. a) tube evacuation b) flame-sealed tube with sample

11. Open B slowly, wait for vacuum to be $<10^{-7}$ mbar. If the vacuum doesn't reach $< 10^{-7}$ mbar, this is because there is either a leak at the connector where the sample bottle is attached. If vacuum does not improve, then remove bottle from the line and re-wash the neck with ethanol and dry with zero grade nitrogen. Every time the bottle is disconnected from the line, the air volume between the sampling bottle and valve D needs to be expanded into the liquid nitrogen trap (with valve B closed) and kept there for at least 3 minutes before opening valve B to pump this air out. This ensures that the water vapour from this air volume

freezes into the trap and it is not subsequently contaminating the line and the pumping station at the pumping down stage.

12. Open A and close C.
13. Open bottleneck valve and record pressure and time.
14. Fill up the cup underneath the collection tube.
15. Control pressure on the vacuum gauge and freeze until 99.7% of the gas is frozen on the sieves. It is calculated as: initial pressure × 0.003; which is the pressure we need to reach to freeze-out of 99.7% of the gas. Record time and pressure in the logbook.
16. Close A. Flame-seal the glass tube with a blowtorch.
17. Place sealed tube in a beaker to cool, then stick a label.
18. Close D and open C
19. Close bottleneck valve and carefully remove the bottle from the line.
20. Top up with liquid nitrogen the dewar with the glass trap.
21. Repeat procedure starting from step 5.

3. Separation of N_2 from O_2 and Ar in automated GC line

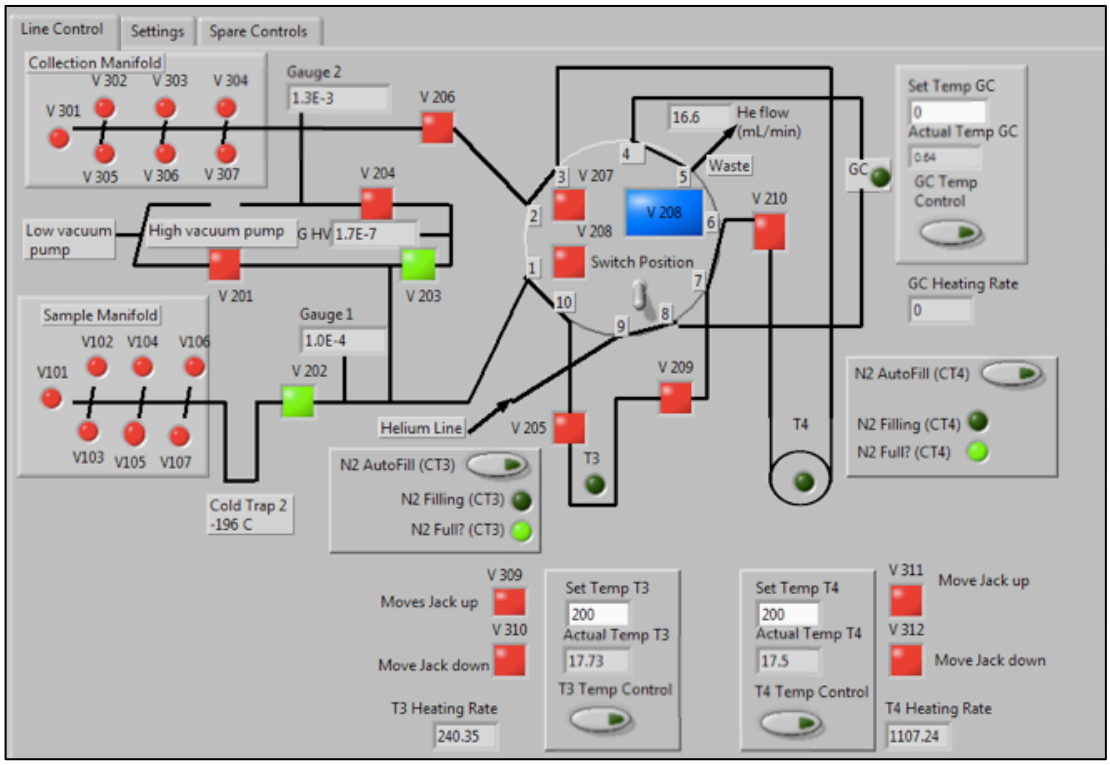

Figure A.10. Schematic diagram of the separation line from the LabVIEW 2013 software.

1. The day before: Select six samples. Make a little scratch in the tube to facilitate clean break when bended inside the corrugate area of the tube cracker. Place the tubes into the tube crackers and connect them to the sample manifold. Connections are finger tight but firmly to avoid leaks.
2. Pump out the 7 ports opening valves V203, V202, and V101 - V107. Leave the line pumping out overnight.
3. On the day: Connect a collection manifold at the other end of the line.
4. Refill with ice/water 70/30 the bucket containing the GC column. Refill with liquid N_2 the dewar in trap 2. Allow one hour.
5. Temperature in the GC column should be 0-0.7˚C and pressure in the line around 1×10^{-7} mbar.
6. Connect a collection manifold at the other end of the line.
7. Close all the valves. Open V204 only. Open manually the valve between the manifold and the line.
8. Connect the black tubes that carry compressed air to the manifold and open V301 - V307 to evacuate the entire manifold.
9. Close all the valves when pressure is 1×10^{-7} mbar.

10. Open all the valves in the line starting from V202 and follow anticlockwise.
11. Add liquid nitrogen to dewars in traps 3 and 4.
12. Expand an aliquot of dry air.
13. Press the start button; a warning message will appear. "Check that the manual valves connecting to the collecting manifold are open and the black tubes connected". Click OK.
14. When the correct pressure is achieved (previously defined on settings) trap 3 automatically goes up. Fill it up with liquid nitrogen.
15. Open manually the valve between the dry air and the line or release a sample by bending the tube cracker.
16. Take note of the initial size of the sample from Gauge 1.
17. Fill up the dewar in the collection manifold.
18. After about 9 minutes the sample will be frozen in trap 3. Valves V101 and V202 will close and trap 4 will go up. Top up trap 4 with liquid nitrogen.
19. Close manually the last valve and open the next one, so the connection tube can be evacuated before releasing the next sample.
20. The rest of the process is automated. It takes around an hour.
21. When all the samples are in the collection manifold close all the valves, and remove all the tube crackers. Remove the rest of the glass from the crackers by blowing them with compressed air.
22. Remove the liquid N_2 from the dewars.
23. Place next 6 samples in the inlet ports and repeat from step 2.

4. Preparation of reference gas (4.7 % Ar in O_2)

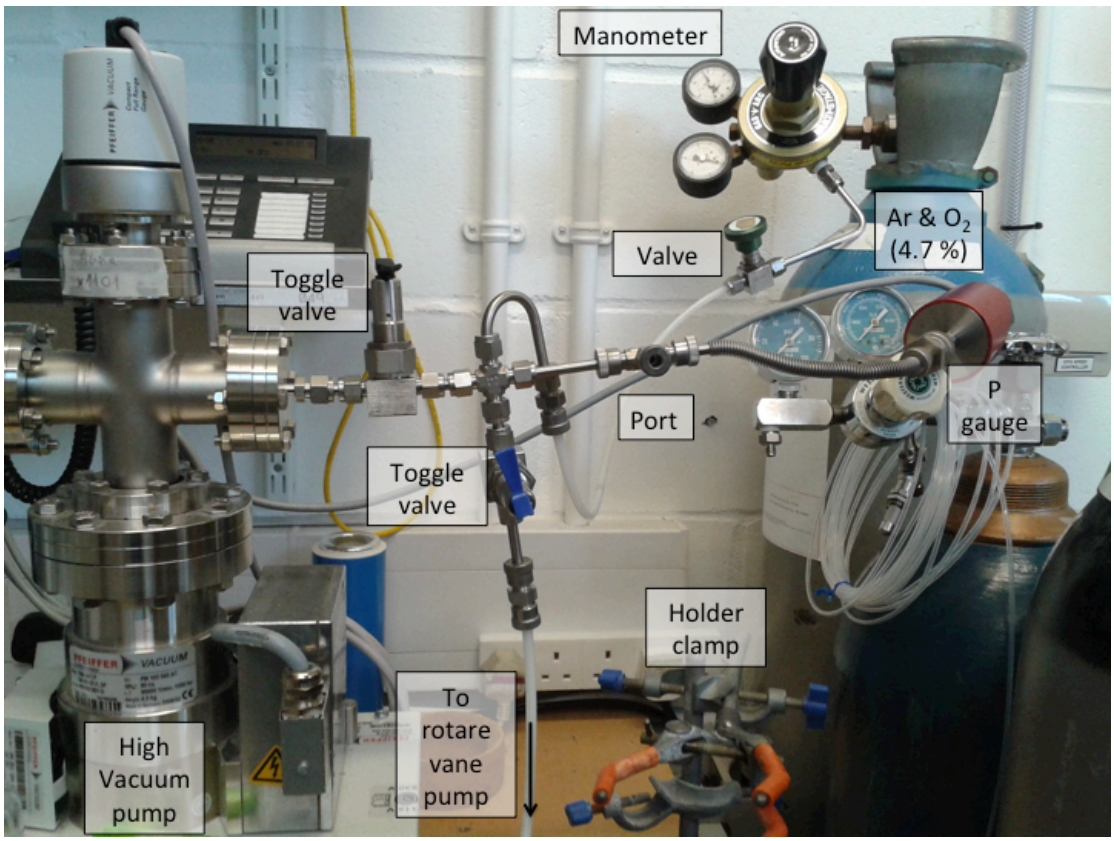

Figure A.11. Setting up for the preparation of Ar and O_2 mixture.

1. Switch on the vacuum station a few hours before using it.
2. On the right side of the vacuum pump: connect a toggle valve, a four ports connection, a toggle valve leading to a rotary vane pump, a connection to the O_2 and Ar cylinder and a T-junction for the pressure gauge and the flask port.
3. The flask that will contain the reference gas can be hold with a clamp.
4. When everything is attached evacuate all the tubes and the flask as well. Always pump out first with the rotary vane pump by opening the blue valve. The pressure gauge should reads 2-3 mbar before using the high vacuum pump in the bench. A good final vacuum should be 1×10^{-5} or better.
5. Once everything is under vacuum fill the flask with Ar/O_2 3-4 times as follow:
6. Close black and blue valves.
7. Open the green valve leading to the gas cylinder slowly and close it when pressure in the pressure gauge shows 1000 mbar.
8. Repeat steps 4 – 7 three times.

9. Last refill should be around 1000 mbar again but this time you have to close the valve on the bottleneck to keep the gas in.
10. Switch off the pump and pump out by the rotary vane pump.

Note: Open Ar/O_2 cylinder open on the top by twisting to the left, but pressure regulator opens by turning to the right.

5. Analysis of stable isotopes in IRMS - MAT 252

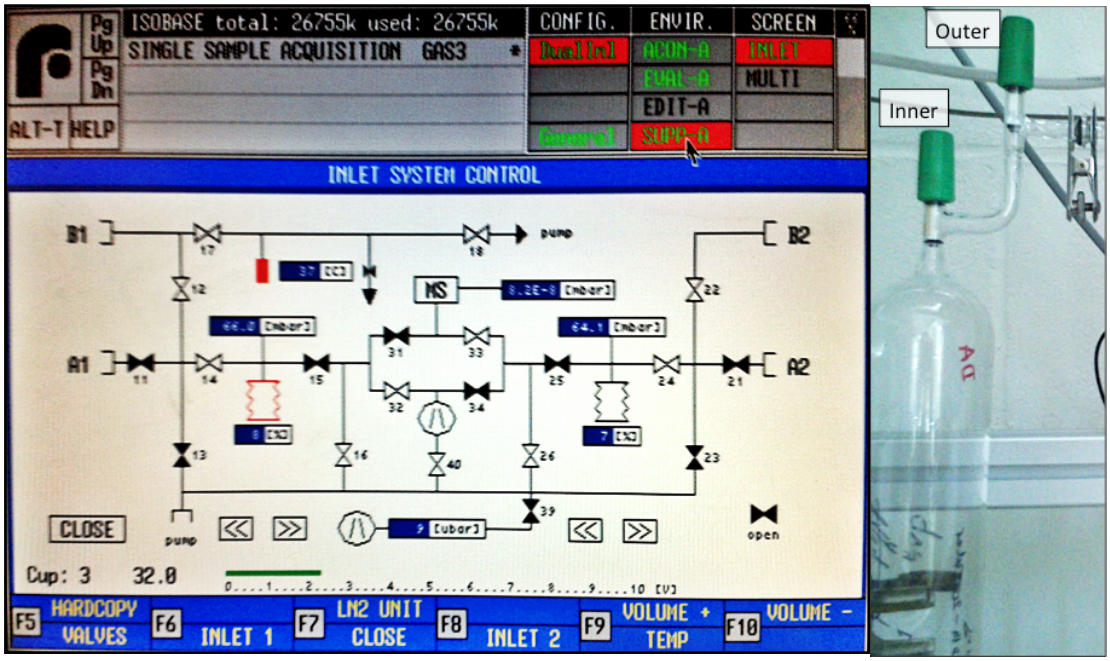

Figure A.12. Schematic diagram of the Dual Inlet System from the MAT 252 and reference gas flask.

Zero enrichment

1. Click on Dual Inl and SUPP-A in the top right menu.
2. Connect the reference gas flask to inlet A2.
3. Open valves 21, 23 and 39 to open the path to the pump. Evacuate for at least 4 minutes.
4. The reference gas flask has two valves: inner and outer valves. Evacuate the inlet of the flask by opening the outer valve while inner one is closed.
5. Close outer valve.
6. Expand an aliquot of gas between the two valves by opening inner valve.
7. After one minute, close inner valve.
8. Close valve 23. Open 24 and 21.
9. Open the outer valve of the flask, allow the aliquot to go into the reference bellow for one minute. Take note of the pressure in mbar at 100 % aperture of the bellow.
10. Close 21 and 24.
11. Isolate the mass spec inlet closing manually the valve between the inlet and the flask. Remove the reference flask and connect to the inlet A1.

12. Repeat steps 3 – 10.
13. Comprise both bellows until you get 70 - 73 mbar.
14. Open 25 and 15. Voltage reading should be around 2.5 (V).
15. Click on ACON. A rename the file: zeroenri_yymmdd(sampling date)/ SAmbar % / ST mbar %. Rename the comment as : yymmdd_vs_yymmdd (date when the O_2/Ar was prepared).
16. Click on Measure. After the Pressure delay message take note of the pressure and % of both bellows.
17. The change over valve switch every 22 seconds doing a total of 30 cycles 3 times. The whole analysis takes 1 h 25 min.
18. Connect the sample manifold to the inlet A1.
19. Submerge the sample manifold in a dewar with boiling water while the zero enrichment analysis.
20. Pump out the remained air by opening the valves 11, 13, 21, 23 and 39 (14 and 24 should be close).

Dry air and samples

1. In ACON-A, take note of the results: δ33, δ34, their standard deviation and values of O_2, Ar and N_2 for reference gas (1,3,5) and for dry air or sample (2, 4, 6)
2. Press Alt + t and then Enter.
3. Click on SUPP-A
4. Close valves 11, 21, 13 and 23.
5. Open valves 15, 16, 25, and 26 to pump all the gas from the bellows (14 and 24 still close).
6. Click in the sample bellow (red icon) on A1 side and click 100% in the scale.
7. Click in the reference bellow (black icon) on A2 side and click 100% in the scale.
8. Click on ACON-A
9. Rename the file yymmdd_samplecode_numberfromthemanifold/ pressureofSA_%/pressureofST_% For dry air the sample code is "DA" for samples is "sam".
10. Click Enter

11. Rename the comment as:
    yymmdd_samplecode_numberfromthemanifold_vs_yymmddref
12. Click Enter
13. After 4 minutes close the valves 15, 16, 25, 26.
14. Expand an aliquot of gas between the two valves by opening inner valve.
15. After one minute close inner valve.
16. Close valve 23. Open 24 and 21.
17. Click in the sample bellow (red icon) on A1 side and click 100% in the scale.
18. Click in the reference bellow (black icon) on A2 side and click 40% in the scale. How much you have to keep the bellow open or close depend on the size of the sample.
19. Open the valves 14, 24, 21 and 11
20. Connect the black tube of compressed air to the sample or dry air from the manifold. Allow 1 min.
21. In the main time take note of the pressures and aperture % in the sample below.
22. Close valve 14.
23. Click in the sample bellow (red icon) on and compress or open the bellow until pressure is around 70 mbar.
24. Repeat steps 6-10 of zero enrichment to load the reference gas.
25. Try to get similar pressures in both bellows by adjusting the opening.
26. Open valves 15 and 25 direct the sample into the MS
27. Open the valves 13 and 23 to pump out the rest of the sample left between the inlet and valves 14 and 24.
28. Click on ACON-A.
29. Click on Measure. After the Pressure delay message take note of the pressure and % of both bellows.
30. After the measurement has finished take note of the pressures and %.
31. Repeat step 1. Alt + T and then Enter to restart again

6. Pressure imbalance test of MAT 252 O_2 isotopologue measurements

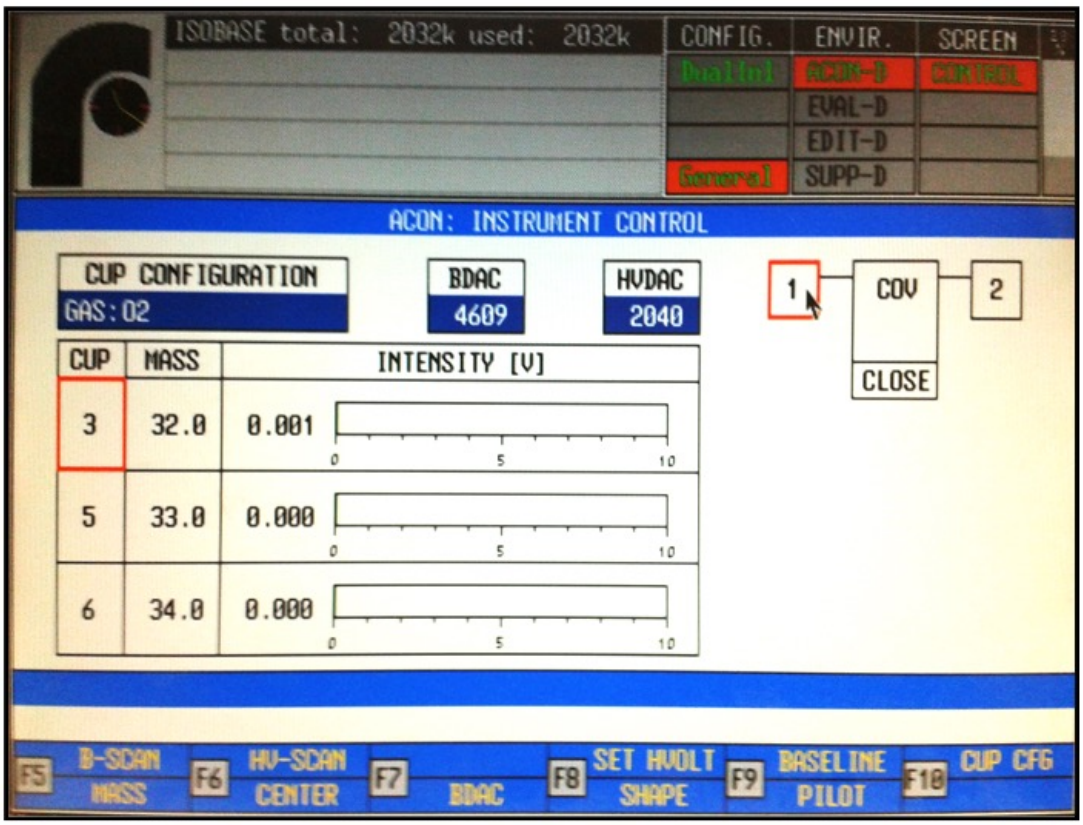

Figure A.13. Screenshot of the ISODAT software control.

1. Prepare two aliquots as for the zero enrichment and keep them in the bellows.
2. Adjust the bellows to a 50% more or less.
3. Open 15 and 25 to direct the gas into the MS.
4. In the ISOBASE, select Dual Inl/ Edit-A/ EDMEN (top right menu).
5. Click on 1Method Editor (EDMEN will change to USR-Edit).
6. Choose the method O_2 imbalance from the list.
7. Click on Experiment or press F6.
8. Click page down button three times (page 3 of 5), choose Order.
9. From the sentence C/P/M30 delete C/P and leave only M30. That will allows you to control parameters manually like pressure.
10. Go to General/ Acon-D/ Control. From this screen allows you to see the voltage of cup 3 in decimals, although you cannot compress bellows from this screen. You can change the voltage by changing the bellows with the arrows in Dual Inl/ Supp-A/ Inlet.
11. Click Center.

12. Click in bellow number 1 (F6) to change the voltage (2.3, 2.4, 2.5, 2.6, or 2.7 V).
13. Keep bellow number 2 (F8) at 2.5 V.
14. Go back to General to check that the values are ok.
15. Click on Dual Inl/ Acon-A/ USR-Acon
16. For the first measurement only: Press F10, Method dir, press page down button (page 2) choose imbalance, left and right mouse click.
17. You will see a window with the method names in Gas 2, and 3. Delete these names and press Enter every time to apply changes. The screen should look as follow:

    Gas 1 O2 imbalance
    Gas 2
    Gas 3
    Automatic Inlet NO
    Save Data to Database COL
    Repeat ACQ 0
    Comment: yymmdd_zeroimb1 / SA mbar_% / ST mbar_% Comment is as follow yymmdd_2.3v_sam_2.5v_ref
18. Click on Measure or (F5). Take note of values.
19. When the measurement has finished go to Supp-A and change the voltage by compressing or opening the bellows and without touching any valve. Use the same gas.
20. Alt + T and Enter and repeat from step 18.
21. To come back to the normal method, use EXIT and repeat the steps from the begging but this time choose the method: O2_Al_Johan_5

7. N_2 interference test of MAT 252 O_2 isotopologue measurements

Figure A.14. Setting up for the preparation of N_2 samples.

8. Connect O_2 with Ar reference gas to the left side of the vacuum line.
9. Connect N_2 gas at the bottom of the line
10. Connect a sample tube containing 10 pellets of molecular sieves in the left side of the line, opposite to the O_2 and Ar flask.
11. Evacuate all the line until 1×10^{-6} mbar and the sample tube in the same way as for the preparation of seawater dissolved gas samples, by heating the pellets with an ethanol flame.
12. Expand an aliquot in the O_2 with Ar gas elbow (valves 6 and 7) and then expand it until valve 2 (valve 1 open).
13. Take note of the pressure and pump out (open valve 5).
14. Expand an aliquot of N_2 until valve 1.
15. Take note of the pressure.
16. Because the volume that both gases have occupied in the line is almost the same, we can now calculate the amount of N_2 to add for different % to the final O_2, Ar, N_2 mixture.

17. The amount of N_2 in the expanded aliquot is far too much, so we will have to pump out a few aliquots before to get the desired amount. For example: if O_2 and Ar aliquot is 8 mbar and we want a final concentration of 0.1 % N_2, then we need to reduce the amount of N_2 until about 8×10^{-3} mbar.
18. Keep the N_2 aliquot between valves 3 and 1.
19. Expand an aliquot of O_2 and Ar until 6, close 7, and open 6 and 1.
20. Take note of the pressure of the gases mixture.
21. Open valve 0 and add liquid nitrogen in the cup surrounding the sample tube.
22. Close 0 when the pressure does not change. Take note of the final pressure.
23. Open valve 5 to evacuate all the line until 1×10^{-6} mbar.
24. Close 6 and 1
25. Start again calculating different N_2 concentrations to the final sample.

8. Bellows calibration in MAT 252

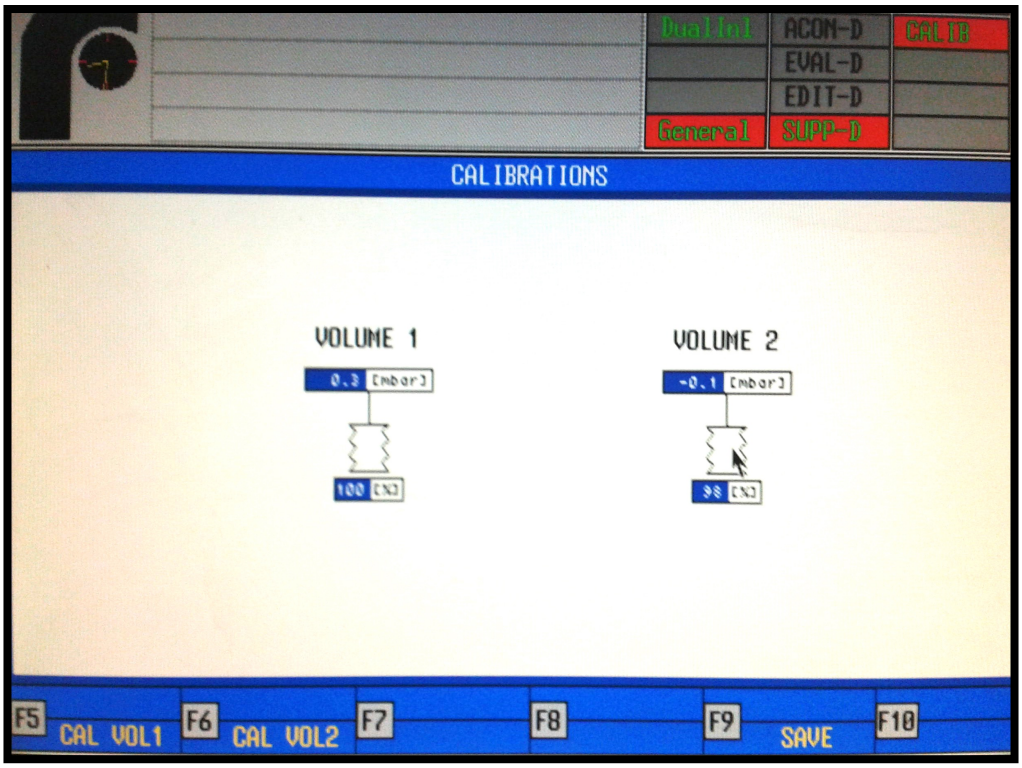

Figure A.15. Screenshot of the ISODAT software control.

It is possible that with the time the bellows loose their calibration. You can detect this when doing a zero enrichment because the pressure difference in the bellows is more than 2 mbar. If the bellows do not open 100 %, you can solve the problem by doing a bellows calibration.

1. Click on General / Supp-A (top right corner).
2. From the three options of the screen click on number 3 (calib. Inlet).
3. A new screen will appear. Volume 1 is referring to the sample (red) bellow, volume 2 to the reference (black) one.
4. Click on Cal vol 1 or press F5 to calibrate sample bellow.
5. Once the bellow have opened and close 100-0-100% click on Save or press F9. Then type Y (yes).
6. Do the same to the reference bellow.
7. To exit hold Alt while you type Q U I T.
8. You need to restart the computer; otherwise the calibration will not take effect.
9. Ctrl + Alt + Delete.
10. Wait and press Y when asked.
11. Wait until microprocessor reset message finish.

12. Ctrl + 2.
13. Type : date and then Enter.
14. Write today's date in the format (mm-dd-yyyy)
15. Enter.
16. Check that time is correct in GMT format.
17. Ctrl + 1.
18. Click on Dual Inl / Supp-A
19. Click on 1- Dual Inlet.
20. Click on Enter when 1- Single Acq. appears on the screen.

9. Data download from MAT 252

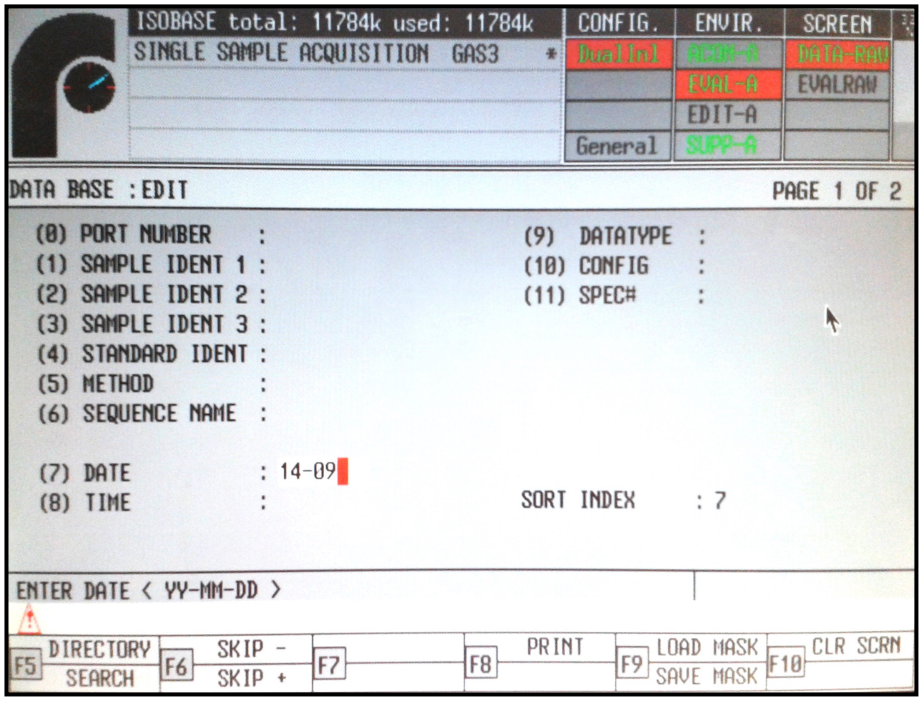

Figure A.16. Screenshot of the ISODAT software control.

You need to exit from the ISOBASE and work in MS-DOS to record the data in a floppy disk. Ctrl + 1 / Ctrl + 2 will allow you to change between the two.

1. From the ISOBASE: click on Dual Inl / Eval – A / Raw Data
2. Click 2 Data Raw Eval
3. Insert a floppy disk in the computer tower.
4. In line (7) Date: introduce year and month of the data to download in the format yy-mm (Fig A.16).
5. Enter.
6. Click on Directory (bottom left). The computer is now looking for all the data of the specified date and the data will appear in the screen.
7. Click on Tag All to select all the data in the present page. Move through pages and click Tag All to select the data in each page. You can select a maximum of 9 pages.
8. Click on Format.
9. Type the name to the file (i.e.) C:\data\yymmdd.asc, yymmraw.asc, yymmraw1.asc. No more than 8 characters are allowed.

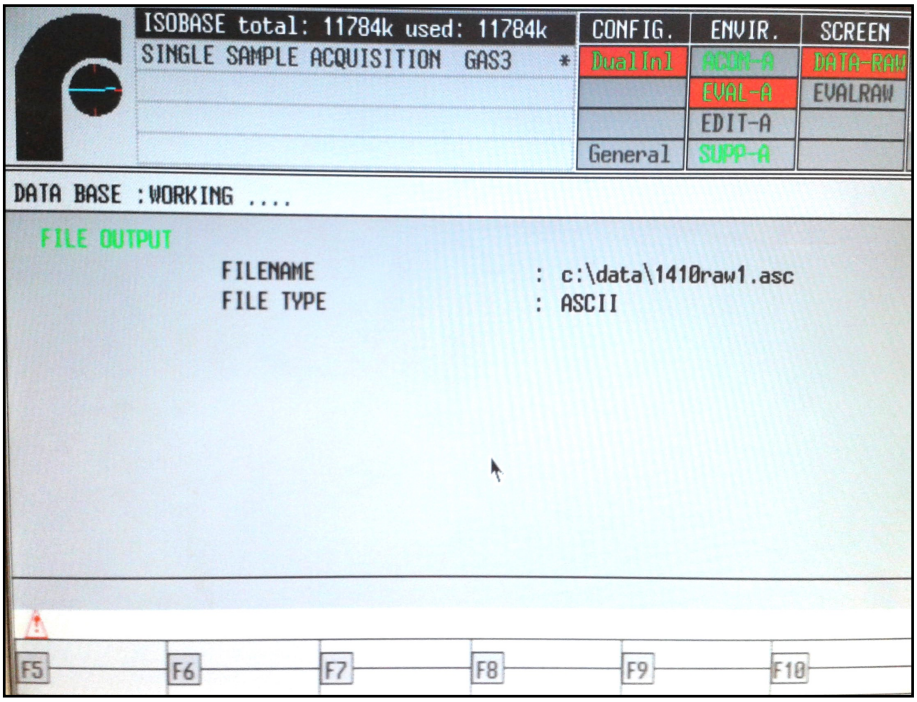

Figure A.17. Screenshot of the ISODAT software control.

10. Enter.
11. Click on Evaluate. This process will take longer or shorter depending the amount of data (Fig A.16).
12. When message "working" disappear click on Exit to return to previous screen.
13. Untag all and Tag the next pages (from 9 to 18 or the end).
14. When the process have finished click Exit twice to come back to the screen were you could select more data by date. Repeat the process until you have chosen all the data you need.
15. Click Ctrl + 2 to switch to MS-DOS.
16. Write the following commands:
17. cd c:\data + Enter
18. dir + Enter
19. copy yymmraw.asc a: Note that if you want to copy all of them in once write *.asc a: Enter
20. Eject the disk when finish copying the data.
21. Insert the disk in another PC tower.
22. Go to My Computer / 3 ½ Floppy (A:) and copy the data in the PC.

Java desktop application

Java desktop is an application designed to interact with a PostgreSQL database for the purposes of parsing, storing and manipulating triple oxygen isotope spectrometer data.
Setting up a remote server:

1. Find the Mass Spec Data base folder/ Access Database in desktop or terminal.app.
2. In the lab computer all the commands will appear automatically as follow:

   C:\ Users\ Labuser\ Documents>cd C:\ Users\Labuser\Documents\ TIA
   C:\ Users\ Labuser\ Documents \ TIA> java –jar "TripleIsotopeApplication.jar"

3. If you want to access from your computer type: mst (an alias for setting up the SSH tunnel via "ssh -fN -L 5433:localhost:5432 massspec@ehost.uea.ac.uk'") and Enter.
4. Type:

   cd ~/Documents/dist
   Enter
   java -jar "TripleIsotopeApplication.jar"

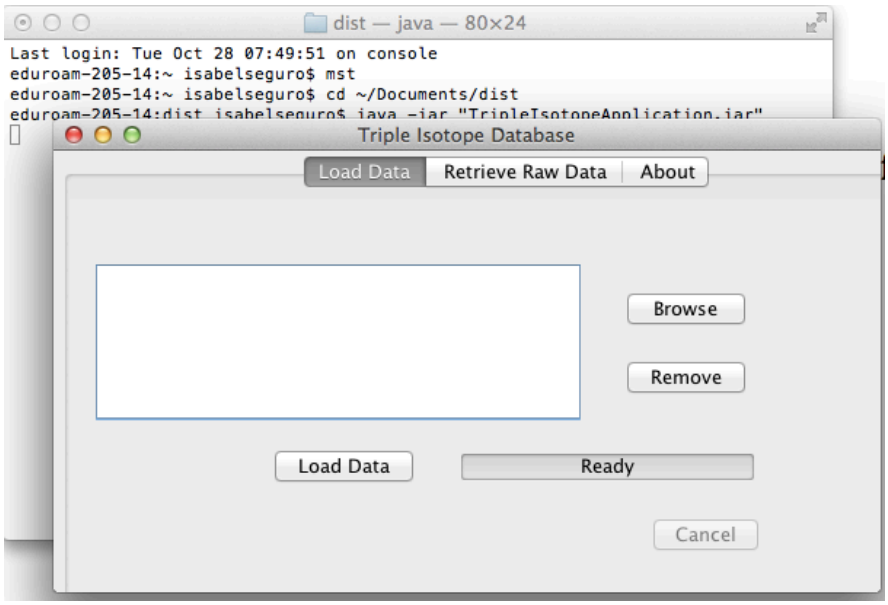

Figure A.18. Screenshot of Triple Isotope Database.

5. A new window will come out called Triple Isotope Database.
6. Click on Retrieve Raw Data.

7. Click on Spec No. or Sample Identity or Date. Look for your data or Load the data, browse and look for the files.

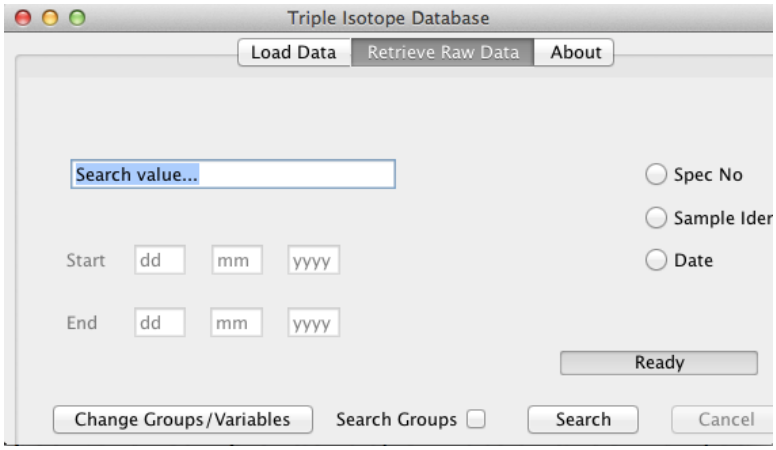

Figure A.19. Screenshot of Triple Isotope Database.

8. Click on search.
9. Select Delta Summaries.
10. Export to a spread sheet and save.

Appendix B: Mixed layer and euphotic zone depths

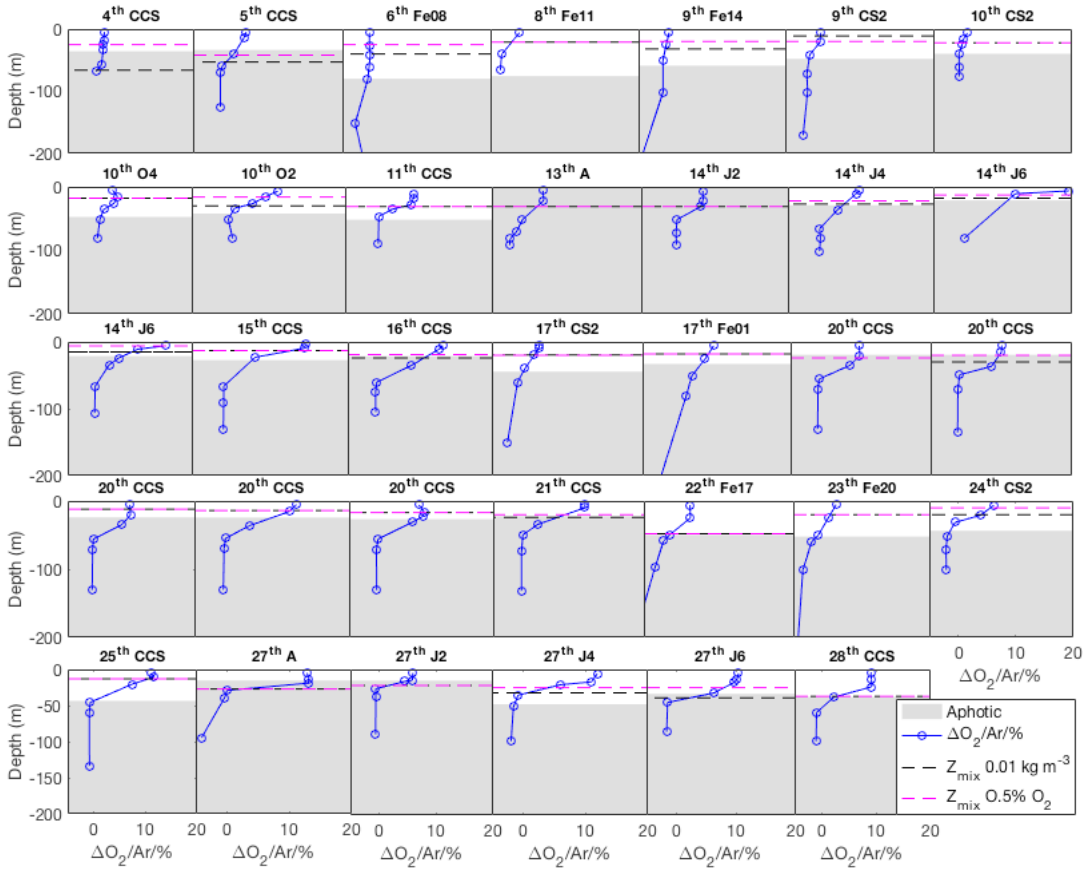

Figure B.1: $\Delta(O_2/Ar)$, mixed layer and euphotic zone from CTD casts. $\Delta(O_2/Ar)$ are plotted as blue lines. The mixed layer depth (z_{mix}) based on the change in density is in dashed black and oxygen in dashed pink. Aphotic zone (less than 1 % of incidental PAR) in shaded grey. For profiles "13th A" and "14th J2" there were no light profile measurements.

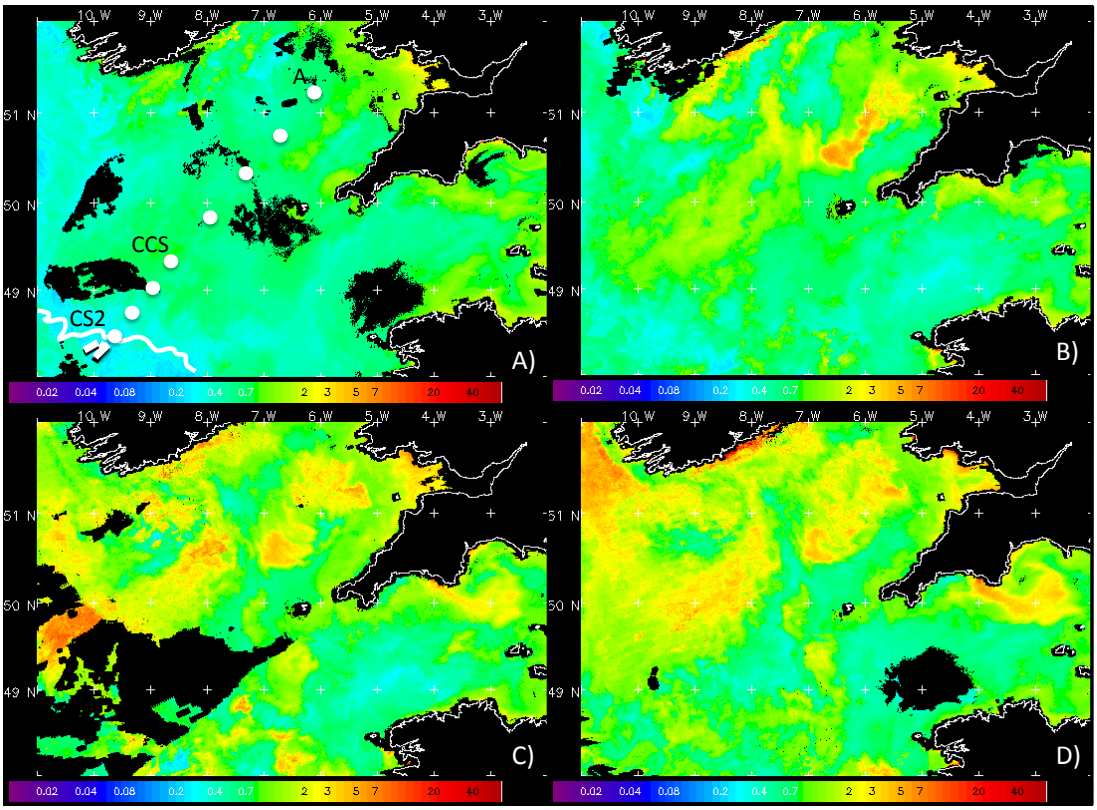

Figure B.2: Satellite images of seven days composite image from VIIRS Chlorophyll OC5 (mg m^{-3}) evolution during the spring bloom 2015. White circles, superimposed to image (A) indicate the approximate station locations (only A, CCS, and CS2 has been labelled). Straight white blocks represent multiple stations outside the shelf. The curved white line indicates the shelf-edge. (A) 1st – 7 April, (B) 8th – 14th April (C) 14 – 20th April, (D) 21 – 27 April. Images courtesy of NEODAAS.

Glossary

$1 - \omega$	Residual unventilated portion of the mixed layer
$1 - f$	Fraction of carbon used for regenerated or recycled production
$^{17,18}\varepsilon_E$	Isotopic fractionations during evasion
$^{17,18}\varepsilon_I$	Isotopic fractionations during invasion
$^{17,18}\varepsilon_R$	Isotopic fractionations during respiration
$^{17,18}\delta_P$	Photosynthetic end-member delta value
$^{17,18}\delta_{sat}$	Delta value at saturation for the measured temperature and salinity
$^{17}\Delta$	^{17}O excess, isotope anomaly or ^{17}O balance
$^{17}\Delta_{DA}$	$^{17}\Delta$ dry air value
$^{17}\Delta_P$	maximum photosynthetic value
$^{17}\Delta_{sat}$	Saturation concentration
α	Mathematical slope
α(Ar)	Ostwald solubility coefficients of argon
$\alpha(O_2)$	Ostwald solubility coefficients of oxygen
α_{sol}	Ostwald solubility coefficient
γ	Triple isotope fractionation coefficient during respiration
δ	Delta
$\Delta(O_2/Ar)$	Oxygen to argon supersaturation
Δz_{mix}	Change in mixed layer depth
ε	Kinetic fractionation constant
ε_f	Chemical enhancement factor
ζ	Optical depth
λ	Mean mass dependent fractionation value
ρ	Density
σPSII	Effective absorption cross section of PSII
ω_t	Ventilation of the mixed layer during the residence time of O_2
a	Isotope fractionation factor
c	Dissolved gas concentration
C	Concentration
C_{atm}	Concentration in atmosphere
CCMP	Cross Calibrated Multi Platform
Chl a	Chlorophyll a

c_{sat}	Saturation concentration
CTD	Conductivity temperature depth
C_{uptake}	Carbon fixation rates
C_w	Concentration in water
D	Coefficient of molecular diffusion
DA	Dry air
DO	Dissolved oxygen
E	Instantaneous irradiance
E_0	Irradiance in the surface water
E_k	Irradiance that represents inflexion
ETR	Electron transport rate
EW	Equilibrated water
E_z	Irradiance at certain depth
F	Flux
f-ratio	Efficiency of the biological pump
F_a	Lateral advection flux
F_{bio}	Biological air-sea exchange flux
F_{bml}	Production below the mixed layer
$f_C(O_2)$	N_C / $G_C(^{17}O)$
F_e	Entrainment into the mixed layer flux
F_m	Maximum fluorescence
F_{nss}	Non steady state flux or temporal change
F_o	Initial fluorescence yield in dark chamber
FRRf	Fast Repetition Rate Fluorometry
F_v	Diapycnal flux
F_v/F_m	Potential photochemical efficiency of open reaction centres
$f(O_2)$	$N(O_2/Ar)$ / $G(^{17}O)$
f_C(historic)	N_C / P_C
g	Ratio of gross oxygen production and influxes from the atmosphere
G HV	High vacuum gauge
$G(^{17}O)$	Gross oxygen production
GC	Gas chromatographic
$G_C(^{17}O)$	Gross production in carbon equivalents

$G_{eu}(^{17}O)$	Gross production in the euphotic zone
$G_{ml}(^{17}O)$	Gross production in the mixed layer
GPP	Gross primary production
$G_{ss}(^{17}O)$	Gross production at steady state
IRMS	Isotope ratio mass spectrometry
k	Gas exchange coefficient
K_0	Partial pressure differences
K_C	Electron requirement for carbon fixation
K_d	Light extinction coefficient
K_{O2}	Electron requirement for oxygen fixation
k_w	Wind speed parameterisation
K_z	Vertical diffusivity coefficient
$m(^{17,18}O)$	Slope found in the relationship of the imbalance with the $\delta^{17}O$ or $\delta^{18}O$
m/z	Mass-charge
MIMS	Membrane inlet mass spectrometer
MLD	Mixed layer depth
MS	Mass spectrometer
m_{water}	Mass of the water
$N(O_2/Ar)$	Net community (oxygen) production
N_C	Net community production in carbon equivalents
NCP	Net community production
$N_{eu}(O_2/Ar)$	Net community production in the euphotic zone
$N_{ml}(O_2/Ar)$	Net community production in the mixed layer
NPP	Net primary production
n_{PSII}	Photosynthetic unit size
PAR	Photosynthetically active radiation
P_C	24 h production in carbon equivalents
pO_2	Partial pressure of oxygen
POC	Particulate organic carbon
PP	Primary production
PQ	Photosynthetic quotient
PSII	Photosystem II reaction centers
Q	Distribution of gases and isotopes between the headspace and water

R	Ratio
R	Ideal gas constant
R, R_{ml}, R_{eu}	Respiration, in the mixed layer and in the euphotic zone
s	O_2/Ar supersaturation
Sc	Schmidt number
SSB	Shelf sea biochemistry
SST	Sea surface temperature
T3,T4	Traps 3 and 4
t_{lab}	Lab temperature
Tw	Water temperature
u	Wind speed
U(32,SA,ST)	Voltage of mass 32 the sample or standard side
u_{10}	Wind speed corrected to 10 meters above the sea level
USW	Underway sea water supply
V 200s	Valve numbers
V_{blank}	Volume of blank
V_{bottle}	Volume of the bottle
V_h	Volume of the head space
v_{mix}	Gas exchange frequency
V_w	Volume of the water phase
$W_{full, empty}$	Weight full and empty
z	Thickness of layer or depth
z_{eu}	Euphotic zone
z_{mix}	Mixed layer depth

References

Abe, O. (2008). Isotope fractionation of molecular oxygen during adsorption/desorption by molecular sieve zeolite. *Rapid Commun Mass Spectrom,* **22,** 2510-4.

Abe, O. and Yoshida, N. (2003). Partial pressure dependency of 17O/16O and 18O/16O of molecular oxygen in the mass spectrometer. *Rapid Commun Mass Spectrom,* **17,** 395-400.

Arandia-Gorostidi, N., Weber, P. K., Alonso-Saez, L., Moran, X. A. and Mayali, X. (2016). Elevated temperature increases carbon and nitrogen fluxes between phytoplankton and heterotrophic bacteria through physical attachment. *ISME J.*

Audi, G. (2006). The history of nuclidic masses and of their evaluation. *International Journal of Mass Spectrometry,* **251,** 85-94.

Barkan, E. and Luz, B. (2003). High-precision measurements of 17O/16O and 18O/16O of O2 and O2/Ar ratio in air. *Rapid Commun Mass Spectrom,* **17,** 2809-14.

Beckmann, K., Messinger, J., Badger, M. R., Wydrzynski, T. and Hillier, W. (2009). On-line mass spectrometry: membrane inlet sampling. *Photosynthesis Research,* **102,** 511-22.

Behrenfeld, M. J., Boss, E., Siegel, D. A. and Shea, D. M. (2005). Carbon-based ocean productivity and phytoplankton physiology from space. *Global Biogeochemical Cycles,* **19**.

Bender, M. (1987). A comparison of four methods for determining planktonic community production. *Limnology & Oceanography,* **32,** 1085-1098.

Bender, M. L., Kinter, S., Cassar, N. and Wanninkhof, R. (2011). Evaluating gas transfer velocity parameterizations using upper ocean radon distributions. *Journal of Geophysical Research,* **116**.

Bender, M. L., Tans, P. P., Ellis, J. T., Orchardo, J. and Habfast, K. (1994). A high precision isotope ratio mass spectrometry method for measuring the O2N2 ratio of air. *Geochimica et Cosmochimica Acta,* **58,** 4751-4758.

Bigeleisen, J. and Mayer, M. G. (1947). Calculation of Equilibrium Constants for Isotopic Exchange Reactions. *The Journal of Chemical Physics,* **15,** 261-267.

Bopp, L. and Le Quéré, C. 2013. Ocean Carbon Cycle. *Surface Ocean–Lower Atmosphere Processes.* American Geophysical Union.

Brown, J., Carrillo, L., Fernand, L., Horsburgh, K. J., Hill, A. E., Young, E. F. and Medler, K. J. (2003). Observations of the physical structure and seasonal jet-like circulation of the Celtic Sea and St. George's Channel of the Irish Sea. *Continental Shelf Research,* **23,** 533-561.

Cassar, N., Barnett, B. A., Bender, M. L., Kaiser, J., Hamme, R. C. and Tilbrook, B. (2009). Continuous High-Frequency Dissolved O2/Ar Measurements by Equilibrator Inlet Mass Spectrometry. *Analytical Chemistry,* **81,** 1855-1864.

Cassar, N., Nevison, C. D. and Manizza, M. (2014). Correcting oceanic O2/Ar-net community production estimates for vertical mixing using N2O observations. *Geophysical Research Letters,* **41,** 8961-8970.

Castro-Morales, K., Cassar, N., Shoosmith, D. R. and Kaiser, J. (2013). Biological production in the Bellingshausen Sea from oxygen-to-argon ratios and oxygen triple isotopes. *Biogeosciences,* **10,** 2273-2291.

Castro-Morales, K. and Kaiser, J. (2012). Using dissolved oxygen concentrations to determine mixed layer depths in the Bellingshausen Sea. *Ocean Science,* **8,** 1-10.

Chen, C.-T. A. 2010. Cross-Boundary Exchanges of Carbon and Nitrogen in Continental Margins. *In:* LIU, K.-K., ATKINSON, L., QUIÑONES, R.andTALAUE-MCMANUS, L. (eds.) *Carbon and Nutrient Fluxes in Continental Margins.* Springer Berlin Heidelberg.

Ciais, P., C. Sabine, G. Bala, L. Bopp, V. Brovkin, J. Canadell, A. Chhabra, R. Defries, J. Galloway, M. Heimann, C. Jones, C. Le Quéré, R.B. Myneni, S. Piao and P. Thornton 2013. Carbon and Other Biogeochemical Cycles. *In:* STOCKER, T. F., D. QIN, G.-K. PLATTNER, M. TIGNOR, S.K. ALLEN, J. BOSCHUNG, A. NAUELS, Y. XIA, V. BEX AND P.M. MIDGLEY (ed.) *Climate Change 2013: The Physical Science Basis. Contribution of Working Group I to the Fifth Assessment Report of the Intergovernmental Panel on Climate Change.* Cambridge, United Kingdom and New York, NY, USA.

Craig, H. and Hayward, T. (1987). Oxygen supersaturation in the ocean: Biological versus physical contributions. *Science,* **235,** 202-205.

Cubasch, U., D. Wuebbles, D. Chen, M.C. Facchini, D. Frame, N. Mahowald, and J.-G. Winther 2013. Introduction. *In:* STOCKER, T. F., D. QIN, G.-K. PLATTNER, M. TIGNOR, S.K. ALLEN, J. BOSCHUNG, A. NAUELS, Y. XIA, V. BEX AND P.M. MIDGLEY (ed.) *Climate Change 2013: The Physical Science Basis. Contribution of Working Group I to the Fifth Assessment Report of the Intergovernmental Panel on Climate Change.* Cambridge, United Kingdom and New York, NY, USA.

Culberson, C. H. (1991). Dissolved oxygen. *WHP Operations and Methods*.

Cullen, J. J. (2001). Primary Production Methods. 2277-2284.

Daniels, C. J., Poulton, A. J., Esposito, M., Paulsen, M. L., Bellerby, R., St John, M. and Martin, A. P. (2015). Phytoplankton dynamics in contrasting early stage North Atlantic spring blooms: composition, succession, and potential drivers. *Biogeosciences,* **12,** 2395-2409.

Davies, J.-M., Hesslein, R. H., Kelly, C. A. and Hecky, R. E. (2003). PCO2 method for measuring photosynthesis and respiration in freshwater lakes. *Journal of Plankton Research,* **25,** 385-395.

Deb, S., Matsushige, K., Fukushima, T., Ikei, M. and Ozaki, N. (1999). In situ measurement of productivity and respiration in aquatic systems by a new box incubation method. *Hydrobiologia,* **394,** 129-144.

Desmarais, D. J. and Hayes, J. M. (1976). Tube cracker for opening glass-sealed ampuls under vacuum. *Analytical Chemistry,* **48,** 1651-1652.

Dixon, W. J. (1950). Analysis of extreme values. *Annals of Mathematical Statistics,* **21,** 488-506.

Eiler, J. M., Clog, M., Magyar, P., Piasecki, A., Sessions, A., Stolper, D., Deerberg, M., Schlueter, H.-J. and Schwieters, J. (2013). A high-resolution gas-source isotope ratio mass spectrometer. *International Journal of Mass Spectrometry,* **335,** 45-56.

Emerson, S., Quay, P. D., Stump, C., Wilbur, D. and Schudlich, R. (1995). Chemical tracers of productivity and respiration in the subtropical Pacific Ocean. *Journal of Geophysical Research,* **100,** 15873.

Emerson, S., Stump, C., Wilbur, D. and Quay, P. (1999). Accurate measurement of O2, N2, and Ar gases in water and the solubility of N2. *Marine Chemistry,* **64,** 337-347.

Eppley, R. W. and Peterson, B. J. (1979). Particulate organic matter flux and planktonic new production in the deep ocean. *Nature,* **282,** 677-680.

Falkowski, P. G. a. a. R., John A 2007. *Aquatic Photosynthesis*, Princeton University Press.

Fujiki, T., Hosaka, T., Kimoto, H., Ishimaru, T. and Saino, T. (2008). In situ observation of phytoplankton productivity by an underwater profiling buoy system: use of fast repetition rate fluorometry. *Marine Ecology Progress Series,* **353,** 81-88.

García, H. E. and Gordon, L. I. (1992). Oxygen Solubility in Seawater: Better Fitting Equations. *Limnology and Oceanography,* **37,** 1307-1312.

García-Martín, E. E., Daniels, C. J., Davidson, K., Lozano, J., Mayers, K. M. J., Mcneill, S., Mitchell, E., Poulton, A. J., Purdie, D. A., Tarran, G. A., Whyte, C. and Robinson, C. (2017). Plankton community respiration and bacterial metabolism in a North Atlantic Shelf Sea during spring bloom development (April 2015). *Progress in Oceanography*.

Garlick, G. D. (1974). The stable isotopes of oxygen, carbon, and hydrogen in the marine environment. *The Sea,* **5,** 393-425.

Gloël, J. 2012. *Triple oxygen isotopes and oxygen/argon ratio measurements to enhance coastal and open ocean production/respiration comparisons.* Doctor of Philosophy, University of East Anglia.

Goldman, J. A., Kranz, S. A., Young, J. N., Tortell, P. D., Stanley, R. H., Bender, M. L. and Morel, F. M. (2015). Gross and net production during the spring bloom along the Western Antarctic Peninsula. *New Phytol,* **205,** 182-91.

GonzáLez-Posada, A. M. 2012. *Biological oxygen production from oxygen-to-argon rations and oxygen isotopologues in the Atlantic Ocean.* Doctor of Philosophy, University of East Anglia.

Grasshoff, K., Kremling, K. Ehrhardt, M. 2007. *Frontmatter, in Methods of Seawater Analysis.,* Weinheim, Germany, Wiley-VCH Verlag GmbH.

Gruber, N., Keeling, C. D. and Stocker, T. F. (1998). Carbon-13 constraints on the seasonal inorganic carbon budget at the BATS site in the northwestern Sargasso Sea. *Deep Sea Research Part I: Oceanographic Research Papers,* **45,** 673-717.

Hamme, R. C., Cassar, N., Lance, V. P., Vaillancourt, R. D., Bender, M. L., Strutton, P. G., Moore, T. S., Degrandpre, M. D., Sabine, C. L., Ho, D. T. and Hargreaves, B. R. (2012). Dissolved O2/Ar and other methods reveal rapid changes in productivity during a Lagrangian experiment in the Southern Ocean. *Journal of Geophysical Research,* **117**.

Hamme, R. C. and Emerson, S. R. (2004). The solubility of neon, nitrogen and argon in distilled water and seawater. *Deep Sea Research Part I: Oceanographic Research Papers,* **51,** 1517-1528.

Hancke, K., Dalsgaard, T., Sejr, M. K., Markager, S. and Glud, R. N. (2015). Phytoplankton Productivity in an Arctic Fjord (West Greenland): Estimating Electron Requirements for Carbon Fixation and Oxygen Production. *PLoS One,* **10,** e0133275.

Haskell, W. Z., Prokopenko, M. G., Hammond, D. E., Stanley, R. H. R. and Sandwith, Z. O. (2017). Annual cyclicity in export efficiency in the inner Southern California Bight. *Global Biogeochemical Cycles,* **31,** 357-376.

Helman, Y., Barkan, E., Eisenstadt, D., Luz, B. and Kaplan, A. (2005). Fractionation of the three stable oxygen isotopes by oxygen-producing and oxygen-consuming reactions in photosynthetic organisms. *Plant Physiology,* **138,** 2292-8.

Hendricks, M. B., Bender, M. L. and Barnett, B. A. (2004). Net and gross O2 production in the southern ocean from measurements of biological O2 saturation

and its triple isotope composition. *Deep Sea Research Part I: Oceanographic Research Papers,* **51,** 1541-1561.

Hendricks, M. B., Bender, M. L., Barnett, B. A., Strutton, P. and Chavez, F. P. (2005). Triple oxygen isotope composition of dissolved O2 in the equatorial Pacific: A tracer of mixing, production, and respiration. *Journal of Geophysical Research,* **110**.

Henson, S., Cole, H., Beaulieu, C. and Yool, A. (2013). The impact of global warming on seasonality of ocean primary production. *Biogeosciences,* **10,** 4357-4369.

Hickman, A. E., Moore, C. M., Sharples, J., Lucas, M. I., Tilstone, G. H., Krivtsov, V. and Holligan, P. M. (2012). Primary production and nitrate uptake within the seasonal thermocline of a stratified shelf sea. *Marine Ecology Progress Series,* **463,** 39-57.

Ho, D. T., Law, C. S., Smith, M. J., Schlosser, P., Harvey, M. and Hill, P. (2006). Measurements of air-sea gas exchange at high wind speeds in the Southern Ocean: Implications for global parameterizations. *Geophysical Research Letters,* **33**.

Hoch, G. and Kok, B. (1963). A mass spectrometer inlet system for sampling gases dissolved in liquid phases. *Archives of Biochemistry and Biophysics,* **101,** 160-170.

Hoefs, J. 2004. *Stable isotope geochemistry*, Springer.

Holt, J. T., James, I. D. and Jones, J. E. (2001). An s coordinate density evolving model of the northwest European continental shelf: 2. Seasonal currents and tides. *Journal of Geophysical Research: Oceans,* **106,** 14035-14053.

Huang, K., Ducklow, H., Vernet, M., Cassar, N. and Bender, M. L. (2012). Export production and its regulating factors in the West Antarctica Peninsula region of the Southern Ocean. *Global Biogeochemical Cycles,* **26,** n/a-n/a.

Jochmann, M. A. and Schmidt, T. C. 2012. *Compound-specific Stable Isotope Analysis*, Royal Society of Chemistry.

Joint, I. and Groom, S. B. (2000). Estimation of phytoplankton production from space: current status and future potential of satellite remote sensing. *Journal of Experimental Marine Biology and Ecology,* **250,** 233-255.

Joint, I., Wollast, R., Chou, L., Batten, S., Elskens, M., Edwards, E., Hirst, A., Burkill, P., Groom, S., Gibb, S., Miller, A., Hydes, D., Dehairs, F., Antia, A., Barlow, R., Rees, A., Pomroy, A., Brockmann, U., Cummings, D., Lampitt, R., Loijens, M., Mantoura, F., Miller, P., Raabe, T., Alvarez-Salgado, X., Stelfox, C. and Woolfenden, J. (2001). Pelagic production at the Celtic Sea shelf break. *Deep Sea Research Part II: Topical Studies in Oceanography,* **48,** 3049-3081.

Joint, I. R. O., N. J. P Pomroy, A. J (1986). Seasonal production of photosynthetic picoplankton and nanoplankton in the Celtic Sea. *Marine Ecology Progress Series,* **28,** 251-258.

Jonsson, B. F., Doney, S. C., Dunne, J. and Bender, M. (2013). Evaluation of the Southern Ocean O2/Ar-based NCP estimates in a model framework. *Journal of Geophysical Research: Biogeosciences,* **118,** 385-399.

Juranek, L. W., Hamme, R. C., Kaiser, J., Wanninkhof, R. and Quay, P. D. (2010). Evidence of O2 consumption in underway seawater lines: Implications for air-sea O2 and CO2 fluxes. *Geophysical Research Letters,* **37**.

Juranek, L. W. and Quay, P. D. (2005). In vitro and in situ gross primary and net community production in the North Pacific Subtropical Gyre using labeled and natural abundance isotopes of dissolved O2. *Global Biogeochemical Cycles,* **19,** n/a-n/a.

Juranek, L. W. and Quay, P. D. (2013). Using triple isotopes of dissolved oxygen to evaluate global marine productivity. *Annual review of marine science,* **5,** 503-24.

Juranek, L. W., Quay, P. D., Feely, R. A., Lockwood, D., Karl, D. M. and Church, M. J. (2012). Biological production in the NE Pacific and its influence on air-sea CO2flux: Evidence from dissolved oxygen isotopes and O2/Ar. *Journal of Geophysical Research,* **117**.

Jurikova, H., Guha, T., Abe, O., Shiah, F.-K., Wang, C.-H. and Liang, M.-C. (2016). Variations in triple isotope composition of dissolved oxygen and primary production in a subtropical reservoir. *Biogeosciences,* **13,** 6683-6698.

Kaiser, J. (2008). Reformulated 17O correction of mass spectrometric stable isotope measurements in carbon dioxide and a critical appraisal of historic 'absolute' carbon and oxygen isotope ratios. *Geochimica et Cosmochimica Acta,* **72,** 1312-1334.

Kaiser, J. (2011a). Corrigendum to "Technical note: Consistent calculation of aquatic gross production from oxygen triple isotope measurements" published in Biogeosciences, 8, 1793–1811, 2011. *Biogeosciences,* **8,** 2561-2565.

Kaiser, J. (2011b). Technical note: Consistent calculation of aquatic gross production from oxygen triple isotope measurements. *Biogeosciences,* **8,** 1793-1811.

Kaiser, J. and Abe, O. (2012). Reply to Nicholson's comment on "Consistent calculation of aquatic gross production from oxygen triple isotope measurements" by Kaiser (2011). *Biogeosciences,* **9,** 2921-2933.

Kaiser, J., Reuer, M. K., Barnett, B. and Bender, M. L. (2005). Marine productivity estimates from continuous O2/Ar ratio measurements by membrane inlet mass spectrometry. *Geophysical Research Letters,* **32**.

Kaiser, J., Reuer, M., Barnett, B., Bender, M. (2005). Marine productivity estimates from continuous O2/Ar ratio measurements by membrane inlet mass spectrometry. *Geophysical Research Letters,* **32**.

Kaiser, J., Röckmann, T. and Brenninkmeijer, C. a. M. (2004). Contribution of mass-dependent fractionation to the oxygen isotope anomaly of atmospheric nitrous oxide. *Journal of Geophysical Research D: Atmospheres,* **109,** D03305 1-10.

Kana, T. M., Darkangelo, C., Oldham, J. B., Bennett, G. E. and Cornwell, J. C. (1994). Membrane inlet mass spectrometer for rapid high-precision determination of N2, O2, and Ar in environmental water samples. *Analytical Chemistry,* **66,** 4166-4170.

Kara, A. B., Rochford, P. A. and Hurlburt, H. E. (2000). An optimal definition for ocean mixed layer depth. *Journal of Geophysical Research: Oceans,* **105,** 16803-16821.

Keeling, R. F., Stephens, B. B., Najjar, R. G., Doney, S. C., Archer, D. and Heimann, M. (1998). Seasonal variations in the atmospheric O2/N2ratio in relation to the kinetics of air-sea gas exchange. *Global Biogeochemical Cycles,* **12,** 141-163.

Kendall, C. and Caldwell, E. A. 1998. Chapter 2 - Fundamentals of Isotope Geochemistry. *Isotope Tracers in Catchment Hydrology.* Amsterdam: Elsevier.

Kendall, C. and Mcdonnell, J. J. 1998. *Isotope tracers in catchment hydrology*.

Kimmance, S. A., Wilson, W. H. and Archer, S. D. (2007). Modified dilution technique to estimate viral versus grazing mortality of phytoplankton: limitations associated with method sensitivity in natural waters. *Aquatic Microbial Ecology,* **49,** 207-222.

Kitidis, V., Tilstone, G. H., Serret, P., Smyth, T. J., Torres, R. and Robinson, C. (2014). Oxygen photolysis in the Mauritanian upwelling: Implications for net community production. *Limnology and Oceanography,* **59,** 299-310.

Knox, M., Quay, P. D. and Wilbur, D. (1992). Kinetic isotopic fractionation during air-water gas transfer of O2, N2, CH4, and H2. *Journal of Geophysical Research,* **97,** 20335.

Kolber, Z. and Falkowski, P. G. (1993). Use of active fluorescence to estimate phytoplankton photosynthesis in situ. *Limnology and Oceanography,* **38,** 1646-1665.

Kolber, Z. S., Prášil, O. and Falkowski, P. G. (1998). Measurements of variable chlorophyll fluorescence using fast repetition rate techniques: defining methodology and experimental protocols. *Biochimica et Biophysica Acta (BBA) - Bioenergetics,* **1367,** 88-106.

Lämmerzahl, P., Röckmann, T., Brenninkmeijer, C. a. M., Krankowsky, D. and Mauersberger, K. (2002). Oxygen isotope composition of stratospheric carbon dioxide. *Geophysical Research Letters,* **29,** 23-1 - 23-4.

Landry, M. R. and Hassett, R. P. (1982). Estimating the grazing impact of marine micro-zooplankton. *Marine Biology,* **67,** 283-288.

Lawrenz, E., Silsbe, G., Capuzzo, E., Ylostalo, P., Forster, R. M., Simis, S. G., Prasil, O., Kromkamp, J. C., Hickman, A. E., Moore, C. M., Forget, M. H., Geider, R. J. and Suggett, D. J. (2013). Predicting the electron requirement for carbon fixation in seas and oceans. *PLoS One,* **8,** e58137.

Laws, E. A. (1991). Photosynthetic quotients, new production and net community production in the open ocean. *Deep Sea Research Part A. Oceanographic Research Papers,* **38,** 143-167.

Laws, E. A., Falkowski, P. G., Smith, W. O., Ducklow, H. and Mccarthy, J. J. (2000). Temperature effects on export production in the open ocean. *Global Biogeochemical Cycles,* **14,** 1231-1246.

Le Quéré, C., Takahashi, T., Buitenhuis, E. T., Rödenbeck, C. and Sutherland, S. C. (2010). Impact of climate change and variability on the global oceanic sink of CO2. *Global Biogeochemical Cycles,* **24,** n/a-n/a.

Lee, S. H., Whitledge, T. E. and Kang, S.-H. (2007). Recent carbon and nitrogen uptake rates of phytoplankton in Bering Strait and the Chukchi Sea. *Continental Shelf Research,* **27,** 2231-2249.

Lefebvre, S., Mouget, J. L., Loret, P., Rosa, P. and Tremblin, G. (2007). Comparison between fluorimetry and oximetry techniques to measure photosynthesis in the diatom Skeletonema costatum cultivated under simulated seasonal conditions. *Journal of Photochem istry and Photobiology B-biology,* **86,** 131-9.

Liss, P. and Merlivat, L. 1986. Air-Sea Gas Exchange Rates: Introduction and Synthesis. *In:* BUAT-MÉNARD, P. (ed.) *The Role of Air-Sea Exchange in Geochemical Cycling.* Springer Netherlands.

Liss, P. S. and Slater, P. G. (1974). Flux of Gases across the Air-Sea Interface. *Nature,* **247,** 181-184.

Lutz, M. J., Caldeira, K., Dunbar, R. B. and Behrenfeld, M. J. (2007). Seasonal rhythms of net primary production and particulate organic carbon flux to depth describe the efficiency of biological pump in the global ocean. *Journal of Geophysical Research,* **112**.

Luz, B. and Barkan, E. (2000). Assessment of oceanic productivity with the triple-isotope composition of dissolved oxygen. *Science,* **288,** 2028-2031.

Luz, B. and Barkan, E. (2005). The isotopic ratios 17O/16O and 18O/16O in molecular oxygen and their significance in biogeochemistry. *Geochimica et Cosmochimica Acta,* **69,** 1099-1110.

Luz, B. and Barkan, E. (2009). Net and gross oxygen production from O2/Ar, 17O/16O and 18O/16O ratios. *Aquatic Microbial Ecology,* **56,** 133-145.

Luz, B., Barkan, E., Bender, M. L., Thiemens, M. H. and Boering, K. A. (1999). Triple-isotope composition of atmospheric oxygen as a tracer of biosphere productivity. *Nature,* **400,** 547-550.

Luz, B., Barkan, E., Sagi, Y. and Yacobi, Y. Z. (2002). Evaluation of community respiratory mechanisms with oxygen isotopes: A case study in Lake Kinneret. *Limnology and Oceanography,* **47,** 33-42.

Luz, B., Barkan, E. and Severinghaus, J. P. (2014). The Stable Isotopic Composition of Atmospheric O2. 363-383.

Macintyre, H. L., Kana, T. M. and Geider, R. J. (2000). The effect of water motion on short-term rates of photosynthesis by marine phytoplankton. *Trends in Plant Science,* **5,** 12-17.

Manning, C. C., Stanley, R. H. R., Nicholson, D. P., Loose, B., Lovely, A., Schlosser, P. and Hatcher, B. G. (2017). Changes in gross oxygen production, net oxygen production, and air-water gas exchange during seasonal ice melt in the Bras d'Or Lake, a Canadian estuary. *Biogeosciences Discussions***,** 1-38.

Mariotti, A., Germon, J. C., Hubert, P., Kaiser, P., Letolle, R., Tardieux, A. and Tardieux, P. (1981). Experimental determination of nitrogen kinetic isotope fractionation: Some principles; illustration for the denitrification and nitrification processes. *Plant and Soil,* **62,** 413-430.

Marra, J. (2002). Approaches to the measurement of plankton production. *Phytoplankton productivity: Carbon assimilation in marine and freshwater ecosystems***,** 78-108.

Matsuhisa, Y., Goldsmith, J. R. and Clayton, R. N. (1978). Mechanisms of hydrothermal crystallization of quartz at 250°C and 15 kbar. *Geochimica et Cosmochimica Acta,* **42,** 173-182.

Migné, A., Davoult, D., Spilmont, N., Menu, D., Boucher, G., Gattuso, J. P. and Rybarczyk, H. (2002). A closed-chamber CO2-flux method for estimating intertidal primary production and respiration under emersed conditions. *Marine Biology,* **140,** 865-869.

Mitchell, B. G. (1994). Coastal zone color scanner retrospective. *Journal of Geophysical Research-Oceans,* **99,** 7291-7292.

Moat, B. I., Yelland, M. J., Pascal, R. W. and Molland, A. F. (2005). An overview of the airflow distortion at anemometer sites on ships. *International Journal of Climatology,* **25,** 997-1006.

Monse, E. U. (1960). Calculation of Equilibrium Constants for Several Isotope Exchange Reactions Involving N2O4. *The Journal of Chemical Physics,* **33,** 312-314.

Mook, W. G. G., Joel R.; Meijer, Harro A.J. (2001). Environmental isotopes in the hydrological cycle: principles and applications. **39**.

Moore, C. M., David, S., Patrick, M. H., Jonathan, S., Edward, R. A., Mike, I. L., Tom, P. R., Neil, R. F., John, H. S. and David, J. H. (2003). Physical controls on phytoplankton physiology and production at a shelf sea front: a fast repetition-rate fluorometer based field study. *Marine Ecology Progress Series,* **259,** 29-45.

Moore, C. M., Suggett, D. J., Hickman, A. E., Kim, Y.-N., Tweddle, J. F., Sharples, J., Geider, R. J. and Holligan, P. M. (2006). Phytoplankton photoacclimation and

photoadaptation in response to environmental gradients in a shelf sea. *Limnology and Oceanography,* **51,** 936-949.
Muller, P. 1994. Glossary of terms used in physical organic chemistry (IUPAC Recommendations 1994). *Pure and Applied Chemistry.*
Muller-Karger, F. E. (2005). The importance of continental margins in the global carbon cycle. *Geophysical Research Letters,* **32**.
Munro, D. R., Quay, P. D., Juranek, L. W. and Goericke, R. (2013). Biological production rates off the Southern California coast estimated from triple O2isotopes and O2: Ar gas ratios. *Limnology and Oceanography,* **58,** 1312-1328.
Neumann, B., Vafeidis, A. T., Zimmermann, J. and Nicholls, R. J. (2015). Future coastal population growth and exposure to sea-level rise and coastal flooding--a global assessment. *PLoS One,* **10,** e0118571.
Nicholson, D., Stanley, R. H. R. and Doney, S. C. (2014). The triple oxygen isotope tracer of primary productivity in a dynamic ocean model. *Global Biogeochemical Cycles,* **28,** 538-552.
Nicholson, D. P., Stanley, R. H. R., Barkan, E., Karl, D. M., Luz, B., Quay, P. D. and Doney, S. C. (2012). Evaluating triple oxygen isotope estimates of gross primary production at the Hawaii Ocean Time-series and Bermuda Atlantic Time-series Study sites. *Journal of Geophysical Research,* **117**.
Nielsen, E. S. (1952). The Use of Radio-active Carbon (C14) for Measuring Organic Production in the Sea. *ICES Journal of Marine Science,* **18,** 117-140.
Nightingale, P. D., Malin, G., Law, C. S., Watson, A. J., Liss, P. S., Liddicoat, M. I., Boutin, J. and Upstill-Goddard, R. C. (2000). In situ evaluation of air-sea gas exchange parameterizations using novel conservative and volatile tracers. *Global Biogeochemical Cycles,* **14,** 373-387.
Nolan, G. and O'boyle, S. (2011). The Influence of Water Column Stratification on Dissolved Oxygen Levels in Coastal and Shelf Waters around Ireland. *Biology & Environment: Proceedings of the Royal Irish Academy,* **110,** 195-209.
Osborn, T. R. (1980). Estimates of the local rate of vertical diffusion from dissipation measurements. *J. Phys. Oceanogr.,* **10,** 83-89.
Painting, S., Collingridge, K., Durand, D., Grémare, A., Bernard, G. and Puillat Felix, I. 2017. JERICO-NEXT. Review of monitoring of environmental threats and pressures in Europe.
Palevsky, H. I., Quay, P. D., Lockwood, D. E. and Nicholson, D. P. (2016). The annual cycle of gross primary production, net community production, and export efficiency across the North Pacific Ocean. *Global Biogeochemical Cycles,* **30,** 361-380.
Palevsky, H. I., Ribalet, F., Swalwell, J. E., Cosca, C. E., Cokelet, E. D., Feely, R. A., Armbrust, E. V. and Quay, P. D. (2013). The influence of net community production and phytoplankton community structure on CO2uptake in the Gulf of Alaska. *Global Biogeochemical Cycles,* **27,** 664-676.
Palmer, M. R., Inall, M. E. and Sharples, J. (2013). The physical oceanography of Jones Bank: A mixing hotspot in the Celtic Sea. *Progress in Oceanography,* **117,** 9-24.
Paterson, H. L., Knott, B., Koslow, A. J. and Waite, A. M. (2008). The grazing impact of microzooplankton off south west Western Australia: as measured by the dilution technique. *Journal of Plankton Research,* **30,** 379-392.
Pingree, R. D., Griffiths, D. K. and Mardell, G. T. (1984). The Structure of the Internal Tide at the Celtic Sea Shelf Break. *Journal of the Marine Biological Association of the United Kingdom,* **64,** 99-113.

Pingree, R. D., Holligan, P. M., Mardell, G. T. and Head, R. N. (1976). The influence of physical stability on spring, summer and autumn phytoplankton blooms in the Celtic Sea. *Journal of the Marine Biological Association of the United Kingdom,* **56,** 845-873.

Poulton, A. J., Stinchcombe, M. C., Achterberg, E. P., Bakker, D. C. E., Dumousseaud, C., Lawson, H. E., Lee, G. A., Richier, S., Suggett, D. J. and Young, J. R. (2014). Coccolithophores on the north-west European shelf: calcification rates and environmental controls. *Biogeosciences,* **11,** 3919-3940.

Prokopenko, M. G., Pauluis, O. M., Granger, J. and Yeung, L. Y. (2011). Exact evaluation of gross photosynthetic production from the oxygen triple-isotope composition of O2: Implications for the net-to-gross primary production ratios. *Geophysical Research Letters,* **38**.

Prytherch, J., Brooks, I. M., Crill, P. M., Thornton, B. F., Salisbury, D. J., Tjernström, M., Anderson, L. G., Geibel, M. C. and Humborg, C. (2017). Direct determination of the air-sea CO2

gas transfer velocity in Arctic sea ice regions. *Geophysical Research Letters*.

Quay, P., Stutsman, J. and Steinhoff, T. (2012). Primary production and carbon export rates across the subpolar N. Atlantic Ocean basin based on triple oxygen isotope and dissolved O2and Ar gas measurements. *Global Biogeochemical Cycles,* **26**.

Quay, P. D., Emerson, S., Wilbur, D. O., Stump, C. and Knox, M. (1993). The δ18O of dissolved O2 in the surface waters of the subarctic Pacific: a tracer of biological productivity. *Journal of Geophysical Research,* **98,** 8447-8458.

Quay, P. D., Peacock, C., Björkman, K. and Karl, D. M. (2010). Measuring primary production rates in the ocean: Enigmatic results between incubation and non-incubation methods at Station ALOHA. *Global Biogeochemical Cycles,* **24**.

Rees, A. P., Joint, I. and Donald, K. M. (1999). Early spring bloom phytoplankton-nutrient dynamics at the Celtic Sea Shelf Edge. *Deep Sea Research Part I: Oceanographic Research Papers,* **46,** 483-510.

Reuer, M. K., Barnett, B. A., Bender, M. L., Falkowski, P. G. and Hendricks, M. B. (2007). New estimates of Southern Ocean biological production rates from O2/Ar ratios and the triple isotope composition of O2. *Deep Sea Research Part I: Oceanographic Research Papers,* **54,** 951-974.

Richier, S., Achterberg, E. P., Dumousseaud, C., Poulton, A. J., Suggett, D. J., Tyrrell, T., Zubkov, M. V. and Moore, C. M. (2014). Phytoplankton responses and associated carbon cycling during shipboard carbonate chemistry manipulation experiments conducted around Northwest European shelf seas. *Biogeosciences,* **11,** 4733-4752.

Robinson, C., Tilstone, G. H., Rees, A. P., Smyth, T. J., Fishwick, J. R., Tarran, G. A., Luz, B., Barkan, E. and David, E. (2009). Comparison of in vitro and in situ plankton production determinations. *Aquatic Microbial Ecology,* **54,** 13-34.

Sakshaug, E., Bricaud, A., Dandonneau, Y., Falkowski, P. G., Kiefer, D. A., Legendre, L., Morel, A., Parslow, J. and Takahashi, M. (1997). Parameters of photosynthesis: Definitions, theory and interpretation of results. *Journal of Plankton Research,* **19,** 1637-1670.

Sarma, V., Abe, O., Hashimoto, S., Hinuma, A. and Saino, T. (2005). Seasonal variations in triple oxygen isotopes and gross oxygen production in the Sagami Bay, central Japan. *Limnology and oceanography,* **50,** 544-552.

Sarma, V., Abe, O. and Saino, T. (2003). Chromatographic separation of nitrogen, argon, and oxygen in dissolved air for determination of triple oxygen isotopes by dual-inlet mass spectrometry. *Analytical Chemistry,* **75,** 4913-4917.

Sarma, V. V., Abe, O., Yoshida, N. and Saino, T. (2006). Continuous shipboard sampling system for determination of triple oxygen isotopes and O2/Ar ratio by dual-inlet mass spectrometry. *Rapid Commun Mass Spectrom,* **20,** 3503-8.

Schuback, N., Schallenberg, C., Duckham, C., Maldonado, M. T. and Tortell, P. D. (2015). Interacting Effects of Light and Iron Availability on the Coupling of Photosynthetic Electron Transport and CO2-Assimilation in Marine Phytoplankton. *PLoS One,* **10,** e0133235.

Seguro, I., García, C. M., Papaspyrou, S., Gálvez, J. A., García-Robledo, E., Navarro, G., Soria-Píriz, S., Aguilar, V., Lizano, O. G., Morales-Ramírez, A. and Corzo, A. (2015). Seasonal changes of the microplankton community along a tropical estuary. *Regional Studies in Marine Science*.

Seguro, I., Marca, A. D., Painting, S. J., Shutler, J. D., Suggett, D. J. and Kaiser, J. (2017). High-resolution net and gross biological production during a Celtic Sea spring bloom. *Progress in Oceanography*.

Sharples, J., Ellis, J. R., Nolan, G. and Scott, B. E. (2013). Fishing and the oceanography of a stratified shelf sea. *Progress in Oceanography,* **117,** 130-139.

Sharples, J., Moore, C. M., Hickman, A. E., Holligan, P. M., Tweddle, J. F., Palmer, M. R. and Simpson, J. H. (2009). Internal tidal mixing as a control on continental margin ecosystems. *Geophysical Research Letters,* **36**.

Sharples, J., Ross, O. N., Scott, B. E., Greenstreet, S. P. R. and Fraser, H. (2006). Inter-annual variability in the timing of stratification and the spring bloom in the North-western North Sea. *Continental Shelf Research,* **26,** 733-751.

Simpson, J. H. and Sharples, J. 2012. *Introduction to the Physical and Biological Oceanography of Shelf Seas*, Cambridge University Press.

Song, H. J., Lee, J. H., Kim, G. W., Ahn, S. H., Joo, H.-M., Jeong, J. Y., Yang, E. J., Kang, S.-H. and Lee, S. H. (2016). In-situ measured primary productivity of ice algae in Arctic sea ice floes using a new incubation method. *Ocean Science Journal,* **51,** 387-396.

Soria-Píriz, S., García-Robledo, E., Papaspyrou, S., Aguilar, V., Seguro, I., Acuña, J., Morales, Á. and Corzo, A. (2017). Size fractionated phytoplankton biomass and net metabolism along a tropical estuarine gradient. *Limnology and Oceanography*.

Stanley, R. H. R., Jenkins, W. J. and Doney, S. C. (2006). Quantifying seasonal air-sea gas exhange processes using noble gas time-series: A design experiment. *Journal of Marine Research,* **64,** 267-295.

Stanley, R. H. R., Jenkins, W. J., Lott, D. E. and Doney, S. C. (2009). Noble gas constraints on air-sea gas exchange and bubble fluxes. *Journal of Geophysical Research: Oceans,* **114,** C11020.

Stanley, R. H. R., Kirkpatrick, J. B., Cassar, N., Barnett, B. A. and Bender, M. L. (2010). Net community production and gross primary production rates in the western equatorial Pacific. *Global Biogeochemical Cycles,* **24,** n/a-n/a.

Stephens, R. J. U. a. J. A. (2007). SEA 8 Technical Report. *Hidrography*.

Suggett, D., Kraay, G., Holligan, P., Davey, M., Aiken, J. and Geider, R. (2001). Assessment of photosynthesis in a spring cyanobacterial bloom by use of a fast repetition rate fluorometer. *Limnology and Oceanography,* **46,** 802-810.

Suggett, D. J., Macintyre, H. L., Kana, T. M. and Geider, R. J. (2009). Comparing electron transport with gas exchange: parameterising exchange rates between alternative photosynthetic currencies for eukaryotic phytoplankton. *Aquatic Microbial Ecology,* **56,** 147-162.

Suggett, D. J., Moore, C. M., Marañón, E., Omachi, C., Varela, R. A., Aiken, J. and Holligan, P. M. (2006). Photosynthetic electron turnover in the tropical and subtropical Atlantic Ocean. *Deep Sea Research Part II: Topical Studies in Oceanography,* **53,** 1573-1592.

Sweeney, C., Gloor, E., Jacobson, A. R., Key, R. M., Mckinley, G., Sarmiento, J. L. and Wanninkhof, R. (2007). Constraining global air-sea gas exchange for CO2 with recent bomb 14C measurements. *Global Biogeochemical Cycles,* **21**.

Thiemens, M. H., Chakraborty, S. and Jackson, T. L. (2014). Decadal Δ17O record of tropospheric CO2: Verification of a stratospheric component in the troposphere. *Journal of Geophysical Research: Atmospheres,* **119,** 6221-6229.

Thiemens, M. H., Jackson, T., Zipf, E. C., Erdman, P. W. and Van Egmond, C. (1995a). Carbon dioxide and oxygen isotope anomalies in the mesosphere and stratosphere. *Science,* **270,** 969-972.

Thiemens, M. H., Jackson, T. L. and Brenninkmeijer, C. a. M. (1995b). Observation of a mass independent oxygen isotopic composition in terrestrial stratospheric CO2, the link to ozone chemistry, and the possible occurrence in the Martian atmosphere. *Geophysical Research Letters,* **22,** 255-257.

Tilstone, G. H., Xie, Y.-Y., Robinson, C., Serret, P., Raitsos, D. E., Powell, T., Aranguren-Gassis, M., Garcia-Martin, E. E. and Kitidis, V. (2015). Satellite estimates of net community production indicate predominance of net autotrophy in the Atlantic Ocean. *Remote Sensing of Environment,* **164,** 254-269.

Tiselius, P. and Kuylenstierna, B. (1996). Growth and decline of a diatom spring bloom phytoplankton species composition, formation of marine snow and the role of heterotrophic dinoflagellates. *Journal of Plankton Research,* **18,** 133-155.

Tolleter, D., Chochois, V., Poire, R., Price, G. D. and Badger, M. R. (2017). Measuring CO_2 and HCO_3^- permeabilities of isolated chloroplasts using a MIMS-18O approach. *Journal of Experimental Botany,* **68,** 3915-3924.

Tortell, P. D. (2005). Dissolved gas measurements in oceanic waters made by membrane Inlet mass spectrometry. *Limnology and Oceanography: Methods,* **3,** 24-37.

Tremblay, J.-E., Klein, B., Legendre, L., Rivkin, R. B. and Therriault, J.-C. (1997). Estimation of f-ratios in oceans based on phytoplankton size structure. *Limnology and Oceanography,* **42,** 595-601.

Urey, H. C. (1947). The thermodynamic properties of isotopic substances. *Journal of the Chemical Society***,** 562-581.

Van Der Meer, A. 2015. *Constraining air-sea equilibrium and biological end-members for marine gross productivity estimates using oxygen triple isotopes.* MSc by Research, University of East Anglia.

Wanninkhof, R. (1992). Relationship between wind speed and gas exchange over the ocean. *Journal of Geophysical Research,* **97,** 7373-7382.

Wanninkhof, R. (2014). Relationship between wind speed and gas exchange over the ocean revisited. *Limnology and Oceanography: Methods,* **12,** 351-362.

Wanninkhof, R., Asher, W. E., Ho, D. T., Sweeney, C. and Mcgillis, W. R. (2009). Advances in quantifying air-sea gas exchange and environmental forcing. *Annual Review of Marine Science,* **1,** 213-44.

Wanninkhof, R. and Knox, M. (1996). Chemical enhancement of CO2 exchange in natural waters. *Limnology and Oceanography,* **41,** 689-697.

Wanninkhof, R. and Mcgillis, W. R. (1999). A cubic relationship between air-sea CO2 exchange and wind speed. *Geophysical Research Letters,* **26,** 1889-1892.

Wanninkhof, R., Park, G.-H., Takahashi, T., Feely, R. A., Bullister, J. L. and Doney, S. C. (2013). Changes in deep-water CO2 concentrations over the last several decades determined from discrete pCO2measurements. *Deep Sea Research Part I: Oceanographic Research Papers,* **74,** 48-63.

Wanninkhof, R. I. K., Ledwell, J. R. and Broecker, W. S. (1985). Gas Exchange-Wind Speed Relation Measured with Sulfur Hexafluoride on a Lake. *Science,* **227,** 1224-1226.

Webb, W. L., Newton, M. and Starr, D. (1974). Carbon dioxide exchange of Alnus rubra. *Oecologia,* **17,** 281-291.

Wieser, M. E. and Berglund, M. (2009). Atomic weights of the elements 2007 (IUPAC Technical Report). *Pure and Applied Chemistry,* **81**.

Wilhelm, C., Becker, A., Toepel, J., Vieler, A. and Rautenberger, R. (2004). Photophysiology and primary production of phytoplankton in freshwater. *Physiologia Plantarum,* **120,** 347-357.

Winkler, L. W. (1888). Die Bestimmung des im Wasser gelösten Sauerstoffes. *Berichte der deutschen chemischen Gesellschaft,* **21,** 2843-2854.

Zhu, Y., Ishizaka, J., Tripathy, S., Wang, S., Mino, Y., Matsuno, T. and Suggett, D. (2016). Variation of the photosynthetic electron transfer rate and electron requirement for daily net carbon fixation in Ariake Bay, Japan. *Journal of Oceanography***,** 1-16.

Zhu, Y., Ishizaka, J., Tripathy, S. C., Wang, S., Sukigara, C., Goes, J., Matsuno, T. and Suggett, D. J. (2017). Relationship between light, community composition and the electron requirement for carbon fixation in natural phytoplankton. *Marine Ecology Progress Series,* **580,** 83-100.